WATER-SOLUBLE POLYISOCYANOPEPTIDES

Development of multifunctional bioconjugates for biomedical applications

ROEL HAMMINK

Water-soluble polyisocyanopeptides

Development of multifunctional bioconjugates for biomedical applications

Proefschrift

ter verkrijging van de graad van doctor aan de Radboud Universiteit Nijmegen op gezag van de rector magnificus prof. dr. J.H.J.M. van Krieken, volgens besluit van het college van decanen in het openbaar te verdedigen op woensdag 16 november 2016 om 10:30 uur precies

door

Roelof Hammink
geboren op 29 juli 1986
te Hengelo

Table of Contents

Table of contents

1

General introduction: Applications of biofunctional water-soluble polyisocyanopeptides
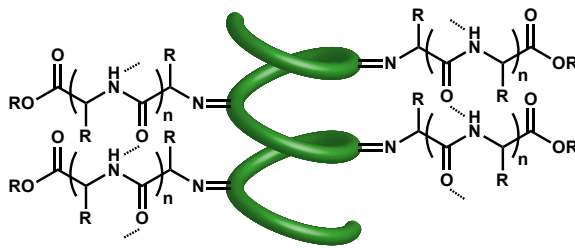
Polyisocyanopeptide

Chapter 1: Applications of biofunctional water-soluble polyisocyanopeptides

Water-soluble polyisocyanopeptides are semi-flexible polymers that can form hydrogels under certain conditions. Their unique properties make these polymers attractive for a large number of biological applications, ranging from drug delivery and diagnostics to tissue engineering and regenerative medicine. This chapter provides a general overview of this new class of polymers. Following a description of the synthesis and characteristics of polyisocyanides and polyisocyanopeptides, the new subclass of water-soluble polyisocyanopeptides is introduced. This chapter focuses on the synthesis as well as on the unique properties of these interesting molecules. It further introduces possible strategies for the biofunctionalization of these polymers in the context of potential applications.

1.1. History of polyisocyanides and polyisocyanopeptides

Polyisocyanides are prepared by the polymerization of isocyanides (Scheme 1.1a). Isocyanides were already discovered in the 1860s[1,2], but only explored further after Ugi introduced an easy synthesis of isocyanides in 1958.[3] The driving force for polymerization is the conversion of the divalent carbon atom of the isocyanide monomer into a tetravalent carbon atom in the polymer, resulting in a heat of polymerization of about 81 kJ/mol.[4] Upon polymerization, a polymer backbone fully consisting of carbon-carbon bonds is formed where every carbon atom in the main chain bears a substituent (Scheme 1.1a). Neighbouring substituents feel steric hindrance, forcing the polymer backbone to adopt a helical conformation.[5]

The ability of isocyanides to polymerize was known for a long time. A first catalysed polymerization reaction was only developed by Millich in the 1970s, however, using acid-coated glass as the catalyst.[6] Another and more frequently used method for the preparation of polyisocyanides is the polymerization with transition metal complexes[7–9], in particular with Ni(II) salts.[10–12] Using these catalysts, polymerization proceeds via the "merry-go-round" mechanism and yields a helical structure with four monomers per turn (4_1 helix) (Scheme 1.1b). [13,14] In this mechanism, the starting point is the formation of a tetrakis isocyanide Ni(II) complex, which can be activated by the addition of a nucleophile, most typically an amine or an alcohol (Scheme 1.1b, step 1).
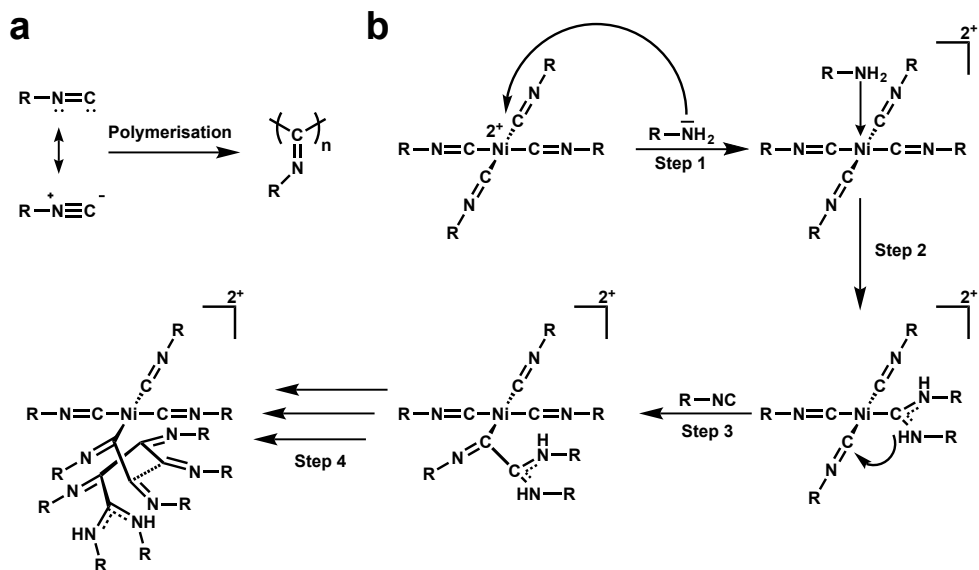
Scheme 1.1. Polyisocyanide structure and polymerization mechanism. a) The polymerization of isocyanides into polyisocyanides. b) Proposed "merry-go-round" mechanism for the nickel catalysed polymerization of isocyanides. Adapted from reference 14.

The nucleophile first coordinates to the nickel centre and subsequently reacts with one of the isocyanide ligands to form a carbene-like ligand (Scheme 1.1b, step 2), which then attacks a neighbouring isocyanide ligand (Scheme 1.1b, step 3). A new monomer from the solution then coordinates to the vacant position of the activated nickel species, facilitating a polymerization reaction that proceeds in the direction of the initial attack (Scheme 1.1b, step 4). As a consequence of this mechanism, one particular helical sense is formed per polymer chain. For an achiral initiator, equal amounts of right- and left-handed helices are formed. In contrast, one helical sense is preferred over the other when a chiral initiator or monomer is used.[15,16] When sufficiently bulky groups are introduced into the side chains, the polymer is locked in a certain conformation and the helical sense of each polymer is preserved.[10] If the side chains are not bulky enough, however, the polymer is more dynamic and conformational changes are possible.[17,18]

Polyisocyanopeptide
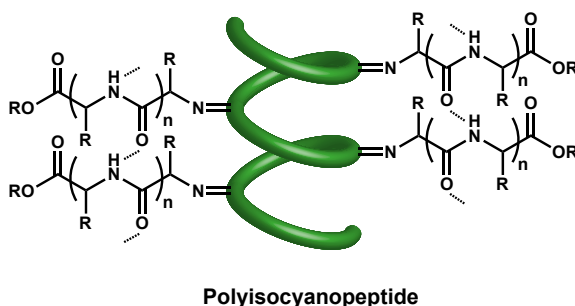
Scheme 1.2. Polyisocyanopeptide stabilized by a hydrogen-bonding network between the side chains. The side chains can either be a di- or a tripeptide (n=1 or n=2).

The helical structure can also be preserved when using side chains that are able to form hydrogen bonds so that a stabilizing hydrogen-bonding network is formed along the polymer. This strategy has been elegantly implemented by Cornelissen *et al.* who synthesized polyisocyanides with di- or tripeptide-functionalized side chains, so-called polyisocyanopeptides (Scheme 1.2).[19–22] Using these peptide side chains, hydrogen bonding occurs between the amide bonds of parallel side chains, i.e. between side chains n and n+4[19]. The distance between the participating amide bonds was estimated to be 0.46 nm and an overall β-sheet-like packing of the side chains was found along the polymer backbone.[19] As a result of this interaction, very long (from 100 nm to several micrometres) and rigid polymers were formed. These polyisocyanopeptides possess persistence lengths up to 76 nm,[23] making these polymers very suitable candidates for ordering electroactive and optically-active (chromophoric) groups in array-like structures.[24,25] Two fundamentally different strategies have been used to introduce these active groups into the polymer. The first strategy is based on the synthesis of 'active' isocyanopeptide monomers that are subsequently polymerized. Over the years many different monomers have been synthesized that carry active groups, such as thiophenes, porphyrins, and perylenes.[26–31]

Although the synthesis of these compounds is feasible, a second strategy using a post-modification approach was developed to functionalize polyisocyanopeptides with active groups. To be able to chemically modify an already polymerized scaffold,[32] monomers carrying an acetylene functional group were developed. After polymerization, the acetylene-containing polymers were reacted with azide-functionalized compounds in an azide-alkyne cycloaddition ('click') reaction.[32] This post-modification approach has allowed for the synthesis of a large number of different functional polymers, e.g. carrying perylenes and phthalocyanines

as active groups. But also oligo (ethylene glycol) groups have been coupled to the polymer with the goal of increasing its water solubility.[33,34]

1.2 Water-soluble polyisocyanopeptides

Polyisocyanopeptides have shown great potential as a scaffold in organic solvents. More recent research has focused on the synthesis of water-soluble derivatives to extend this potential to biological applications. In a first attempt, Schwartz *et al*. co-polymerized an azide-bearing isocyanopeptide monomer **IAA-N$_3$** with D-isocyanoalanyl-L-alanine methyl ester **IAA-OMe** (Scheme 1.3a).[35] Upon saponification (hydrolysis of the methyl ester), this polymer became soluble in water, resulting from the large number of newly generated carboxylic acid groups. Subsequently, the azide groups were used in a post-modification step, using a copper-catalysed azide–alkyne cycloaddition reaction (CuAAC).[36] The obtained polymer was characterized with circular dichroism (CD) spectroscopy to determine its secondary structure. Comparing the polymer before and after saponification, showed very similar secondary structure characteristics, however, the signal intensity was slightly lower after ester hydrolysis. This was attributed to the long hydrolysis process that may partly unfold a small portion of the helix.
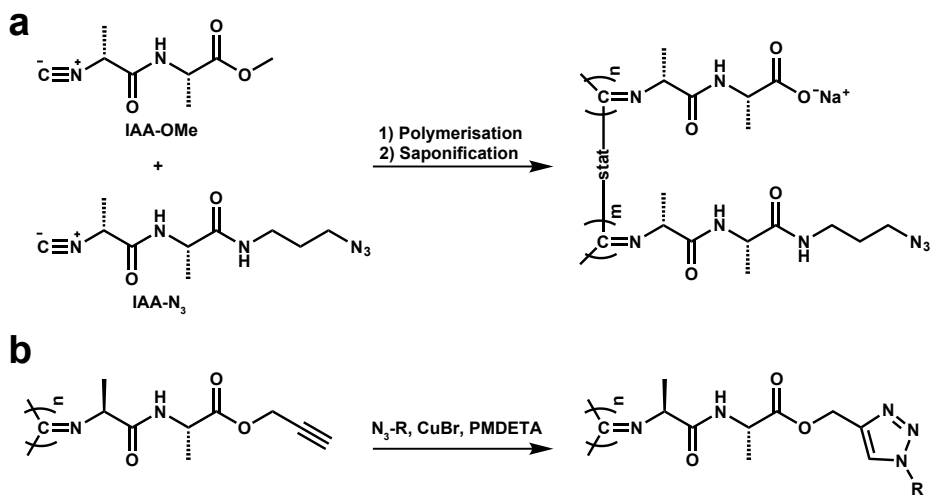
Scheme 1.3. Post-modification strategies to obtain water-soluble polyisocyanopeptides. a) Azide-functionalized monomers are polymerized with methyl ester-containing monomers, yielding a statistical distribution of functional monomers in the polymer backbone. Saponification of the methyl ester results in a water-soluble polymer. b) Acetylene-functionalized polyisocyanopeptides able to react with azides in a copper catalyzed azide-alkyne cycloaddition reaction.

To obtain a non-ionic, water-soluble polyisocyanopeptide analogue, acetylene-bearing homo-polymers were reacted with azide-functionalized oligo ethylene glycol chains (Scheme 1.3b). [34] Although the resulting polymer was water-soluble, a change in the CD spectrum was observed for the post-modified polymer. Again this may be a result of partial unfolding. Alternatively, the polymer may remain in a folded, helical state characterized by a different side chain arrangement.

In addition to the post-modification approach using oligo ethylene glycol chains, also the possibility of polymerizing oligo ethylene glycol-containing isocyanopeptide monomers was investigated. [37] The size of the oligo ethylene glycol chain was varied from m=2 to m=4 (**PIAA-OEG$_2$-OMe, PIAA-OEG$_3$-OMe** and **PIAA-OEG$_4$-OMe**) (Figure 1.1a). Polymers could be synthesized from all three monomers and an extensive structure determination was carried out for these polymers. CD spectroscopy showed very different spectra for these polymers when compared to polyisocyanopeptides that lack the oligo ethylene glycol tail. Without the tail, a strong cotton effect centred around λ = 310 nm was found. In contrast, the CD spectrum of **PIAA-OEG$_{2,3,4}$-OMe** showed two peaks: a positive peak at λ = 272 nm and a smaller negative peak at λ = 360 nm. [37] To confirm that the helical backbone of the polymer was not disrupted, the CD measurements were complemented with IR measurements. Focussing on the N-H stretches of the amide bond in the hydrogen-bonding peptide side chains, it was shown that the oligo ethylene glycol-containing polymers possess a slightly less defined hydrogen-bonding network. The altered CD spectra may be directly attributed to this effect while the polymer still follows the classical 4_1 structure.

In the next step, the water solubility of **PIAA-OEG$_{2,3,4}$-OMe** was examined. Whereas **PIAA-OEG$_2$-OMe** did not dissolve in water, a good water solubility was observed for the polymers **PIAA-OEG$_{3,4}$-OMe**. Non-linear poly ethylene glycol (PEG) analogues, such as the newly synthesized polymers, frequently show a thermo-responsive behaviour in aqueous solution. This is directly related to the properties of the PEG side chains, which dehydrate upon heating. This dehydration may decrease the water solubility of the polymer, leading to precipitation above a certain temperature. This temperature, the so-called lower critical solution temperature (LCST), can be determined when testing polymer solubility over a range of temperatures. Both polymers **PIAA-OEG$_3$-OMe** and **PIAA-OEG$_4$-OMe** showed a phase transition with LCST values of ~20-25 °C (n=3) and ~42-50 °C (n=4). [37] The different LCSTs can be explained with the fact that the longer oligo ethylene glycol chains in the **PIAA-OEG$_4$-OMe** polymer interact with a larger number of water molecules so that more energy is required to dehydrate the polymer.
The most interesting result of this experiment was that these polymers did not precipitate above the LCST, but were trapped in a gel state instead. Remarkably,

these hydrogels formed at very low concentrations, as low as 0.006 (wt.%).[38] To understand the gelation mechanism and the mechanical properties of this hydrogel, it was characterized with a number of different techniques.[38] Atomic force microscopy and cryo-scanning electron microscopy revealed a bundled structure of the hydrogel (Figure 1.1b). This bundling behaviour is a direct result of the LCST behaviour. Upon heating, the entropic desolvation of the oligo ethylene glycol tails increases the hydrophobicity of the side chains. These more hydrophobic chains increasingly interact with each other (instead of water), bundle up and remain kinetically trapped in a network state. Surprisingly, the bundle dimensions were independent of polymer concentration. Higher concentrations of polymer only resulted in a higher number of bundles and, consequently, a denser bundle network. This makes the polymer concentration an effective parameter to tune the pore size of the gel.

a

m = 2, PIAA-OEG$_2$-OMe
m = 3, PIAA-OEG$_3$-OMe
m = 4, PIAA-OEG$_4$-OMe

b

c

d
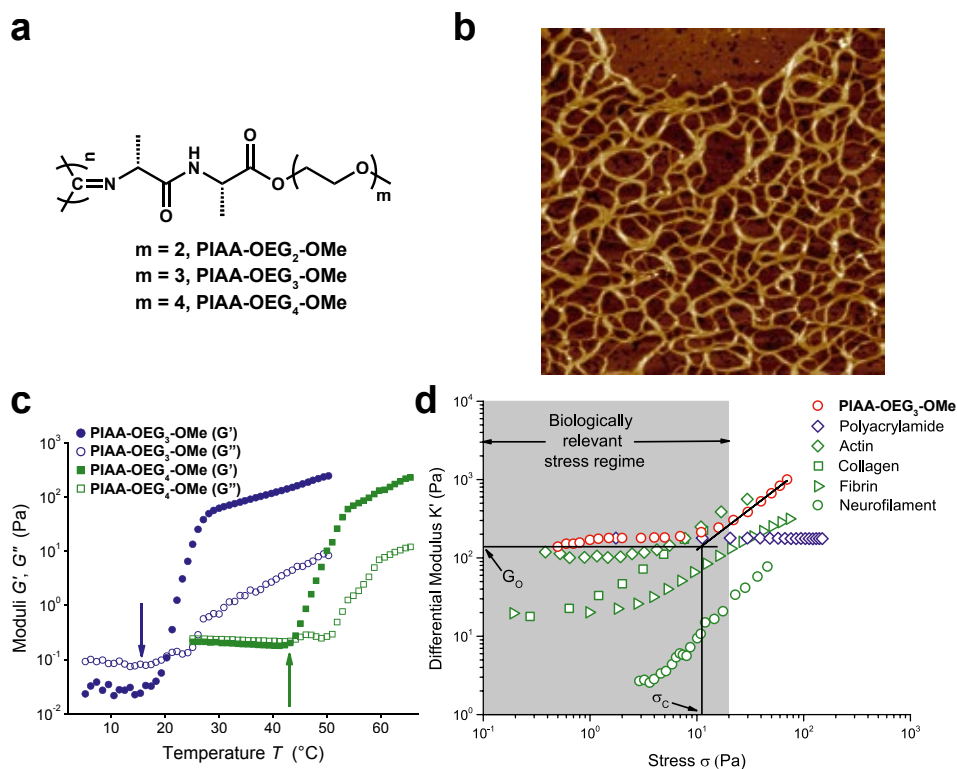
Figure 1.1. Water-soluble polyisocyanopeptides. a) Molecular structure of oligo ethylene glycol-functionalized polyisocyanopeptides. b) Bundled structure of the polyisocyanopeptide hydrogel as measured with atomic force microscopy. The size of the image is 1x1 µm² (reproduced with permission from reference 38). c) Rheology measurements of *G'* (storage modulus) and *G"* (loss modulus) for **PIAA-OEG$_3$-OMe** and **PIAA-OEG$_4$-OMe** (reproduced with permission from reference 38). d) Stress-stiffening of polyisocyanopeptide hydrogels, as indicated by the differential modulus K'. For comparison also the synthetic hydrogel polyacrylamide is shown along with hydrogels formed from natural biopolymers (reproduced with permission from reference 42).

Using rheology, the mechanical properties of the hydrogels were investigated. In general, the two main parameters extracted from these measurements are the *G'* (storage modulus) and *G''* (loss modulus), where *G'* gives insight into the elastic properties and *G''* reflects the viscous properties of a material. The temperature where the value of *G'* crosses *G''* is defined as the precise gel point of a hydrogel. For **PIAA-OEG$_3$-OMe** and **PIAA-OEG$_4$-OMe** gel points of 20 °C and 42 °C were found, respectively (Figure 1.1c), matching the previously determined LCST values. The mechanical properties of these gels are characterized by an unexpected stress-stiffening behaviour, which is usually only observed for natural hydrogels formed from biological polymers, such as actin, collagen and intermediate filaments.[39,40] This non-linear stress-stiffening behaviour describes the increased resistance of these biopolymer gels to a mechanical deformation.[40]

This mechanism, which protects biological materials from mechanical damage, is rarely observed for synthetic hydrogels. The surprising result that polyisocyanopeptide hydrogels exhibit this behaviour[38,41,42] can be explained when considering the helical nature of polyisocyanopeptides and the stiffness of the polymer chains in water. The persistence length L$_p$ of individual **PIAA-OEG$_3$-OMe** and **PIAA-OEG$_4$-OMe** polymers is on the order of 5-10 nm.[38,43] This L$_p$ is ~1/10th of the polymer length, making these polymers semi-flexible. During bundling, the L$_p$ increases quadratically with the number of polymers per bundle, leading to very stiff bundles.[38] As a consequence, the L$_P$ value of the bundles (460 nm) is of a similar value as the pore size of the hydrogel (110 nm).

For biopolymer networks it has been shown theoretically and experimentally that this relationship between pore size and L$_p$ is sufficient to explain their stress-stiffening behaviour. Polyisocyanopeptides consequently form hydrogels with a similar network structure as biopolymer hydrogels. More interestingly, even the stress range where the non-linear properties become dominant is very similar to that of biopolymers (Figure 1.1d). More recently, the influence of polymer length, polymer concentration and the addition of salts has been investigated and it has been shown that these are all good parameters to tune the mechanical properties of the hydrogels.[41,44]

Their long helical structure and their ability to form hydrogels that closely mimic natural filaments make these water-soluble polyisocyanopeptides very interesting candidates for a range of biomedical applications. At the physiologically relevant temperature of 37 °C, **PIAA-OEG$_3$-OMe** forms a hydrogel whereas **PIAA-OEG$_4$-OMe** does not. This opens up a number of fundamentally different applications for these two structurally similar, thermo-responsive polymers. Hydrogels consisting of **PIAA-OEG$_3$-OMe** could be suitable as wound dressing materials, cell growth matrixes or even in tissue engineering. On the other hand, freely soluble **PIAA-**

OEG$_4$-OMe polymers are ideal fibre-like, multivalent scaffolds for drug delivery or other *in vivo* applications that utilize polymer-drug conjugates. For all these applications, the polyisocyanopeptide polymers have to be decorated with bioactive compounds such as peptides, proteins, antibodies or drugs. In the next sections, possible applications of polyisocyanopeptides as functional hydrogels or *in vivo* multivalent therapeutic scaffolds are introduced and the required biofunctionalization strategies are addressed.

1.3. Polyisocyanopeptides as multivalent scaffolds

Many biological processes start with the binding of a multivalent ligand to a cell receptor. A prototype example of such a multivalent interaction is the binding of a virus to the cell surface. Another well-studied example is the interaction of cells with their extracellular matrix via multicomponent focal adhesion complexes. Also the communication between different cells of the immune system requires the formation of well-defined multivalent interactions, e.g. between T cells and dendritic cells. To trigger and influence all these processes artificially, scaffolds have been developed to mimic the multivalent interaction in a 'natural way'. Synthetic polymers are one possible scaffold to obtain a multivalent ligand-functionalized structure. The research described in this thesis aims to develop a polyisocyanopeptide-based, multivalent structure that is able to activate T cells and to test the potential of this artificial multivalent scaffold in immunotherapeutic applications.

Immunotherapy has become one of the prime treatments for cancer. The idea behind this therapy is to redirect the immune system in such a way that it can recognize dangerous cancer cells and destroy them. One of the key players in the immune system is the dendritic cell (DC), which is a natural antigen-presenting cell (APC). DCs encounter and take up antigens, process the antigenic component intracellularly and present small parts of it on their surface. Other cells of the immune system, primarily T cells, recognize these antigen fragments and become activated. When exposed to cancer specific antigens DCs will consequently display the corresponding cancer-related antigen fragments and the immune system will become activated against the cancer cells. Several studies have highlighted the potential of *in vivo* administered or *ex vivo* loaded DCs in cancer treatment.[45,46] The clinical use of DCs remains limited, however, as this treatment is very costly and laborious. Cells have to be harvested and processed for every individual patient.[47,48] To overcome these limitations, artificial antigen-presenting cells (aAPCs) have been developed. Synthetic variants are much cheaper and easier to make so that an "off-the-shelf" approach can potentially be implemented.[49]

Over the years, many aAPC scaffolds have been investigated, varying in shape, size and presented ligands (Figure 1.2).[50] When looking at the natural

multivalent DC - T cell interaction, the requirements for aAPC design can be established. The initial contact between DCs and T cells involves the multivalent binding of the T cell receptor (TCR) to the antigen fragments, displayed on the DC surface via the major histocompatibility complex (MHC). Adhesion molecules stabilize this interaction further. It has been shown that binding first occurs in small micro-domains. Later, these micro-domains cluster together into the so-called immune synapse (IS).[51,52] Thus, activation of T cells by DCs requires a multivalent interaction between many different binding partners, which are mobile on the cell membrane allowing the required spatial rearrangements to occur.
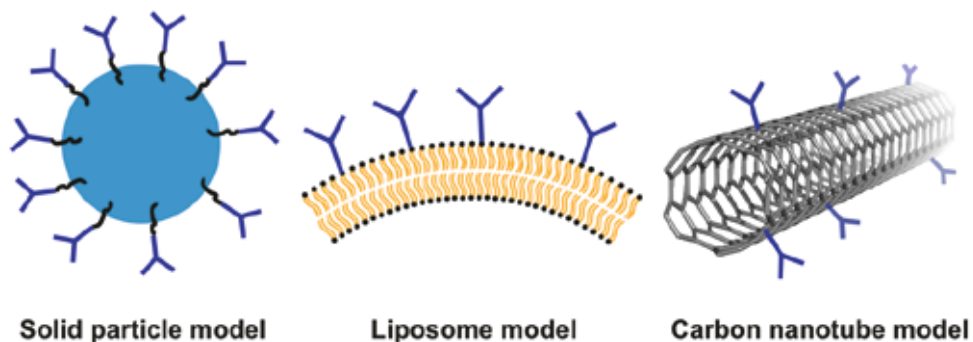
Figure 1.2. Design principles of artificial antigen-presenting cells. Shown are examples using either solid particle, liposomal or rigid carbon nanotube scaffolds.

The first generation of aAPCs was based on solid microbead-like scaffolds that were functionalized with T cell-stimulating molecules (Figure 1.2).[53] Although these beads were able to form multiple interactions with a T cell, they represent a rigid scaffold lacking the possibility for ligand and receptor rearrangement. This limitation can be overcome when using liposomal aAPCs. Their fluidic membrane allows the receptors to cluster more efficiently (Figure 1.2).[54] In general, however, the use of micrometre-sized spherical structures is not favourable. Only a small number of aAPC-bound ligands are involved during the activation, as the contact area between the surface of the aAPC and the T cell is small. To overcome this limitation, structures with higher aspect ratios such as rod-shaped carbon nanotubes and filomicelles could be used (Figure 1.2).[55,56] Carbon nanotubes are extremely rigid, however, and filomicelles have a large size of 6-7 μm. The ideal scaffold would combine a high aspect ratio with the ability to form multiple interactions and the flexibility to rearrange the bound ligands or receptors. Water-soluble polyisocyanopeptides with tetra ethylene glycol side chains (**PIAA-OEG$_4$-OMe**) are ideal candidates as they fulfil all these requirements. They are semi-flexible (L_p in the order of 10 nm[43]) and long filamentous structures (hundreds of nanometres) that are easily functionalized with different ligands through post-modification reactions.

Chapters 2, 3 and 4 focus on this topic, describing biofunctionalization strategies developed for coupling T cell interacting ligands to **PIAA-OEG$_4$-OMe** polymers. These chapters further describe a number of approaches to optimize the multivalent interaction and to increase the specificity of the T cell response.

1.4. Polyisocyanopeptide hydrogels

A hydrogel is a natural or synthetic polymeric material that is able to absorb a high content of water. Prominent natural examples of hydrogels are the cytoskeleton (actin, microtubules and intermediate filaments) and the extra cellular matrix (ECM; collagen and fibrin) that are composed of protein-based biopolymers. But also carbohydrate-based structures are able to form hydrogels, such as hyaluronic acid, alginate and carrageenan. Over the years, hydrogels have gained increasing attention for a large number of biomedical applications. For example, they are used as coating for contact lenses and as hygiene products and wound dressing materials.[57,58] Considering the function of their natural counterparts, they have further found application as 2D and 3D ECM mimics. Lastly, stimuli-responsive hydrogels have been developed for drug delivery applications.

The applications of synthetic ECM mimics range from fundamental studies aimed at investigating the physical nature of the cell-matrix interaction to applications in tissue engineering and regenerative medicine.[59,60] Many studies have indicated that the mechanical properties of an ECM mimicking hydrogel influence the behaviour of cells, e.g. determining cell size and shape as well as migration and differentiation. For example, Engler *et al.* have shown that human mesenchymal stem cells cultured on soft (0.1-1 kPa) and stiff (8-18 kPa) polyacrylamide gels (collagen I coated to facilitate cell adhesion), committed into softer neuronal tissue or stiffer muscle tissue, respectively.[61] So far, many of these studies have been conducted on 2D substrates. These 2D cell culture systems are easy to handle, but do not always resemble the complexity of the ECM in three dimensions.[59] Furthermore, the ECM consists of natural filaments that show stress-stiffening behaviour. Although synthetic hydrogels allow for a great deal of control, they lack this unusual mechanical response. On the other hand, hydrogels made from biopolymers are stress-stiffening. For natural hydrogels it is impossible, however, to decouple their mechanical (e.g. stiffness) and their biochemical properties (e.g. ligand density). This makes it very difficult to assess the influence of these different parameters on cellular behaviour. The ideal ECM combines the mechanical properties of natural hydrogels with the same level of control that is available when designing synthetic hydrogels.

Water-soluble polyisocyanopeptides with tri ethylene glycol side chains (**PIAA-OEG₃-OMe**) have the potential to fulfil all these requirements. The synthetic hydrogel formed from **PIAA-OEG₃-OMe** polymers possesses stress-stiffening behaviour and its mechanical properties are easily tuned. To allow for cell adhesion to occur, the hydrogel can be functionalized with cell-adhesive ligands that are able to bind to integrin receptors on the cell surface. A common integrin ligand for cell adhesion is the RGD peptide.[62,63] This small peptide is able to bind to many types of integrins, thus providing a general anchor point for cells. When functional monomers are built into the polymer, the RGD ligand can easily be attached to the polymer via post-modification. Chapter 5 introduces the synthesis and application of this synthetic stress-stiffening hydrogel as a 3D ECM mimic for stem cell differentiation.

Stimuli-responsive polymer hydrogels are an interesting class of smart materials with an increasing number of possible applications. With their ability to adapt to a changing environment, they play an important role in novel drug delivery systems, diagnostics and as sensing materials.[64] These smart materials respond to changes in temperature, pH, electrical or magnetic fields or to chemical signals. One prominent class of stimuli-responsive hydrogels is based on polymeric DNA-hybrid materials.[65] DNA allows for a great deal of control as the nucleotide sequences can be fully controlled and designed by the user. Furthermore, DNA sequences can be developed in such a way that they respond to various external stimuli, like pH, temperature or the addition of complementary DNA. As mentioned in the previous section, these DNA-containing hydrogels lack the ability to stress-stiffen and fail to closely mimic typical natural hydrogel materials. Water-soluble polyisocyanopeptides decorated with DNA molecules are a potential DNA-responsive stress-stiffening hydrogel scaffold. Chapter 6 aims at the development of such a DNA-responsive, stress-stiffening hydrogel based on **PIAA-OEG₃-OMe** that may find application in drug delivery and sensing.

1.5. Aim and outline of this thesis

To fully use the favourable properties of water-soluble polyisocyanopeptides for the above-mentioned applications, the polymers have to be functionalized with biomolecules such as antibodies, proteins, peptides or DNA oligonucleotides. As the required bioconjugation reactions are usually carried out in aqueous buffer systems, a post-modification approach is required. For this purpose, all polyisocyanopeptide polymers need to be equipped with a functional group during synthesis that can then be used for coupling the biomolecule in a second step. It is one goal of this thesis to develop water-soluble, azide-functionalized polyisocyanopeptides that can then be "clicked" with acetylene-functionalized biomolecules. An azide group is chosen as a functional handle on the polymer as a number of azide-containing polymers were

already shown to be functional in other applications. Instead of coupling a terminal alkyne in a CuAAC reaction, a strain-promoted azide-alkyne cycloaddition (SPAAC) reaction has been selected, as this reaction does not require a catalyst. More specifically, the strained alkynes bicyclononyne (BCN) and azadibenzocyclooctyne (DBCO) are used for bioconjugation (Figure 1.3).[66–68] The second, and more important goal of this thesis is to test the potential of these newly synthesized bioconjugates and hydrogels in the previously described applications.
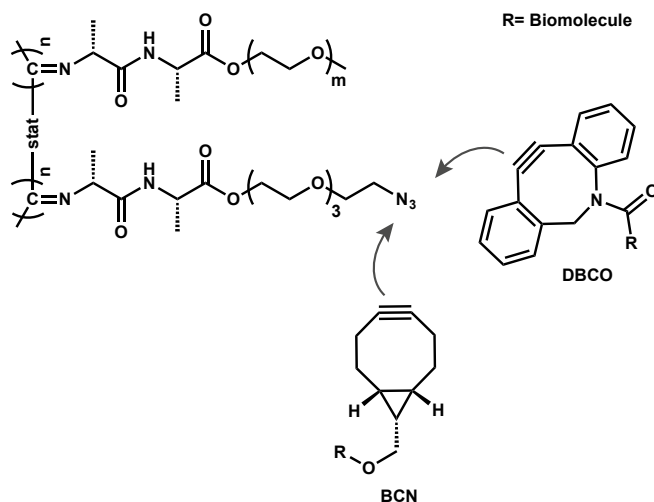
Figure 1.3. Functionalization of water-soluble polyisocyanopeptides with biomolecules using a post-modification approach. The polymer carries a statistical ratio of azide-functionalized monomers that can be reacted with strained alkyne modified biomolecules in a strain-promoted azide-alkyne cycloaddition reaction.

After this introductory chapter, this thesis continues with a description of the synthesis of the proposed azide-containing polyisocyanopeptide polymers and the biofunctionalization of the **PIAA-OEG₄-OMe** scaffold with T cell activating antibodies. These bioconjugates are tested for their ability to stimulate T cells and compared to spherical particles carrying the same antibody (Chapter 2). Chapter 3 describes the effect of polymer length and antibody spacing on T cell activation. It further highlights the T cell stimulating effect of the antibody-functionalized polyisocyanopeptide at different points in time, comparing early and late markers of T cell activation. Chapter 4 introduces a strategy to functionalize the scaffold with a second antibody that shapes the specificity of the T cell response.

In chapter 5, azide-functionalized **PIAA-OEG₃-OMe** polymers are used as a scaffold to synthesize bioactive hydrogels for cell culture applications. The hydrogel is functionalized with integrin-binding GRGDS peptides and the impact of stress-stiffening on stem cell differentiation is investigated. In chapter 6, the

polyisocyanopeptide is functionalized with DNA oligonucleotides. These short DNA molecules are subsequently hybridized with a complementary sequence that allows for the formation of specific DNA cross-links. In this way, a stimuli-responsive, dynamic and tuneable hydrogel is obtained whose mechanical properties can be controlled by the addition of specific DNA sequences.

The synthesis of many of the described polymer bioconjugates requires extensive and difficult purification steps. Based on the experience gained in the previous chapters, a new affinity-based purification method is introduced. This new method facilitates an easier, faster and better purification of the bioconjugates (chapter 7).

This thesis finishes with a discussion of the knowledge obtained from the tested biofunctionalized scaffolds and highlights future directions for the design and application of this interesting class of polymers (chapter 8).

1.6 References

(1)   Lieke, W. *Justus Liebigs Ann. Chem.* **1859**, *112* (3), 316–321.
(2)   Gautier, A. *Justus Liebigs Ann. Chem.* **1867**, *142* (3), 289–294.
(3)   Ugi, I.; Meyr, R. *Angew. Chem.* **1958**, *70* (22-23), 702–703.
(4)   Nolte, R. M.; Drenth, W. In *Recent Advances in Mechanistic and Synthetic Aspects of Polymerization SE - 35*; Fontanille, M., Guyot, A., Eds.; NATO ASI Series; Springer Netherlands, **1987**; *215*, 451–464.
(5)   Schwartz, E.; Koepf, M.; Kitto, H. J.; Nolte, R. J. M.; Rowan, A. E. *Polym. Chem.* **2011**, *2* (1), 33–47.
(6)   Millich, F. *Chem. Rev.* **1972**, *72* (2), 101–113.
(7)   Onitsuka, K.; Joh, T.; Takahashi, S. *Angew. Chem., Int. Ed. Engl.* **1992**, *31* (7), 851–852.
(8)   Onitsuka, K.; Yamamoto, M.; Mori, T.; Takei, F.; Takahashi, S. *Organometallics* **2006**, *25* (5), 1270–1278.
(9)   Ito, Y.; Ihara, E.; Murakami, M.; Shiro, M. *J. Am. Chem. Soc.* **1990**, *112* (17), 6446–6447.
(10)   Van Beijnen, A. J. M.; Nolte, R. J. M.; Naaktgeboren, A. J.; Zwikker, J. W.; Drenth, W.; Hezemans, A. M. F. *Macromolecules* **1983**, *16* (11), 1679–1689.
(11)   Deming, T. J.; Novak, B. M. *Macromolecules* **1991**, *24* (1), 326–328.
(12)   Nolte, R. J. M.; Stephany, R. W.; Drenth, W. *Recl. des Trav. Chim. des Pays-Bas* **1973**, *92* (1), 83–91.
(13)   Nolte, R. J. M. *Chem. Soc. Rev.* **1994**, *23* (1), 11–19.
(14)   Cornelissen, J. J. L. M.; Rowan, A. E.; Nolte, R. J. M.; Sommerdijk, N. A. J. M. *Chem. Rev.* **2001**, *101* (12), 4039–4070.
(15)   Kamer, P. C. J.; Nolte, R. J. M.; Drenth, W. *J. Am. Chem. Soc.* **1988**, *110* (20), 6818–6825.
(16)   Kamer, P. C. J.; Cleij, M. C.; Nolte, R. J. M.; Harada, T.; Hezemans, A. M. F.; Drenth, W. *J. Am. Chem. Soc.* **1988**, *110* (5), 1581–1587.
(17)   Huang, J.-T.; Sun, J.; Euler, W. B.; Rosen, W. *J. Polym. Sci., Part A: Polym. Chem.* **1997**, *35* (3), 439–446.
(18)   Green, M. M.; Gross, R. A.; Schilling, F. C.; Zero, K.; Crosby, C. *Macromolecules* **1988**, *21* (6), 1839–1846.
(19)   Cornelissen, J. J.; Donners, J. J.; de Gelder, R.; Graswinckel, W. S.; Metselaar, G. A.; Rowan, A. E.; Sommerdijk, N. A.; Nolte, R. J. *Science* **2001**, *293* (5530), 676–680.
(20)   Cornelissen, J. J. L. M.; Graswinckel, W. S.; Adams, P. J. H. M.; Nachtegaal, G. H.; Kentgens, A. P. M.; Sommerdijk, N. A. J. M.; Nolte, R. J. M. *J. Polym. Sci., Part A: Polym. Chem.* **2001**, *39* (24), 4255–4264.
(21)   Metselaar, G. A.; Adams, P. J. H. M.; Nolte, R. J. M.; Cornelissen, J. J. L. M.; Rowan, A. E. *Chem. - Eur. J.* **2007**, *13* (3), 950–960.
(22)   Cornelissen, J. J. L. M.; Graswinckel, W. S.; Rowan, A. E.; Sommerdijk, N. A. J. M.; Nolte, R. J. M. *J. Polym. Sci., Part A: Polym. Chem.* **2003**, *41* (11), 1725–1736.
(23)   Samorí, P.; Ecker, C.; Gössl, I.; de Witte, P. A. J.; Cornelissen, J. J. L. M.; Metselaar, G. A.; Otten, M. B. J.; Rowan, A. E.; Nolte, R. J. M.; Rabe, J. P. *Macromolecules* **2002**, *35* (13), 5290–5294.
(24)   Palermo, V.; Schwartz, E.; Finlayson, C. E.; Liscio, A.; Otten, M. B. J.; Trapani, S.; Müllen, K.; Beljonne, D.; Friend, R. H.; Nolte, R. J. M.; Rowan, A. E.; Samorì, P. *Adv. Mater.* **2010**, *22* (8), E81–E88.
(25)   Schwartz, E.; Le Gac, S.; Cornelissen, J. J. L. M.; Nolte, R. J. M.; Rowan, A. E. *Chem. Soc. Rev.* **2010**, *39* (5), 1576–1599.
(26)   Dabirian, R.; Palermo, V.; Liscio, A.; Schwartz, E.; Otten, M. B. J.; Finlayson, C. E.; Treossi, E.; Friend, R. H.; Calestani, G.; Müllen, K.; Nolte, R. J. M.; Rowan, A. E.; Samorì, P. *J. Am. Chem. Soc.* **2009**, *131* (20), 7055–7063.
(27)   de Witte, P. A. J.; Castriciano, M.; Cornelissen, J. J. L. M.; Monsù Scolaro, L.; Nolte, R. J. M.; Rowan, A. E. *Chem. - Eur. J.* **2003**, *9* (8), 1775–1781.
(28)   Finlayson, C. E.; Friend, R. H.; Otten, M. B. J.; Schwartz, E.; Cornelissen, J. J. L. M.; Nolte, R. J. M.; Rowan, A. E.; Samorì, P.; Palermo, V.; Liscio, A.; Peneva, K.; Müllen, K.; Trapani, S.; Beljonne, D. *Adv. Funct. Mater.* **2008**, *18* (24), 3947–3955.
(29)   Palermo, V.; Otten, M. B. J.; Liscio, A.; Schwartz, E.; de Witte, P. A. J.; Castriciano, M. A.; Wienk, M. M.; Nolde, F.; De Luca, G.; Cornelissen, J. J. L. M.; Janssen, R. A. J.; Müllen, K.; Rowan, A. E.; Nolte, R. J. M.; Samorì, P. *J. Am. Chem. Soc.* **2008**, *130* (44), 14605–14614.
(30)   Vriezema, D. M.; Hoogboom, J.; Velonia, K.; Takazawa, K.; Christianen, P. C. M.; Maan, J. C.; Rowan, A. E.; Nolte, R. J. M. *Angew. Chem., Int. Ed.* **2003**, *42* (7), 772–776.

(31)   Schwartz, E.; Palermo, V.; Finlayson, C. E.; Huang, Y.-S.; Otten, M. B. J.; Liscio, A.; Trapani, S.; González-Valls, I.; Brocorens, P.; Cornelissen, J. J. L. M.; Peneva, K.; Müllen, K.; Spano, F. C.; Yartsev, A.; Westenhoff, S.; Friend, R. H.; Beljonne, D.; Nolte, R. J. M.; Samorì, P.; Rowan, A. E. *Chem. - Eur. J.* **2009**, *15* (11), 2536–2547.

(32)   Schwartz, E.; Kitto, H. J.; de Gelder, R.; Nolte, R. J. M.; Rowan, A. E.; Cornelissen, J. J. L. M. *J. Mater. Chem.* **2007**, *17* (19), 1876–1884.

(33)   López-Duarte, I.; Martínez-Díaz, M. V.; Schwartz, E.; Koepf, M.; Kouwer, P. H. J.; Rowan, A. E.; Nolte, R. J. M.; Torres, T. *ChemPlusChem* **2012**, *77* (8), 700–706.

(34)   Kitto, H. J.; Schwartz, E.; Nijemeisland, M.; Koepf, M.; Cornelissen, J. J. L. M.; Rowan, A. E.; Nolte, R. J. M. *J. Mater. Chem.* **2008**, *18* (46), 5615–5624.

(35)   Schwartz, E.; Koepf, M.; Kitto, H. J.; Espelt, M.; Nebot-Carda, V. J.; De Gelder, R.; Nolte, R. J. M.; Cornelissen, J. J. L. M.; Rowan, A. E. *J. Polym. Sci., Part A: Polym. Chem.* **2009**, *47* (16), 4150–4164.

(36)   Rostovtsev, V. V; Green, L. G.; Fokin, V. V; Sharpless, K. B. *Angew. Chem., Int. Ed.* **2002**, *41* (14), 2596–2599.

(37)   Koepf, M.; Kitto, H. J.; Schwartz, E.; Kouwer, P. H. J.; Nolte, R. J. M.; Rowan, A. E. *Eur. Polym. J.* **2013**, *49* (6), 1510–1522.

(38)   Kouwer, P. H. J.; Koepf, M.; Le Sage, V. A. A.; Jaspers, M.; van Buul, A. M.; Eksteen-Akeroyd, Z. H.; Woltinge, T.; Schwartz, E.; Kitto, H. J.; Hoogenboom, R.; Picken, S. J.; Nolte, R. J. M.; Mendes, E.; Rowan, A. E. *Nature* **2013**, *493* (7434), 651–655.

(39)   Janmey, P. A.; Hvidt, S.; Kas, J.; Lerche, D.; Maggs, A.; Sackmann, E.; Schliwa, M.; Stossel, T. P. *J. Biol. Chem.* **1994**, *269* (51), 32503–32513.

(40)   Storm, C.; Pastore, J. J.; MacKintosh, F. C.; Lubensky, T. C.; Janmey, P. A. *Nature* **2005**, *435* (7039), 191–194.

(41)   Jaspers, M.; Dennison, M.; Mabesoone, M. F. J.; MacKintosh, F. C.; Rowan, A. E.; Kouwer, P. H. J. *Nat. Commun.* **2014**, *5*.

(42)   Das, R. K.; Gocheva, V.; Hammink, R.; Zouani, O. F.; Rowan, A. E. *Nat. Mater.* **2016**, *15* (3), 318–325.

(43)   van Buul, A. M. Polyisocyanides: A single molecule story, **2014**.

(44)   Jaspers, M.; Rowan, A. E.; Kouwer, P. H. J. *Adv. Funct. Mater.* **2015**, *25* (41), 6503–6510.

(45)   Butler, M. O.; Lee, J.-S.; Ansén, S.; Neuberg, D.; Hodi, F. S.; Murray, A. P.; Drury, L.; Berezovskaya, A.; Mulligan, R. C.; Nadler, L. M.; Hirano, N. *Clin. Cancer Res.* **2007**, *13* (6), 1857–1867.

(46)   Steenblock, E. R.; Wrzesinski, S. H.; Flavell, R. A.; Fahmy, T. M. *Expert Opin. Biol. Ther.* **2009**, *9* (4), 451–464.

(47)   Eggermont, L. J.; Paulis, L. E.; Tel, J.; Figdor, C. G. *Trends Biotechnol.* **2014**, *32* (9), 456–465.

(48)   Maus, M. V; Fraietta, J. A.; Levine, B. L.; Kalos, M.; Zhao, Y.; June, C. H. *Annu. Rev. Immunol.* **2014**, *32* (1), 189–225.

(49)   Kim, J. V; Latouche, J.-B.; Riviere, I.; Sadelain, M. *Nat Biotech* **2004**, *22* (4), 403–410.

(50)   van der Weijden, J.; Paulis, L. E.; Verdoes, M.; van Hest, J. C. M.; Figdor, C. G. *Chem. Sci.* **2014**, *5* (9), 3355–3367.

(51)   Yokosuka, T.; Sakata-Sogawa, K.; Kobayashi, W.; Hiroshima, M.; Hashimoto-Tane, A.; Tokunaga, M.; Dustin, M. L.; Saito, T. *Nat. Immuno.l* **2005**, *6* (12), 1253–1262.

(52)   Grakoui, A.; Bromley, S. K.; Sumen, C.; Davis, M. M.; Shaw, A. S.; Allen, P. M.; Dustin, M. L. *Science* **1999**, *285* (5425), 221–227.

(53)   Garlie, N. K.; LeFever, A. V; Siebenlist, R. E.; Levine, B. L.; June, C. H.; Lum, L. G. *J. Immunother.* **1999**, *22* (4), 336–345.

(54)   Zappasodi, R.; Di Nicola, M.; Carlo-Stella, C.; Mortarini, R.; Molla, A.; Vegetti, C.; Albani, S.; Anichini, A.; Gianni, A. M. *Haematologica* **2008**, *93* (10), 1523–1534.

(55)   Geng, Y.; Dalhaimer, P.; Cai, S.; Tsai, R.; Tewari, M.; Minko, T.; Discher, D. E. *Nat. Nanotechnol.* **2007**, *2*, (4) 249–255.

(56)   Fadel, T. R.; Steenblock, E. R.; Stern, E.; Li, N.; Wang, X.; Haller, G. L.; Pfefferle, L. D.; Fahmy, T. M. *Nano Lett.* **2008**, *8* (7), 2070–2076.

(57)   Caló, E.; Khutoryanskiy, V. V. *Eur. Polym. J.* **2015**, *65*, 252–267.

(58)   Hoffman, A. S. *Adv. Drug Deliv. Rev.* **2002**, *54* (1), 3–12.

(59)   Schwartz, M. A.; Chen, C. S. *Science* **2013**, *339* (6118), 402–404.

(60)   Das, R. K.; Zouani, O. F. *Biomaterials* **2014**, *35* (20), 5278–5293.

(61)   Engler, A. J.; Sen, S.; Sweeney, H. L.; Discher, D. E. *Cell* **2006**, *126* (4), 677–689.

(62)   Ruoslahti, E.; Pierschbacher, M. D. *Science* **1987**, *238* (4826), 491–497.

(63)   Ruoslahti, E. *Annu. Rev. Cell Dev. Biol.* **1996**, *12*, 697–715.

(64)   Stuart, M. A. C.; Huck, W. T. S.; Genzer, J.; Muller, M.; Ober, C.; Stamm, M.; Sukhorukov, G. B.; Szleifer, I.; Tsukruk, V. V; Urban, M.; Winnik, F.; Zauscher, S.; Luzinov, I.; Minko, S. *Nat. Mater.* **2010**, *9* (2), 101–113.

(65)   Guo, W.; Lu, C.-H.; Qi, X.-J.; Orbach, R.; Fadeev, M.; Yang, H.-H.; Willner, I. *Angew. Chem., Int. Ed.* **2014**, *53* (38), 10134–10138.

(66)   Dommerholt, J.; Schmidt, S.; Temming, R.; Hendriks, L. J. A.; Rutjes, F. P. J. T.; van Hest, J. C. M.; Lefeber, D. J.; Friedl, P.; van Delft, F. L. *Angew. Chem., Int. Ed.* **2010**, *49* (49), 9422–9425.

(67)   Kolb, H. C.; Finn, M. G.; Sharpless, K. B. *Angew. Chemie Int. Ed.* **2001**, *40* (11), 2004–2021.

(68)   Debets, M. F.; van Berkel, S. S.; Schoffelen, S.; Rutjes, F. P. J. T.; van Hest, J. C. M.; van Delft, F. L. *Chem. Commun.* **2010**, *46* (1), 97–99.

2

Towards Novel Synthetic Dendritic Cells for Immunotherapy
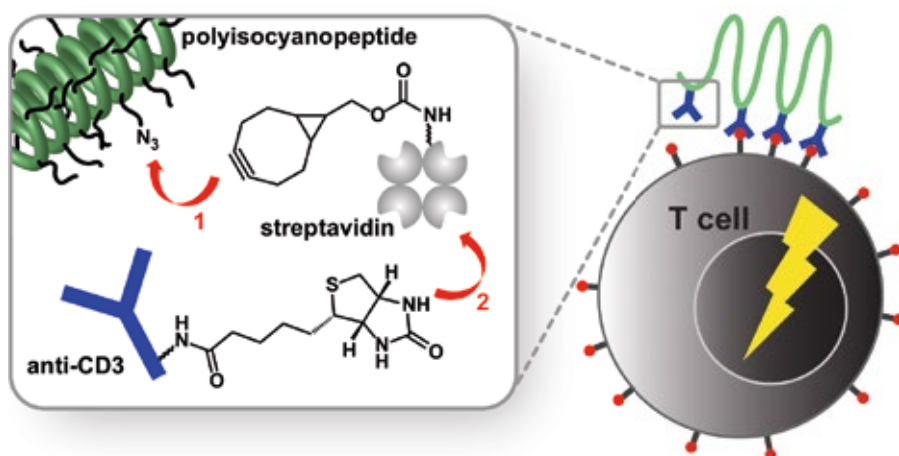
Chapter 2: Towards Novel Synthetic Dendritic Cells for Immunotherapy

2.1 Introduction

The innate immune system is the body's first line of defence against invaders like pathogens and cancerous cells. Among the various cell types of the innate immune system, dendritic cells (DCs), also known as "professional" antigen-presenting cells (APCs) are of prime importance.[1] The knowledge about DCs has increased tremendously in the last 30 years[2] and their applicability for cancer immunotherapy has been investigated. *Ex-vivo* generated DCs, when loaded with tumour lysates, tumour antigen-derived peptides or whole tumour proteins, have demonstrated enhanced anti-cancer immune responses.[3] Clinical studies have shown the potential of DCs as an autologous vaccine for cancer immunotherapy.[4,5] In spite of their potency, the application of *ex-vivo* DCs is so far limited by their availability. Growth of *ex-vivo* DCs is both labour and resource intensive. The requirement to generate a tailor made vaccine for every patient[6,7] means that *ex-vivo* DCs are not economically sustainable. The aforementioned inefficiencies in the production of *ex-vivo* DC's has inspired investigators to design artificial antigen-presenting cells (aAPCs) as alternatives.

Extensive studies on DC/T cell interactions *in vitro* have shown that the activation of T cells proceeds *via* a pre-clustering of MHC-peptide complexes in microdomains. These microdomains subsequently cluster into the so-called 'immune synapse' (IS).[8,9] Similar to many extracellular biological recognition processes, T cell activation consequently requires the simultaneous multivalent interaction of a number of receptors to initiate clustering. Molecular constructs that are able to mimic this simultaneous multivalent binding have a higher efficacy by increasing the avidity.[10–12] Further, activation does not only involve one type of receptor but multiple receptors instead that interact with different activation inducing molecules (*i.e.* MHC/peptides, co-stimulatory adhesion molecules, *etc.*).

The first generation of aAPCs, microbead-based DCs, have shown a marked advantage in expanding specific T cells under laboratory conditions compared to free MHC peptide complexes. Their efficacy for long-term T cell expansion has been limited, however.[13] Unlike aAPCs, natural APCs have the ability to conform to the cell surface topography and allow the dynamic movement of receptor-ligand complexes to form the IS that ultimately causes T cell activation. Most likely the rigid sphere morphology of these microbead

based aAPCs hinders the efficient formation of multivalent interactions with the T cells.[14,15] These aAPCs lack the plasma membrane fluidity of natural APCs that allows for the dynamic movement of these complexes to the IS site.[16] Soft spherical aAPCs, such as liposomes,[17] have overcome the membrane fluidity constraint enhancing T cell activation over and above that observed for the rigid sphere models, suggesting that the IS can form more efficiently if a dynamic movement of both binding partners can take place (Figure 2.1).
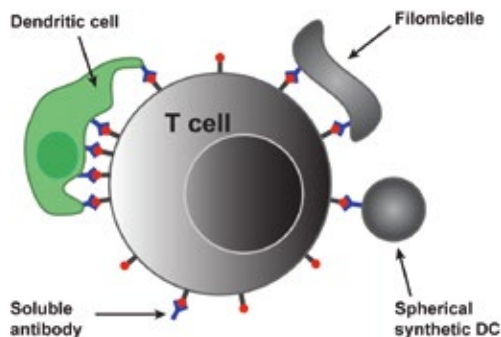
Figure 2.1. Schematic diagram illustrating different systems for T cell activation.

Besides an efficient formation of the IS, also the number of receptor-ligand interactions involved in IS formation is known to play an important role in T cell activation. The number of interactions is dictated by the size and the morphology of the particle. In general, for rigid spherical particles the number of ligands available to participate in the required simultaneous interaction is limited by its topology.[17–19] Second-generation immunotherapeutic delivery vehicles have, therefore, explored extended aspect ratio topologies such as filamentous or rod-like particles. These extended aspect ratio structures have utilized either copolymer filomicelles[20] or decorated carbon nanotubes (CNTs).[21] Both filomicelles and CNTs have demonstrated a higher activity compared to their spherical counterparts.[21,22] This marked increase in efficacy is most likely a result of the larger surface-to-volume ratio that allows a more effective loading. If the micelle area is held constant for a given mass of co-polymer their effective loading is increased by 50 % compared to the corresponding sphere.[20] Besides the increased effective loading that may aid in enhancing multivalent binding, filamentous or rod-like particles also show longer circulation times in the body that might play an additional advantageous role in T cell activation.[20]

The design criteria for an ideal synthetic dendritic cell (sDC) should incorporate the described knowledge gained from aAPCs and commonly used therapeutic delivery vehicles. It should combine the above characteristics of a high aspect ratio, a flexible architecture and multiple interactions to achieve highly efficient T cell activation. The sDCs should further possess an extended half-life and a low systemic toxicity.[23–25]

Here, a fundamentally new design of sDCs is proposed that has the potential to fulfil all of the above criteria. The strategy to building these novel delivery vehicles is based on a new class of rod-like, semi-stiff and water-soluble polymers derived from oligo ethylene oxide-substituted polyisocyanopeptides.[26,27] Polyisocyanopeptides consist of a helical polyisocyanide backbone. This backbone carries peptide-functionalized side chains that are attached to every carbon stabilizing the helix through hydrogen bonding.[28–30] These polymers can be up to 2 μm long and exhibit a well-defined stereoregularity[31] as well as a controlled stiffness that can be tuned between persistence lengths (L_P) of 5 nm to 200 nm.[27,32] Since in principle every individual monomer can be substituted with a functional unit, a versatile synthon for the design of multivalent filamentous sDCs is easily obtained (Figure 2.2).
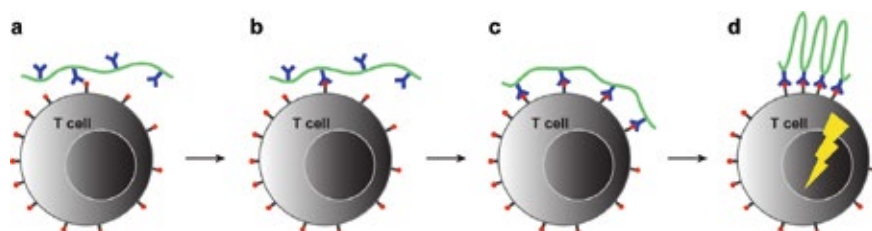
Figure 2.2. Stages of sDC binding and T cell activation. a) the mobility of the sDC assists in locating the T cell; b) sDC docks onto the T cell; c) attachment to multiple recognition sites; d) sDC contracting/clustering at the recognition sites, IS formation.

This design is based on the following hypothesis: First, the semi-stiff polyisocyanopeptide decorated with effector molecules docks on T cells (Figure 2.2a/b). The semi-stiffness of the polyisocyanopeptide will then allow all effector molecules on the sDC to bind to neighbouring receptors on the same cell (Figure 2.2c). This is not possible for a rigid spherical bead or a flexible random-coil polymer, where multivalent interactions require entropically non-favourable, extended polymer conformations.[10,12] Subsequently, using a semi-stiff polymer, these receptor sites will be able to

cluster with a concomitant contraction of the polymer backbone to form the IS while retaining the activated state (Figure 2.2d). To test the design strategy, sDCs were functionalized with anti-CD3 antibodies (αCD3-sDC) that are known to cause T cell activation and the efficacy of these sDCs was compared with microbead based aAPCs (αCD3-PLGA) and free αCD3 antibodies.

2.2 Results and Discussion

2.2.1 Synthesis and Characterization of the αCD3-sDCs

Synthetic dendritic cells (sDCs) carrying T cell stimulating αCD3 antibodies have been synthesized from semi-stiff polyisocyanopeptides. To obtain these sDCs, an azide-containing polyisocyanopeptide was synthesized in the first step (see experimental section for synthesis details). This was achieved by co-polymerizing a mixture of an azide-functionalized monomer and a methoxy-functionalized monomer using a 1:100 molar ratio resulting in a random copolymer (Scheme 2.1).
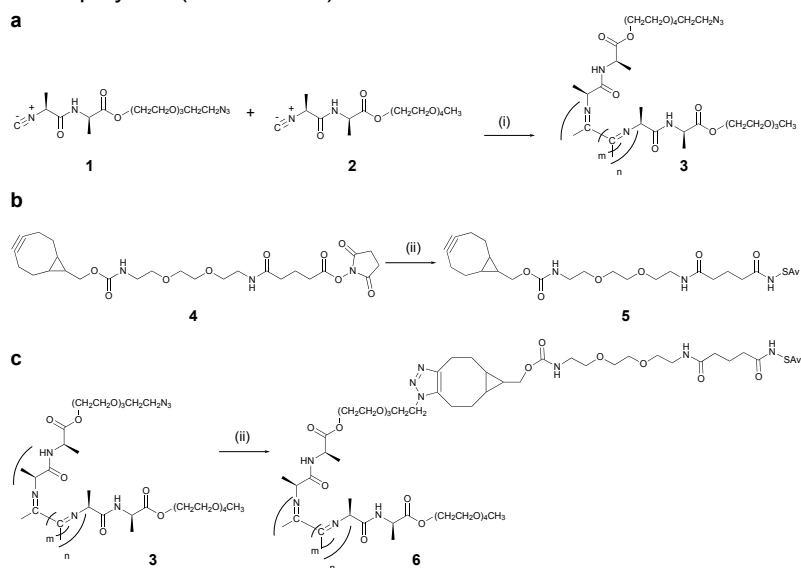
Scheme 2.1. Synthetic scheme to obtain Streptavidin (SAv)-functionalized polyisocyanopeptides. a) random co-polymerization of the azide (**1**) and the methoxy (**2**) monomers to obtain the azide-functionalized polymer (**3**), i) Ni(Cl$_2$O$_4$)$_2$ • 6 H$_2$O, toluene; b) coupling of BCN-NHS (**4**) to SAv, ii) 4 days at 4 °C in 10 mM borate buffer pH 8.5; c) synthesis of the SAv-polymer bioconjugate (6), iii) 4 days at 4 °C in 10 mM borate buffer pH 8.5.

The obtained polymers have a degree of polymerization DP = 1633 and a length between 150 nm and 200 nm (Table 2.1). The statistical spacing between azide groups is 10 nm. These azide groups were subsequently used to couple BCN-functionalized streptavidin (SAv) to the polymer backbone using a strain-promoted azide alkyne cycloaddition (SPAAC) reaction.[33]
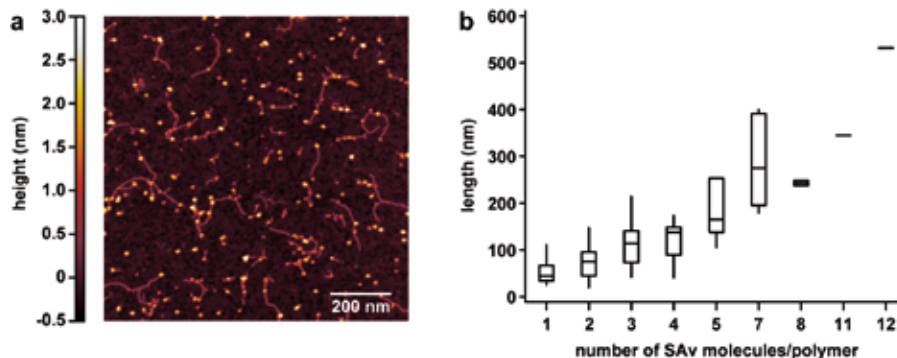
Figure 2.3. AFM analysis of SAv-functionalized polyisocyanopeptides. a) representative AFM image clearly showing the SAv molecules (bright dots) attached to the polymer; b) number of SAv molecules per polymer.

The obtained SAv-functionalized polymer contains on average one SAv molecule every 40-50 nm (Figure 2.3), as determined with AFM. sDCs were obtained by adding biotinylated αCD3 antibodies yielding αCD3-sDC. When preparing the αCD3-sDC, the ratio of αCD3 to SAv on the polymer was adjusted such that on average every SAv was bound to one αCD3 antibody (Figure A2.1.6). Consequently, an average polymer with a length of 150-200 nm contains between 3 and 5 αCD3 antibodies.

2.2.2 Cell viability measurements

Before testing the efficacy of these novel sDCs on peripheral blood lymphocytes (PBLs), cell viability studies were carried out to study their biocompatibility. PBLs exposed to αCD3-sDC or free αCD3 at different concentrations exhibited no significant decrease in cell viability (MTT assay; Figure 2.4a). At higher αCD3 concentrations even an increase in the number of cells was observed, which can be explained by induction of T cell proliferation by the αCD3 antibodies (*vide infra*). Even after prolonged

incubation times, cell viability remained constant between 90-100 % even up to 72 hours (Trypan Blue assay; Figure 2.4b).
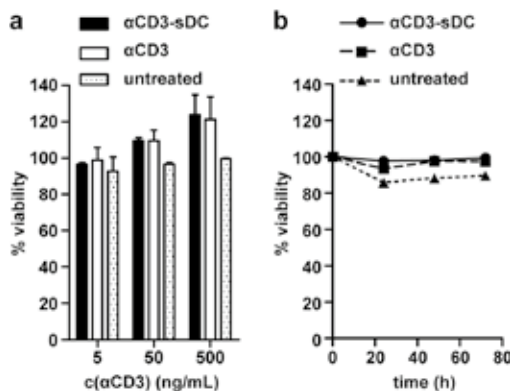
Figure 2.4. Viability of PBLs exposed to αCD3-sDC. a) MTT assay showing cell viability as a function of αCD3 concentration (incubation time 24 h) b) Trypan Blue assay showing cell viability as a function of incubation time (αCD3 concentration of 200 ng/mL for both αCD3-sDC and free αCD3). The results represent the mean ± s.e.m. (*n* = 3).

2.2.3 T cell activation

In subsequent experiments, the capacity of αCD3-sDC to activate T cells was determined in comparison to free αCD3 antibodies, streptavidin-bound αCD3 (αCD3-SAv) and the corresponding isotype control (mIgG2a-sDC). After clustering of CD3 on the T cells, intracellular signalling results in direct activation as demonstrated by expression of the early T cell activation marker CD69.[34] Activated T cells further show enhanced secretion of IFNγ as a late activation event[35] and eventual T cell proliferation is observed.[36]

At saturating concentrations (>50 ng/mL), CD69 expression was at its maximum, for both the αCD3-sDC and the controls including free αCD3 and αCD3-SAv (Figure 2.5a). At low concentrations (1-20 ng/mL), however, the αCD3-sDCs were ~2.5 fold more effective in inducing T cell activation when compared to the αCD3 and αCD3-SAv controls. Similarly, the αCD3-sDC activated T cells released 2-3 fold higher amounts of IFNγ than the tested controls (Figure 2.5b). Taken together, these findings and the additional controls shown in Figure A2.1.7 indicate that αCD3-sDC induces a more robust T cell activation when compared to T cells exposed to free αCD3 or αCD3-SAv.
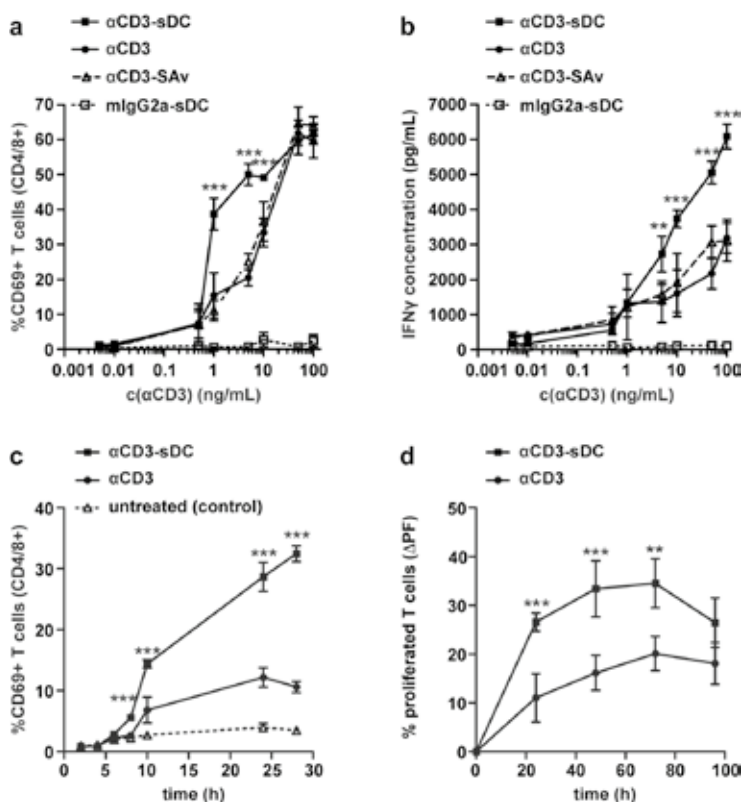
Figure 2.5. T cell activation profile upon treatment at different concentrations and after different time points. a) percentage of T cells showing CD69 expression and b) IFNγ release at different αCD3 concentrations (incubation time 24 h); c) percentage of T cells showing CD69 expression after different incubation times (αCD3 concentration 5 ng/mL); d) T cell proliferation estimated using a CFSE assay (αCD3 concentration 50 ng/mL). The values were normalized against the untreated control. Each value represents the mean ± s.e.m. (*n* = 4). The asterisks (*) indicate the statistical significance (*, **, *** p ≤ 0.05, 0.01, 0.001) of αCD3-sDC compared to αCD3.

To substantiate the above findings, T cell activation was followed over time at a low effective treatment concentration (5 ng/mL αCD3 for both αCD3-sDC and free αCD3). The αCD3-sDC treated T cells were activated at significantly earlier time points (Figure 2.5c). Over prolonged exposure, T cell activation increased up to ~35 %. In comparison, T cell activation following treatment with free αCD3 shows a delay in T cell activation (10 hours *vs.* 7 hours for αCD3-sDC) and a lower percentage of activated T cells (only ~10-15 %). Finally, the ability of αCD3-sDC to induce T cell proliferation was tested (50 ng/mL αCD3 for both αCD3-sDC and free αCD3). In line with the above results, a 2-3 fold higher number of proliferated T cells was detected

when the T cells were treated with αCD3-sDC (Figure 2.5d). Treatment with αCD3-sDC leads to a constant increase in the proliferation rate until 72 h of treatment. The observed decrease in the number of T cells at 96 h is likely resulting from nutrient depletion in the growth medium at high cell concentrations.

To investigate the importance of the structural architecture of the novel sDCs, their efficacy was compared to spherical αCD3-PLGA particles (1.8 µm diameter, see experimental section). The worm-like αCD3-sDCs were ~7 fold more efficient in stimulating T cell activation (CD69 expression) when compared to αCD3-PLGA particles, even at concentrations as low as 1 ng/mL (Figure 2.6a). Also the production of IFNγ was ~3 fold higher when compared to αCD3-PLGA particles (Figure 2.6b). Together these observations indicate that the αCD3-sDCs do not only activate T cells significantly better at lower concentrations. They also induce the highest IFNγ production when compared with solid particle based DCs.
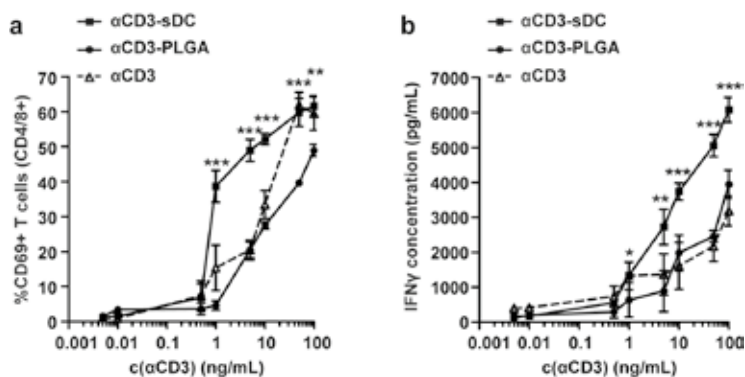
Figure 2.6. Comparison of αCD3-sDC with spherical αCD3-PLGA. a) percentage of T cells showing CD69 expression and b) IFNγ release at different αCD3 concentrations (incubation time 24 h); The results represent the mean ± s.e.m. (n = 3). The asterisks (*, **, *** $p \leq 0.05$, 0.01, 0.001) indicate the statistical significance of αCD3-sDC compared to αCD3.

This difference in efficacy cannot be explained with the number of receptor-ligand interactions that can form when using αCD3-sDCs (~3-5 interactions) or αCD3-PLGA particles (~1-10 interactions; see appendix 2.2). This similar number of possible interactions for both geometries clearly suggests that it is not the density of αCD3 but the ability of polymer-based sDCs to flexibly adjust to the spacing of receptors and to dynamically form the immune synapse that leads to the superior activity of the sDCs. In other

words, multiple static interactions are not sufficient. It has been postulated that a more dynamic anisotropic interaction between the binding partners is required to induce and enhance T cell activation.[37,38] Unlike the static shape of the hard sphere model, the controlled stiffness of the αCD3-sDC filament has the capacity to 'concertina' in response to the receptor clustering events associated with the formation of the immune synapse (Figure 2.2).

2.2.4 Localization of αCD3-sDC on the cell surface

To investigate the molecular process in more detail and to understand how the sDCs interact with T cells, binding studies were performed with fluorescently labelled αCD3-sDCs. The PBLs were incubated with different concentrations of either fluorescein labelled αCD3-sDCs (FαCD3-sDC) or free αCD3 (FαCD3) for 24 hours (see experimental section). Subsequently, the number of fluorescent cells was determined using a laser scanning confocal microscope (Figures 2.7 and A.2.1.9).
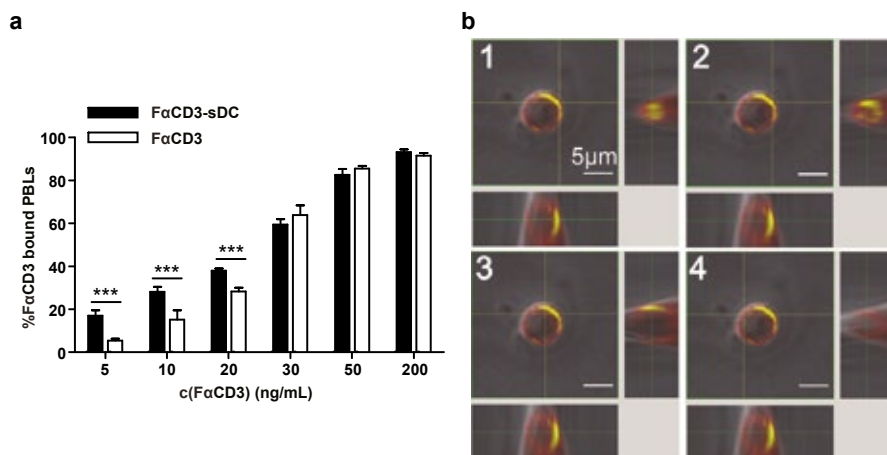
Figure 2.7. αCD3-sDC binding and location on the cell. a) percentage of PBLs showing bound FαCD3 or FαCD3-sDC after 24 hours of treatment. The result shows the mean ± s.e.m. (*n* = 3). The significance of αCD3-sDC compared to αCD3 is indicated by the asterisks (*** p≤ 0.001). b) orthographic projection of one PBL illustrating αCD3-sDC clustering/binding (yellow; co-localization of red and green fluorescence). The fluorescence image is merged with a DIC image. The series shows optical cross sections over the y-coordinate (x- and z-coordinate constant), demonstrating the αCD3-sDC distribution on the cell.

At high concentrations (50 and 100 ng/mL) the relative number of T cells that show binding of FαCD3-sDC on their surface was comparable to the percentage of cells that have been treated with free FαCD3. In the low concentration range (≤20 ng/mL), however, a higher fraction of PBLs carrying

FαCD3-sDC was observed when compared to the cells treated with free FαCD3. This result clearly explains the higher efficacy of the αCD3-sDCs in the low concentration range (Figure 2.7a). Besides more efficient binding, 3D images taken after 24 hours further reveal that FαCD3-sDC remained co-localized on the membrane indicating that no receptor internalization has been taking place (Figure 2.7b).

Summarizing the above results, this new class of semi-stiff and filamentous polymers serves as an ideal scaffold for functionalization with antibodies to allow for multiple, simultaneous receptor interactions. These novel sDCs do not only activate T cells at significantly lower concentrations than free antibodies and their rigid sphere-like PLGA counterparts but also induce a faster T cell response. Docking of the first antibody to the T cell increases the effective molarity of αCD3 at the cell surface thereby increasing the probability for the remaining antibodies to bind (Figure 2.2b). It is known that T cell stimulation by αCD3 in solution causes internalization of the CD3 leading to termination of the T cell response.[39] The experiments with fluorescently labelled FαCD3-sDC have indicated that FαCD3-sDC remains bound on the T cell surface even after 24 h of treatment. The semi-stiff, filamentous morphology of the αCD3-sDCs consequently does not only lead to a significantly higher and earlier (CD69 expression) but also to a more sustained T cell response compared to the free antibody and the spherical geometry. This result is supported by the expression of the late stage activation marker INFγ and the associated higher T cell proliferation rates. These findings have important consequences for the therapeutic use of αCD3 antibodies, which show *in vivo* toxicity at high concentrations.[40] As our αCD3-sDCs show T cell activation at lower concentrations compared to free αCD3 antibodies, this new design can help to overcome these toxicity problems and widen the therapeutic window of αCD3 antibodies.

Despite their clearly proven potential as DC mimic, a number of open questions remain. The stiffness of the polymer combined with the density of effector molecules appears to be the crucial parameter for efficient T cell activation. Antibody-functionalized polyisocyanopeptides are an ideal scaffold to investigate the importance of these parameters in a systematic way. Both the density of effector molecules as well as the polymer stiffness can be easily tuned for this new class of functional polymers. Experiments to study the role of effector molecule spacing and polymer length are described in chapter 3.

2.3 Conclusions

In this chapter it was demonstrated that multivalency in combination with a controlled semi-stiffness are key parameters for designing potentially therapeutically active vehicles that closely mimic natural DCs. Using a novel sDC design, a more efficient as well as more sustained T cell response was observed. This enhanced activity clearly validates the final stage of the proposed binding mechanism (Figure 2.2d) that requires the sDC to respond to the processes occurring on the T cell surface during formation of the immune synapse. Having shown the potency of the sDCs, the next goal is a more detailed investigation of the sDC induced T cell activation mechanism. This will ultimately allow for increasing their efficacy even further. To develop the presented sDC system for clinical applications against cancer, the αCD3 antibodies will be replaced with MHC-peptide complexes and co-stimulatory molecules, necessary for highly efficient T cell activation. Cytokines can be coupled in addition to further shape the T cell response. Ultimately, after characterization of their *in vivo* behaviour, sDCs have the potential to become a highly efficient and cost-effective nanovaccine for cancer immunotherapy. Besides cancer immunotherapy, the semi-stiff polyisocyanopeptides scaffold might be used for other applications where multivalent binding is essential. Multivalency, for example, plays an important role in drug targeting. Functionalization of the scaffold with effector molecules as well as targeting and imaging moieties can potentially lead to a more efficient accumulation and detection of the therapeutic agent at the desired site of action opening up a far bigger range of possible therapeutic and diagnostic applications.

2.4 Experimental section

Materials

Unless otherwise stated, all chemicals were obtained from Sigma Aldrich (Zwijndrecht, The Netherlands) and used without further purification. Toluene was distilled over sodium. Dichloromethane was distilled over phosphorous pentoxide. Column chromatography was performed using silica gel (0.060-0.200 mm) provided by Baker (Deventer, The Netherlands). Thin layer chromatography (TLC) analyses were carried out on silica 60 F254 coated glass obtained from Merck Millipore (Schiphol-Rijk, The Netherlands). The compounds were visualized using Ninhydrin or basic aqueous $KMnO_4$ solutions. ^1H NMR and ^{13}C NMR spectra were recorded on a Bruker AC-300 MHz instrument (Delft, The Netherlands) operating at 300 MHz and 75 MHz, respectively. *J* values are given in Hz and chemical shifts are reported in ppm. Me_4Si was used as the internal standard. FT-infrared spectra of the compounds were measured using a Thermo Nicolet IR300 FT-IR spectrometer (Thermo Fisher Scientific, Breda, The Netherlands) equipped with a Harrick ATR unit. UV/VIS measurements were done using a Varian Cary 50 spectrometer (Agilent Technologies, Amstelveen, The

Netherlands). For mass spectrometry a LCQ Advantage MAX instrument (Thermo Fisher Scientific) was used.

Monomer synthesis

Synthesis of the azide-functionalized isocyanide monomer (1)

The synthesis of (R)-2-(2-(2-(2-azidoethoxy)ethoxy)ethoxy)ethyl 2-((S)-2-isocyano propanamido)propanoate **(1)** was performed as shown in scheme S1 and is described below. Tetraethylene glycol was tosylated to yield **S1**. Compound **S1** was then coupled to Boc-(*L*)-alanine *via* a carbodiimide coupling using *N,N'*-dicyclohexylcarbodiimide (DCC) in the presence of 0.1 mol equivalents of 4-dimethylaminopyridine (DMAP) resulting in **S2**. The Boc group was removed using a HCl saturated ethyl acetate solution. Deprotection was monitored by TLC (SiO$_2$, 10 % MeOH/CH$_2$Cl$_2$). The deprotected ethylene glycol-functionalized amino acid was treated with *N,N*-Diisopropylethylamine (DIPEA) before being coupled to Boc-(*D*)-alanine *via* a DCC coupling in the presence of N-Hydroxybenzotriazole (HOBt) yielding **S3**. Again, the Boc protecting group of **S3** was removed using a HCl saturated ethyl acetate solution. Formamide **S4** was obtained by refluxing with 4 eq of sodium formate using ethyl formate as the solvent. Nucleophilic substitution of the tosyl-group with sodium azide resulted in **S5**. Finally, compound **S5** was dehydrated using diphosgene to obtain the isocyanide **1**.
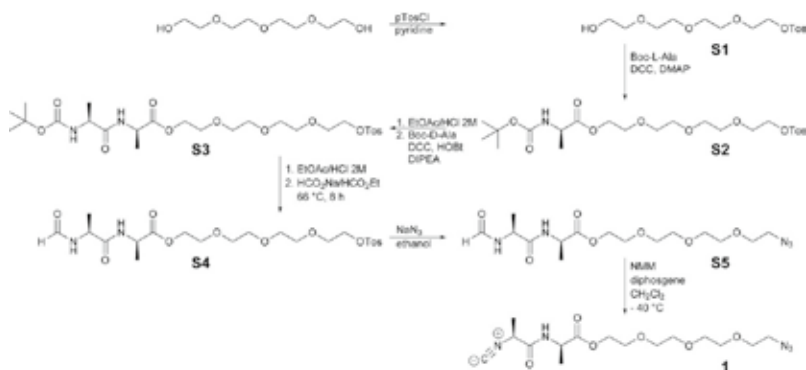
Scheme S1. Synthetic route towards the azide-functionalized monomer **(1)**

*Synthesis of 2-(2-(2-(2-hydroxyethoxy)ethoxy)ethoxy)ethyl 4-methylbenzene sulfonate (**S1**)*

Tetraethylene glycol (28.5 mL, 164.3 mmol) was dissolved in 50 mL pyridine. The solution was subsequently cooled to 0° C while stirring. Argon was bubbled through the solution for 15 minutes. Tosylchloride (21.93 g, 115 mmol) was added portion wise to the stirring solution. The mixture was further stirred at room temperature for 12 hours. The reaction mixture was diluted with 50 mL of 10 % citric acid. The mixture was extracted three times into 250 mL of chloroform. The combined organic layers were dried over anhydrous Na$_2$SO$_4$, filtered and evaporated under vacuum. The resulting yellow oil was purified using column chromatography (SiO$_2$, 0.060 - 0.200 mm; ethyl acetate as eluent) to yield **S1** as a pale yellow oil (11.69 g, 33.6 mmol, 29 %); R$_f$ = 0.4 (ethyl acetate). FT-IR (cm^{-1}, ATR) 3442 (O-H), 2870 (C-H), 1597 (N-H), 1453 (C-H), 1352 (S=O), 1175 (S=O), 1096 (C-O); ^{1}H NMR δ_H(300 MHz; CDCl$_3$; Me$_4$Si) 7.80 (dd, *J* = 7.81 Hz, 2H, -C$\underline{H}_{Ar}$-), 7.33 (d, *J* = 7.35 Hz, 2H, -C$\underline{H}_{Ar}$-S), 4.17 (m,

2H, O-CH$_2$-CH$_2$-), 3.65 (m, 16H, -CH$_2$-), 2.45 (s, 3H, -CH$_3$); ^{13}C NMR δ_C(75 MHz; CDCl$_3$; Me$_4$Si) 21.16 (1C, CCH$_3$), 61.0 (1C, COH), 68.13(1C, COS), 69.0 (1C, OCH$_2$), 70.0, 70.1, 70.1, 70.2 (4C, OCH$_2$), 70.8, 72.0 (2C, OCH$_2$), 127.5 (2C, CHCCH), 129.5 (2C, CHCCH), 139.7 (1C, CCH$_3$), 144.5 (1C, CHCS).

Synthesis of (R)-2-(2-(2-(2-(tosyloxy)ethoxy)ethoxy)ethoxy)ethyl 2-((tert-butoxycarbonyl)amino)propanoate (S2)

Compound **S1** (5.23 g, 15.01 mmol), *N*-Boc-(*L*)-alanine (2.86 g, 15.01 mmol) and DMAP (0.198 g, 1.65 mmol) were dissolved in 25 mL of freshly distilled CH$_2$Cl$_2$ and cooled to 0° C while stirring. DCC (3.12 g, 15.01 mmol) was added portion wise. The mixture turned yellow and was stirred for 1 h at 0° C followed by stirring for 3 h at room temperature. The precipitated dicyclohexyl urea was removed by filtration and washed with ethyl acetate (3 x 20 mL). The organic layer was concentrated under vacuum. The crude product was purified using column chromatography (SiO$_2$, 0.060 - 0.200 mm; 1 % MeOH/CH$_2$Cl$_2$ as eluent) to yield **S2** as a light orange oil (5.49 g, 11.4 mmol, 76 %); R$_f$ = 0.4 (10 % MeOH/CH$_2$Cl$_2$). FT-IR (cm^{-1}, ATR) 2924 (C-H), 1745 (C=O ester), 1712 (C=O amide), 1597 (N-H), 1452 (C-H), 1352 (S=O), 1173 (S=O), 1120 (C-O); ^{1}H NMR δ_H(300 MHz; CDCl$_3$; Me$_4$Si) 7.79 (d, *J* = 8.4 Hz, 2H, -CH$_{Ar}$-), 7.33 (d, *J* = 8.1 Hz, 2H, -CH$_{Ar}$-), 5.02 (s, 1H, -NH-), 4.28 (m, 3H, -CH(CH$_3$)-, COOCH$_2$-), 4.15 (m, 2H, O-CH$_2$-CH$_2$-), 3.69 (m, 14H, O-CH$_2$-CH$_2$-), 2.44 (s, 3H, -CH$_3$), 1.44 (s, 9H, -OC(CH$_3$)$_3$), 1.37 (d, *J* = 7.2 Hz, 3H, -CH(CH$_3$)-); ^{13}C NMR δ_C(75 MHz; CDCl$_3$; Me$_4$Si) 18.8 (1C, CHCH$_3$), 21.7 (1C, CCH$_3$), 28.4 (3C, C(CH$_3$)$_3$), 49.4 (1C, O(C=O)CHNH), 64.5 (1C, Boc-OCH$_2$), 68.9 (2C, OCH$_2$), 69.4 (1C, OCH$_2$), 70.7 (4C, OCH$_2$), 80.3 (1C, C(CH$_3$)$_3$), 128.2 (2C, CHCCH), 130.0 (2C, CHCCH), 145.0 (1C, CCH$_3$), 155.4 (1C, CHCS), 173.6 (1C, CH(C=O)NH), 176.7 (1C, CH(C=O)O); MS (ESI) m/z [M+Na]$^+$ calcd 542.2; found 542.2.

Synthesis of (R)-2-(2-(2-(2-(tosyloxy)ethoxy)ethoxy)ethoxy)ethyl 2-((S)-2-((tert-butoxycarbonyl)amino)propanamido)propanoate (S3)

Compound **S2** (5.94 g, 11.4 mmol) was dissolved in 60 mL of HCl saturated ethyl acetate and stirred for 2 h at room temperature. The solvent was evaporated under vacuum and the excess of HCl was removed by adding 30 mL of CH$_2$Cl$_2$ and 1 mL of n-BuOH followed by evaporation. The residual n-BuOH was removed *via* azeotropic distillation with 3x 30 mL CH$_2$Cl$_2$. The resulting HCl salt of **S2**, *N*-Boc-(*D*)-alanine (2.14 g, 11.4 mmol) and *N*-hydroxybenzotriazole monohydrate (HOBt; 1.74 g, 11.4 mmol) were dissolved in 40 mL freshly distilled CH$_2$Cl$_2$. DIPEA (2 mL, 11.4 mmol) was added drop wise and the mixture was stirred at room temperature until everything was dissolved. The solution was cooled to 0 °C and DCC (2.35 g, 11.4 mmol) was added portion wise. A white precipitate was formed and the mixture was stirred for 1 h at 0° C followed by 3 h of stirring at room temperature. The precipitate was filtered off, washed with ethyl acetate (3x 30 mL) and the solvent was evaporated under vacuum. The crude product was purified using column chromatography (SiO$_2$, 0.060 - 0.200 mm; 2 % MeOH/CH$_2$Cl$_2$ as eluent) to yield **S3** as a pale yellow oil (3.37 g, 5.7 mmol, 52 %); R$_f$ = 0.3 (10 % MeOH/CH$_2$Cl$_2$). FT-IR (cm^{-1}, ATR) 2876 (C-H), 1740 (C=O ester), 1718 (C=O amide), 1667 (N-H), 1522 (N-H), 1452 (C-H), 1365 (S=O), 1161 (S=O), 1105 (C-O); ^{1}H NMR δ_H(300 MHz; CDCl$_3$; Me$_4$Si) 7.80 (d, *J* = 8.4, 2H, -CH$_{Ar}$- C-S), 7.36 (d, *J* = 8.1, 2H, -CH$_{Ar}$-), 6.91 (s, 1H, -NH), 5.00 (s, 1H, -NH), 4.58 (m, 1H, -NHCH(CH$_3$)-), 4.28 (m, 2H, -COOCH$_2$-), 4.14 (m, 2H, O-CH$_2$-CH$_2$-), 3.61 (m, 12H, -C(O)OCH$_2$CH$_2$O(CH$_2$CH$_2$O)$_3$-), 2.45 (s, 3H, -CH$_3$), 1.45 (s, 9H, -OC(CH$_3$)$_3$), 1.40 (d, *J* =

7.2, 3H, -CH(C$\underline{H}_3$)-), 1.35 (d, *J* = 7.2, 3H, -CH(C$\underline{H}_3$)-); ^{13}C NMR δ_C(75 MHz; CDCl$_3$; Me$_4$Si) 18.2 (2C, CHCH$_3$), 21.7 (1C, CCH$_3$), 28.4 (3C, C(CH$_3$)$_3$), 47.2 (1C, NCH), 50.0 (1C, NCH), 64.5 (1C, Boc-OCH$_2$), 68.7 (2C, OCH$_2$), 69.3 (1C, OCH$_2$), 70.6 (4C, OCH$_2$), 80.2 (1C, C(CH$_3$)$_3$), 128.0 (2C, CHCCH), 129.9 (2C, CHCCH), 133.1 (1C CCH$_3$), 144.9 (1C, CHCS), 172.7 (2C, C=O); MS (ESI) m/z [M+Na]$^+$ calcd 613.2; found 613.1.

Synthesis of (R)-2-(2-(2-(2-(tosyloxy)ethoxy)ethoxy)ethoxy)ethyl 2-((S)-2-formamidopropanamido)propanoate (S4)

Compound **S3** (1.70 g, 2.85 mmol) was deprotected following the same procedure as described for compound **S2** and used without further purification. The crude product was dissolved in 25 mL ethyl formate. Sodium formate (0.97 g, 14.25 mmol) was added and the mixture was heated for 8 hours at 66 °C. The mixture was cooled to room temperature and the solid was filtered off. The solvent was evaporated under vacuum. The crude product was purified using column chromatography (SiO$_2$, 0.060 - 0.200 mm; 4 % MeOH/CH$_2$Cl$_2$ as eluent) to yield **S4** as a light yellow oil (0.79 g, 1.52 mmol, 54 %); R$_f$ = 0.3 (10 % MeOH/CH$_2$Cl$_2$). FT-IR (cm^{-1}, ATR) 2873 (C-H), 1738 (C=O), 1653 (N-H), 1532 (N-H), 1452 (C-H), 1352 (S=O), 1174 (S=O), 1097 (C-O); ^{1}H NMR δ_H(300 MHz; CDCl$_3$; Me$_4$Si) 8.18 (s, 1H, $\underline{H}$C(O)NH-), 7.79 (d, *J* = 8.4, 2H, -C$\underline{H}_{Ar}$- C-S), 7.35 (d, *J* = 8.7, 2H, -C$\underline{H}_{Ar}$-), 6.78 (s, 1H, -N$\underline{H}$), 6.55 (s, 1H, -N$\underline{H}$), 4.55 (m, 2H, -NHC$\underline{H}$(CH$_3$)-), 4.30 (m, 2H, -COOC$\underline{H}_2$-), 4.13 (m, 2H, O-C$\underline{H}_2$-CH$_2$-), 3.61 (m, 12H, -(C$\underline{H}_2$C$\underline{H}_2$O)$_3$-), 2.44 (s, 3H, -C$\underline{H}_3$), 1.42 (m, 6H, -CH(C$\underline{H}_3$)-); ^{13}C NMR δ_C(75 MHz; CDCl$_3$; Me$_4$Si) 17.9 (1C, CHCH$_3$), 18.2 (1C, CHCH$_3$), 21.7 (1C, CCH$_3$), 47.2 (1C, O(C=O)HNCH), 48.1 (1C, HNHC(C=O)), 64.5 (1C, OCH$_2$), 68.7 (2C, OCH$_2$), 69.3 (1C, OCH$_2$), 70.6 (4C, OCH$_2$), 128.0 (2C, CHCCH), 129.9 (2C, CHCCH), 133.1 (1C, CCH$_3$), 144.9 (1C, CHCCH), 161.0 (1C, H(C=O)NH), 172.6 (1C, CH(C=O)NH), 173.2 (1C, CH(C=O)O); MS (ESI) m/z [M+Na]$^+$ calcd 541.2; found 541.2.

Synthesis of (R)-2-(2-(2-(2-azidoethoxy)ethoxy)ethoxy)ethyl 2-((S)-2-formamido propanamido)propanoate (S5)

Compound **S4** (0.550 g, 1.06 mmol) was dissolved in 40 mL of absolute EtOH. Sodium azide (0.38 g, 5.9 mmol) was added and the mixture was refluxed overnight. Once cooled to room temperature, the solids were removed by filtration and the filtrate was dried under vacuum. The crude product was purified using column chromatography (SiO$_2$, 0.060 - 0.200 mm; 4 % MeOH/CH$_2$Cl$_2$ as eluent) to yield **S5** a pale orange oil (0.32 g, 0.82 mmol, 78 %); R$_f$ = 0.4 (10 % MeOH/CH$_2$Cl$_2$). FT-IR (cm^{-1}, ATR) 3309 (N-H), 2875 (C-H), 2105 (N3), 1737 (C=O), 1651 (N-H), 1529 (N-H), 1453 (C-H), 1133 (C-O); ^{1}H NMR δ_H(300 MHz; CDCl$_3$; Me$_4$Si) 8.20 (s, 1H, $\underline{H}$C(O)NH-), 6.84 (s, 1H, -N$\underline{H}$), 6.60 (s, 1H, -N$\underline{H}$), 4.60 (m, 2H, NHC$\underline{H}$(CH$_3$)), 4.26 (m, 2H, -C(O)OC$\underline{H}_2$-), 3.68 (m, 12H, -(C$\underline{H}_2$C$\underline{H}_2$O)$_3$-), 3.40 (m, 2H, N$_3$C$\underline{H}_2$-), 1.42 (m, 6H, -CH(C$\underline{H}_3$)-); ^{13}C NMR δ_C(75 MHz ; CDCl$_3$; Me$_4$Si) 17.9 (1C, CH$_3$), 18.2 (1C, CH$_3$), 47.4 (1C, CH$_2$N$_3$), 48.4 (1C, H(C=O)HNCH), 50.7 (1C, HNC(CH$_3$)C=O), 69.0 (1C, CH$_2$CH$_2$O), 70.1 (1C, OCH$_2$CH$_2$), 70.6 (2C, OCH$_2$), 70.7 (2C, OCH$_2$), 161.4 (1C, H(C=O)NH), 172.7 (1C, CH(C=O)NH), 172.9 (1C, CH(C=O)O); MS (ESI) m/z [M+Na]$^+$ calcd 412.2; found 412.2.

Synthesis of (R)-2-(2-(2-(2-azidoethoxy)ethoxy)ethoxy)ethyl 2-((S)-2-isocyanopropanamido)propanoate (1)

Compound **S5** (221 mg, 0.57 mmol) and N-methylmorpholine (NMM; 0.24 mL, 2.27 mmol) were dissolved in 150 mL freshly distilled CH_2Cl_2 and cooled down to -40 °C (dry acetone bath) under an argon atmosphere. A solution of diphosgene (0.048 mL, 0.398 mmol) in 10 mL of freshly distilled CH_2Cl_2 was added drop wise under argon over 1 h. While adding diphosgene, the mixture was stirred and kept strictly at -40° C. Once the mixture began to turn yellow, the reaction was rapidly quenched with an excess of sodium bicarbonate (5 g). The quenched mixture was stirred for 5 minutes at -40 °C. The reaction mixture was passed over a short silica column plug (SiO_2, 0.060 - 0.200 mm). The plug was packed with CH_2Cl_2 but the desired compound was eluted with CH_2Cl_2/acetonitrile (3:1) to yield **1** as a pale yellow oil (48.1 mg, 0.48 mmol, 27 %); R_f = 0.5 (10 % $MeOH/CH_2Cl_2$). FT-IR (cm^{-1}, ATR) 3318 (N-H), 2875 (C-H), 2142 (C≡N), 2105 (N3), 1744 (C=O), 1540 (N-H), 1453 (C-H), 1123 (C-O); ^1H NMR δ_H(300 MHz; $CDCl_3$; Me_4Si) 7.00 (bd, 1H, -N$\underline{H}$-), 4.59 (m, 1H, -NHC$\underline{H}$(CH_3)C(O)O-), 4.32 (m, 3H, (-C(O)OC$\underline{H}_2$CH_2O-), -C≡NC$\underline{H}$(CH_3)C(O)NH-), 3.67 (m, 12H, -(OC$\underline{H}_2$C$\underline{H}_2$)_3), 3.39 (m, 2H, N_3C$\underline{H}_2$-), 1.65 (d, J = 7.2, 3H, C≡NCH(C$\underline{H}_3$)C(O)-), 1.48 (d, J = 7.2, 3H, C≡NCH(C$\underline{H}_3$)C(O)-); ^{13}C NMR δ_C(75 MHz; $CDCl_3$; Me_4Si) 170.69 (1C, CH(CH_3)$\underline{C}$(O)OCH_2), 165.72 (1C, CH(CH_3)$\underline{C}$(O)NH), 70.69, 70.65, 70.61, 70.56, 70.02, 68.81 (1 C, $\underline{C}H_2CH_2O$), 50.66 (1C, $\underline{C}H_2N_3$), 48.56 (C≡N$\underline{C}$H), 19.66, 18.04 (1C, CH($\underline{C}H_3$)CO); MS (ESI) m/z $[M+Na]^+$ ($C_{15}H_{25}N_5O_6Na$), calcd 394.17; found 394.1.

Synthesis of the methoxy-functionalized isocyanide monomer (2)

The synthesis of (S)-2,5,8,11-tetraoxatridecan-13-yl 2-((R)-2-isocyanopropanamido) propanoate **(2)** was performed as shown in scheme S2 and has been reported previously.[26,27] Tetraethylene glycol monomethyl ether was coupled to Boc-(*L*)-alanine to obtain **S6** *via* DCC coupling in the presence of 0.1 mol equivalents of DMAP. **S6** was deprotected using a HCl saturated ethyl acetate solution. After deprotection, **S6** was coupled to Boc-(*D*)-alanine *via* a DCC coupling in the presence of HOBt. The product **S7** was again deprotected using a HCl saturated ethyl acetate solution until no more starting material could be observed by TLC analysis (SiO_2, 5 % $MeOH/CH_2Cl_2$). The deprotected amine was formylated with sodium formate to obtain formamide **S8**. After purification, **S8** was dehydrated with diphosgene to obtain the isocyanide **2**.
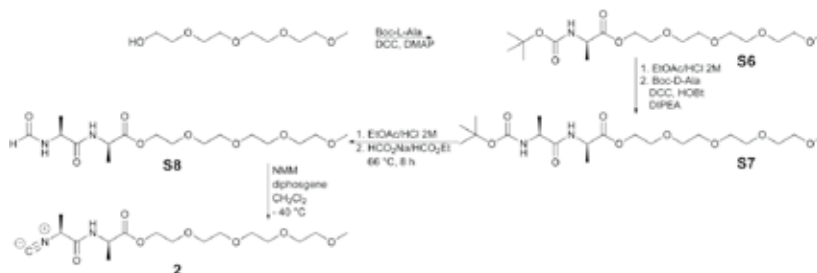
Scheme S2. Synthetic route towards the methoxy-functionalized monomer **(2)**

Synthesis of (R)-2,5,8,11-tetraoxatridecan-13-yl 2-((tert-butoxycarbonyl)amino) propanoate (S6)

Tetraethylene glycol monomethylether (5.01 g, 24.1 mmol), N-Boc-(*L*)-alanine (4.47 g, 23.6 mmol) and DMAP (0.37 g, 3.0 mmol) were dissolved in 30 mL of freshly distilled CH_2Cl_2 and cooled to 0 °C while stirring. DCC (4.96 g, 24.0 mmol) was added and the mixture turned yellow gradually. It was stirred for 1 h at 0 °C and allowed to heat up to room temperature for another 3 h. The precipitate was filtered off, washed with ethyl acetate (3 x 20 mL) and the filtrate was dried under vacuum. The crude product was purified using column chromatography (SiO_2, 0.060 - 0.200 mm; 1 % MeOH/CH_2Cl_2 as eluent) to yield **S6** as an orange oil (7.24 g, 19.08 mmol, 80.7 %); R_f = 0.8 (CH_2Cl_2). FT-IR (cm^{-1}, ATR): 3344 (N-H), 2878 (C-H), 1757 (C=O ester), 1712 (C=O protecting group), 1520 (N-H), 1453 (C-H), 1165 (C-O); ^{1}H NMR δ_H(300 MHz; $CDCl_3$; Me_4Si) 5.08 (s, 1H, -N<u>H</u>-), 4.29 (m, 3H, -CH(C<u>H</u>$_3$)-, COOC<u>H</u>$_2$-), 3.65 (m, 14H, -C<u>H</u>$_2$-), 3.38 (s, 3H, -OC<u>H</u>$_3$), 1.43 (d, *J* = 1.39 Hz, 9H, -C(C<u>H</u>$_3$)-), 1.37 (s, 3H, -CH(C<u>H</u>$_3$)-).

Synthesis of (R)-2,5,8,11-tetraoxatridecan-13-yl 2-((S)-2-((tert-butoxycarbonyl) amino)propanamido)propanoate (S7)

Compound **S7** was synthesized according to the same procedure as compound **S3**. The crude product was purified using column chromatography (SiO_2, 0.060 - 0.200 mm; 2 % MeOH/CH_2Cl_2 as eluent) to yield **S7** as a slightly yellow oil (4.43 g, 9.5 mmol, 63 %); R_f = 0.5 (10 % MeOH/CH_2Cl_2). FT-IR (cm^{-1}, ATR) 3317 (N-H), 2876 (C-H), 1739 (C=O ester), 1671 (N-H), 1517 (N-H), 1452 (C-H), 1163 (C-O); ^{1}H NMR δ_H(300 MHz; $CDCl_3$; Me_4Si) 6.80 (s, 1H, -N<u>H</u>CH-), 5.11 (bs, 1H, -N<u>H</u>CH), 4.60 (q, *J* = 8.56 Hz, 1H, -NHC<u>H</u>(CH$_3$)-), 4.28 (m, 3H, -C(O)OC<u>H</u>$_2$CH$_2$O-, -C<u>H</u>(CH$_3$)COO-), 3.73-3.64 (m, 14H, -C(O)OCH$_2$C<u>H</u>$_2$O(C<u>H</u>$_2$CH$_2$O)$_3$-), 3.39 (s, 1H, -OC<u>H</u>$_3$), 1.46 (s, 9H, -OC(C<u>H</u>$_3$)$_3$), 1.43 (d, *J* = 1.40 Hz, 3H, -NHCH(C<u>H</u>$_3$)-), 1.36 (d, *J* = 1.33 Hz,3H, -NHCH(C<u>H</u>$_3$)-).

Synthesis of (S)-2,5,8,11-tetraoxatridecan-13-yl 2-((R)-2-formamidopropan amido)propanoate (S8)

Compound **S8** was synthesized according to the same procedure as described for compound **S4**. The crude product was purified using column chromatography (SiO_2, 0.060 - 0.200 mm; 4 % MeOH/CH_2Cl_2 as eluent) to yield **S8** as a colorless oil (1.74 g, 4.6 mmol, 69 %); R_f = 0.4 (10 % MeOH/CH_2Cl_2). FT-IR (cm^{-1}, ATR) 3297 (N-H), 2875(C-H), 1739 (C=O ester), 1653 (N-H), 1529(N-H), 1452 (C-H), 1101 (C-O); ^{1}H NMR δ_H(300 MHz; $CDCl_3$; Me_4Si) 8.21 (s, 1H, -C(O)NH-), 6.96 (bd, *J*=7.5Hz, 1H, -NHCH-), 6.79 (bd, *J*=7.5Hz, 1H, -N<u>H</u>CH-), 4.58 (m, 2H, NHC<u>H</u>(CH$_3$)), 4.31 (m, 2H, -C(O)OC<u>H</u>$_2$-), 3.67-3.56 (m, 14H, -C(O)OCH$_2$C<u>H</u>$_2$O(C<u>H</u>$_2$CH$_2$O)$_3$-), 3.39 (s, 3H, -OC<u>H</u>$_3$), 1.43 (m, 6H, -NHCH(C<u>H</u>$_3$)-, -NHCH(C<u>H</u>$_3$)-).

Synthesis of (S)-2,5,8,11-tetraoxatridecan-13-yl 2-((R)-2-isocyanopropanamido) propanoate (2)

Compound **2** was synthesized according to the same procedure as compound **1**. The crude product was purified using column chromatography (SiO_2, 0.060 - 0.200 mm; CH_2Cl_2/acetonitrile 3:1 as eluent) to yield **2** as a colorless oil (174 mg, 0.48 mmol, 63 %); R_f = 0.4 (10 % MeOH/CH_2Cl_2). FT-IR (cm^{-1}, ATR) 3250 (N-H, amide), 2875 (C-H), 2140 (C≡N, isocyanide), 1741 (C=O, ester), 1682 (C=O, amide), 1100 (C-O, ether); ^{1}H NMR δ_H(300 MHz;

CDCl$_3$; Me$_4$Si) 6.99 (bd, 1H, -N*H*-), 4.58 (m, 1H, -NHC*H*(CH$_3$)C(O)O-), 4.32 (m, 2H, -C(O)OC*H*$_2$CH$_2$O-), 4.25 (m, 1H, C≡NC*H*(CH$_3$)C(O)NH-), 3.73-3.53 (m, 14H, -OCH$_2$C*H*$_2$(OC*H*$_2$C*H*$_2$)$_3$OCH$_3$), 3.37 (s, 3H, -OC*H*$_3$), 1.64 (d, *J* = 7.2 Hz, 3H, C≡NCH(C*H*$_3$)C(O)-), 1.49 (d, *J* = 7.2 Hz, 3H, -NHCH(C*H*$_3$)C(O)O-); ^{13}C NMR δ_C(75 MHz; CDCl$_3$; Me$_4$Si) 171.98 (-CH(CH$_3$)*C*(O)OCH$_2$-), 165.73 (-CH(CH$_3$)*C*(O)NH-), 160.9 (*C*≡N-), 71.92 (-*C*H$_2$CCH), 70.60, 70.60, 70.60, 70.51, 70.51, 68.8, 65.55 (-O*C*H$_2$CH$_2$O)$_3$-), 64.72 (-C(O)O*C*H$_2$-), 59.00 (-O*C*H$_3$), 48.58 (C≡N*C*H(CH$_3$)CONH-), 48.58 (-NH*C*H(CH$_3$)C(O)O-), 19.66 (C≡NCH(*C*H$_3$)CONH-), 18.02 (NHCH(*C*H$_3$)C(O)O-); MS (ESI) m/z [M+Na]$^+$ (C$_{18}$H$_{39}$N$_2$O$_7$Na), calcd 383.1; found 383.2.

Polymer synthesis (3)

Compound **1** (3.1 mg, 8.3 · 10^{-3} mmol) and compound **2** (300 mg, 8.3 · 10^{-1} mmol) were dissolved in 30 mL of distilled toluene yielding a ratio of azide-functionalized monomers **(1)** to methoxy-functionalized monomers **(2)** of 1:100. The catalyst stock solution was prepared separately by dissolving Ni(Cl$_2$O$_4$)$_2$•6 H$_2$O (30.7 mg, 8.4 · 10^{-2} mmol) in 10 mL of absolute ethanol and 90 mL of toluene. From the catalyst stock solution 8.3 · 10^{-5} mmol was added to the reaction mixture. The mixture was stirred for 3 days at room temperature (RT). The reaction was followed by IR until all isocyanide was consumed (peak at 2142 cm^{-1}). The polymer (compound **3**) was isolated *via* precipitation into diisopropylether. This precipitation cycle was repeated thrice to obtain 299.6 mg, 78 % yield.

Polymer characterization

The molecular weight M_w of the resulting polymer was determined from both viscosity and size exclusion chromatography (SEC) measurements. In addition, the polymer length was determined using atomic force microscopy (AFM). The corresponding experiments are described in detail below. The results are summarized in table 2.1.

Table 2.1. Summary of molecular weight M_w and polymer length l

	molecular weight M_w (kg/mol)	apparent polymer length l (nm)
M_v viscosity	421	123[a]
M_w SEC	588	172[a]
AFM	677[b]	197

[a]The apparent polymer length l was calculated from the measured molecular weight:

$$l = M_w \cdot \frac{1}{4} \cdot \frac{1}{360 \ g/mol} \cdot 0.42 \ nm$$

[b]The molecular weight M_w was calculated from the experimentally determined polymer length:

$$M_w = l \cdot 4 \cdot 360 \ g/mol \cdot \frac{1}{0.42 \ nm}$$

Viscosity measurements

The intrinsic viscosity of polymer **3** was obtained from measurements with an Ubbelohde viscometer (Schott Instruments, Mainz, Germany). A stock solution (4 mg/mL) of polymer **3** was prepared in acetonitrile. From this stock solution, 4 mL of the following concentrations were prepared: 0.6; 0.5; 0.4; 0.3; 0.2 and 0.1 mg/mL. The solutions were loaded into a

viscometry tube (nr. 1053431; Schott Instruments). The tube was placed into the water bath (25 °C) and allowed to equilibrate for 15 min before the measurement. The flow speed for each sample was measured four times and used to determine the kinematic viscosity v. From this data, the reduced viscosity η_{red} and the inherent viscosity η_{inh} were calculated[41] and plotted against the polymer concentration. The intrinsic viscosity [η] represents the limiting value of η_{red} or η_{inh} at infinite dilution of the polymer, *i.e.* $\left[\eta \right] = \lim_{c \to 0} \eta_{inh}$. From extrapolation of η_{red} to c = 0, an intrinsic viscosity [η] = 9.64 dL·g^{-1} was obtained (Figure A2.1.1). Based on [η], a molecular weight of 421 kg/mol was determined using the Mark-Houwink equation $\left[\eta \right] = K \overline{M_v}^a$. The constants K = 1.4·10^{-9} dL·mol^a·g$^{-(1+a)}$ and a = 1.75 for a rigid polyisocyanide have been reported previously.[42] The average polymer length was calculated to be 123 nm (Table 2.1).

Size exclusion chromatography

Polymer **3** was further analyzed by size exclusion chromatography (SEC) to determine its hydrodynamic radius. The SEC system was equipped with a Waters 1515 Isocratic HPLC pump, a Waters 2414 refractive index detector, a Waters 2707 autosampler, a PSS PFG guard column followed by 2 PFG-linear-XL (7 µm, 8*300 mm) columns in series. The system was run at 40 °C. Hexafluoroisopropanol (HFIP, Biosolve) with potassium trifluoroacetate (3 g/L) was used as eluent at a flow rate of 0.8 mL/min. The molecular weights were calculated against poly(methyl methacrylate) standards (M$_p$ = 580 Da up to M$_p$ = 7.1·10^6 Da; Agilent). The measurement yielded a molecular weight of 588 kg/mol and the average polymer length was calculated to be 172 nm (Figure A2.1.2 and Table 2.1).

AFM measurements

The polymer sample was diluted in 1 mM sodium acetate buffer pH 4.5 to obtain a concentration between 0.5 µg/mL and 5 µg/mL. The samples were drop casted onto freshly cleaved and polylysine coated mica and incubated for 10 minutes. The remaining liquid was removed and the sample was dried in a stream of N$_2$. AFM images were recorded in tapping mode in air using a Nanoscope IV instrument (Bruker) and NSG-10 tapping mode tips (NT-MDT, Limerick, Ireland). The polymer length was determined by hand using the program ImageJ[43] (Figure A2.1.3 and Table 2.1).

Synthesis and characterization of the SAv-polymer bioconjugate (6)
Functionalization of Streptavidin with BCN-NHS (5)

Streptavidin (SAv) was obtained from Thermo Fisher Scientific (Etten-Leur, The Netherlands) and 2,5-dioxopyrrolidin-1-yl 1-(bicyclo[6.1.0]non-4-yn-9-yl)-3,14-dioxo-2,7,10-trioxa-4,13-diazaoctadecan-18-oate (BCN-NHS; compound **4**) was obtained from Synaffix (Nijmegen, The Netherlands). SAv (34.5 mg, 5.2·10^{-4} mmol) was dissolved in 7 mL of borate buffer (10 mM, pH 8.5) and BCN-NHS (1.7 mg, 3.1·10^{-3} mmol) was added to the SAv solution. The mixture was kept at 4 °C for four days. BCN-functionalized SAv (compound **5**) was purified by gel filtration (PD 10 column, GE Healthcare) followed by ultrafiltration (Amicon Ultra-4, 10 kDA; Merck Millipore). The final yield of **5** was determined by measuring absorption at 280 nm. Using an extinction coefficient of ε = 167280 mol^{-1} cm^{-1}, the yield was determined to be 26.1 mg, 76 %. The conjugate was further characterized using MALDI-ToF to obtain the labelling ratio. MALDI-ToF was performed using a Bruker Biflex III MALDI-ToF spectrometer.

SAv and SAv-BCN samples were prepared using α-Cyano-4-hydroxycinnamic acid as the matrix. The mass obtained for SAv (monomer) was determined to be 13280 Da [$M^+ H^+$]. This served as a reference for **5**. Compound **5** shows both the peak of the non-functionalized monomer of 13280 Da [$M^+ H^+$] as well as the mass of **5** carrying one BCN-group coupled to the SAv monomer: 13783 Da [$M^+ 2K^+$] (Figure A2.1.4). No peak corresponding to a doubly labelled monomer was visible. Consequently, the degree of functionalization is between 0 and 4 BCN-groups for the SAv tetramer.

Synthesis of the SAv-polymer conjugate (6)

Polymer **3** in 10 mL of 10 mM borate buffer (10 mg, $2.7 \cdot 10^{-5}$ mmol) was mixed with SAv-BCN (26 mg, $3.9 \cdot 10^{-7}$ mmol) in 4 mL of 10 mM borate buffer. The mixture was incubated at 4 °C for four days to obtain polymer **6**. Polymer **6** was purified by dialysis against water at 4 °C for 2 days using a membrane with cut-off of 100 kDa.

Characterization of the SAv-polymer conjugate (6)

Circular dichroism measurements

To ensure that the bioconjugation does not affect the structure of the poly(isocyanopeptide) polymer, circular dichroism spectra were recorded for both polymer **3** and polymer **6**. The measurements were performed at 20 °C at a concentration of 1 mg/mL in 50 mM borate buffer pH 8.5 using a Jasco J-810 CD spectrometer (de Meern, The Netherlands). Both polymers showed identical spectra (Figure A2.1.5) clearly indicating that the coupling of SAv does not influence the secondary structure of the SAv-polymer conjugate.

AFM measurements

The SAv loading of **6** was determined with AFM using the same procedure as for polymer **3**. The results of this analysis are shown in Figure 2.3.

Synthesis and characterization of αCD3-sDCs

To obtain the αCD3-sDCs, the αCD3 antibodies were first biotinylated with EZ-Link Sulfo-NHS-LC-Biotin (Thermo Fisher Scientific) to allow for binding to SAv on polymer **6**. Before preparing the αCD3-sDCs, the molecular ratio of αCD3:SAv bound to the sDCs was optimized using a biotinylated AlexaFluor488-labelled αCD3 antibody. Using the fluorescently labelled antibody, it was possible to determine the αCD3 concentration while measuring the total protein concentration in the same sample. First, the SAv concentration on polymer **6** was determined using a BCA micro assay (Thermo Fisher Scientific). Then polymer **6** was mixed with the AlexaFluor488-labelled and biotinylated αCD3 antibody using 4:1, 6:1 and 8:1 molar ratios of αCD3:SAv. The mixture was left at 4 °C for 24 h. After removing the free αCD3 by ultrafiltration (Nanosep Omega, cut-off of 300 kDa, PALL Life Sciences, Zaventem, Belgium) the total protein concentration was again determined using the BCA assay. In addition, the fluorescence originating from the AlexaFluor488-labelled antibody was determined from a fluorescence measurement in a microplate reader (Cytofluor II, PerSeptive Biosystems, Framingham, MA, USA). The αCD3 concentration was calculated from a standard curve of AlexaFluor488-labelled αCD3. Subtracting the Alexa488-αCD3 concentration from the total protein concentration, the SAv concentration as well as the αCD3:SAv ratio was determined. For a 4:1 mixing ratio of αCD3:SAv approximately one αCD antibody was bound per SAv molecule (Figure A2.1.6). To prepare the sDCs for the T cell experiments, a 4:1 mixing ratio

was used following exactly the same protocol as used in the preliminary experiment described above. Assuming that the ratio of bound αCD3:SAv will be identical, the concentration of αCD3 could now be determined from the total protein concentration without the need for fluorescently labelling the αCD3 antibody. For the T cell experiments, all the treatment concentrations were based on the concentration of αCD3 present on the sDC backbone, on the microbead system or as free αCD3.

Cell preparation and cell culture

Peripheral Blood Lymphocytes (PBLs) were isolated from the buffy-coat obtained from a healthy volunteer via Ficoll density gradient centrifugation (Lucron Bioproducts, Sint Martens-Latem, Belgium). The PBLs and OKT3 hybridoma cells were always maintained in RPMI-1640 medium (Life Technologies, Bleiswijk, The Netherlands) containing 10 % Fetal Bovine Serum (FBS) (Greiner Bio-One B.V., Alphen a/d Rijn, The Netherlands), 1 % glutamine (Lonza, Breda, The Netherlands) and 1x Antibiotic-Antimycotic (Life Technologies). For the αCD3 production, OKT3 hybridoma cells (at confluence) were transferred into Protein Free Hybridoma Medium (PFHM-II, Life Technologies). These cells were cultured for 3-4 days in PFHM-II before purifying the αCD3 monoclonal antibodies using HiTrap™ Protein G HP Columns (GE Healthcare).

Cell viability measurements

MTT assay

The cytotoxic effect of the αCD3-sDCs was determined using a standard MTT assay.[44] PBLs (10^5 cells/well) were treated with αCD3-sDC, αCD3 or left untreated (control) for 24 h using different concentrations (5, 50, 500 ng/mL) of the respective molecules. After washing twice, the cells were incubated with MTT (5 mg/mL; Sigma Aldrich) for 2 h. The medium was then replaced with 100 µl of DMSO. After solubilization, the microplates were read at 550 nm using a microplate reader (iMark, Bio-Rad, Veenendaal, The Netherlands). The results were derived from three independent experiments (with three replicates per experiment).

Trypan Blue assay

In addition, the cell viability was estimated over time. Viable and non-viable cells were counted after αCD3-sDC treatment using the hemacytometer method by means of a Trypan Blue assay.[45] The percentage of viable cells was determined upon exposure to αCD3-sDC, αCD3, and untreated (control) in a concentration of 200 ng/mL and incubation times of 0, 24 and 72 h. The percentage of viable cells was calculated according to the formula: 100 x (number of viable cells in treated samples/total number of cell counted). The results were obtained from three independent experiments (with three replicates per experiment).

T cell activation

Flow cytometry (CD69 expression)

The estimation of activated T cells (CD69+ T cells) upon αCD3-sDC treatment was determined using Fluorescence Activated Cell Scanning (FACS). Briefly, PBLs (10^5/well) were treated with the respective molecules for 24 h at different concentrations (0.005, 0.01, 1, 5, 10, 50, 100 ng/mL). In addition to these concentration dependent experiments, also time dependent T cell activation studies were performed. The T cells were treated with αCD3-sDC and αCD3 using a concentration of 5 ng/mL and incubation times of 2, 4, 6, 8, 10, 24, 28 and

30 h. The treated cells were washed with PBS containing 10 % BSA (PBA; Sigma Aldrich). Subsequently, the cells were incubated with Fluorescein-labelled mouse anti-human CD69 mAb (activated T cell marker, BD Biosciences, Breda, The Netherlands) and APC-labelled mouse anti-human CD4/8 mAb (T cell marker, BD Biosciences). After washing twice with PBA, FACS analysis was performed using a CyAn™ ADP Analyzer instrument (Beckman Coulter, Woerden, The Netherlands). The results were analyzed using Flow-Jo ver. 9.2 software (Tree Star Inc., Ashland, OR, USA). The above experiment was repeated four independent times (with three replicates per experiment).

Enzyme-linked immunosorbent assay (ELISA; IFNγ secretion)

The level of secreted IFNγ was determined in the culture supernatants using a standard sandwich ELISA method. After coating overnight at 4 °C with mouse anti-human IFNγ antibody (Thermo Fisher Scientific), the 96-well microplates (Nunc Immunomodules; Thermo Fisher Scientific) were washed with PBS/Tween (0.05 %) and blocked with PBS-1 % BSA. Subsequently, the IFNγ standards (Thermo Fisher Scientific) and the supernatants were added into the wells and incubated for 1 hour at room temperature. Following washing with PBA for three times, the presence of IFNγ was detected using a biotinylated mouse anti-human IFNγ antibody (Thermo Fisher Scientific) and a streptavidin-horseradish peroxidase (HRP) conjugate (Life Technologies). HRP activity was detected using tetramethyl benzidine (TMB; Sigma Aldrich). The absorption was measured at 450 nm using an iMark Microplate Reader (Bio-Rad). The experiments were conducted for four independent times.

Summary of all controls for CD69 expression and IFNγ secretion

The level of CD69 expression as well as the concentration of the secreted IFNγ was determined for αCD3-sDC and for the following controls: non-biotinylated, free αCD3 antibodies (αCD3); biotinylated αCD3 bound to streptavidin (αCD3-SAv); biotinylated αCD3 bound to streptavidin-functionalized PLGA particles (αCD3-PLGA); non-biotinylated αCD3 mixed with polymer **6** (polymer 6 + αCD3); polymer **6** alone (polymer 6); polymer **3** alone (polymer 3); streptavidin alone (SAv); non-biotinylated, free mouse anti-human IgG$_{2a}$ antibodies as αCD3 isotype control (mIgG$_{2a}$); biotinylated mIgG$_{2a}$ antibodies bound to polymer **6** (mIgG$_{2a}$-sDC). The results of all treatment conditions are summarized in Figure A2.1.7.

CFSE assay

T cell proliferation induced by αCD3-sDC was assessed using a CFSE assay.[46] PBLs (10^5) were pre-labelled with 5 µM CFSE (Life Technologies). Free CFSE was quenched with FBS. αCD3-sDC and αCD3 was added to the CFSE-labelled PBLs (10^5/well) at a concentration of 5 ng/mL. Treated cells were incubated overnight along with untreated control cells. After incubation times of 0, 24, 48, 72 and 96 h, the treated cells were used for FACS analysis. T cells were identified based on labelling with a mouse APC-labelled anti-human CD4/8 antibody. T cell proliferation was assessed from determining the CFSE staining intensity. The results were interpreted by considering the % decrease in fluorescence intensity as a corresponding % increase in T cell proliferation. The % difference in T cell proliferation (%ΔPF) was determined by normalizing the treated value against the untreated (control) value. Cyton software was utilized to analyze the number of cells proliferated per generation (Figure A2.1.8).[47] The results were derived from four independent experiments (with three replicates per experiment).

Statistical analysis

Two-way ANOVA and Bonferroni post-tests were performed for a pair wise comparison between the variables using Graphpad Prism 5 software (San Diego, CA, USA). The statistical significance is defined as $p < 0.05$. The asterisk '*', '**', '***' represents p values <0.05, <0.01 and <0.001

Confocal imaging

The binding of αCD3-sDC on the T cell surface was analyzed by confocal imaging using sDCs carrying a fluorescein-labelled αCD3 antibody (FαCD3-sDC). PBLs (10^5/well) were treated for 24 h with FαCD3-sDC and FαCD3 (F-Fluorescein, λ_{ex} = 488 nm, λ_{em} = 520 nm) at different concentrations (5, 10, 20, 30, 50, 200 ng/mL). Further, these cells were labelled with the membrane dye PKH26 (λ_{ex} = 551 nm, λ_{em} = 567 nm; Sigma Aldrich) following the manufacturer's protocol. These labelled PBLs were fixed in 4 % paraformaldehyde. The fixed cells were quenched with glycine (0.1 mM) in PBS. The cover slips were mounted onto microscope slides (Thermo Fisher Scientific) using MOWIOL (Merck Millipore). The slides were imaged using a Confocal Laser Scanning Microscope (Olympus FV1000) equipped with a 63x oil immersion objective. The cells that show bound FαCD3-sDC were counted manually and compared to the number of FαCD3-sDC-free cells (Figure A2.1.9) using the program ImageJ. All the experiments were repeated three independent times using PBLs from three different healthy donors.

Comparison of aCD3-sDC efficacy with aCD3-PLGA particles
Synthesis of αCD3-PLGA particles

A particle-based DC system was prepared using PLGA particles as described previously[48] with the following modifications. To attach the αCD3 antibody to PLGA *via* the SAv-biotin interaction, SAv was covalently coupled to the PLGA particles (PLGA-SAv). In brief, protected sulfhydryl groups were introduced into SAv using N-Succinimidyl S-Acetylthiopropionate (SATP; Thermo Scientific) and deprotected with hydroxylamine hydrochloride (Thermo Scientific) using the manufacturer's protocol. Thereafter, the free thiol-groups on the SAv were reacted with the maleimide group of the DSPE-PEG-maleimide (MW = 2000 g/mol) that is present on the PLGA surface. After washing with PBS, the biotinylated αCD3 antibody was bound to PLGA-SAv to obtain αCD3-PLGA.

Characterization of αCD3-PLGA particles

The size and concentration of the SAv-PLGA and αCD3-PLGA were determined using Transmission Electron Microscopy (TEM; JEOL TEM 1010, Nieuw-Vennep, The Netherlands) (Figures A2.1.10a and A2.1.10b) and Differential Interference Contrast (DIC; Figure A2.1.10c) using a confocal microscope (FluoView FV1000, Olympus, Zoeterwoude, The Netherlands). To obtain the particle concentration, the particle suspension was imaged using a Bürker chamber. The suspension was imaged under semi-dry conditions on the Bürker chamber grid to ensure that all particles had settled on the grid surface. The number of particles on the square grid was counted using the program ImageJ. For the αCD3-PLGA particles, the concentration was calculated to be $1.24 \cdot 10^{17}$ particles per mL. To estimate the amount of αCD3 bound per αCD3-PLGA particle, a biotinlyated and AlexaFluor488-labelled αCD3 antibody was used in the same way as described for the αCD3-sDCs described above. This

experiment yielded an amount of 3795 αCD3 antibodies per PLGA particle. For the T cell experiments, where no fluorescently labelled antibody was used, it has been assumed that the amount of bound αCD3 will be the same for identical experimental conditions.

2.5 Appendix 2.1: Supplementary figures
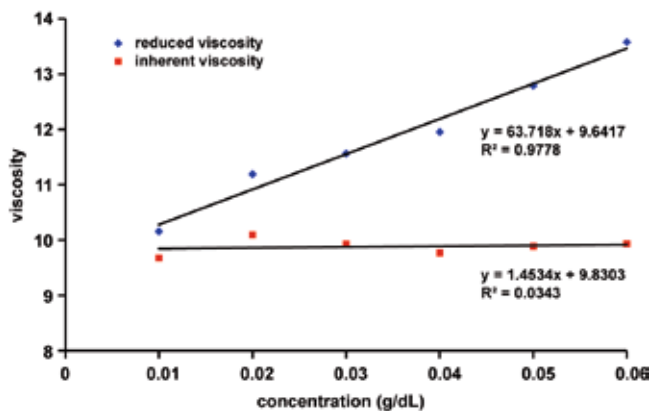
Figure A2.1.1. Ostwald viscosity measurement. The intrinsic viscosity was determined experimentally from both the reduced viscosity and the inherent viscosity for different concentrations of the polymer in acetonitrile. The value for the intrinsic viscosity $[\eta]$ = 9.64 dL·g^{-1} was obtained from extrapolation to c = 0 g/dL.
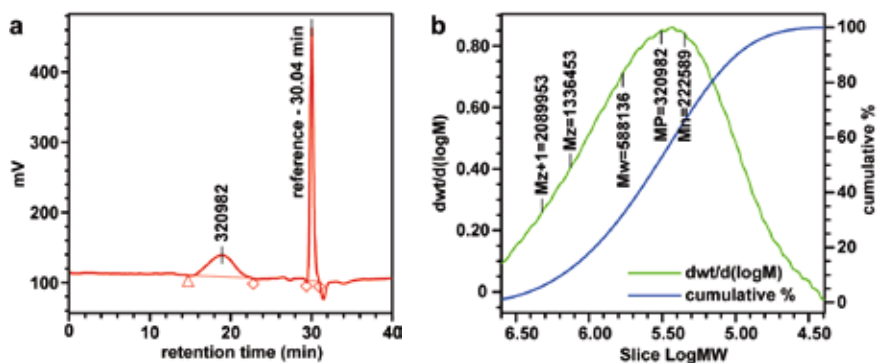
Figure A2.1.2. Size exclusion chromatography. a) Compound **3** eluted at 18.5 min. b) This corresponds to a weighted average molecular weight M_w of 588 kg/mol (PMMA standards) and a PDI of 2.6.
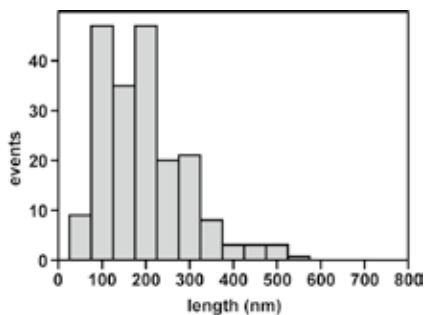
Figure A2.1.3. Measurement of the polymer length with AFM. The mean value is 197 nm (*n* = 198).
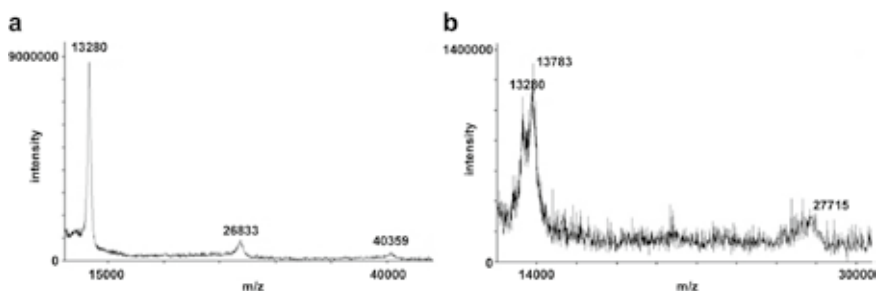
Figure A2.1.4. MALDI-ToF analysis. a) SAv before addition of BCN-NHS; b) BCN-functionalized SAv.
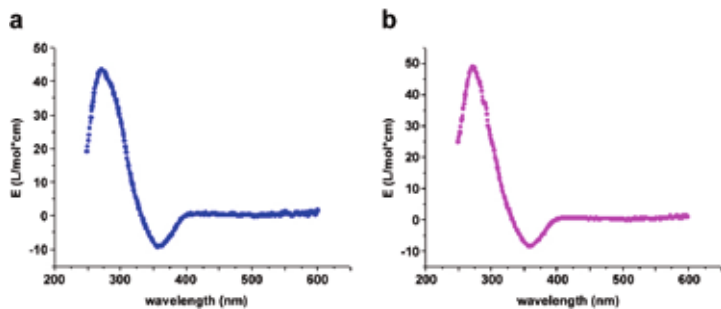
Figure A2.1.5. Circular dichroism spectra. a) polymer **3**; b) SAv-polymer conjugate **6**.
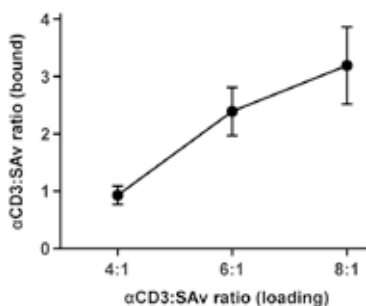
Figure A2.1.6. Loading of polymer 6 with αCD3 antibodies. Different ratios of biotinylated, AlexaFluor488-labelled αCD3 were added to polymer **6** (αCD3:SAv ratio = 4:1, 6:1 and 8:1). For a ratio of 4:1, an average number of 0.93 αCD3 molecules was obtained per SAv molecule. For 6:1 and 8:1, a final ratio of 2.69 and 3.37 αCD molecules were bound per SAv molecule, respectively. Mean values and standard deviations were determined from 8 experiments (n = 8).
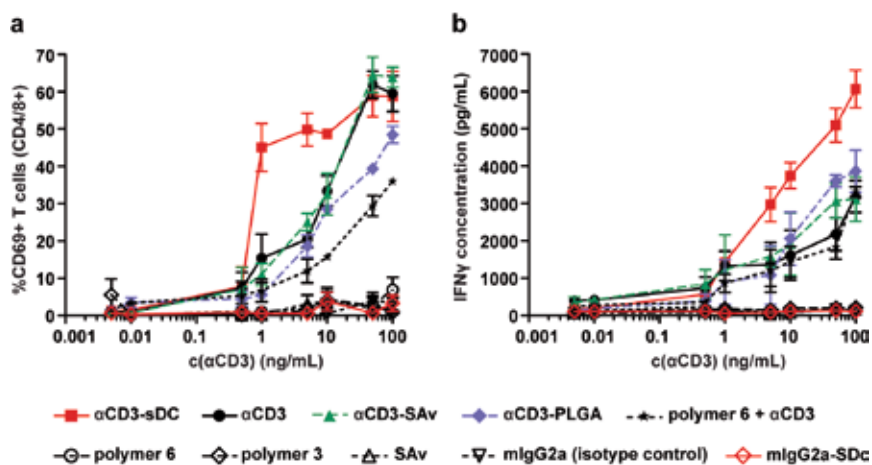
Figure A2.1.7. T cell activation profile based on the early activation marker CD69. a) and late activation marker IFNγ. b) Each value represents the mean ± s.e.m. of three independent donors.
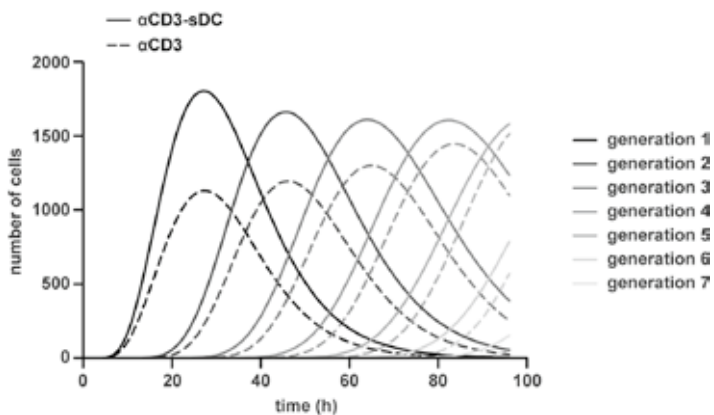
Figure A2.1.8. T cell proliferation determined with a CFSE assay. The graph represents the increase in the number of T cells per generation after treatment with αCD3-sDC and soluble αCD3, respectively. In the case of the αCD3-sDC treatment, the cell proliferation rate increases to a maximum in the first generation. This proliferation rate was maintained over the following generations (for the complete time period analyzed). When treating the T cells with soluble αCD3, the cell number only gradually increases per generation.
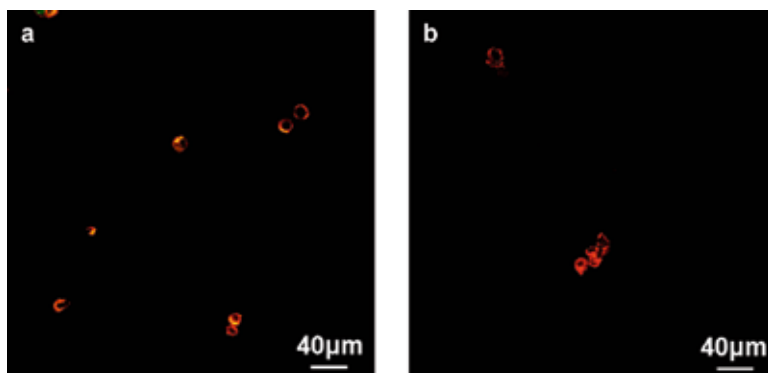
Figure A2.1.9. Overview images illustrating co-localization (yellow) of a) Fluorescein-labelled αCD3 (FαCD3, green) loaded onto polymer **6** (FαCD3-sDCs) and b) free FαCD3 on the PBL membrane (stained with the membrane specific dye PKH26, red).
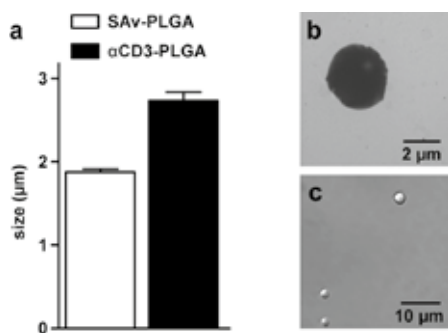
Figure A2.1.10. Characterization of αCD3-PLGA particles. a) Particle size obtained from TEM. The result represents mean ± s.e.m. (*n* = 300 particles). b) representative TEM image of αCD3-PLGA. c) representative DIC image of αCD3-PLGA.

2.6 Appendix 2.2: Estimation of the contact area and the number of possible interactions

Based on the measurement of 3795 αCD3 antibodies per PLGA particle, the surface density of αCD3 antibodies on the PLGA particles can be calculated. The average number of 3795 αCD3 molecules per PLGA particle corresponds to 1 αCD3 antibody within 2688 nm^2 and an average distance between antibodies of roughly 50 nm. Based on these values, the number of possible interactions with the cell surface can be obtained. Before this number can be calculated, the contact area of the PLGA particle with the cell has to be determined first. The calculation of the contact area is based on Hertz theory (Figure A2.2.1):[49]
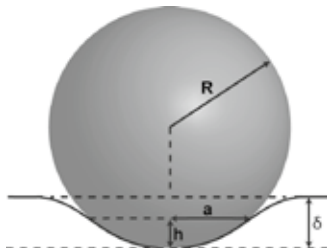
Figure A2.2.1. Geometry of the particle membrane interaction; with *R* - particle radius, d - indentation depth, a - radius of the contact area.

The contact area *A* is described by $A = 2\pi R h = 2\pi R^2 \left(1 - \sqrt{1 - \dfrac{a^2}{R^2}}\right)$ (1)

with $a^2 = R\delta$

To obtain the contact area, first the force *F* that the particle exerts on the cell surface and the corresponding indentation depth d are calculated:

The indentation depth d and the Force *F* are related by the following equations:

$$F = \frac{4}{3} E^* R^{\frac{1}{2}} \delta^{\frac{3}{2}}$$ (2)

and

$$\delta = \left(\frac{3}{4}\frac{F}{E^*}\right)^{\frac{2}{3}} \cdot R^{-\frac{1}{3}}$$ (3)

with the combined elastic modulus $\dfrac{1}{E^*} = \dfrac{1 - v^2_{cell}}{E_{cell}} + \dfrac{1 - v^2_{particle}}{E_{particle}}$ (4)

To model the natural "bouncing" of the sphere into the cell membrane in an aqueous environment, the corresponding force is first modelled as a function of gravity. A radius of *R* = 0.9 µM has been determined for the SAv-PLGA particles (Figure A2.1.10). These particles have a density that is 1.2x larger than the density of water. Using equation (5)[50] the maximum speed v_a that a PLGA particle can reach in an aqueous environment can be calculated:

$$v_a = \frac{2R^2 \Delta D_r g}{9\eta} \tag{5}$$

with ΔD_r - difference in density, g – gravitational acceleration, η – viscosity of water

For the PLGA particles the value for the maximum speed is:

$$v_a = 0.353 \; \mu m/s$$

The corresponding force can then be calculated for low Reynolds number (Re << 1):

$$F = f \cdot v \tag{6}$$

where f depends on the particle radius R and the viscosity of the environment η via

$$f = 6\pi\eta R \tag{7}$$

In this way the force exerted by the particle on a cell can be estimated as

$$F = 6 \cdot 10^{-15} N \text{ for } v = v_a$$

Cells are known to have a Young's Modulus of ≈ 400 Pa – 2500 Pa,[51] which is much smaller than that of PLGA particles. Therefore, E^* can be simplified as:

$$\frac{1}{E^*} = \frac{1-v_{cell}^2}{E_{cell}} + \frac{1-v_{particle}^2}{E_{particle}} \approx \frac{1-v_{cell}^2}{E_{cell}} \tag{8}$$

Using equations (1) – (8), a PLGA particle consequently indents a cell by $\delta = 0.16 \; nm$. The corresponding contact area between the cell and the PLGA particle is $A = 450 \; nm^2$ meaning that the PLGA particle interacts with the cell over a distance of roughly 25 nm. Without the 20 nm PEG spacers used for antibody attachment maximally 1 or 2 antibodies could interact with the cell at the same time. Considering the flexible spacers, up to 10 antibodies are able to interact with the cell simultaneously. Based on these results it can be concluded that multivalent interactions can also take place when using αCD3-PLGA particles. More importantly, the total number of antibodies able to interact with the cell and the spacing between them is nearly the same for both the αCD3-PLGA particles and the αCD3-sDCs (approx. 50 nm in both cases).

2.7 References

(1) Banchereau, J.; Steinman, R. M. *Nature* **1998**, *392* (6673), 245–252.
(2) Steinman, R. M.; Cohn, Z. A. *J. Exp. Med.* **1973**, *137* (5), 1142–1162.
(3) Fong, L.; Engleman, E. G. *Annu. Rev. Immunol.* **2000**, *18*, 245–273.
(4) Houtenbos, I.; Westers, T. M.; Ossenkoppele, G. J.; van de Loosdrecht, A. A. *Immunobiology* **2006**, *211* (6-8), 677–685.
(5) Ballestrero, A.; Boy, D.; Moran, E.; Cirmena, G.; Brossart, P.; Nencioni, A. *Adv. Drug Deliv. Rev.* **2008**, *60* (2), 173–183.
(6) Oelke, M.; Krueger, C.; Giuntoli, R. L.; Schneck, J. P. *Trends Mol. Med.* **2005**, *11* (9), 412–420.
(7) Gong, W.; Ji, M.; Cao, Z.; Wang, L.; Qian, Y.; Hu, M.; Qian, L.; Pan, X. *Cell. Mol. Immunol.* **2008**, *5* (1), 47–53.
(8) Dustin, M. L. *Immunity* **2004**, *21* (3), 305–314.
(9) Giannoni, F.; Barnett, J.; Bi, K.; Samodal, R.; P., L.; Marchese, P.; Billetta, R.; Vita, R.; Klein, M. R.; Prakken, B.; Kwok, W. W.; Sercarz, E.; Altman, A.; Alban, S. *J. Immunol.* **2005**, *174* (6), 3204–3211.
(10) Fasting, C.; Schalley, C. A.; Weber, M.; Seitz, O.; Hecht, S.; Koksch, B.; Dernedde, J.; Graf, C.; Knapp, E. W.; Haag, R. *Angew. Chem., Int. Ed.* **2012**, *51* (42), 10472–10498.
(11) Liu, S.; Maheshwari, R.; Kiick, K. L. *Macromolecules* **2009**, *42* (1), 3–13.
(12) Liu, S.; Kiick, K. L. *Macromolecules* **2008**, *41* (3), 764–772.
(13) Laux, I.; Khoshnan, A.; Tindell, C.; Bae, D.; Zhu, X.; June, C. H.; Effros, R. B.; Nel, A. *Clin Immunol.* **2000**, *96* (3), 187–197.
(14) Anderson, H. A.; Hiltbold, E. M.; Roche, P. A. *Nat. Immunol.* **2000**, *1* (2), 156–162.
(15) Vogt, A. B.; Spindeldreher, S.; Kropshofer, H. *Immuno.l Rev.* **2002**, *189*, 136–151.
(16) Prakken, B.; Wauben, M.; Genini, D.; Samodal, R.; Barnett, J.; Mendivil, A.; Leoni, L.; Albani, S. *Nat. Med.* **2000**, *6* (12), 1406–1410.
(17) Zappasodi, R.; Di Nicola, M.; Carlo-Stella, C.; Mortarini, R.; Molla, A.; Vegetti, C.; Albani, S.; Anichini, A.; Gianni, A. M. *Haematologica* **2008**, *93* (10), 1523–1534.
(18) Koffeman, E.; Keogh, E.; Klein, M.; Prakken, B.; Albani, S. *Methods Mol. Med.* **2007**, *136*, 69–86.
(19) Schütz, C.; Oelke, M.; Schneck, J. P.; Mackensen, A.; Fleck, M. *Immunotherapy* **2010**, *2* (4), 539–550.
(20) Cai, S.; Vijayan, K.; Cheng, D.; Lima, E. M.; Discher, D. E. *Pharm. Res.* **2007**, *24* (11), 2099–2109.
(21) Geng, Y.; Dalhaimer, P.; Cai, S.; Tsai, R.; Tewari, M.; Minko, T.; Discher, D. E. *Nat. Nanotechnol.* **2007**, *2* (4), 249–255.
(22) Fadel, T. R.; Steenblock, E. R.; Stern, E.; Li, N.; Wang, X.; Haller, G. L.; Pfefferle, L. D.; Fahmy, T. M. *Nano Lett.* **2008**, *8* (7), 2070–2076.
(23) Shuvaev, V. V; Ilies, M. A.; Simone, E.; Zaitsev, S.; Kim, Y.; Cai, S.; Mahmud, A.; Dziubla, T.; Muro, S.; Discher, D. E.; Muzykantov, V. R. *ACS Nano* **2011**, *5* (9), 6991–6999.
(24) Rajagopal, K.; Christian, D. A.; Harada, T.; Tian, A.; Discher, D. E. *Int. J. Polym. Sci.* **2010**, ID 379286.
(25) Heister, E.; Neves, V.; Tîlmaciu, C.; Lipert, K.; Beltra, V. S.; Coley, H. M.; Silva, S. R. P.; McFadden, J. *Carbon N. Y.* **2009**, *47* (9), 2152–2160.
(26) Koepf, M.; Kitto, H. J.; Schwartz, E.; Kouwer, P. H. J.; Nolte, R. J. M.; Rowan, A. E. *Eur Polym J* **2013**, *49* (6), 1510–1522.
(27) Kouwer, P. H. J.; Koepf, M.; Le Sage, V. A. A.; Jaspers, M.; van Buul, A. M.; Eksteen-Akeroyd, Z. H.; Woltinge, T.; Schwartz, E.; Kitto, H. J.; Hoogenboom, R.; Picken, S. J.; Nolte, R. J. M.; Mendes, E.; Rowan, A. E. *Nature* **2013**, *493* (7434), 651–655.
(28) Visser, H. G. J.; Nolte, R. J. M.; Drenth, W. *Macromolecules* **1985**, *18*, 1818–1825.
(29) Cornelissen, J. J.; Donners, J. J.; de Gelder, R.; Graswinckel, W. S.; Metselaar, G. A.; Rowan, A. E.; Sommerdijk, N. A.; Nolte, R. J. *Science* **2001**, *293* (5530), 676–680.
(30) van der Eijk, J. M.; Nolte, R. J. M.; Drenth, W.; Hezemans, A. M. F. *Macromolecules* **1980**, *13*, 1391–1397.
(31) Wu, Z. Q.; Nagai, K.; Banno, M.; Okoshi, K.; Onitsuka, K.; Yashima, E. *J. Am. Chem. Soc.* **2009**, *131* (19), 6708–6718.
(32) van Buul, A. M.; Schwartz, E.; Brocorens, P.; Koepf, M.; Beljonne, D.; Maan, J. C.; Christianen, P. C. M.; Kouwer, P. H. J.; Nolte, R. J. M.; Engelkamp, H.; Blank, K.;

Rowan, A. E. *Chem. Sci.* **2013**, *4*, 2357–2363.

(33)   Dommerholt, J.; Schmidt, S.; Temming, R.; Hendriks, L. J. A.; Rutjes, F. P. J. T.; van Hest, J. C. M.; Lefeber, D. J.; Friedl, P.; van Delft, F. L. *Angew. Chem., Int. Ed.* **2010**, *49* (49), 9422–9425.

(34)   Yamashita, I.; Nagata, T.; Tada, T.; Nakayama, T. *Int. Immunol.* **1993**, *5* (9), 1139–1150.

(35)   Murphy, M.; Loudon, R.; Kobayashi, M.; Trinchieri, G. *J. Exp. Med.* **1986**, *164*, 263–279.

(36)   Kay, J. E. *Immunol. Lett.* **1991**, *29* (1-2), 51–54.

(37)   Zanders, E. D.; Lamb, J. R.; Feldmann, M.; Green, N.; Beverley, P. C. L. *Nature* **1983**, *303* (5918), 625–627.

(38)   Balmert, S. C.; Little, S. R. *Adv. Mater.* **2012**, *24*, 3757–3778.

(39)   Calabia-Linares, C.; Robles-Valero, J.; de la Fuente, H.; Perez-Martinez, M.; Martin-Cofreces, N.; Alfonso-Perez, M.; Gutierrez-Vazquez, C.; Mittelbrunn, M.; Ibiza, S.; Urbano-Olmos, F. R.; Aguado-Ballano, C.; Sanchez-Sorzano, C. O.; Sanchez-Madrid, F.; Veiga, E. *J. Cell. Sci.* **2011**, *124* (Pt 5), 820–830.

(40)   Ellenhorn, J. D.; Hirsch, R.; Schreiber, H.; Bluestone, J. A. *Science* **1988**, *242* (4878), 569–571.

(41)   Teraoka, I. *Polymer Solutions: An Introduction to Physical Properties*; John Wiley & Sons: New York, **2002**.

(42)   van Beijnen, A. J. M.; Nolte, R. J. M.; Drenth, W.; Hezemans, A. M. F.; Vandecoolwijk, P. J. F. M. *Macromolecules* **1980**, *13* (6), 1386–1391.

(43)   Schneider, C. A.; Rasband, W. S.; Eliceiri, K. W. *Nat Meth* **2012**, *9* (7), 671–675.

(44)   Supino, R.; Walker, J. M. In *In Vitro Toxicity Testing Protocols*; O'Hare, S., Atterwill, C. K., Eds.; Humana Press: Totowa (NJ), **1995**, *43*, 137–149.

(45)   Freshney, R. I. In *Culture of Animal Cells: A Manual of Basic Techniques*; Freshney, R. I., Ed.; Alan R. Liss : New York, **2000** 173.

(46)   Wells, A. D.; Gudmundsdottir, H.; Turka, L. A. *J. Clin. Invest.* **1997**, *100* (12), 3173–3183.

(47)   Hawkins, E. D.; Hommel, M.; Turner, M. L.; Battye, F. L.; Markham, J. F.; Hodgkin, P. D. *Nat. Protoc.* **2007**, *2*, 2057–2067.

(48)   Cruza, L. J.; Tacken, P. J.; Fokkink, R.; Joosten, B.; Stuart, M. C.; Albericio, F.; Torensma, R.; G., F. C. *J. Control. Release* **2010**, *144* (2), 118–126.

(49)   Popov, V. L. *Contact Mechanics and Friction: Physical Principles and Applications*; Springer: Berlin, **201**0.

(50)   Newman, J. *Physics of the Life Sciences*; Springer: New York, 2008.

(51)   Shimizu, Y.; Kihara, T.; Haghparast, S. M. A.; Yuba, S.; Miyake, J. *PLoS One* **2012**, *7* (3), e34305.

3

Controlling T cell activation with synthetic Dendritic Cells using the multivalency effect
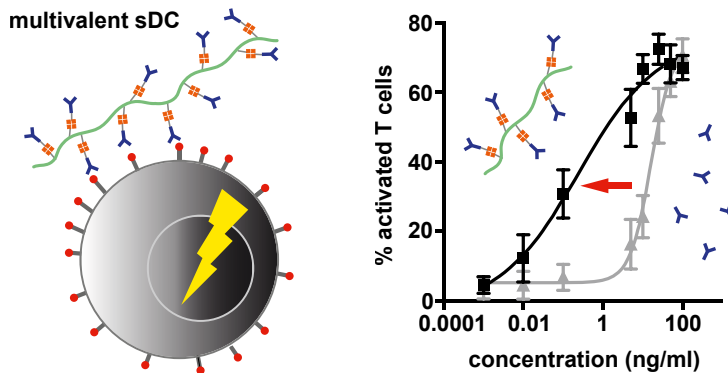
Parts of this chapter will be published:

Chapter 3: Controlling T cell activation with synthetic Dendritic Cells using the multivalency effect

3.1 Introduction

One important goal of cancer immunotherapy is the replacement of costly dendritic cells (DCs) vaccines, which have to be generated for every individual patient, with synthetic variants.[1] These synthetic variants, called artificial antigen presenting cells (aAPCs), are designed to prime T cells against cancer specific antigens. These aAPCs can be produced in a straightforward manner from synthetic building blocks, opening up the possibility for standardized "off-the-shelf" protocols[2] and circumventing elaborate and expensive personalized medicine. Different aAPC designs have been synthesized over the last years with scaffolds varying from polymer beads,[3,4] carbon nanotubes,[5] liposomes[6] and many others.[7] In general, the design of aAPCs is inspired by the natural DC and its interaction with the T cell. DC binding to T cells involves three main signals that are all required to fully activate the T cell: antigen-loaded major histocompatibility complexes (MHC) of the DC bind to specific T cell receptors (TCR; signal 1). At the same time, co-stimulatory molecules on the DC surface interact with their T cell binding partners (signal 2). In addition to these receptor interactions, also soluble factors (cytokines) are involved in T cell activation (signal 3). In the first stage of activation, signal 1 and 2 interactions are arranged in microclusters (around 20-300 TCRs per cluster).[8–10] These nanometre-sized contact areas between both cells are stabilized by a number of different adhesion molecules. After the initial stimulation, triggered microclusters move towards the so-called supramolecular adhesion complex (SMAC) where receptors and adhesion molecules are rearranged to form a 'bulls eye' pattern of micrometre size.[11] This process clearly involves the dynamic multivalent binding of many (different) binding partners.

Multivalent interactions generally form at the interface between two objects that carry multiple, complementary functionalities.[12,13] The simultaneous interaction between these functionalities enhances the binding strength (avidity), sometimes by several orders of magnitude compared to the affinity of the monovalent interaction.[14] This enhancement mainly originates from an increase in the effective concentration of the binding partners. Once the first ligand is bound, the 'search volume' is reduced and the following binding events occur with a higher probability.[15] In chapter 2 of this thesis a new multivalent aAPC design for activating T cells was introduced: synthetic Dendritic Cells (sDCs).[16,17] In this design, anti-CD3 antibodies (αCD3), which are known to trigger the TCR (signal 1), were bound to a semi-flexible and linear polyisocyanopeptide scaffold with a length of ~200 nm. Using these novel sDCs, T

cell activation occurred at much lower doses of antibody compared to unbound αCD3.

In this chapter a series of experiments was designed with the goal of investigating the importance of multivalent binding in more detail. A library of αCD3-sDCs, containing sDCs with different polymer lengths and αCD3 densities, was synthesized and the influence of these parameters on T cell activation was investigated. Incubating T cells with these different αCD3-sDCs, it is shown that an increase in polymer length or effector molecule density boosts both early (Ca^{2+}-signalling) and late (interferon γ release) stages of T cell activation and that this effect goes beyond a simple avidity increase. A positive effect on T cell signalling is further demonstrated after removal of the αCD3-sDCs. T cell activation is sustained for extended periods of time (days), as confirmed by prolonged Ca^{2+}-signalling, expression of the early activation marker CD69 and the release of interferon γ (IFNγ).

3.2 Results and discussion

3.2.1 Synthesis of αCD3-sDCs

All polymer-αCD3 conjugates (i.e. the αCD3-sDCs) were synthesized according to the method described in chapter 2 (Figure 3.1).[16,17] The sDC scaffold is based on a water-soluble polyisocyanopeptide co-polymer bearing non-functional methoxy and functional azide groups. The corresponding methoxy and azide isocyanide monomers were polymerized using a nickel catalyst to obtain azide-functionalized polyisocyanopeptide polymers. The azide groups were subsequently utilized in a strain-promoted azide-alkyne cycloaddition (SPAAC) reaction with bicyclononyne-functionalised streptavidin (BCN-SAv).[18] The SAv molecules allow for the binding of biotinylated αCD3 antibodies to yield the αCD3-sDCs (Figure 3.1a). In all experiments, the ratio between SAv and αCD3 was tuned to be 1:1 (see experimental section 3.4 for synthetic details).
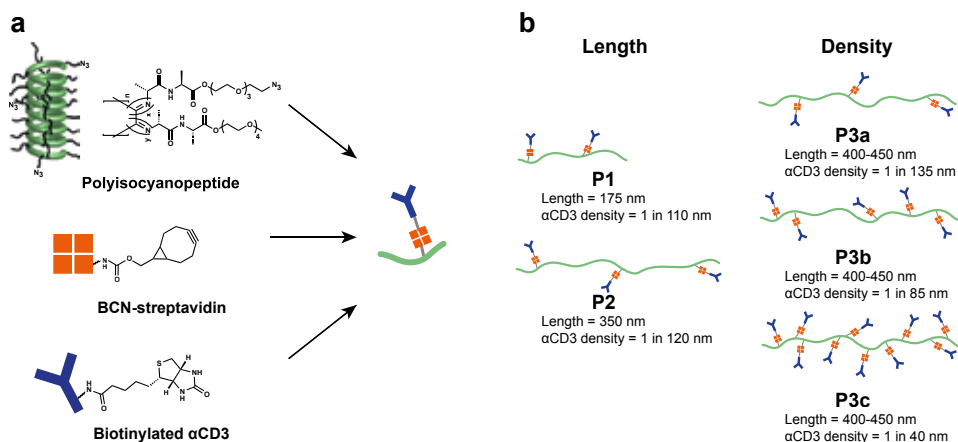
Figure 3.1. Schematic overview of the sDC library. a) Experimental design for sDC synthesis. b) Overview of the sDCs used in this study (**P1-P3**) showing the corresponding polymer lengths and αCD3 densities.

3.2.2 Influence of αCD3-sDC length on T cell activation

Polyisocyanopeptides of different length were synthesized using a different catalyst-to-monomer ratio during the polymerisation reaction (Table 3.1). Two polymers of different average lengths (**P1'** = 175 nm and **P2'** = 350 nm; azide:methoxy = 1:100) were synthesized using this strategy (Figures. A3.1.1 and A3.1.2; Table 3.1). The density of SAv per polymer chain was determined using atomic force microscopy (AFM imaging; Figures A3.1.1 and A3.1.3; Table 3.1). The **P1-SAv** and **P2-SAv** conjugates possess an average density of 1 SAv molecule per 110 nm and 120 nm, respectively. As the synthetic protocol was optimized such that one αCD3 antibody is bound per SAv molecule (chapter 2), it can be assumed that these values also represent the densities of αCD3 antibodies on the αCD3-sDC conjugates **P1** and **P2** (Figure 3.1b)**.** This means that **P1** carries 1-2 αCD3 antibodies per polymer, whereas the total number of αCD3 antibodies on **P2** is ~3.

Table 3.1. Characteristics of the polymers used in this study.

Polymer	Catalyst ratio	N$_3$ ratio	Mv (kg/mol)[a]	SAv equivalents	Mean length (nm)[b]	Mean SAv distance (nm-1)[b]
P1	1:200	1:100	200	1	175	110
P2	1:10000	1:100	628	1	350	120
P3a-c	1:10000	1:70	577			
P3a				0.5	400	134
P3b				1	442	85
P3c				5	438	43

[a] Determined from viscosity measurements
[b] Determined from AFM measurements

P1 and **P2** were compared to unbound αCD3 in a single-cell Ca^{2+}-signalling experiment (Figure 3.2a). Ca^{2+}-release from the endoplasmic reticulum is one of the

earliest activation events when triggering T cells at the TCR level. The subsequent complex interplay between Ca^{2+}-release from the endoplasmic reticulum and calcium influx across the plasma membrane via Ca^{2+}-release activated Ca^{2+} (CRAC) channels leads to oscillations of cytoplasmic calcium.[19] These calcium oscillations, which have a direct influence on T cell gene expression, were monitored using peripheral blood lymphocytes (PBLs) loaded with the Ca^{2+}-sensitive fluorescent dye FURA-2 (for experimental details see Table 3.2, Figure A3.1.4) [20] Determination of the number of Ca^{2+}-signalling cells during the first hour of treatment with **P1**, **P2** or αCD3 revealed that both the two αCD3-sDCs and unbound αCD3 caused a marked increase in the number of Ca^{2+}-signalling cells when using concentrations of 5 and 50 ng/ml. At 0.5 ng/ml this effect was only seen for **P2** and not for **P1** or unbound αCD3.
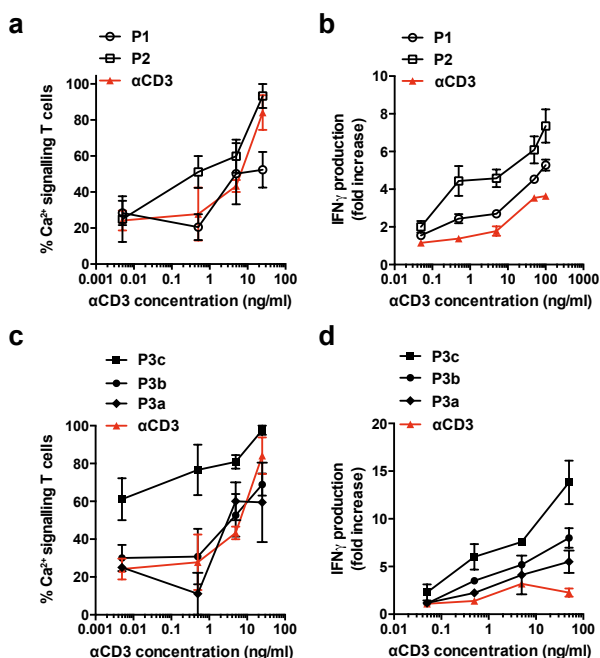
Figure 3.2. T cell activation using sDCs of different length and αCD3 density. a) Fraction of activated T cells as determined from single-cell Ca^{2+}-signalling measurements performed within the first hour of stimulation with **P1**, **P2** and unbound αCD3. b) Relative increase in the concentration of IFNγ secreted by T cells treated with **P1**, **P2** and unbound αCD3 for 16 hours. Untreated PBLs were used as a reference. c) Fraction of activated T cells as determined from single-cell Ca^{2+}-signalling measurements performed within the first hour of stimulation with **P3a**, **P3b**, **P3c** and unbound αCD3 for 1 hour. d) Relative increase in the concentration of IFNγ secreted by T cells treated with **P3a**, **P3b**, **P3c** and unbound αCD3 for 16 hours. Untreated PBLs were used as a reference. For a)-c) the data represents the mean ± SEM of 3 independent experiments performed with T cells from different donors. For d) the data represents the mean ± SEM of 2 independent experiments performed with T cells from different donors.

To probe the effect of the two αCD3-sDCs on a late and more robust event in T cell activation, PBLs were stimulated for 16 hours with **P1, P2** and αCD3 and the release of IFNγ was measured. Both αCD3-sDCs stimulated the production of IFNγ over a range of concentrations from 0.05 to 100 ng/ml (Figure 3.2b). At all concentrations tested, the effect of **P2** was most pronounced. Considering that **P1** and **P2** possess the same αCD3 density, these results suggest that polymer length is a crucial design parameter. It increases the total number of αCD3 molecules per αCD3-sDC, thereby causing the stronger T cell stimulating effect.

3.2.3 Influence of αCD3 density on T cell activation

The previous experiment has shown that a density of one αCD3 antibody in 110-120 nm combined with a polymer length of maximally 350 nm (**P2**) leads to a small but clearly detectable increase in T cell activation. To investigate the multivalency effect over a larger dynamic range, it was therefore decided to increase both the polymer length and the αCD3 density. Increasing the number of azide functional groups (azide:methoxy = 1:70), polymer **P3'** with an average length of 400-450 nm was synthesized (Figures A3.1.1 and A3.1.2, Table 3.1). This polymer was then functionalized with a different number of SAv molecules per polymer, using a different ratio of BCN-SAv:azide in the coupling reaction (0.5, 1 and 5 equivalents of BCN-SAv). Using AFM imaging, the average SAv density on these polymer conjugates was determined to be 1 SAv molecule in every 130 nm (**P3a-SAv**, 0.5 eq.), 85 nm (**P3b-SAv**, 1 eq.) and 40 nm (**P3c-SAv**, 5 eq.) (Figure 3.1b, Figures A3.1.1 and A3.1.3, Table 3.1). Again, it was assumed that these values correspond to the density of αCD3 antibodies so that the αCD3-sDCs carry an average of 3-4 (**P3a-SAv**), 5 (**P3b-SAv**) or 10-11 (**P3c-SAv**) antibodies per polymer.

The single-cell Ca^{2+} signalling assay shows a marked increase already at the lowest tested concentration of **P3c** (0.005 ng/ml; Figure 3.2c). In sharp contrast, **P3a** and **P3b** displayed the same dose-dependency as unbound αCD3. Also for these αCD3-sDCs a more clear difference was observed in the IFNγ release assay. All three αCD3-sDCs cause significantly higher IFNγ secretion than unbound αCD3 (Figure 3.2d). Most importantly, a positive correlation was observed between αCD3 density and IFNγ release over the full range of tested concentrations (0.05-50 ng/ml). At the highest αCD3 concentration of 50 ng/ml, **P3a**, **P3b** and **P3c** induced a 2.4-, 3.5- and 6.1-fold increase of secreted IFNγ compared to unbound αCD3, respectively. Clearly in addition to polymer length, αCD3 density is an important determinant for T cell activation by αCD3-sDCs.

3.2.4 Quantification of the multivalent enhancement factor

The above results show that both polymer length and αCD3 density are crucial design parameters for sDCs. Together, these parameters determine the number of interactions that can form between the polymer and the T cell. To quantify the enhancement of the multivalent binding strength, dose-response curves were established for both unbound αCD3 and the best performing αCD3-sDC (**P3c**). The dose-response curves provide the basis for determining the EC_{50} values and allow for calculating an enhancement factor for the multivalent interaction. To construct these dose-response curves, single-cell Ca^{2+}-signalling experiments were performed over an extended range of αCD3 concentrations (0.001-100 ng/ml). Even though T cell activation was more difficult to quantify in the Ca^{2+}-signalling experiment, this readout parameter was chosen as it corresponds to a very early activation event. It can be assumed that an early readout parameter is more relevant for quantifying the multivalent binding strength than downstream parameters as signal amplification may have taken place.
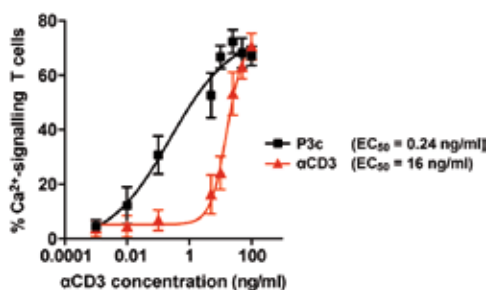
Figure 3.3. Dose-response curves for T cells treated with **P3c** and unbound αCD3 as determined from single-cell Ca^{2+}-signalling experiments. EC_{50} values were determined using a four-parameter fit. The multivalent enhancement factor is calculated by dividing the EC_{50} of unbound αCD3 by the EC_{50} of **P3c**. The data represents the mean ± SEM of 3 independent experiments performed with T cells from different donors.

When PBLs were treated with **P3c**, the first effect on the number of Ca^{2+}-signalling cells was detected at a ~200-300 fold lower concentration as observed with unbound αCD3 (Figure 3.3), which is in line with the results presented in chapter 2.[16] EC_{50} values were determined from a four-parameter fit to the dose-response curves. For unbound αCD3 an EC_{50} value of 16 ng/ml was found, whereas an EC_{50} value of 0.24 ng/ml was obtained for the multivalent **P3c**. This yields an enhancement factor of ~67 for the multivalent system (Figure 3.3).[21] This remarkable enhancement clearly indicates that multivalency is one of the key parameters responsible for the increased potency of αCD3-sDCs. It is worth noting that the slope of the dose-

response curve does usually contain additional information, e.g. about positive or negative cooperativity. The sDC polymers are heterogeneous, however, when considering both their length and the αCD3 density. It is therefore highly likely that the more gradual response to increasing the concentration of **P3c** is a direct result of this heterogeneity.

Assuming that the enhancement factor purely characterizes the avidity increase of the multivalent interaction, the question remains if enhanced binding of the αCD3-sDC is the only parameter that determines T cell activation or if T cell signalling is also affected. The polymer linkage between several αCD3 antibodies efficiently directs these polymer-coupled αCD3 antibodies to the same microcluster even if the overall αCD3 concentration is very low. Considering the sequence of events occurring during T cell activation, this may directly lower the threshold for T cell activation. A first indication for this can be obtained when re-considering the results obtained for the αCD3-sDCs **P3a**, **P3b** and **P3c** (Figure 3.2c, d) that all bind in a multivalent fashion. During all experiments the data was normalized to the αCD3 concentration so that the polymer concentration (i.e. the αCD3-sDC concentration) varies between the different samples. When normalizing the data with respect to the polymer concentration, it becomes evident that a 1000-fold lower concentration of **P3c** is sufficient to obtain the same effect as with **P3a** (Figure A3.1.7). This value is a lot larger than the multivalent enhancement factor determined above and suggests that the co-localization of αCD3 in a small area on the cell surface is a key factor that determines T cell activation. Interestingly, a total number of ~10 αCD3 antibodies distributed over an area of several tens of nanometres matches with the predicted size of TCR nanodomains that are pre-formed on the T cell surface.[22,23] It may therefore be speculated that αCD3-sDCs form a highly specific, multivalent interaction with these nanodomains and that T cell fate is already determined at this very early stage of activation.

3.2.5 Long-term effect of αCD3-sDC binding on T cell signalling

To investigate the effect of the αCD3-sDCs on T cell signalling in more detail, a new series of experiments was designed to obtain information about sustained T cell activation. Instead of measuring T cell activation in the continuous presence of the αCD3-sDCs or unbound antibodies, excess stimulant was washed off after 1 hour of treatment and T cell activation was analysed at several time points after removal of the stimulant. This allowed for determining the long-term effect of the initial stimulation, as no free stimulant was available for binding to the T cells after the medium was replaced. To quantify the effect, again single-cell Ca^{2+}-signalling experiments were performed and the secretion of IFNγ was determined. In addition,

the expression of the surface activation marker CD69 was measured, which is another indicator of early T cell activation.
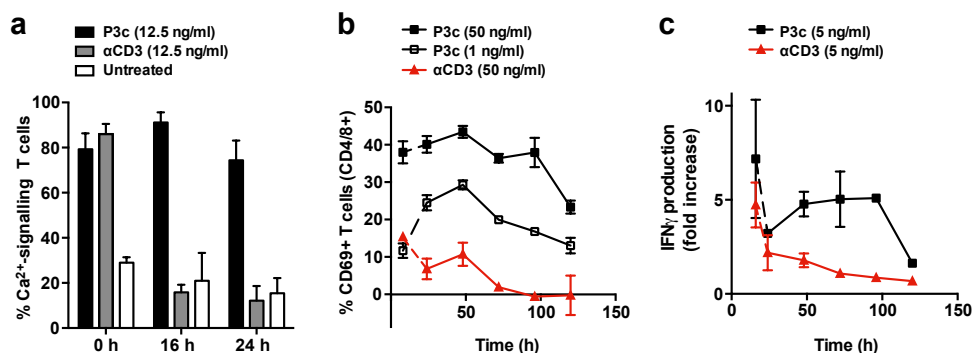

Figure 3.4. Analysis of sustained T cell activation. a) Long-term Ca^{2+}-signalling when treating PBLs with 12.5 ng/ml **P3c** or αCD3 for 1 hour. The first measurement (0 h) was performed directly on the microscope during incubation with the stimulant. The other time points represent the total time of the experiment (i.e. 1 hour incubation with the stimulant + incubation time after removal of the stimulant). For all experiments the data represents the mean ± SEM of 3 independent experiments performed with T cells from different donors. b) Fraction of T cells expressing CD69 after treatment with **P3c** or αCD3 for 8 hours. For **P3c** a concentration of 1 and 50 ng/ml was used. For αCD3 a concentration of 50 ng/ml was used. The first measurement was performed directly before the stimulant has been removed (8 hours). The other time points represent the total time of the experiment. For all experiments the data represents the mean ± SEM of 3 independent experiments performed with T cells from different donors. c) Concentration of secreted IFNγ after treating PBLs with 5 ng/ml **P3c** or αCD3 for 16 hours. The first measurement was performed directly before the stimulant has been removed (16 hours). The other time points represent the total time of the experiment. For all experiments the data represents the mean ± SEM of 3 independent experiments performed with T cells from different donors.

For the Ca^{2+}-signalling measurements, PBLs were treated with unbound αCD3 or **P3c** (12.5 ng/ml) for 1 hour. The stimulant was then removed, fresh medium was added and the cells were incubated without stimulant for 15 or 23 hours. The fraction of Ca^{2+}-signalling cells was determined at the respective time points (16 and 24 h time points after the initial addition of the stimulant; see Figure A3.1.5 for a detailed timeline) and compared to a reference sample that was imaged while adding the stimulant (0 h, Figure A3.1.5). This reference measurement, performed exactly as described above, confirms the results presented in Figure 3.1c (80% of signalling cells for both αCD3 and **P3c** in Figure 3.4a). In samples treated with unbound αCD3 the fraction of Ca^{2+}-signalling T cells was significantly reduced at both post-stimulation time points. In sharp contrast, the vast majority of **P3c**-treated T cells remained active after removal of the stimulant. Even at 24 h hours after the initial stimulation with **P3c**, the fraction of Ca^{2+}-signalling T cells was still ~75%, indicating

that the multivalent sDC causes a sustained stimulation of the intracellular pathways involved in Ca^{2+}-responses. Negative controls involving an isotope control ($mIgG_{2a}$ antibody), polymers with SAv but no αCD3 and non-treated cells did not show high amounts of activated T cells before and after removal of the stimulant (Figure A3.1.6).

To support the results from the single-cell Ca^{2+}-signalling experiments, FACS analysis was performed to determine the expression of the surface marker CD69. PBLs were treated with 1 and 50 ng/ml of unbound αCD3 or **P3c** for 8 hours before placing the cells in fresh medium. At the time of removal of the stimulant, higher numbers of CD69 expressing T cells were observed than when the PBLs were treated with unbound αCD3 (Figure 3.4b, Figures A3.1.8 and A3.19). Considering the multivalent enhancement factor of 67, one would expect a similar level of activation for PBLs treated with either 50 ng/ml of unbound or with 1 ng/ml of **P3c**. When comparing this initial time point, already a large difference is observed for these two treatment conditions. The **P3c** treated sample contains a significantly higher amount of CD69 expressing cells that remains fairly constant until 96 hours of measurement time. In contrast, the population of CD69+ T cells stimulated with unbound αCD3 decreased rapidly from its initial value (Figure 3.4b).

To further confirm that T cells were showing sustained and robust activation for an extended period of time, IFNγ release assays were performed. PBLs were treated with 5 ng/ml **P3c** or unbound αCD3 for 16 hours, after which the cells where washed and new medium was added. The supernatant was tested for IFNγ directly before the removal of the stimulant (16 hours) and a high concentration of IFNγ was determined for both treatment conditions as expected. At all subsequent time points (24, 48, 72, 96 and 120 hours after the initial stimulation, a clear difference was seen between PBLs treated with **P3c** or unbound αCD3 (Figure 3.4c). PBLs treated with unbound αCD3 do not seem to produce new IFNγ and a decrease in the IFNγ level is seen over time. In contrast, PBLs stimulated with **P3c** produced new IFNγ. Until the 96 hour time point an approximately constant level of IFNγ was maintained, after which a decrease of the IFNγ concentration was observed. Taken together, these results show that sDCs stimulate T cells over much longer periods of time compared to unbound αCD3 and this effect is observed for both early and late T cell activation markers.

3.3 Conclusion

In summary, this chapter shows that polymer length and effector molecule density are key design parameters in the development of sDCs. These parameters have a direct effect on the valency of the sDC and, consequently, on the effective concentration required for T cell activation. In addition to this enhancement of the

binding strength, robust and sustained T cell activation was observed that goes beyond a pure avidity effect. These results show that the multivalent scaffold also affects T cell signalling pathways. Co-localization of several effector molecules in the same microcluster leads to a long lasting activation that cannot be achieved with free, unbound antibodies. Future studies will be directed at elucidating the mechanistic origin of this sustained T cell response.

3.4 Experimental section

Synthesis and characterization of synthetic dendritic cells (sDCs)

Polymer synthesis (P1'-P3')

Water-soluble polyisocyanopeptides were synthesized as described in chapter 2.[16] For the synthesis of **P1'** and **P2',** the functional azide monomer (N_3) and the non-functional methoxy monomer (OMe) were polymerized in a 1:100 ratio. For **P3',** a 1:70 N_3:OMe ratio was used to increase the number of possible coupling sites. The polymer length was controlled by the amount of nickel catalyst added in the polymerization reaction. A 1:200 ratio of catalyst:monomer was used for the synthesis of **P1'**. For **P2'** and **P3',** a 1:10000 catalyst:monomer ratio was used (Table 3.1). The molecular weight of the polymers was determined from viscosity measurements (Table 3.1) as described in chapter 2.[16]

Synthesis of polymer-streptavidin conjugates

Streptavidin (SAv, Thermo Fisher Scientific) was functionalized with BCN-POE$_3$-NH-C(O)CH$_2$CH$_2$CH$_2$C(O)OSu (BCN-NHS; Synaffix) to couple it to the azide-groups on the polymer in a strain-promoted azide-alkyne cycloaddition (SPAAC) reaction.[18] The reaction was performed in borate buffer (10 mM, pH 8.5) using a 5 to 6-fold excess of BCN-NHS. Following incubation for 1.5 hours at room temperature, the mixture was purified by ultrafiltration (10 kDa cut-off) and gel filtration (PD-10 desalting column; GE Healthcare) to remove non-reacted BCN-NHS. During purification, the buffer was changed to phosphate buffered saline (PBS, pH 7.4). Mass spectrometry analysis (ESI-TOF) revealed that 1-4 BCN moieties were coupled per streptavidin molecule (BCN-SAv). BCN-SAv was subsequently reacted with azide-bearing polyisocyanopeptide polymers. A 1:1 molar ratio of N_3:BCN-SAv was used for the synthesis of **P1-SAv** and **P2-SAv**. N_3:BCN-SAv ratios of 1:0.5, 1:1 and 1:5 were used for the synthesis of **P3a-SAv**, **P3b-SAv** and **P3c-SAv**, respectively. All reactions were performed in PBS. The reaction mixtures were first incubated at room temperature for 1 hour and subsequently stirred at 4° C for 2.5 days. The resulting polymer-SAv conjugates were purified by ultrafiltration (100 kDa cut-off).

Characterization of polymer-streptavidin conjugates

The average polymer length and SAv density was determined with atomic force microscopy (AFM) using the method described in chapter 2[16] (Figure A3.1.1). The resulting histograms, displaying the distribution of polymer length and SAv distance of at least 41 individual polymers, are shown in Figure A3.1.2 and Figure A3.1.3.

Synthesis of sDCs (P1, P2, P3a-c)

The polymer-SAv conjugates were incubated with biotinylated, monoclonal mouse anti-human CD3 antibodies (αCD3; clone OKT3) to obtain the αCD3-functionalized polymers **P1**, **P2**, **P3a**, **P3b** and **P3c.** The polymer-SAv conjugates were incubated with the biotinylated antibodies in a 4:1 αCD3/SAv

molar ratio. As described in chapter 2,[16] this 4:1 αCD3/SAv molar loading ratio yields a 1:1 binding ratio of αCD3 and SAv on the polymer backbone (αCD3-sDC).

Cell preparation and cell culture

Peripheral blood lymphocytes (PBLs) were obtained from buffy-coats of healthy individuals in accordance with institutional guidelines.[16] Briefly, peripheral blood mononuclear cells were obtained from Ficoll density centrifugation. Monocytes were removed using the plastic flask adherence method. The non-adherent PBLs were then maintained at 37 °C and 5 % CO_2 in complete medium: RPMI-1640 (Lonza); containing 10 % (v/v) fetal bovine serum (FBS, Gibco), 1 % (w/v) glutamine (Lonza), and 1x Antibiotic-Antimycotic (Gibco).

Analysis of T cell activation

Single-cell Ca^{2+}-signalling

General procedure

The fraction of T cells responding to the αCD3-sDC treatment was determined in a single-cell Ca^{2+}-signalling assay using the ratiometric Ca^{2+}-indicator Fura-2. PBLs (10^5 cells) were loaded with 3 µM Fura-2 AM (Invitrogen) in complete medium supplemented with HEPES buffered saline (20 mM HEPES pH 7.4, 115 mM NaCl, 5.4 mM KCl, 1 mM $CaCl_2$, 0.8 mM $MgCl_2$, 13.8 mM glucose) for 1 hour at 37 °C and 5 % CO_2. Fura-2-loaded PBLs were washed twice with HEPES buffered saline and allowed to adhere to poly-D-L-lysine-coated (0.05 mg/ml; Sigma-Aldrich) glass bottom dishes (Nunc) at room temperature. Single-cell Ca^{2+}-measurements were performed as described before.[24] Dishes were placed on the stage of an inverted microscope (Axiovert 200M; Zeiss) equipped with a temperature-controlled CO_2 stage incubator (37 °C and 5 % CO_2) and a 63x, 1.25 NA objective (Plan NeoFluar). Fura-2 was excited at 340 and 380 nm alternatingly, using a monochromator (Polychrome IV; TILL Photonics). The emitted light was directed through a 415 DCLP dichroic mirror (Omega Optical) and a 510WB40 emission filter (Omega) onto a CoolSNAP HQ monochrome CCD camera (Roper Scientific). The camera exposure time was 30 ms and the time between two ratio images was 2-4 s. All hardware was controlled with Metafluor 6.0 software (Universal Imaging).

The images obtained were analysed using Image-Pro Plus software (Media Cybernetics). Regions of interest (ROIs) corresponding to individual PBLs were selected together with a cell-free ROI for background correction. For each ROI, the average pixel intensity was calculated for each excitation wavelength. After subtraction of the corresponding background value, the 340 nm/380 nm fluorescence emission ratio was calculated as a measure of the cytosolic Ca^{2+}-concentration. Increases in cytosolic Ca^{2+}-concentration were identified with GraphPad Prism 5 (GraphPad Software), using as criterion that the increase in the 340 nm signal is mirrored by a decrease in the 380 nm signal.

Early effects on single-cell Ca^{2+}-signalling

To investigate the early effects of different αCD3-sDCs on Ca^{2+}-signalling, a series of experiments was performed. These experiments include measurements to compare the effect of different αCD3-sDCs (experiments 1 and 2 in Table 3.2) and the dose dependences of **P3c** and free αCD3 (experiment c in Table 3.2). For these experiments, the Fura-2 loaded T cells were first placed onto the microscope and the baseline Ca^{2+}-concentration was determined. The different stimulants were added while the T cells were placed on the microscope, 5 min after the onset of imaging. After 1 h of imaging, 1 µg/mL of ionomycin was added to test for cell viability (Figure A3.1.4). Each experiment was performed with PBLs from three independent healthy donors.

Table 3.2. Treatment conditions for the Ca^{2+}-signalling experiments. The concentration always refers to the amount of αCD3 bound to the αCD3-sDCs or in soluble form.

Experiment	Stimulant	Imaging time	αCD3 concentration
1. sDC length	i. **P1** ii. **P2** iii. free αCD3 iv. untreated	5 min (baseline Ca^{2+}); 1 h treatment; 5 min ionomycin	0.005, 0.5, 5, 25 ng/mL
2. αCD3 density	i. **P3a** ii. **P3b** iii. **P3c** iv. free αCD3 v. untreated	5 min (baseline Ca^{2+}); 1 h treatment; 5 min ionomycin	0.005, 0.5, 5, 25 ng/mL
3. dose-response curves	i. **P3c** ii. free αCD3 iii. untreated	5 min (baseline Ca^{2+}); 1 h treatment; 5 min ionomycin	0.001, 0.01, 0.1, 5, 10, 25, 50, 100 ng/mL

A representative data set for PBLs treated with free αCD3 or with the αCD3-sDC **P3c** is shown in Figure A3.1.4. This data set shows that PBLs display different patterns of Ca^{2+} signalling. In this study, only the fraction of Ca^{2+} signalling cells was analysed and plotted as a function of the stimulant concentration.

Long-term effects on single-cell Ca^{2+}-signalling
To determine the long-term effect of **P3c** on Ca^{2+}-signalling, PBLs were treated with the respective stimulant for a short time (1 h), followed by incubation without stimulant for an extended period of time (15 h and 23 h). Following this post-stimulation period, the cells were imaged as described under 3.1.1, with the only difference that Fura-2 loading was performed for 20 min. The following stimulants were used: untreated, **P3c**, free αCD3, **P3-mIgG$_{2a}$** (isotype control; 40 nm mIgG$_{2a}$ spacing) and **P3c-SAv** (lacking αCD3).

In more detail, PBLs (10^5 cells) were incubated with the respective stimulant (12.5 ng/ml) for 1 hour at 37 °C and 5 % CO_2. The cells were then washed with RPMI-1640 medium without serum and antibiotics to remove the stimulant. They were re-suspended with fresh complete medium with serum and maintained at 37 °C and 5 % CO_2 for another 15 h or 23 h. Fura-2 loading was performed 20 min before the end of the respective incubation time (Figure A3.1.5). The respective samples were washed twice with PBS-1 % BSA (PBA) and the cells were imaged under the microscope for 1 h. Again, cell viability was assessed at the end of the measurement (treatment with ionomycin for 5 min). To be able to compare the results at 16 h and 24 h with the previously obtained data, a '0 h' time point was taken where the PBLs (10^5 cells) were first loaded with Fura-2 for 20 min, placed onto the microscope and imaged exactly as described above. The results of this experiment are summarized in Figure A3.1.6 as well as in Figure 3.4a. A clear difference is observed between the post-stimulation signaling of αCD3-sDC treated and αCD3 treated cells, as well as the untreated control. The untreated

control shows a small fraction of PBLs that display spontaneous increases in the cytosolic Ca^{2+}-concentration (white bars), which is known to occur for up to 30 % of untreated cells.

Enzyme-linked immunosorbent assay (ELISA; IFNγ secretion)

To investigate the effect of the different αCD3-sDCs on IFNγ secretion, PBLs (10^5 cells/well) were seeded in 96 well plates and treated with **P1**, **P2**, **P3a**, **P3b** and **P3c** or unbound antibodies (αCD3) at different concentrations (0.05, 0.5, 5, 50 and 100 ng/mL) for 16 h at 37 °C and 5 % CO_2. To determine the effect of polymer length, the treatment variables were **P1**, **P2** and unbound αCD3 along with an untreated control. **P3a**, **P3b**, **P3c** were used to investigate the effect of αCD3 density (again using unbound αCD3 and untreated cells as a control). IFNγ released by the T cells was determined using a sandwich ELISA as described in chapter 2.[16,17] Briefly, 96 well plates (Nunc Immunomodules) were coated with mouse anti-human IFNγ antibody (Thermo Fisher Scientific). After incubation at 4 °C overnight, the plates were washed and blocked with PBS/Tween (0.05 %) and PBS-1 % BSA (PBA), respectively. IFNγ standards (Thermo Fisher Scientific) and supernatants (from treated and untreated cells) were added into the respective wells and incubated for 1 h at room temperature. After washing 3x with PBA, the concentration of IFNγ was detected using a biotinylated mouse anti-human IFNγ antibody (Thermo Fisher Scientific) and a streptavidin-horseradish peroxidase (HRP) conjugate (Life Technologies). HRP activity was detected using tetramethyl benzidine (TMB; Sigma Aldrich). Absorption at 450 nm was measured using an iMark Microplate Reader (Bio-Rad). The results of this experiment, normalized to the concentration of αCD3, are shown in Figure 3.2. Figure A3.1.7 shows the same data set re-normalized to the polymer concentration (i.e. αCD3-sDC concentration).

To measure the long-term effect of the αCD3-sDC treatment, PBLs (10^5 cells/well) were seeded in 96 well plates and treated with the respective stimulant (at 5 ng/mL). The cells were incubated with the stimulant for 16 h at 37 °C and 5 % CO_2. After this incubation, the cells were washed with RPMI-1640 medium without serum and antibiotics. They were then re-suspended with fresh complete medium with serum to observe the activation state of the cells after the treatment was removed. The IFNγ concentration was determined directly before the medium was removed (16 hours) and at the following time points after the initial stimulation: 24, 48, 72, 96 and 120 h.

Flow cytometry (CD69 expression)

To measure the long-term effect of the αCD3-sDC treatment on CD69 expression, PBLs (10^5 cells/well) were seeded in 96 well plates and treated with the respective stimulant (5 ng/mL). The cells were incubated with the stimulant for 8 h at 37 °C and 5 % CO_2. After this incubation, a sample was taken for analysis. The remaining cells were washed with RPMI-1640 medium without serum and antibiotics. They were then re-suspended with fresh complete medium with serum to observe the activation state of the cells after the treatment was removed. The cell suspensions were collected at the respective time points (24, 48, 72, 96 and 120 h after the initial stimulation) and used for flow cytometric analysis (CyAn ADP; Beckman Coulter) following the same methodology as described chapter 2.[16,17]

Briefly, PBLs (treated or untreated) were washed twice with PBA to remove unbound sDCs or antibodies. PBLs were stained with antibodies specific for the CD4/8+ T cell subpopulations (APC-labelled mouse anti-human CD4/8 mAb; T cell marker; BD Pharmingen) and with PE-labelled mouse anti-human CD69 (marker for T cells, eBioSciences). After 1 hour of incubation, the cells were again washed twice with PBA before performing flow cytometric analysis. The data obtained were analysed by using FlowJo ver. 9.2 Software (TreeStar Inc.). The gating strategy to identify the population of CD69+ T cells is shown in Figure A3.1.8. Additional results of treatment concentrations not shown in the main text are summarized in Figure A3.1.9.

3.5 Appendix 3.1: Supporting figures
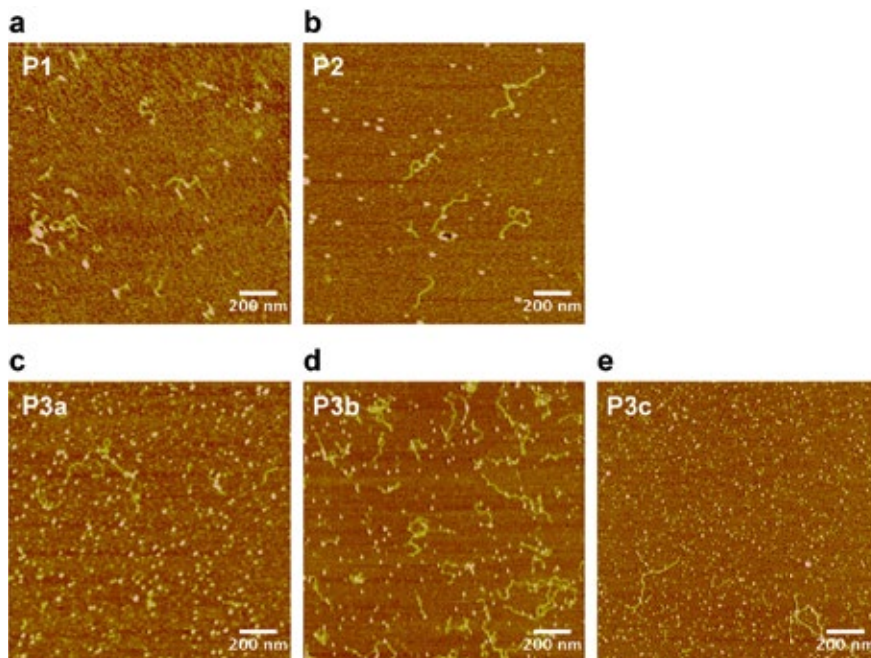
Figure A3.1.1. Representative AFM images of the polymer-SAv conjugates of **P1-P3c** drop-casted on poly lysine treated mica. Scale bar: 200 nm for a)-e).
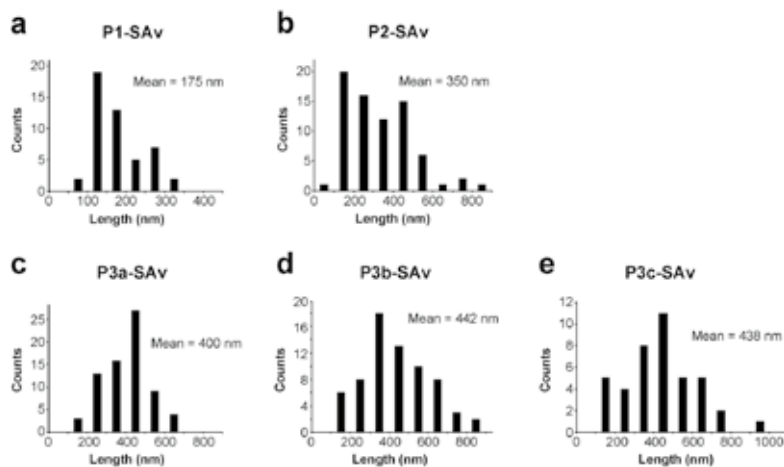
Figure A3.1.2. Length distribution of the different polymer-SAv conjugates as determined from AFM images. Each histogram contains at least 41 polymers: a) **P1-SAv**, n = 48; b) **P2-SAv**, n = 74; c) **P3a-SAv**, n = 72; d) **P3b-SAv**, n = 68; e) **P3c-SAv**, n = 41.
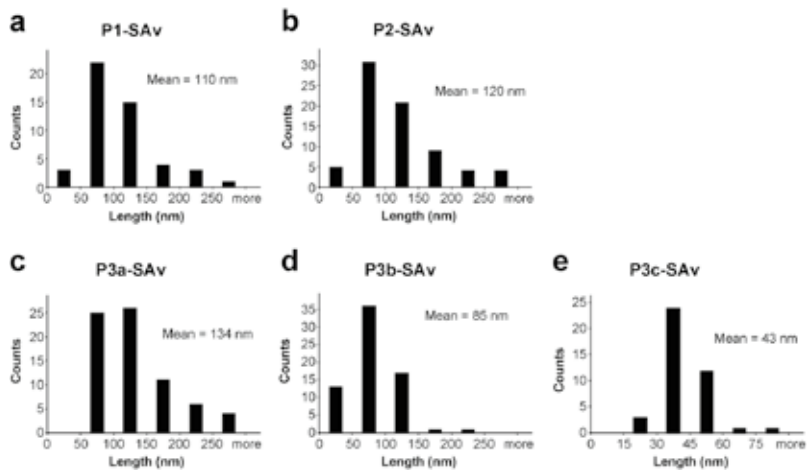
Figure A3.1.3. Average distance between SAv molecules determined from the AFM images. Each histogram contains at least 41 polymers: a) **P1-SAv**, n = 48; b) **P2-SAv**, n = 74; c) **P3a-SAv**, n = 72; d) **P3b-SAv**, n = 68; e) **P3c-SAv**, n = 41.
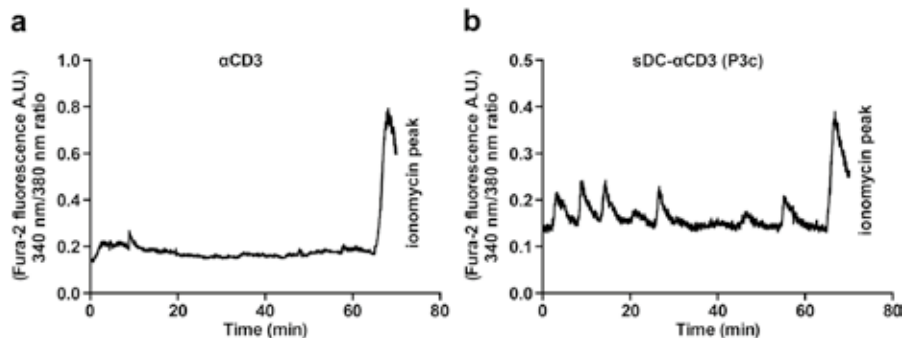
Figure A3.1.4. Single-cell Ca^{2+}-signalling experiments. Representative time traces (340 nm/380 nm ratio) for PBLs treated with free αCD3 a) or **P3c** b).
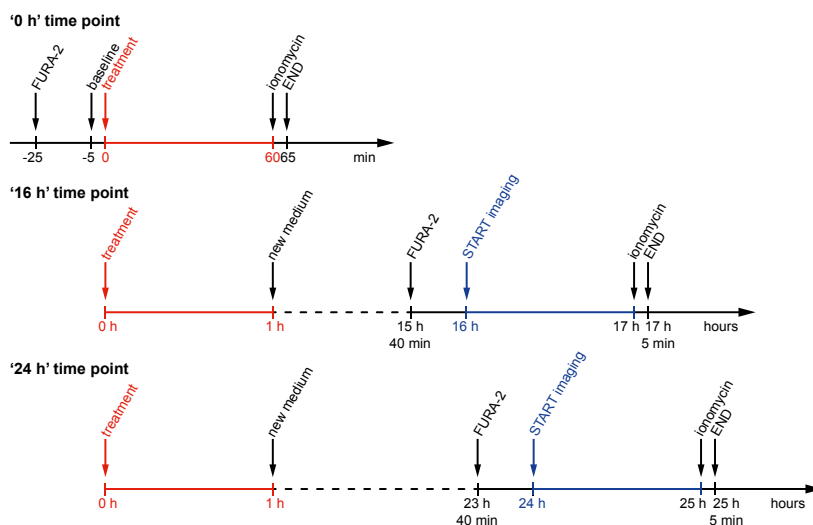
Figure A3.1.5. Timeline of the long-term single-cell Ca^{2+}-signalling experiment. To obtain the '0 h' time point, the PBLs were loaded with Fura-2, treated with the stimulant directly under the microscope and imaged. For the '16 h' and '24 h' time points the cells were first treated with the respective stimulant for 1 h and then incubated without stimulant for 15 h or 23 h, respectively. Before imaging was started, the cells were loaded with Fura-2 for 20 min. At the end of the 1 h imaging period, all samples were treated with ionomycin to determine cell viability. In this experiment, the baseline intensity was only determined for the '0 h' time point.
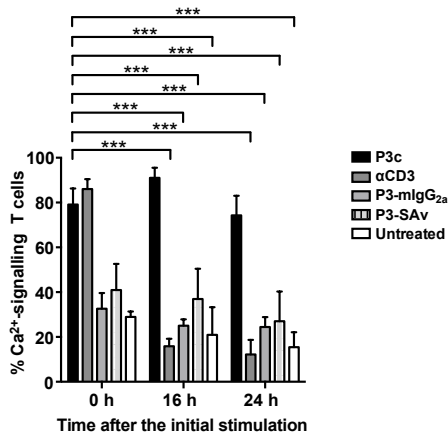
Figure A3.1.6. Post-stimulation Ca^{2+}-signalling. T cells were treated with 12.5 ng/ml **P3c** or αCD3 for 1 h. The stimulant was removed and the cells were incubated in fresh medium. Ca^{2+}-imaging was performed 16 h or 24 h after starting the treatment (15 h or 23 h after removal of the stimulant). As a reference, T cells were also imaged under the microscope while the stimulant was added (0 h). The graph further shows data obtained for T cells treated with the following controls: **P3-SAv**, **P3-mIgG$_{2a}$** (isotype control) or medium (untreated). The asterisks represent the statistical significance at 'p' values of 0.001 (***).
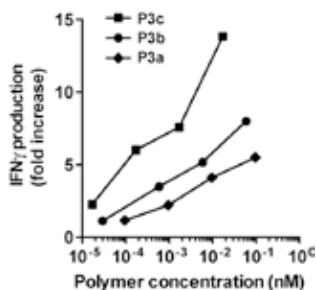
Figure A3.1.7. IFNγ secretion of T cells treated with **P3a**, **P3b** or **P3c** normalized to polymer concentration.
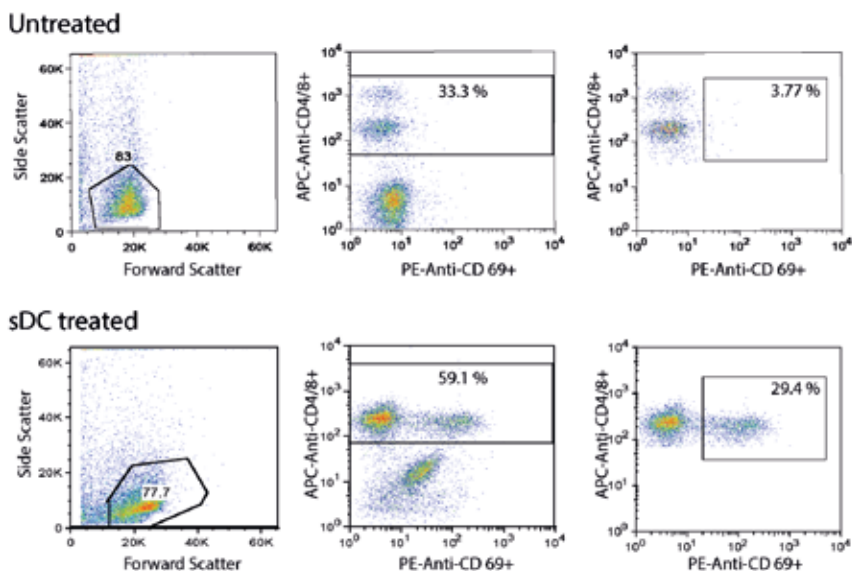
Figure A3.1.8. FACS analysis of sDC-treated (**P3c**) and untreated PBLs. After identification of CD4/8+ T cells, the percentage of CD69+ cells was determined.
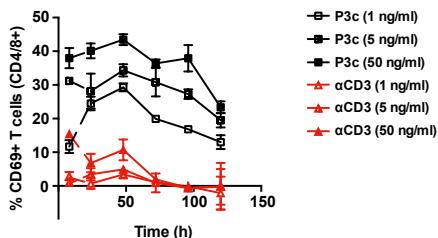
Figure A3.1.9. Long-term analysis of CD69 expression. Percentage of CD69 expressing T cells after treatment with different concentrations of **P3c** or αCD3.

3.6 References

(1)   Banchereau, J.; Steinman, R. M. *Nature* **1998**, *392* (6673), 245–252.
(2)   Eggermont, L. J.; Paulis, L. E.; Tel, J.; Figdor, C. G. *Trends Biotechnol.* **2014**, *32* (9), 456–465.
(3)   Hardy, N. M.; Mossoba, M. E.; Steinberg, S. M.; Fellowes, V.; Yan, X. Y.; Hakim, F. T.; Babb, R. R.; Avila, D.; Gea-Banacloche, J.; Sportes, C.; Levine, B. L.; June, C. H.; Khuu, H. M.; Carpenter, A. E.; Krumlauf, M. C.; Dwyer, A. J.; Gress, R. E.; Fowler, D. H.; Bishop, M. R. *Clin. Canc. Res.* **2011**, *17* (21), 6878–6887.
(4)   Garlie, N. K.; LeFever, A. V; Siebenlist, R. E.; Levine, B. L.; June, C. H.; Lum, L. G. *J. Immunother.* **1999**, *22* (4), 336–345.
(5)   Fadel, T. R.; Sharp, F. A.; Vudattu, N.; Ragheb, R.; Garyu, J.; Kim, D.; Hong, E.; Li, N.; Haller, G. L.; Pfefferle, L. D.; Justesen, S.; Herold, K. C.; Fahmy, T. M. *Nat. Nanotechnol.* **2014**, *9* (8), 639–647.
(6)   Prakken, B.; Wauben, M.; Genini, D.; Samodal, R.; Barnett, J.; Mendivil, A.; Leoni, L.; Albani, S. *Nat. Med.* **2000**, *6* (12), 1406–1410.
(7)   van der Weijden, J.; Paulis, L. E.; Verdoes, M.; van Hest, J. C. M.; Figdor, C. G. *Chem. Sci.* **2014**, *5* (9), 3355–3367.
(8)   Yokosuka, T.; Saito, T. *Immunol. Rev.* **2009**, *229* (1), 27–40.
(9)   Varma, R.; Campi, G.; Yokosuka, T.; Saito, T.; Dustin, M. L. *Immunity* **2006**, *25* (1), 117–127.
(10)   Choudhuri, K.; Dustin, M. L. *FEBS Lett.* **2010**, *584* (24), 4823–4831.
(11)   Fooksman, D. R.; Vardhana, S.; Vasiliver-Shamis, G.; Liese, J.; Blair, D. A.; Waite, J.; Sacristán, C.; Victora, G. D.; Zanin-Zhorov, A.; Dustin, M. L. *Annu. Rev. Immunol.* **2010**, *28* (1), 79–105.
(12)   Mulder, A.; Huskens, J.; Reinhoudt, D. N. *Org. Biomol. Chem.* **2004**, *2* (23), 3409–3424.
(13)   Krishnamurthy, V. M.; Estroff, L. A.; Whitesides, G. M. In *Fragment-based Approaches in Drug Discovery*; Wiley-VCH Verlag GmbH & Co. KGaA, **2006** 11–53.
(14)   Kitov, P. I.; Bundle, D. R. *J. Am. Chem. Soc.* **2003**, *125* (52), 16271–16284.
(15)   Huskens, J. *Curr. Opin. Chem. Biol.* **2006**, *10* (6), 537–543.
(16)   Mandal, S.; Eksteen-Akeroyd, Z. H.; Jacobs, M. J.; Hammink, R.; Koepf, M.; Lambeck, A. J. a.; van Hest, J. C. M.; Wilson, C. J.; Blank, K.; Figdor, C. G.; Rowan, A. E. *Chem. Sci.* **2013**, *4* (11), 4168–4174.
(17)   Mandal, S.; Hammink, R.; Tel, J.; Eksteen-Akeroyd, Z. H.; Rowan, A. E.; Blank, K.; Figdor, C. G. *ACS Chem. Biol.* **2015**, *10* (2), 485–492.
(18)   Dommerholt, J.; Schmidt, S.; Temming, R.; Hendriks, L. J. A.; Rutjes, F. P. J. T.; van Hest, J. C. M.; Lefeber, D. J.; Friedl, P.; van Delft, F. L. *Angew Chem Int Ed* **2010**, *49* (49), 9422–9425.
(19)   Joseph, N.; Reicher, B.; Barda-Saad, M. *Biochim. Biophys. Acta - Biomembr.* **2014**, *1838* (2), 557–568.
(20)   Williams, D. A.; Fogarty, K. E.; Tsien, R. Y.; Fay, F. S. *Nature* **1985**, *318* (6046), 558–561.
(21)   Montet, X.; Funovics, M.; Montet-Abou, K.; Weissleder, R.; Josephson, L. *J. Med. Chem.* **2006**, *49* (20), 6087–6093.
(22)   Lillemeier, B. F.; Mortelmaier, M. A.; Forstner, M. B.; Huppa, J. B.; Groves, J. T.; Davis, M. M. *Nat. Immunol.* **2010**, *11* (1), 90–96.
(23)   Dinic, J.; Riehl, A.; Adler, J.; Parmryd, I. *Sci. Rep.* **2015**, *5*, 10082.
(24)   Visch, H.-J.; Koopman, W. J. H.; Zeegers, D.; van Emst-de Vries, S. E.; van Kuppeveld, F. J. M.; van den Heuvel, L. W. P. J.; Smeitink, J. A. M.; Willems, P. H. G. M. *Am. J. Physiol. Cell Physiol.* **2006**, *291* (2), C308–C316.

4

Polymer-based synthetic dendritic cells for tailoring robust and multifunctional T cell responses
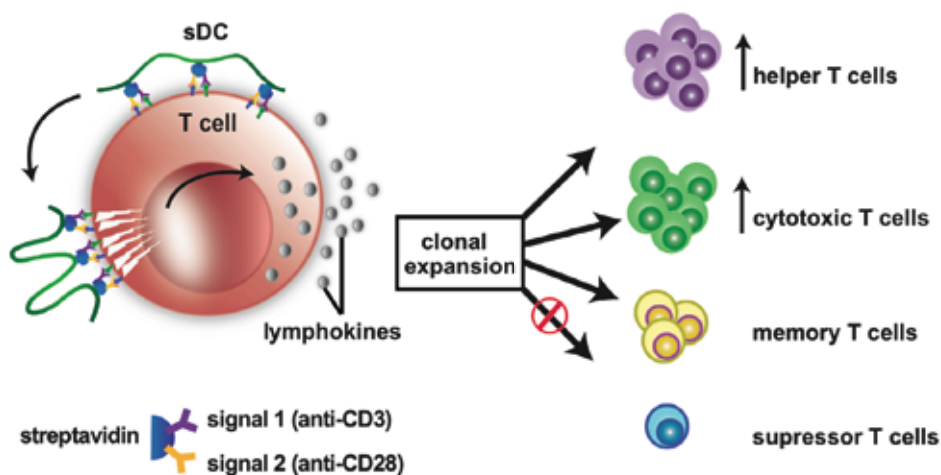
Chapter 4: Polymer-based synthetic dendritic cells for tailoring robust and multifunctional T cell responses

4.1 Introduction

Vaccination is one of the most successful and cost-effective health interventions. Worldwide, it prevents several millions of deaths every year. Most commonly used vaccines consist of inactivated pathogens and an additional component (adjuvant) that potentiates the immune response. More recently, therapeutic vaccines have also been developed to fight cancer.[1] Most vaccines designed so far target antigen presenting cells, in particular professional antigen presenting dendritic cells (DCs). DCs process exogenously encountered antigens and subsequently present them on their surface to T cells.[2] Subsequent antigen specific activation and expansion of T cells is crucial for the development of protective immunity against pathogens or for eliciting cytotoxic responses against cancer.[3]

An efficient and robust anti-cancer immune response critically depends on the induction of a multifunctional T cell response involving the activation and proliferation of helper, cytotoxic and memory T cells. Cytotoxic T cells directly attack the tumor cells and are responsible for their elimination. The recruitment of helper T cells aids the development and activation of cytotoxic T cells, while memory T cells provide a long-term response against reoccurring antigenic stimuli.[4,5] Although vaccination studies have clearly demonstrated the immunogenicity of tumor antigen-loaded DCs, the number of objective clinical responses remains limited, hampering the implementation of DC-targeted vaccination as a novel form of standard treatment.[6,7] One possible reason for the low success of many currently used anti-cancer vaccines is that they also induce the hyperactivation of regulatory T cells (Tregs)[8]. Tregs are able to suppress tumor-specific responses, thus counteracting the function of cytotoxic T cells. It is now widely accepted that a successful anti-cancer vaccine should not stimulate Tregs.[7,9,10]

Instead of using DC vaccines, new approaches directly target the T cells. The focus lies on the development of artificial antigen presenting cells (aAPCs) that replace natural, activated DCs.[11–14] aAPCs can be synthesized as an "off-the-shelf" product thereby overcoming the need for preparing a tailor-made and expensive, natural DC vaccine for each patient. In order to achieve effective T cell activation, *ex vivo* or *in vivo*, the aAPCs need to engage with the T cell in a way similar to that of natural DCs. T cell activation involves three main signals.[2,15] The first two of these signals are highly coordinated on the T cell surface. The T cell receptor (TCR) binds to the peptide antigen presented by the major histocompatibility (MHC) complex on

the DC (signal-1). Following binding, the TCR/CD3 complexes rearrange to form microclusters, leading to immediate T cell activation.[16,17] Co-stimulatory molecules on the DC such as B7-1 and B7-2 provide the second signal for T cell activation lowering the activation threshold.[1,18] These ligands bind to the CD28 receptor located in close proximity to the TCR.[19] CD28 ligands (signal-2) are only present on activated DCs providing a safety mechanism against activation by self-antigens. T cell activation without proper co-stimulation of CD28 leads to naïve, memory and effector T cell anergy and immune tolerance.[15,20] Together, signal-1 and signal-2 lead to the release of soluble cytokines (signal-3) that further shape the development of the immune response.[21] In a later stage, the microclusters containing the TCR/CD3 complex and the CD28 receptor rearrange to form the immunological synapse (IS). [16,17,22] Ultimately, the immune response is terminated by endocytosis of the engaged receptors.[23]

Bead-based aAPCs that carry effector molecules on their surface are currently in clinical trials.[12,13] These aAPCs are used for the *ex vivo* activation and expansion of T cells allowing for their adoptive transfer into patients. Despite their clearly proven potential for activating T cells, their efficiency remains low as the rigid sphere geometry does not allow for the required movement of the effector molecules to facilitate T cell receptor clustering.[11,14,17] Liposome-based aAPCs do provide this essential flexibility.[11,14] Depending on their shape and size, however, only a limited number of effector molecules are able to interact with the T cell.[24] To enhance ligand binding, a novel aAPC design utilizing semi-flexible polymers was introduced in chapters 2[25] and 3. In contrast to spherical bead- or liposome-based aAPCs, the polymer-based design features a semi-flexible geometry that allows both efficient multivalent binding and receptor clustering. When functionalizing the polymer with signal-1 (anti-CD3 antibodies known to cause polyclonal T cell activation),[26] an enhanced and sustained T cell response was observed compared to soluble anti-CD3 antibodies (αCD3) or αCD3-functionalized beads (PLGA particles; poly lactic-co-glycolic acid).

In this chapter, a new generation of sDCs is introduced with the ultimate goal of developing a functional synthetic dendritic cell (sDC) that can be used to activate and expand T cells. This new sDC design carries both signal-1 and signal-2 (anti-CD28 antibodies; αCD28).[19,20] The importance of the presence of signal-2 for T cell activation is investigated and the results are compared to sDCs that carry only signal-1. More importantly, the immunophenotypes and functional states of the expanded polyclonal T cell population are characterized to determine if the bi-functional and semi-flexible sDC design is able to activate helper, cytotoxic and memory T cells without stimulating Tregs.

4.2 Results

4.2.1 Design and characterization of sDCs

A functional synthetic dendritic cell (sDC) needs to provide multiple interactions for stimulation of both the TCR/CD3 complex as well as the CD28 receptor. The ideal design does not only carry a sufficient number of signal-1 (αCD3) but also signal-2 (αCD28) effector molecules. More importantly, the scaffold geometry needs to allow for efficient multivalent binding and receptor clustering. In contrast to PLGA particles, a semi-flexible polymeric scaffold based on polyisocyanopeptides combines these properties in an ideal way.[25] On the polymer, all antibodies are in principle available for receptor binding. At the same time, the polymer flexibility allows for the spatial rearrangement required for optimal intracellular signaling and T cell activation. The polyisocyanopeptide polymer[27,28] is a copolymer consisting of azide-functionalized monomers and methoxy-terminated monomers (Figure 4.1). The ratio of these monomers was chosen such that the average distance between azide groups was 10 nm. The average length of the complete polymer varied from 150 nm to 200 nm. To provide maximum flexibility in subsequent bioconjugation reactions, streptavidin was coupled to the azide groups using a strain-promoted azide-alkyne cycloaddition (SPAAC) reaction.[29] In total 3–5 streptavidin molecules were coupled per polymer with an average spacing between 40 nm and 50 nm. In the next step, biotinylated monoclonal anti-human CD3 antibodies (αCD3) were bound to the polymer in a 1:1 molar ratio so that on average one antibody was bound per streptavidin molecule.[25] The obtained αCD3-sDC polymers were split into two fractions. One fraction was directly used for the T cell experiments. The second fraction was further functionalized with biotinylated anti-human αCD28 antibodies (αCD28) to yield αCD3/αCD28-sDC. Again the concentration was adjusted such that one αCD28 antibody was bound per streptavidin molecule (Figure 4.1 and Supplementary Figure A4.1.1). Consequently, the αCD3/αCD28-sDC polymer contains exactly the same number of 3–5 αCD3 antibodies plus the additional αCD28 antibodies in a 1:1 molar ratio.
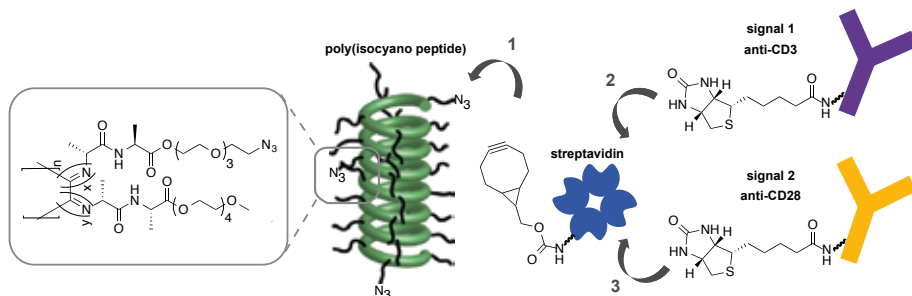
Figure 4.1. Synthesis of the polymer-based sDCs. Copolymerization of a methoxy-terminated and an azide-terminated isocyanide monomer yields a random copolymer with a statistical spacing of azide groups (average distance ~10 nm). The azide groups were utilized in a strain-promoted azide-alkyne cycloaddition reaction. A total number of 4–5 BCN-functionalized streptavidin molecules were coupled to the polymer with an average spacing between 40–50 nm, leaving most available azides unreacted (1). Subsequently, the streptavidin-polymer was further functionalized with biotinylated anti-CD3 antibodies (2) and biotinylated anti-CD28 antibodies (3) in a 1:1:1 molar ratio.

4.2.2 Synthetic dendritic cells efficiently bind T cells

In a first series of experiments the ability of sDCs containing both signal-1 and signal-2 to interact with T cells was investigated. Using the same procedure as shown in Figure 4.1, fluorescently labeled sDCs containing AlexaFluor488-lableled αCD3 (^{488}αCD3) and ATTO565-labeled CD28 (^{565}αCD28) were prepared. The binding of these fluorescently labeled ^{488}αCD3/^{565}αCD28-sDCs was observed with a confocal microscope (Appendix 4.2). After only 10 min of incubation with ^{488}αCD3/^{565}αCD28-sDC (at an αCD3 concentration of 50 ng ml^{-1}), both ^{488}αCD3 and ^{565}αCD28 fluorescence signals were detected on the T cell surface indicating binding of the sDC to the T cell. The fluorescence signals were co-localized in multiple stable complexes presumably representing the microclusters formed upon T cell activation (Appendix 4.2).[17] After 16 hours of incubation these microclusters were concentrated in one area on the T cell surface as is expected once the immunological synapse (IS) has formed (Appendix 4.2). These findings show that the sDCs are able to bind to the T cell surface and allow microcluster and IS formation, which are important processes following T cell activation.

4.2.3 αCD3/αCD28-sDCs are superior in activating and expanding human polyclonal T cells

Having obtained a first indication that the αCD3/αCD28-sDC polymer does not only bind to T cells but also activates them, the next goal was to probe the T cell priming capacity of the sDCs. For this purpose the expression of the surface marker

CD69, the release of the cytokine interferon-γ (IFNγ) as well as the proliferation of T cells was followed. CD69 is an early activation marker as it is one of the first inducible cell surface glycoproteins expressed upon T cell activation. On the other hand, IFNγ secretion and T cell proliferation are typical late activation markers, indicating sustained T cell activation.
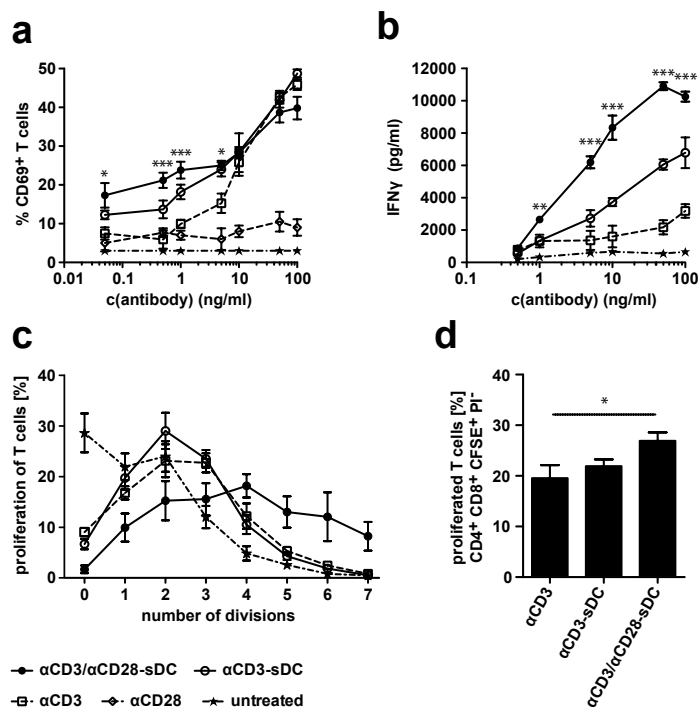
Figure 4.2. Comparative T cell activation profile of αCD3/αCD28-sDC, αCD3-sDC and freely soluble antibodies. a) Percentage of T cells expressing the early activation marker CD69 after 16 h of treatment. b) Concentration of secreted IFNγ after 16 h of treatment. c) Proliferation of T cells depicted as the number of divisions, measured by CFSE dilution. The graph represents the fraction of T cells per generation after 4 days of treatment with the respective stimulants at a concentration of 5 ng ml^{-1}. d) Total fraction of proliferated T cells after treating the T cells as indicated above. The values are corrected for the fraction of proliferated T cells in the untreated sample. For the αCD3/αCD28-sDC treatment, the antibody concentration refers to the concentration of αCD3 antibodies. The data represents the mean ± SEM of at least 3 independent experiments performed with T cells from different donors. The asterisks represent the statistical significance relative to the αCD3 treatment at 'p' values of 0.05 (*), 0.01 (**) and 0.001 (***), respectively.

Both polymeric sDCs (αCD3-sDC and αCD3/αCD28-sDC) activate T cells more efficiently than the freely soluble antibodies (Figure 4.2). This is evident for all 3 markers and confirms our previous results for the αCD3-sDC polymer.[25] Moreover, a clear difference is observed between the polymer carrying only signal-1 (αCD3-sDC)

and the polymer carrying both signals (αCD3/αCD28-sDC). Especially in the low concentration range (<5 ng ml^{-1}), the expression of CD69 was increased when treating the T cells with αCD3/αCD28-sDC (Figure 4.2a). More importantly, significantly more IFNγ was secreted (Figure 4.2b) and an increased T cell proliferation was detected (Figure 4.2c and 4.2d). The co-functionalization of the polymer with signal-2 clearly leads to a more efficient T cell activation, proving that both the αCD3 and the αCD28 antibody are able to interact with the T cell in the desired way.

The reason for the superior activity of the αCD3/αCD28-sDC polymer was investigated in more detail (Figure 4.3). Using the polymeric system, co-stimulation with αCD3 and αCD28 can be achieved in different ways. Both antibodies can be bound to the same polymer (αCD3/αCD28-sDC) or to different polymers, using a mixture. The results clearly show that the αCD3/αCD28-sDC polymer activated the T cells significantly better than an equimolar mixture of αCD3-sDC and αCD28-sDC polymers (Figure 4.3b). This result provides strong evidence that the superior performance of αCD3/αCD28-sDC requires both effector molecules to be bound in close proximity, *i.e.* on the same polymer molecule.

To test the importance of scaffold flexibility, the αCD3/αCD28-sDC polymer was compared with rigid PLGA particles (diameter 1.8 μm[25]) functionalized with both αCD3 and αCD28 antibodies (see experimental section). Even though the PLGA particles also carry both signals on the same particle and the number of possible interactions is similar,[25] their efficacy is lower than for αCD3/αCD28-sDC. This result supports the hypothesis that scaffold flexibility is a crucial requirement to allow for the required close proximity of the effector molecules. Taken together, these results show that a combination of multivalent binding and scaffold geometry as well as flexibility is important for effective T cell activation.
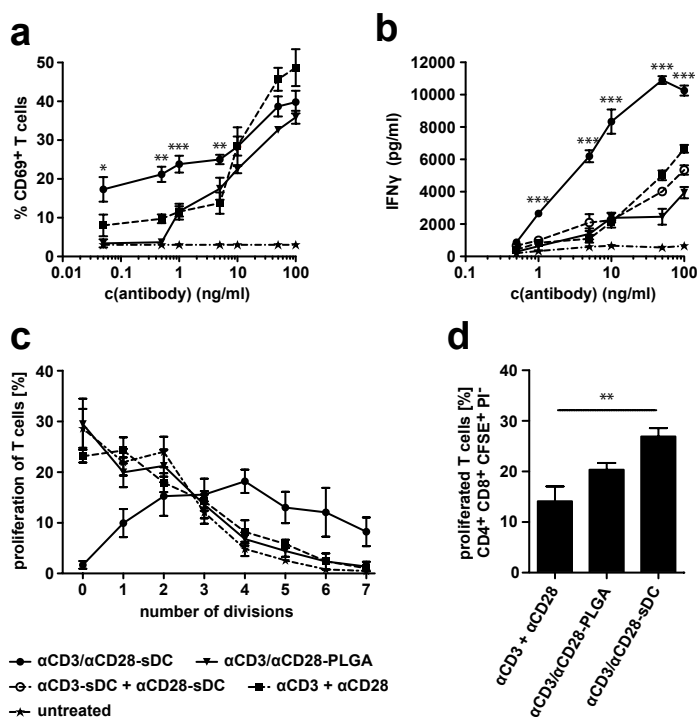
Figure 4.3. Geometry effects on T cell activation. a) Percentage of T cells expressing the early activation marker CD69 after 16 h of treatment. b) Concentration of secreted IFNγ after 16 h of treatment. c) Proliferation of T cells depicted as the number of divisions, measured by CFSE dilution. The graph represents the fraction of T cells per generation after 4 days of treatment with the respective stimulants at a concentration of 5 ng ml^{-1}. d) Total fraction of proliferated T cells after treating the T cells as indicated above. The values are corrected for the fraction of proliferated T cells in the untreated sample. In all experiments, the antibody concentration refers to the concentration of αCD3 antibodies. The data represents the mean ± SEM of at least 3 independent experiments performed with T cells from different donors. The asterisks represent the statistical significance relative to the treatment with freely soluble αCD3 and αCD28 at 'p' values of 0.05 (*), 0.01 (**) and 0.001 (***), respectively.

4.2.4 αCD3/αCD28-sDCs predominantly activate effector CD8$^+$ and effector memory CD4$^+$ T cells

Having obtained additional evidence that αCD3/αCD28-sDC is a highly potent inducer of T cell activation, the next step was to evaluate the immunophenotype and function of the expanded polyclonal T cell population. T cells were stimulated overnight with αCD3/αCD28-sDC, αCD3-sDC or cells were left untreated as a negative control. First, it was investigated whether helper T cells (T$_H$ cells; CD4$^+$) or cytotoxic T cells (CTLs; CD8$^+$) were responsible for the observed activation. After sorting the CD4$^+$ and CD8$^+$ T cell populations, CD69 expression and IFNγ secretion

were measured separately for these populations. Treatment with αCD3/αCD28-sDC induced a profound upregulation of CD69 on CD8^{+} cells, but much less on CD4^{+} cells (Figure 4.4a). In contrast, both the CD8^{+} and CD4^{+} cell populations secreted similarly high levels of IFNγ (Figure 4.4b). When comparing the effect of αCD3/αCD28-sDC with αCD3-sDC, a similar overall activation pattern was observed for both CD4^{+} and CD8^{+} cells. For all subpopulations the activation was stronger, however, when treating the T cells with αCD3/αCD28-sDC. This again confirms the importance of αCD28 on the αCD3/αCD28-sDC.
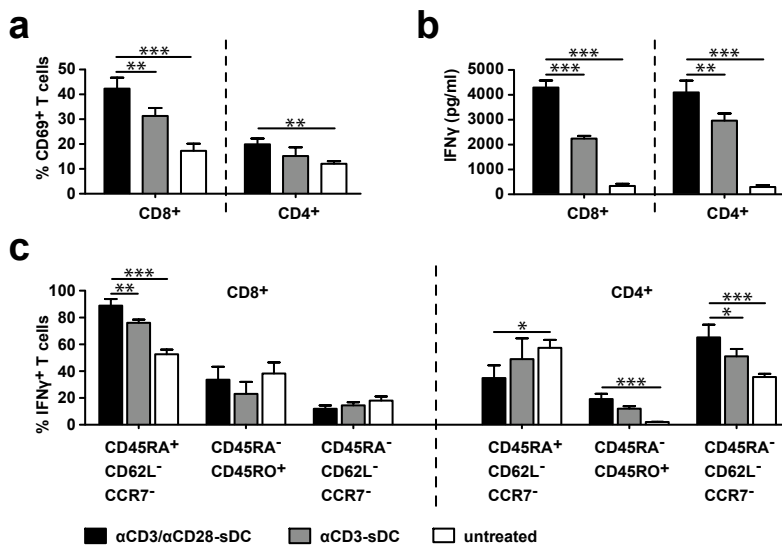
Figure 4.4. Immunophenotypes of activated T cells. a) The CD69 expression profile shows the highest number of activated cytotoxic (CD8^{+}) and helper (CD4^{+}) T cells after 16 hours of treatment with αCD3/αCD28-sDC when compared to T cells treated with only αCD3-sDC. b) Both CD8^{+} and CD4^{+} T cells, treated with αCD3/αCD28-sDC for 16 hours, release significantly higher amounts of IFNγ when compared to T cells treated with αCD3-sDC. c) Immunophenotyping of the FACS-sorted, activated (intracellular IFNγ^{+}) CD8^{+} T cells shows that the number of CD8^{+} effector T cells (CD45RA^{+} CD62L^{-} CCR7^{-}) is significantly increased after 4 days of treatment with the polymeric sDCs (both αCD3/αCD28-sDC and αCD3-sDC) while the number of CD8^{+} memory (CD45RA^{-} CD45RO^{+}) and CD8^{+} effector memory (CD45RA^{-} CD62L^{-} CCR7^{-}) T cells is not significantly affected. In contrast, treatment with the polymeric sDCs results in a slightly lower number of CD4^{+} effector T cells while the number of CD4^{+} memory and CD4^{+} effector memory T cells is increased. In all cases the observed difference is bigger for αCD3/αCD28-sDC than for αCD3-sDC. In all experiments an αCD3 concentration of 5 ng ml^{-1} was used. The data represents the mean ± SEM of 3 independent experiments with T cells from different donors. The asterisks represent the statistical significance at 'p' values of 0.05 (*), 0.01 (**) and 0.001 (***), respectively.

Depending on their function, CD4$^+$ and CD8$^+$ T cells can be further divided into the following subtypes: effector T cells, memory T cells and effector memory T cells.[30] Activated human effector T cells are characterized by a CD45RA$^+$ CD62L$^-$ CCR7$^-$ phenotype, memory T cells by CD45RA$^-$ CD45RO$^+$, and effector memory T cells by CCR7$^-$ CD45RA$^-$ CD62L$^-$. A detailed phenotypic analysis of the IFNγ$^+$ CD8$^+$ population revealed that predominantly effector CD8$^+$ T cells were induced following treatment with αCD3/αCD28-sDC and αCD3-sDC (Figure 4.4c). In contrast, an increase in the number of memory and effector memory T cells was observed in the IFNγ$^+$ CD4$^+$ cell compartment along with a small decrease in the number of effector CD4$^+$ T cells (Figure 4.4c). The activation of an effector memory CD4$^+$ T cell population may play a supportive role, prolonging the cytotoxic effect.

4.2.5 αCD3/αCD28-sDCs do not show any significant activation of regulatory T cells

Having shown that sDCs activate the required CD8$^+$ effector cells as well as CD4$^+$ memory and effector memory cells, an important remaining question to be addressed is the effect of sDCs on CD4$^+$ cells that develop into undesired regulatory T cells thereby inhibiting immune reactivity. The frequency of Tregs, characterized by a CD4$^+$ FoxP3$^+$ CD69$^+$ phenotype, was evaluated after treatment with αCD3/αCD28-sDC along with a number of controls. T cells incubated with soluble αCD3 and αCD28 showed a higher number of Tregs than untreated T cells (Figure 4.5a). Incubation with αCD3-sDC also caused Treg activation, but to a lower extend. Interestingly, a small reduction in the number of activated CD69$^+$ Tregs was observed when the T cells were treated with αCD3/αCD28-sDC (Figure 4.5a). Taken together, these results clearly show that the polymeric sDC design carrying both signal-1 and signal-2 is a potent immunotherapeutic agent that predominantly activates CD8$^+$ effector cells as well as memory and effector memory CD4$^+$ T$_H$1 cells without inducing the activation of Tregs.
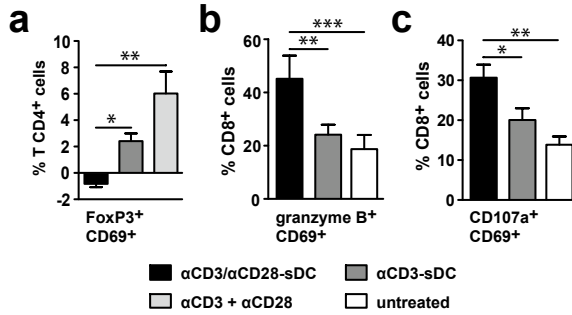
Figure 4.5. Functional analysis of T cells. a) FACS analysis of the activated CD4^{+} T cell population shows that the number of regulatory T cells is lowest when the T cells are treated with αCD3/αCD28-sDC when compared to T cells treated with freely soluble αCD3 and αCD28 antibodies (1:1 molar ratio) or polymer-bound αCD3 alone (αCD3-sDC). b) The number of cytotoxic T cells characterized as granzyme B^{+} and CD69^{+} in the population of activated CD8^{+} cells is highest upon treatment with αCD3/αCD28-sDC. c) Also the number of degranulated CD8^{+} T cells (CD107a^{+} CD69^{+}) is highest upon treatment with αCD3/αCD28-sDC. In all experiments an αCD3 concentration of 5 ng ml^{-1} was used and the T cells were treated at each condition for 4 days. The data represents the mean ± SEM of 3 independent experiments with T cells from different donors. The asterisks represent the statistical significance at 'p' values of 0.05 (*), 0.01 (**) and 0.001 (***), respectively.

4.2.6 αCD3/αCD28-sDCs activate multifunctional killer T cells

Recent studies indicate that disease control depends on the quality rather than on the quantity of cytotoxic CD8^{+} T cells.[31,32] CTLs only become effective killer cells if they are fully activated by the correct stimuli. They are characterized by multiple functions: proliferation, cytokine release as well as their killing capacity. Above, the capacity of αCD3/αCD28-sDCs to induce both proliferation and cytokine secretion by CD8^{+} T cells was already demonstrated. In Figure 4.5b and 4.5c the capacity of αCD3/αCD28-sDCs to induce T cells that are able to exert cytotoxic activity is shown. The secretion of the protease granzyme B and the expression of the degranulation marker CD107a on the cell surface was analyzed, which are typical markers characterizing active multifunctional killer cells.[33] Expression of granzyme B was clearly induced for activated CD69^{+}CD8^{+} T cells after stimulation with αCD3/αCD28-sDCs. In contrast, the level of granzyme B expression was not increased above the level of untreated cells when the T cells were incubated with αCD3-sDC (Figure 4.5b). Moreover, the CD107a degranulation marker was upregulated on activated CD69^{+} CD8^{+} T cells only upon stimulation with αCD3/αCD28-sDCs, but not with αCD3-sDC (Figure 4.5c). These findings reveal that providing co-stimulatory signals in the near proximity of CD3 stimulation not only warrants but also is crucial for the generation of multifunctional killer T cells.

4.3 Discussion and conclusion

The results obtained in this chapter confirm and expand earlier findings that polymeric sDCs are highly potent activators of T cells. In contrast to spherical bead-based designs, all effector molecules on the polymer can potentially interact with the cell surface. The efficiency of our polyisocyanopeptide scaffold may further be a direct result of the semi-flexible nature of the polymer. This semi-flexibility allows for the proper arrangement and clustering of antigen and co-stimulatory receptors warranting strong T cell activation and propagation. To facilitate stable multivalent binding, a certain stiffness is required for energetic reasons. When using a highly flexible polymer, multivalent interactions of the attached effector molecules are not favored as they lead to a loss of conformational entropy of the polymer.[34] Stiff scaffolds cannot adjust to the optimal receptor spacing on the cell surface and might prevent receptor rearrangement. A semi-flexible polymer backbone facilitates multivalent binding and also allows for molecular rearrangements of the bound components. This is required for microcluster and IS formation, which are crucial requirements for downstream signaling during T cell activation.

The activation of T cells by natural DCs is achieved mainly by two prime signals: signal-1, recognition of the MHC-peptide complex by the TCR/CD3 complex; and signal-2, acquisition of co-stimulation via the CD28 receptor. To investigate the efficacy of the sDC design as a potent inducer of T cell activation, the sDCs were decorated with αCD3 and αCD28 antibodies to mimic signal-1 and -2, respectively. The results clearly show that the highest level of polyclonal T cell activation is only obtained when the sDCs carry signal-1 and -2 on one and the same polymer. Adding signal-2 on different polymers (αCD3-sDC + αCD28-sDC) does not show any favorable effect on T cell activation when compared to αCD3-sDC alone. The presence of signal-1 and -2 on the same polymer might influence both binding itself but also T cell signaling in a number of ways. The additional αCD28 antibodies might cause stronger binding of αCD3/αCD28-sDC to the T cell. Compared to αCD3-sDC, αCD3/αCD28-sDC carries twice the amount of antibodies leading to an increased multivalency effect. No difference in the binding efficiency between αCD3-sDC and αCD3/αCD28-sDC was observed, however (Appendix 4.2). Even though the additional antibodies have only a minor effect on the overall binding strength of sDCs, the effective local concentration of the antibodies is higher after the first antibody has docked onto the cell. This high effective concentration combined with the spatial proximity of αCD3 and αCD28 on the polymer increases the probability for both antibodies to bind. Co-stimulation with αCD28 is known to decrease the number of TCR/CD3 complexes that need to be stimulated for T cell activation.[18,19] This lower activation threshold might directly explain the higher efficiency of αCD3/αCD28-sDC in the low concentration range when compared to αCD3-sDC. Lastly, co-stimulation

with αCD28 might crucially influence T cell signaling, leading to a stronger and more defined T cell activation.[19]

A functional sDC is required to induce helper, cytotoxic and memory T cells while preventing the activation of regulatory T cells. The results in this chapter show that αCD3/αCD28-sDCs predominantly induced the activation of CD8^{+} effector T cells and CD4^{+} T$_H$1 cells. Moreover, the addition of αCD3/αCD28-sDC did not activate Tregs when compared to the addition of soluble αCD3 and αCD28. Further investigation showed that the activated CD8[+] T cell population even developed cytotoxic functions producing the cytolytic effector molecule granzyme B and expressing the degranulation marker CD107a. This suggests that αCD3/αCD28-sDC induced cytotoxic T cells are acutely activated and can exert multiple effector functions. It is note worthy that also the polymer carrying only αCD3 was able to specifically activate CD8[+] effector T cells and CD4[+] T$_H$1 cells, but to a smaller extend. Granzyme B expression and degranulation crucially required the presence of αCD28. Also the number of regulatory T cells was unfavorably higher for αCD3-sDC. The presence of αCD28 on the polymer clearly shapes the immune response ensuring that only the desired T cell populations are activated that are essential for effective anti-cancer immunotherapy.

In this context it is important to discuss the requirement for both αCD3 and αCD28 to be bound on the same polymer from a mechanistic point of view. The obtained results suggest that αCD3 and αCD28 need to be bound to the T cell in close proximity, most likely in the same microcluster.[17,19] If αCD3 and αCD28 are bound to the T cell in different surface areas, T cell activation is obtained but the immune response is less defined. It is currently not clear what shapes the immune response in the desired direction. The required co-localization of αCD3 and αCD28 in the same microcluster suggests that the fate of the activated T cell is determined shortly after sDC binding and does not require complete IS formation.[17,22] The polymer provides a physical link between αCD3 and αCD28 that might keep both receptors in proximity even within a fully mature IS. This might directly affect both the structure and the dynamics within the IS, eventually leading to a sustained and long lasting activation.[16,17] This cannot be achieved with PLGA particles due to their larger size and rigidity. In this context, sDCs provide a unique and promising tool for studying receptor rearrangements in the IS in more detail in future experiments.

In conclusion, polymer-based DCs decorated with T cell receptor stimulating agents and co-stimulatory molecules are highly efficient activators of T cells. Their unique features, such as semi-flexibility, bi-functionality and capacity of multivalent binding, make them excellent mimics of natural DCs. Their 'natural' behavior, reminiscent of plasma membrane embedded proteins, is essential for lowering the activation threshold and the specific programming of T cells. As a consequence,

sDCs overcome crucial drawbacks of many previously reported aAPC designs and have the potential to emerge as a novel, fully synthetic system for inducing antigen specific immune responses. More importantly, this novel vaccine design might be tuned to maintain immune responses over prolonged periods of time without the risk of Treg development. This sDC design has the potential to fulfill all criteria required for a highly efficient and successful anti-cancer vaccine.

4.4 Experimental section

Purification of anti-CD3 antibodies

For the production of αCD3 (mouse anti-human CD3, IgG2a monoclonal antibodies) OKT-3 hybridoma cells (ATCC, CRL-8001) were maintained in RPMI-1640 medium containing 10 % (v/v) FBS, 1 % (w/v) Glutamine and 1× AA. After reaching confluence, cells were transferred to protein free hybridoma medium (PFHM-II). After 3 days in culture, αCD3 antibodies were isolated from the supernatant by Protein G affinity chromatography (HiTrap Protein G HP; GE Healthcare), following the manufacturer's protocol.

Polymer synthesis

The polyisocyanopeptide polymer molecule was synthesized and characterized according to our published method.[25,35] Briefly, the sDC backbone was synthesized by polymerizing the azide-functionalized and the methoxy non-functionalized isocyanopeptides in a 1:100 ratio. The obtained 150–200 nm long polyisocyanopeptide possess an azide group every 10 nm (statistical average). Streptavidin (SAv; Thermo Fisher Scientific) was functionalized with BCN-POE$_3$-NH-C(O)CH$_2$CH$_2$CH$_2$C(O)OSu (BCN-NHS; Synaffix). The reaction was carried out in borate buffer (10 mM, pH 8.5) at 4 °C for 4 days. The reaction mixture contained a 6-fold molar excess of BCN-NHS. Unreacted BCN-NHS was removed by gel filtration, followed by ultrafiltration with a 10 kDa cut-off. These reaction conditions yielded approximately 1–4 BCN functional groups per SAv molecule as determined by MALDI-ToF. Subsequently, the BCN-functionalized SAv was conjugated to the azide-bearing polyisocyanopeptide in a strain-promoted azide-alkyne cycloaddition (SPAAC) reaction.[29] The conjugation reaction (BCN-SAv:N$_3$ = 1:1) was performed in borate buffer. After incubating the mixture for 4 days at 4 °C, the resulting SAv-polymer conjugate was purified by dialysis against water using a membrane with a 100 kDA cut-off. The average polymer contained 3–5 SAv molecules as determined using AFM imaging. The characterization data for this previously used SAv-polymer conjugate is described in chapter 2. The characterization also includes negative controls testing for non-specific T cell activation of the polymer itself and the SAv-polymer conjugate. This previously described SAv-polymer conjugate was subsequently incubated with biotinylated monoclonal anti-human CD3 antibodies (αCD3) in a 4:1 αCD3:SAv molar ratio. As shown previously,[25] this 4:1 ratio yielded a 1:1 ratio of αCD3 and SAv bound to the polymer backbone (αCD3-sDC). αCD3-sDC obtained in this way was subsequently functionalized with biotinylated monoclonal anti-human CD28 antibodies (αCD28; clone CD28.2, isotype IgG1, κ; BioLegend) using a similar procedure (αCD3/αCD28-sDC). The ideal labeling ratio to obtain a 1:1:1 αCD3: αCD28:SAv molar ratio was determined using fluorescently labeled antibodies as described in the next section.

Preparation of fluorescently labeled sDCs

The αCD3 and the αCD28 antibodies were labeled with AlexaFluor488-NHS (Life Technologies) and ATTO565-NHS (ATTO-TEC), respectively. In the first step the SAv-functionalized polymer was incubated with AlexaFluor488-labeled and biotinylated αCD3 ([488]αCD3) in the previously determined 4:1 molar ratio (chapter 2 and reference 25). The sample was purified by ultrafiltration (300 kDa cut-off) to remove unbound antibodies. Subsequently, the sample was incubated with ATTO565-labeled and biotinylated αCD28 ([565]αCD28) in a 4:1, 10:1 and 20:1 molar ratio. After overnight incubation, the sample was again purified by ultrafiltration (300 kDa cut-off) to yield [488]αCD3/[565]αCD28-sDC in phosphate buffered saline (PBS). Following purification, the total protein concentration was determined using a standard BCA assay (Thermo Fisher Scientific) according to the manufacturer's protocol. In addition, the concentrations of the fluorescently labeled [488]αCD3 and [565]αCD28 were determined based on the fluorescence intensity at the respective excitation wavelengths (495 nm for [488]αCD3; 563 nm for [565]αCD28). Calibration curves were established using the fluorescently-labeled pure [488]αCD3 and [565]αCD28 antibodies. Knowing the total protein concentration as well as the concentrations of both antibodies, the molar ratios of all polymer-bound components could be determined (Figure A4.1.1). All tested conditions yielded approximately a 1:1 molar ratio of αCD3:αCD28 (Figure A4.1.1) showing that maximally 2 biotin binding sites are able to bind a biotinylated antibody. This is most likely a result of the reduced accessibility of the additional 2 binding sites after 2 biotin binding sites are occupied by the large, bulky antibody molecules.

The results of this experiment formed the foundation for the preparation of non-fluorescently labeled αCD3/αCD28-sDC polymers. The previously described and characterized αCD3-sDC polymer (carrying 3-5 αCD3 antibodies[25]) was used as the starting point. This polymer was incubated with a 4:1 molar excess of αCD28 antibodies over polymer-bound αCD3 antibodies. Assuming that the fluorescence labeling does not alter the binding of the antibodies to the polymer, this excess of αCD28 yields the desired 1:1 molar ratio of bound αCD3 and αCD28 antibodies, corresponding to 3–5 αCD3 and 3–5 αCD28 molecules per polymer.

Preparation of antibody functionalized PLGA particles

PLGA (poly lactic-co-glycolic acid) particles were synthesized as described in Cruza et al.[37] The particles were covalently modified with streptavidin (SAv) following the same protocol as described in Mandal et al.[25] In fact the same batch of SAv-functionalized PLGA particles (SAv-PLGA) was used as in Mandal et al.[25] The size of the SAv-PLGA particles was determined to be 1.8 μm using Transmission Electron Microscopy (TEM; JEOL TEM 1010) and Differential Interference Contrast (DIC) microscopy (FluoView FV1000, Olympus).

As described in chapter 2 and reference 25, the particle concentration was determined using a Bürker chamber and the number of bound antibodies was optimized using fluorescently-labeled antibodies. The amount of bound αCD3 per αCD3-PLGA particle was optimized in the same way as for the polymer using biotinylated and AlexaFluor488-labeled αCD3 antibodies ([488]αCD3). Subsequently, αCD28 antibodies labeled with ATTO647-NHS (ATTO-TEC; [647]αCD28) were used to optimize the amount of αCD28 antibodies. Following the same method as described for the polymer, [647]αCD28 antibodies were incubated with [488]αCD3-PLGA in different ratios to obtain [488]αCD3/[647]αCD28-PLGA. A 1:1 molar ratio of [488]αCD3/[647]αCD28 on the PLGA particles was obtained when a 10:1 excess of [647]αCD28 over bound [488]αCD3 was used for the incubation step. Again assuming that the fluorescence labeling does not affect antibody binding to SAv-PLGA, the exactly same conditions were subsequently used to obtain non-fluorescent αCD3/αCD28-PLGA particles for the T cell activation experiments.

T cell activation studies

Peripheral Blood Lymphocytes (PBLs) were obtained from buffy coats of healthy individuals in accordance to institutional guidelines. Peripheral blood mononuclear cells were obtained by Ficoll density centrifugation and monocytes were removed by plastic adherence. The non-adherent PBLs were maintained at 37°C in RPMI-1640 medium containing 10 (v/v) % FBS, 1% (w/v) glutamine and 1× AA. PBLs (10^5 cells/well) were seeded in 96 well plates and treated with sDCs or soluble antibodies at different concentrations (0.5, 1, 5, 10, 50 and 100 ng ml^{-1}) for 16 h at 37˚C and 5% CO_2. The treatment variables were αCD3/αCD28-sDC, αCD3-sDC + αCD28-sDC (1:1 molar ratio), αCD3-sDC, αCD3 + αCD28 (1:1 molar ratio) and αCD3 along with an untreated control. If αCD3 was used in the respective samples, the concentration refers to the amount of αCD3 bound to the sDCs or in soluble form. If αCD28 was present in the sample in addition, the overall antibody concentration was twice as high as when αCD3 was used alone. If no αCD3 was used, the antibody concentration refers to the amount of αCD28. Following treatment, the cells and the respective supernatants were analyzed further using either flow cytometry (CD69 expression, immunophenotyping and functional analysis), ELISA (IFNγ) or T cell proliferation tests (CFSE assay).

T cell activation assays

Flow cytometry

Flow cytometric analysis was performed using a CyAn™ ADP Analyzer FACS instrument (Beckman Coulter). The treated PBLs were washed twice with PBS + 1% (w/v) BSA (PBA) to remove unbound sDCs or antibodies. For the characterization of CD69 expression in the complete T cell population and the CD4$^+$ and CD8$^+$ subpopulations the following procedure was used. The treated PBLs were stained with antibodies specific for the CD4$^+$ and CD8$^+$ T cell subpopulations (anti-CD4-FITC and anti-CD8-APC, BD Pharmingen). In addition, an anti-CD69-PE antibody (eBioSciences) was added to test for CD69 as an early T cell activation marker. After 1 hour of incubation with the antibodies, the cells were washed twice with PBA before FACS analysis. The data was further analyzed using FlowJo Software (TreeStar Inc.). The gating strategy to identify the population of CD69$^+$ T cells is shown in Supplementary Figure A4.1.2.

For the immunophenotyping analysis CD8$^+$ T cells and CD4$^+$ T cells were first sorted from the overall cell population by positive selection using anti-CD4- or anti-CD8-conjugated magnetic microbeads (Miltenyi Biotec). Before sorting, the corresponding CD4$^+$ and CD8$^+$ T cell populations were visualized by FACS (Supplementary Figure A4.1.3a–b and Supplementary Figure A4.1.4a–b). The sorted CD8$^+$ T cell and CD4$^+$ T cell subpopulations were then activated as described above for 4 days. To evaluate the phenotype of the activated CD8$^+$ T cells and CD4$^+$ T cells after treatment, the cells were stained with the specific markers as listed in table 4.1. The corresponding gating strategies are shown in the Supplementary Figs. A4.1.3 and A4.1.4. To determine the Treg population among the activated (CD69$^+$) T cells, the expression level of the intracellular marker FoxP3$^+$ was analyzed (Supplementary Figure A4.1.5). For characterizing the population of activated CD8$^+$ T cells having cytotoxic function the following markers were used: granzyme B as cytolytic effector marker and CD107a as degranulation marker (Supplementary Figures. A4.1.6 and A4.1.7).

Table 4.1. List of antibodies used for FACS analysis

phenotype	marker	antibody	company
early T cell activation	CD69	PerCP anti-CD69	eBiosciences
Late T cell activation	IFN (intracellular)	PE anti-IFN	eBiosciences
CD8 subpopulation*	CD8	FITC anti-CD8	BD Pharmingen
CD4 subpopulation*	CD4	FITC anti-CD4	BD Pharmingen
effector and effector memory	CCR7 CD45RA	PerCP anti-CCR7 APC anti-CD45RA	BD Pharmingen eBiosciences
memory	CD62L CD45RA CD45RO	PECy7 anti-CD62L PECy5 anti-CD45RA APC anti-CD45RO	eBiosciences BD Pharmigen eBiosciences
cytotoxic T cells (CTLs)	granzyme B	PE anti-granzyme B	eBiosciences
degranulated CTLs	intracellular CD107a	PE anti-CD107a	
regulatory T cells	FoxP3	PE anti-FoxP3	

* MACS sorted subpopulation

ELISA (IFNγ detection)

IFNγ secretion was analyzed using a sandwich ELISA. 96-well microplates (Nunc Immunomodules) were coated at 4 °C with a mouse anti-human IFNγ antibody (Pierce). After overnight incubation, the plates were washed with PBS + 0.05 % (v/v) Tween 20 and blocked with PBA. In the next step, the plates were incubated with the supernatants (obtained from the complete PBL population or the CD4$^+$ and CD8$^+$ subpopulations, as mentioned in the flow cytometry section) as well as the respective standards (IFNγ, Pierce). After 1 hour of incubation at room temperature, the plates were washed 3x with PBA. The concentration of captured IFNγ was detected after adding a biotinylated mouse anti-human IFNγ antibody (Pierce) and a horseradish peroxidase streptavidin conjugate (Molecular Probes). The color reaction was developed using 3,3',5,5'-Tetramethylbenzidine (TMB microwell peroxidase substrate, Lucron). The absorbance of the colored solution was measured at 450 nm and corrected for adsorption at 540 nm in an iMark Microplate Reader (Bio-Rad).

T cell proliferation (CFSE assay)

T cell proliferation induced by sDC treatment was assessed using the CFSE assay. PBLs (10^5) were pre-labeled with 5 μM carboxyfluorescein diacetate succinimidyl ester (CFSE; Life Technologies). After quenching free CFSE with fetal bovine serum (FBS), the CFSE-labeled cells were washed twice with PBA. The PBLs (10^5 cells/well) were then treated with αCD3, αCD3-sDC and αCD3/αCD28-sDC at an αCD3 concentration of 5 ng ml^{-1}. In addition, PBLs were incubated with an equimolar mixture of αCD3 and αCD28 as well as with αCD3/αCD28-PLGA particles, again using an αCD3 concentration of

5 ng ml^{-1}. Untreated cells were taken as control. At 0, 24, and 96 h after start of the experiment, the respective samples were incubated with a mouse anti-human CD4/8 mAb (APC labeled; BD Biosciences; T cell marker) as well as with propidium iodide (PI). The PI was used to assess the cell viability through the dye exclusion method. Live cells have intact membranes that exclude a variety of dyes that easily penetrate the damaged, permeable membranes of non-viable cells. T cell proliferation was measured using flow cytometry following the evolution of the CFSE signal. The data was analyzed using FlowJo version 9.2 software (TreeStar Inc.). Following gating for viable T cells (see Figure A4.1.8) for the gating strategy and the raw data), the generation gate width was set automatically by the program.

Statistical analysis

The results represent the mean ± standard error of the mean (SEM) of at least three independent experiments performed with different donors. Samples from each donor were measured in duplicate or triplicate as indicated. Because two categorical variables were used, two-way ANOVA tests were used for data analysis. Bonferroni post-tests were performed to compare the replicate mean by column using GraphPad Prism 5 software. The statistical significance level was defined as $p < 0.05$. The asterisks '*', '**', '***' represent p values < 0.05, < 0.01 and < 0.001.

4.5 Appendix 4.1: Supplementary figures
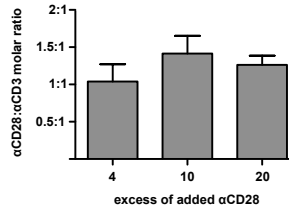
Figure A4.1.1. Number of αCD28 molecules bound per molecule of αCD3 on the polymer. The x-axis represents the excess of αCD28 added to the αCD3-sDC solution (relative to the concentration of αCD3). The y-axis shows the molar ratio of actually bound [565]αCD28:[488]αCD3 on the [488]αCD3/[565]αCD28-sDC polymer after purification. The data represents the mean ± SEM of 4 independent experiments.
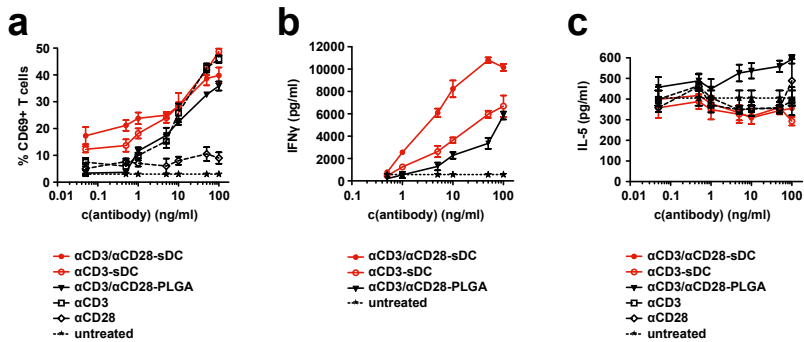
Figure A4.1.2. Expression of the early activation marker CD69. The flow cytometry plots show the relative number of cells in the respective populations (mean; %). a) Gating for live T cells, b) collective gating for CD4^{+} and CD8^{+} T cells and c) gating for CD69^{+} T cells. Isotype controls were used for setting the negative or positive gate.
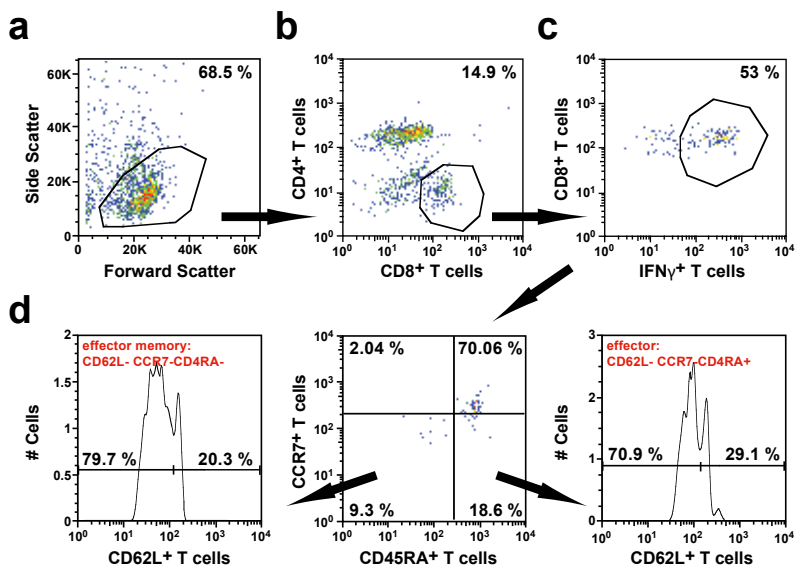
Figure A4.1.3. Immunophenotype determination of CD8^{+} T cells. Shown are the flow cytometry plots of activated (intracellular IFNγ^{+}) CD8^{+} T cell indicating the relative number of cells in the respective populations (mean; %). a) Gating for live T cells and b) gating for CD8^{+} T cells. The CD8^{+} T cell population was sorted before gating for intracellular IFNγ^{+} CD8^{+} T cells c). In the IFNγ^{+} CD8^{+} T cell population the relative number of effector cells (CD62L^{−} CCR7^{−} CD45RA^{−}; left) and effector memory cells (CD62L^{−} CCR7^{−} CD45RA^{+}; right) was determined d). Isotype controls were used for setting the negative or positive gate.
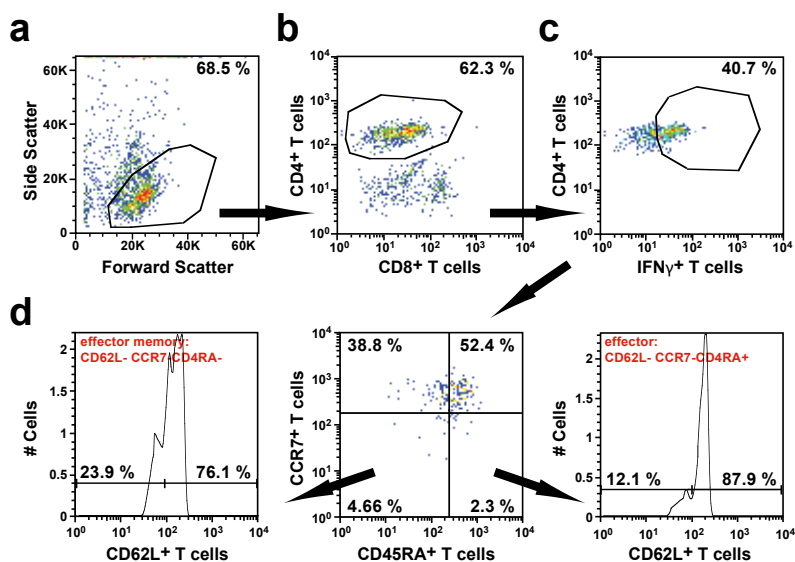
Figure A4.1.4. Immunophenotype determination of CD4$^+$ T cells. Shown are the flow cytometry plots of activated (intracellular IFNγ$^+$) CD4$^+$ T cells indicating the relative number of cells in the respective populations (mean; %). a) Gating for live T cells and b) gating for CD4$^+$ T cells. The CD4$^+$ T cell population was sorted before gating for intracellular IFNγ$^+$ CD4$^+$ T cells c). In the IFNγ$^+$ CD4$^+$ T cell population the relative number of effector cells (CD62L$^-$ CCR7$^-$ CD45RA$^-$; left) and effector memory cells (CD62L$^-$ CCR7$^-$ CD45RA$^+$; right) was determined d). Isotype controls were used for setting the negative or positive gate.
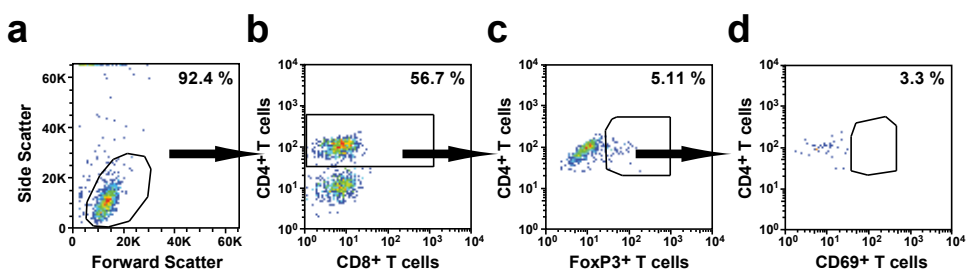

Figure A4.1.5. Identification of regulatory T cells (Tregs). The flow cytometry plots show the relative number of cells in the respective populations (mean; %) used to identify the population of activated (CD69$^+$) CD4$^+$ Tregs. a) Gating for live T cells, b) gating for CD4$^+$ T cells, c) gating for FoxP3$^+$ CD4$^+$ T cells. d) selected population of active Tregs (CD69$^+$ FoxP3$^+$ CD4$^+$). Isotype controls were used for setting the negative or positive gate.
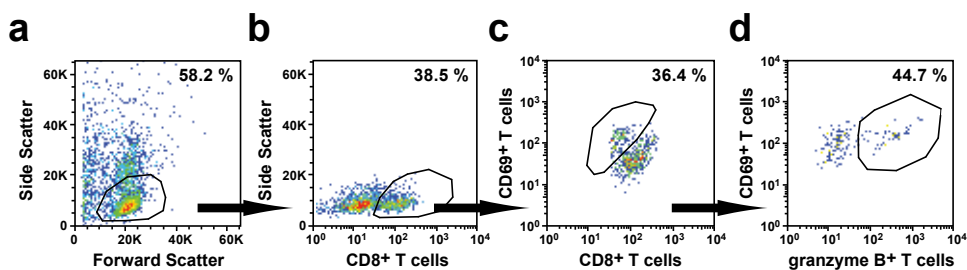
Figure A4.1.6. Flow cytometry plots used to identify the population of granzyme B expressing T cells among the population of activated (CD69$^+$) CD8$^+$ T cells. The dot plots show the gating strategy as well as the relative number of cells in the respective populations (mean; %). a) gating for live T cells, b) gating for CD8$^+$ T cells, c) gating for CD69$^+$ CD8$^+$. (d) Population of intracellular granzyme B positive T cells (granzyme B$^+$ CD69$^+$ CD4$^+$). Isotype controls were used for setting the negative or positive gate.
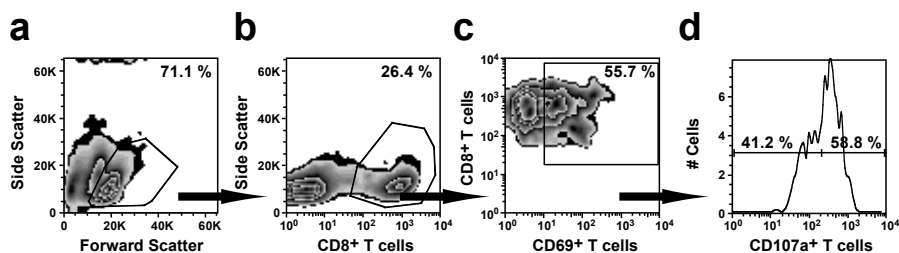
Figure A4.1.7. Flow cytometry plots used to identify the population of T cells expressing the degranulation marker CD107a among the population of activated (CD69$^+$) CD8$^+$ T cells. The dot plots show the gating strategy as well as the relative number of cells in the respective populations (mean; %). a) Gating for live T cells, b) gating for CD8$^+$ T cells, c) gating for CD69$^+$ CD8$^+$. (d) Population of CD107a positive T cells (CD107a$^+$ CD69$^+$ CD8$^+$). Isotype controls were used for setting the negative or positive gate.
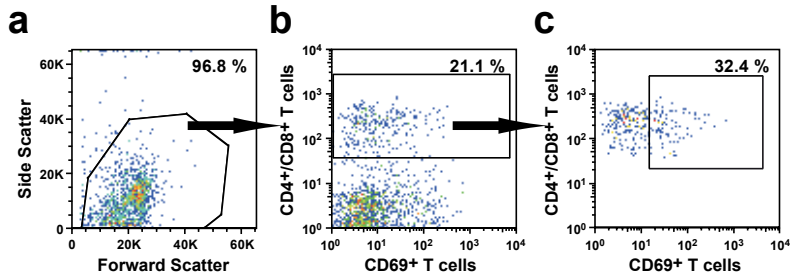
Figure A4.1.8. FACS raw data of the CFSE assay (T cell proliferation). a) Gating for T cells. b) Gating for viable CD4$^+$ and CD8$^+$ T cells. Dead T cells were identified by staining with PI. c) CFSE staining profile of the CFSE$^+$ T cell population at the start of the experiment (day 0). (d) CFSE staining profile of the CFSE$^+$ T cell population measured after 1 and 4 days of treatment. The decrease in the CFSE staining intensity relative to the starting population indicates cell division. The brackets from right to left represent the number of generations from 0 to 7. The values above the brackets show the relative number of T cells belonging to each specific generation.

4.6 Appendix 4.2: Binding efficiency analysis of sDCs (confocal microscopy)

The fluorescently labeled sDCs have not only been used for optimizing the number of αCD3 and αCD28 bound to the polymer. Further, [488]αCD3/[565]αCD28-sDC was used for confocal imaging, to determine the binding efficiency of sDCs to T cells. For confocal analysis, peripheral blood lymphocytes (PBLs; 10^6 cells/well) were treated overnight with different concentrations (5, 10, 50, 100 ng ml^{-1}) of [488]αCD3/[565]αCD28-sDC, [488]αCD3-sDC, [488]αCD3 and [565]αCD28. Moreover, to determine the effect of having signal-1 ([488]αCD3) and signal-2 ([565]αCD28) on the same polymer backbone, the above experiment was also performed with an equimolar mixture of [488]αCD3-sDC and [565]αCD28-sDC at a concentration of 50 ng ml^{-1}. After incubation, the treated T cells were washed twice with PBS + 1 % (w/v) BSA (Sigma Aldrich; PBA). The washed T cells were fixed in 4 % formaldehyde for 10 min at room temperature and quenched in 0.1 M glycine solution for 20 min. These fixed cells were mounted onto microscope slides (Thermo Fisher Scientific) using MOWIOL (Calbiochem). They were analyzed under a confocal laser scanning microscope (CLSM, Olympus FV1000) using a 63× oil immersion objective. ImageJ software version 1.43 was used for image processing.[36]

After 10 min of incubation, binding of [488]αCD3/[565]αCD28-sDC (at a concentration of 50 ng ml^{-1}) is observed on the T cells (Figure A4.2.1a). After overnight incubation (16 h) the fluorescence from both antibodies is concentrated at one area on the T cell surface suggesting formation of the immunological synapse (IS) (Figure A4.2.1b). A more detailed analysis of the confocal images obtained from the concentration series described above (Figure A4.2.1c) provides information about the binding efficiency of the [488]αCD3/[565]αCD28-sDCs and the respective controls.

In the high concentration range (>50 ng ml^{-1}), the relative number of T cells that showed AlexaFluor488 fluorescence (in samples where the αCD3 was present) or ATTO565 fluorescence (αCD28 only) was similar for all treatment conditions indicating that all available binding sites were occupied by the sDC or the soluble antibody. In the low concentration range, however, both [488]αCD3/[565]αCD28-sDC and [488]αCD3-sDC showed superior binding compared to the soluble αCD3 or αCD28 antibodies. The higher binding efficiency is a strong indication that the ability to form multivalent interactions increases the avidity of the sDCs. Interestingly, no difference in the binding efficiency is observed for the sDCs carrying only αCD3 and the sDCs carrying both the αCD3 and the αCD28 antibodies. Obviously, the presence of the additional αCD28 antibodies does not increase the avidity of the sDC any further. This observation was confirmed when also comparing the binding of efficiency of [565]αCD28-sDC (Figure A4.2.1d). No significant difference in the number of fluorescently labeled T cells was observed for [488]αCD3-sDC, [565]αCD28-sDC and [488]αCD3/[565]αCD28-sDC when only one of these polymers was added to the T cells. When the equimolar mixture of [488]αCD3-sDC and [565]αCD28-sDC was used, however, a lower binding of [565]αCD28-sDC was observed. It is currently not clear why the binding of [565]αCD28-sDC was reduced in this experiment.
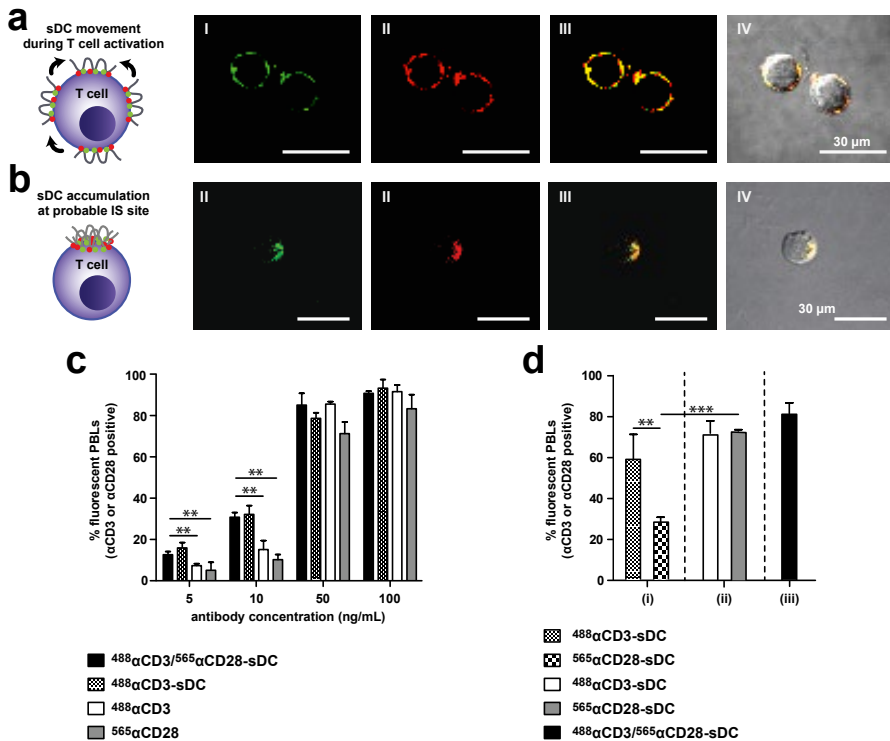
Figure A4.2.1. Confocal analysis of the binding efficiency of sDCs and free antibodies to the T cells. a) Representative confocal image of [488]αCD3/[565]αCD28-sDC bound to a single T cell taken after 10 min (early binding; microcluster formation as shown in the schematic image). b) Representative confocal image of [488]αCD3/[565]αCD28-sDC bound to a single T cell taken after 16 h (late binding; accumulation at the immunological synapse as shown in the schematic diagram). An antibody concentration of 50 ng ml^{-1} [488]αCD3 and 50 ng ml^{-1} [565]αCD28 was used for the experiment. The sequence (I) – (IV) shows the following series of images: bound [488]αCD3 (green); (II) [565]αCD28 (red); (III) merge of image I and II showing co-localization (yellow); and (IV) image III merged with a bright field image. c) Statistical analysis of the sDC ([488]αCD3/[565]αCD28-sDC) binding efficiency at different antibody concentrations. The incubation time was 16 hours. The polymer carrying both antibodies was compared with the polymer containing only αCD3 ([488]αCD3-sDC) as well as with free signal-1 ([488]αCD3) and free signal-2 ([565]αCD28). The x-axis represents the concentration of [488]αCD3 on the sDCs or free in solution. In cases where both [488]αCD3 and [565]αCD28 were present in the sample, the total antibody concentration was twice as high. For the [565]αCD28 sample the αCD28 concentration was used. d) Comparative binding analysis of sDCs. The cells were incubated with 50 ng ml^{-1} of (i) [488]αCD3-sDC and [565]αCD28-sDC (1:1 molar ratio), (ii) [488]αCD3-sDC or [565]αCD28-sDC added separately to different samples, or (iii) [488]αCD3/[565]αCD28-sDC. The cells were incubated with the sDCs for 16 h. The data represents the mean ± standard error of the mean (SEM) of 3 independent experiments with samples from different donors. The asterisks ** and *** presents the statistical significance at 'p' values < 0.01 and 0.001, respectively.

4.7 References

(1)   Paulis, L. E.; Mandal, S.; Kreutz, M.; Figdor, C. G. *Curr. Opin. Immunol.* **2013**, *25* (3), 389–395.
(2)   Banchereau, J.; Steinman, R. M. *Nature* **1998**, *392* (6673), 245–252.
(3)   Schuler, G.; Steinman, R. M. *J. Exp. Med*. **1997**, *186* (8), 1183–1187.
(4)   Janssen, E. M.; Lemmens, E. E.; Wolfe, T.; Christen, U.; von Herrath, M. G.; Schoenberger, S. P. *Nature* **2003**, *421* (6925), 852–856.
(5)   Klebanoff, C. A.; Gattinoni, L.; Torabi-Parizi, P.; Kerstann, K.; Cardones, A. R.; Finkelstein, S. E.; Palmer, D. C.; Antony, P. A.; Hwang, S. T.; Rosenberg, S. A.; Waldmann, T. A.; Restifo, N. P. *Proc. Natl. Acad. Sci. USA* **2005**, *102* (27), 9571–9576.
(6)   Barratt-Boyes, S. M.; Figdor, C. G. *Cytotherapy* **2004**, *6* (2), 105–110.
(7)   Vieweg, J.; Su, Z.; Dahm, P.; Kusmartsev, S. *Clin. Canc. Res* **2007**, *13* (2 Pt 2), 727s – 732s.
(8)   Banerjee, D. K.; Dhodapkar, M. V; Matayeva, E.; Steinman, R. M.; Dhodapkar, K. M. *Blood* **2006**, *108* (8), 2655–2661.
(9)   Dannull, J.; Su, Z.; Rizzieri, D.; Yang, B. K.; Coleman, D.; Yancey, D.; Zhang, A.; Dahm, P.; Chao, N.; Gilboa, E.; Vieweg, J. *J. Clin. Invest.* **2005**, *115* (12), 3623–3633.
(10)   Yan, L.; Teng, M. *J. Hematol.l Malig.* **2011**, *1* (1), 35–48.
(11)   Prakken, B.; Wauben, M.; Genini, D.; Samodal, R.; Barnett, J.; Mendivil, A.; Leoni, L.; Albani, S. *Nat. Me.d* **2000**, *6* (12), 1406–1410.
(12)   Thompson, J. A.; Figlin, R. A.; Sifri-Steele, C.; Berenson, R. J.; Frohlich, M. W. *Clin. Canc. Res.* **2003**, *9* (10 Pt 1), 3562–3570.
(13)   Laport, G. G.; Levine, B. L.; Stadtmauer, E. A.; Schuster, S. J.; Luger, S. M.; Grupp, S.; Bunin, N.; Strobl, F. J.; Cotte, J.; Zheng, Z.; Gregson, B.; Rivers, P.; Vonderheide, R. H.; Liebowitz, D. N.; Porter, D. L.; June, C. H. *Blood* **2003**, *102* (6), 2004–2013.
(14)   Zappasodi, R.; Di Nicola, M.; Carlo-Stella, C.; Mortarini, R.; Molla, A.; Vegetti, C.; Albani, S.; Anichini, A.; Gianni, A. M. *Haematologica* **2008**, *93* (10), 1523–1534.
(15)   Bakdash, G.; Sittig, S. P.; van Dijk, T.; Figdor, C. G.; de Vries, I. J. *Front. Immunol.* **2013**, *4*, 53.
(16)   Varma, R.; Campi, G.; Yokosuka, T.; Saito, T.; Dustin, M. L. *Immunity* **2006**, *25* (1), 117–127.
(17)   Yokosuka, T.; Kobayashi, W.; Sakata-Sogawa, K.; Takamatsu, M.; Hashimoto-Tane, A.; Dustin, M. L.; Tokunaga, M.; Saito, T. *Immunity* **2008**, *29* (4), 589–601.
(18)   Viola, A.; Lanzavecchia, A. *Science* **1996**, *273* (5271), 104–106.
(19)   Acuto, O.; Michel, F. *Nat Rev Immunol* **2003**, *3* (12), 939–951.
(20)   Harding, F. A.; McArthur, J. G.; Gross, J. A.; Raulet, D. H.; Allison, J. P. *Nature* **1992**, *356* (6370), 607–609.
(21)   Kalinski, P.; Hilkens, C. M.; Wierenga, E. A.; Kapsenberg, M. L. *Immunol. Today* **1999**, *20* (12), 561–567.
(22)   Grakoui, A.; Bromley, S. K.; Sumen, C.; Davis, M. M.; Shaw, A. S.; Allen, P. M.; Dustin, M. L. *Science* **1999**, *285* (5425), 221–227.
(23)   Cemerski, S.; Das, J.; Giurisato, E.; Markiewicz, M. A.; Allen, P. M.; Chakraborty, A. K.; Shaw, A. S. *Immunity* **2008**, *29* (3), 414–422.
(24)   Shuvaev, V. V; Ilies, M. A.; Simone, E.; Zaitsev, S.; Kim, Y.; Cai, S.; Mahmud, A.; Dziubla, T.; Muro, S.; Discher, D. E.; Muzykantov, V. R. *ACS Nano* **2011**, *5* (9), 6991–6999.
(25)   Mandal, S.; Eksteen-Akeroyd, Z. H.; Jacobs, M. J.; Hammink, R.; Koepf, M.; Lambeck, A. J. a.; van Hest, J. C. M.; Wilson, C. J.; Blank, K.; Figdor, C. G.; Rowan, A. E. *Chem. Sci.* **2013**, *4* (11), 4168–4174.
(26)   Tsoukas, C. D.; Landgraf, B.; Bentin, J.; Valentine, M.; Lotz, M.; Vaughan, J. H.; Carson, D. A. *J. Immunol.* **1985**, *135* (3), 1719–1723.
(27)   Kouwer, P. H. J.; Koepf, M.; Le Sage, V. A. A.; Jaspers, M.; van Buul, A. M.; Eksteen-Akeroyd, Z. H.; Woltinge, T.; Schwartz, E.; Kitto, H. J.; Hoogenboom, R.; Picken, S. J.; Nolte, R. J. M.; Mendes, E.; Rowan, A. E. *Nature* **2013**, *493* (7434), 651–655.
(28)   Cornelissen, J. J.; Donners, J. J.; de Gelder, R.; Graswinckel, W. S.; Metselaar, G. A.; Rowan, A. E.; Sommerdijk, N. A.; Nolte, R. J. *Science* **2001**, *293* (5530), 676–680.
(29)   Dommerholt, J.; Schmidt, S.; Temming, R.; Hendriks, L. J. A.; Rutjes, F. P. J. T.; van Hest, J. C. M.; Lefeber, D. J.; Friedl, P.; van Delft, F. L. *Angew. Chem., Int. Ed.* **2010**, *49* (49), 9422–9425.
(30)   Broere, F.; Apasov, S. G.; Sitkovsky, M. V; van Eden, W. In *Principles of Immunopharmacology*; Nijkamp, F. P., Parnham, M. J., Eds.; Springer: Basel, **2011** 15–27.
(31)   Betts, M. R.; Nason, M. C.; West, S. M.; De Rosa, S. C.; Migueles, S. A.; Abraham, J.; Lederman, M. M.; Benito, J. M.; Goepfert, P. A.; Connors, M.; Roederer, M.; Koup, R. A. *Blood* **2006**, *107* (12), 4781–4789.

(32)   Ma, C.; Cheung, A. F.; Chodon, T.; Koya, R. C.; Wu, Z.; Ng, C.; Avramis, E.; Cochran, A. J.; Witte, O. N.; Baltimore, D.; Chmielowski, B.; Economou, J. S.; Comin-Anduix, B.; Ribas, A.; Heath, J. R. *Cancer Discov.* **2013**, *3* (4), 418–429.

(33)   Peters, P. J.; Borst, J.; Oorschot, V.; Fukuda, M.; Krahenbuhl, O.; Tschopp, J.; Slot, J. W.; Geuze, H. J. *J. Exp. Med.* **1991**, *173* (5), 1099–1109.

(34)   Fasting, C.; Schalley, C. A.; Weber, M.; Seitz, O.; Hecht, S.; Koksch, B.; Dernedde, J.; Graf, C.; Knapp, E. W.; Haag, R. *Angew Chem., Int. Ed.* **2012**, *51* (42), 10472–10498.

(35)   Koepf, M.; Kitto, H. J.; Schwartz, E.; Kouwer, P. H. J.; Nolte, R. J. M.; Rowan, A. E. *Eur. Polym. J.* **2013**, *49* (6), 1510–1522.

(36)   Schneider, C. A.; Rasband, W. S.; Eliceiri, K. W. *Nat. Meth.* **2012**, *9* (7), 671–675.

(37)   Cruza, L. J.; Tacken, P. J.; Fokkink, R.; Joosten, B.; Stuart, M. C.; Albericio, F.; Torensma, R.; G., F. C. *J. Control. Release* **2010**, *144* (2), 118–126.

5

Stress-stiffening-mediated stem-cell commitment switch in soft responsive hydrogels
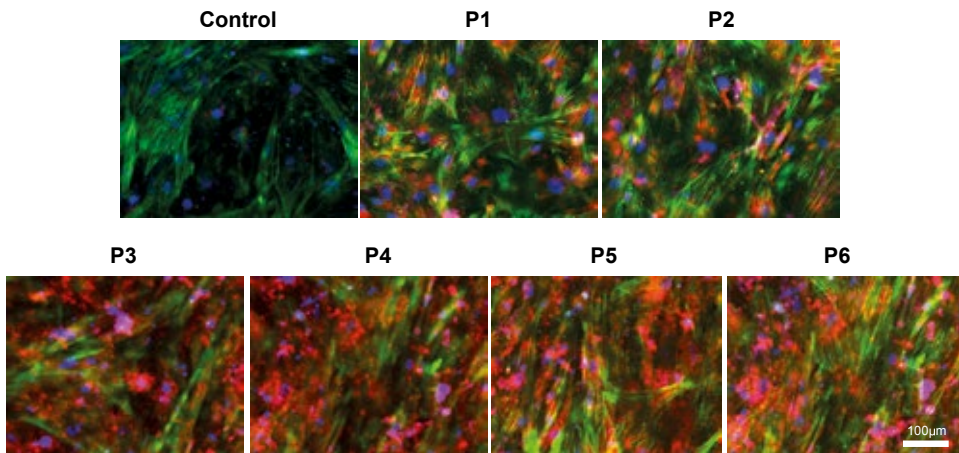
Chapter 5: Stress-stiffening-mediated stem-cell commitment switch in soft responsive hydrogels

5.1 Introduction

Cellular interactions with the extracellular matrix (ECM) mediate important cell functions such as survival, proliferation, migration and differentiation.[1–5] The extracellular stimuli include soluble and adhesive ligands that provide chemical and mechanical cues which have been shown to govern cell physiology[1]. It has recently been demonstrated that physical cues from the matrix, especially the matrix stiffness and topography, can initiate intracellular biochemical signals through mechanotransduction and thus dictate the cell differentiation pathways.[6–8] Understanding the role of these microenvironmental physical cues has profound implications for realizing the full therapeutic potential of stem cell research in tissue engineering applications.[9–17]

Three classical cell culture systems have been widely utilized to underpin the effect of the ECM properties on stem cell fate. Firstly, natural ECM-protein derived hydrogels prepared at different densities have been shown to significantly influence cell adhesion, cell shape and various cell functions.[18] However, changing the density of these proteins does not only change the gel stiffness, but also alters the surface ligand concentration. Thus, in this type of culture system, it is difficult to de-couple and interpret the effect of the matrix stiffness and ligand density on cellular response. The second class of culture system employs synthetic polymer gels as ECM mimetic scaffolds for stem cell fate control.[17,19,20] In this case, the gel stiffness can be modulated by altering the amount of a cross-linker, however, the porosity and the polymer surface chemistry also change as a function of the cross-linker amount.[21,22] The stem cells are therefore likely interpreting the combined effect of these parameters for their fate control, although it has recently been suggested that substrate porosity in 2D cell culture conditions does not affect stem cell fate.[8] A third class of culture system is based on elastomeric micropost arrays, where different post heights are interpreted as different rigidities by the cells.[16] This system provides an approach to de-couple the effect of the substrate stiffness from alterations in the surface chemical properties. The micropost diameter dictates a limiting size of the focal adhesions, however, and restricts focal contact maturation. The 2D nature of the micropost culture system further fails to mimic 3D physiological conditions.

In this chapter, a new class of cell culture systems is introduced based on fully synthetic biomimetic physically cross-linked soft (~0.2-0.4 kPa) hydrogels derived from helical oligo ethylene glycol polyisocyanopeptides (PIC).[23] The application of this novel 3D matrix for studying stem cell function is demonstrated. These soft

thermo-responsive hydrogels are formed at extremely low polymer concentrations (99.95% water) and possess pore sizes of nanometer dimension (~100-150 nm).[24] Their mechanical properties are similar to those of biopolymer hydrogels assembled from microtubules, F-actin, fibrin, and collagen. These hydrogels exhibit a non-linear stress response beyond a critical stress σ_C (stress-stiffening).[24] When the stress is increased beyond this value, the matrices become stiffer with increasing applied stress.

Janmey *et al.* demonstrated that different types of cells, for example, fibroblasts and human mesenchymal stem cells (hMSCs), adopt a stretched morphology when cultured on soft fibrin gels (2D substrates). This is a clear indication that the cells deform these gels and gain access to the high strain moduli in the stress-stiffening regime.[25] It is important to note that the onset of stiffening for the ECM proteins occurs at extremely small values of the applied stresses. The PIC hydrogels introduced here show stress-stiffening in the biologically relevant stress regime, as demonstrated in Figure 5.1. PIC hydrogels are therefore the first fully synthetic system that allows for investigating how stress-stiffening influences 3D stem cell differentiation as part of the mechanisms underlying the physiology of adult stem cell niches.

It is shown in this chapter that hMSCs encapsulated in these biomimetic gels (functionalized with cell-adhesive GRGDS peptides) prefer osteogenesis over adipogenesis. This differentiation can be induced in an extremely soft microenvironment simply by increasing the polymer length. Different polymer lengths only affect σ_C without altering the bulk gel stiffness and ligand density of the matrix. This fully synthetic culture system therefore presents a model to study the effect of this physiologically important parameter (stress-stiffening) on cells encapsulated in a 3D microenvironment. It is further shown that the cellular sensing of stress-stiffening affects the microtubule-associated protein DCAMKL1 in the mechanotransduction pathway, suggesting a role of microtubule dynamics in hMSCs fate control.

5.2 Results

5.2.1 Synthesis and characterization of polymers.

To construct a 3D cell culture matrix for studying the effect of stress-stiffening on stem cell fate, PIC hydrogels were chosen. This choice was motivated by the fact that they demonstrate stress-stiffening behavior[24] in the biologically relevant stress regime (*vide supra*, Figure 5.1), unlike other synthetic materials. At the same time they allow for deconstituting some of the key parameters of generally complex

biological systems (lack of simultaneous control on ligand density and stiffness, enzyme degradability, etc.).
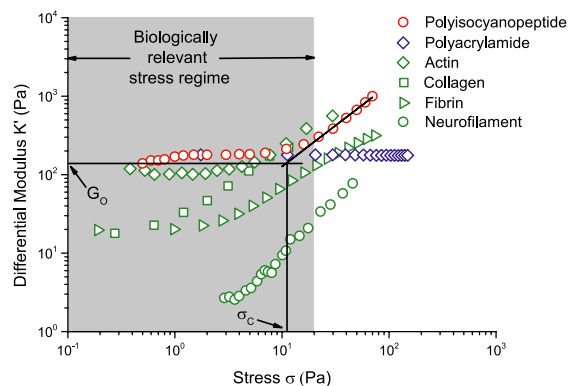
Figure 5.1. Differential modulus K' as a function of stress σ for intracellular and extracellular filamentous biopolymer gels that show stress-stiffening. For comparison, the rheology data for a representative synthetic gel (polyacrylamide) and the biomimetic stress-stiffening polyisocyanopeptide hydrogel are included. G_o indicates the equilibrium bulk stiffness and $σ_C$ denotes the critical stress for the onset of stress-stiffening of the polymer gel.

These synthetic polymers were functionalized with the basic cell adhesive peptide GRGDS in order to promote stem cell adhesion to the matrix. This short peptide ligand can be homogeneously distributed and allows for a direct sensing of the substrate mechanical properties since there is a single anchoring point per ligand. This is a major advantage of the PIC system compared to previously developed substrates (e.g. collagen[26]) and facilitates an unambiguous interpretation of the effect of stress-stiffening. The peptide ligand has been grafted to the polymer via a short spacer, which is 24 atoms long and equivalent to a short PEG chain of approximately 8 units. This spacer was optimized according to molecular modeling so as not to play a role in cell-substrate interactions. However, the length of the peptide tether was not varied to investigate its influence on the cell-substrate interaction, although it may play a role.[27]

Polyisocyanopeptides (**P1'-P6'**) were synthesized by a nickel(II)-catalyzed co-polymerization of triethylene glycol functionalized isocyano-(D)-alanyl-(L)-alanine monomer **1** and the azide-appended monomer **2** (Figure 5.2a), with the molar ratio of **1/2** = 100. This ratio should yield polymers with statistically one azide-functionality every 11.5 nm of the polymer chain.

Table 5.1. Characterization of the synthesized polymers and the gels in alpha-MEM.

Catalyst/monomer	Viscosity derived molecular weight (N_3-polymer; kg /mol)	Average spacing of $-N_3$ on the polymer chain (nm)	Mean (GRGDS functionalized) polymer length from AFM (nm)	Mean Critical Stress (σ_c, Pa) in alpha-MEM gels at 2mg/mL concentration
1/1000	307	14	182	9.4
1/2500	426	14	226	9.9
1/3000	491	18	250	12.8
1/4000	571	15.6	309	14.6
1/6000	591	14	367	16.6
1/8000	685	17	434	19.3

The catalyst to monomer molar ratio was varied from 1:1000 to 1:8000 to obtain polymers of increasing molecular weight (**P1'-P6'**; determined by viscosity measurements, Table 5.1). These azide-functionalized polymers were then subjected to a strain-promoted azide-alkyne cycloaddition (SPAAC) reaction with BCN-GRGDS (BCN: Bicyclo[6.1.0]non-4-yn-9-ylmethyl) to obtain cell adhesive GRGDS functionalized polymers **P1-P6** (Figure 5.2b-c and Experimental Section). of increasing chain lengths. The resulting polymers were characterized with atomic force microscopy (AFM) to determine the polymer length (Table 5.1; Figure A5.1.1 and A5.1.2**)**. To determine the concentration of azide groups, a rhodamine dye-functionalized with a strained alkyne was reacted with the azides on the polymer (Table 5.1 and Experimental section). This control experiment revealed a spacing of 14-18 nm for the azide groups on the polymer, which is close to the predicted value of 11.5 nm.

After dissolving these polymers in alpha-MEM (Minimum Essential Medium) at a fixed concentration of 2 mg/mL they formed transparent gels upon warming (above ~15 °C; determined by temperature sweep rheology; Figure 5.2d). The mechanical properties of the GRGDS-functionalized polymer gels were further investigated in more detail using rheological analysis. Temperature sweep experiments (heating up to 37 °C) followed by a time sweep at 37 °C revealed that all the gels **P1-P6** were soft and exhibited a similar stiffnesses (0.2-0.4 kPa at 37 °C; Figure 5.2e). It has already been shown that hydrogels of non-functionalized PIC polymers show a biomimetic stress-stiffening behavior.[24] Using the same pre-stress protocol[28], the critical stresses (σ_C) of **P1-P6** hydrogels were measured (Figure A5.1.3). The critical stress (σ_C), describing the non-linear behavior of these gels, was found to increase linearly as a function of the polymer chain length (Figure 5.2f and Table 5.1).[29] The

σ_C values range from ~9 Pa in the **P1** gel (average polymer length = 182 nm) to ~19 Pa in the **P6** gel (average polymer length = 434 nm). Although there seems to be a 1.5-fold increase in the mean gel stiffness upon increasing the mean polymer length from ~180 nm to ~240 nm (Figure 5.2e), this difference is small in the context of cellular perception of bulk stiffness.[17] Regarding the σ_C values, a linear relationship is observed between this parameter and the mean polymer length (Figure 5.2f). As the error range for σ_C is smaller, this increase is considered to be significant.
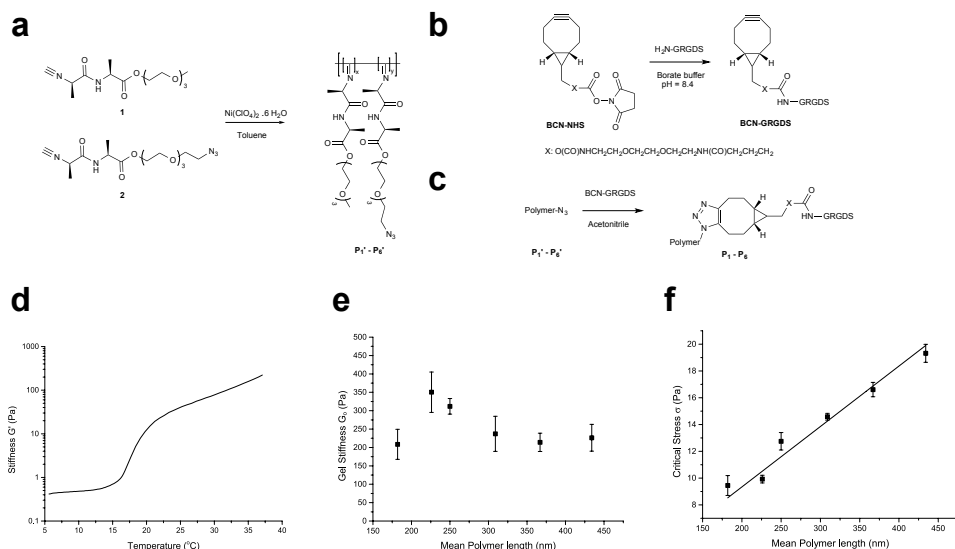
Figure 5.2. Synthesis of polymers of different chain length and characterization of polymer hydrogels. a) Co-polymerization of the non-functionalized monomer **1** and the azide-functionalized monomer **2** at different catalyst to monomer molar ratios yields polymers of different chain lengths (**P1'-P6'**). b) and c) Functionalization of the azide-functionalized polymers **P1'-P6'** with the GRGDS-peptide. d) Representative temperature sweep rheology experiment of a PIC hydrogel. The onset of gelation was observed to occur at ~15 °C. e) The storage modulus (G_o) at 37 °C appears to be independent of polymer length (0.2-0.4 kPa), considering the error in this experiment. f) The critical stress σ_C varies linearly as a function of polymer length. The error bars represent standard errors of the mean (n = 3).

5.2.2 Stress-stiffening-mediated hMSC differentiation

To investigate the effect of stress-stiffening on stem cell fate, hMSCs were mixed with a cold polymer solution (~10 °C) in alpha-MEM. The mixture was then warmed to 37 °C to form the 3D matrix with encapsulated hMSCs. The polymer solution forms a gel immediately after incubation at 37 °C as revealed by kinetic rheology experiments (Figure A5.1.4). Afterwards, the gel becomes stiffer with time and attains the final stiffness in 2-3 minutes. This strategy ensures that the cells are supported in 3D and prevents settling of the cells at the bottom. The cells were

homogeneously distributed throughout the gel as indicated by confocal microscopy (Figure A5.1.5). Investigation of hMSCs morphology after 36 h in culture revealed that the cells remained spherical in all of the gels (**P1-P6**; Figure 5.3a). The cells exhibited only limited cortical F-actin protrusions into the surrounding microenvironment (Phalloidin staining, Figure A5.1.6**)** and showed no significant modifications in their nuclear morphology, as shown by a representative DAPI fluorescence image of the cell nucleus after 36 h of culture (Figure 5.3b). These observations are consistent with recent reports of hMSCs in 3D cell cultures.[19,30] Live/dead assays (calcein-AM and MTT) performed after 36 h of culture in growth media indicated excellent viability (>95%) of the encapsulated cells in all the gels and the non-functionalized control gel (Figure 5.3c and d and Figure A5.1.7), as also confirmed by confocal microscopy (Figure A5.1.5). In addition, no significant cell proliferation was detected for the various gels as determined using the PicoGreen assay (Figure A5.1.8).

The lineage commitment of the gel-encapsulated hMSCs after 96 h of culture was investigated in bipotential differentiation medium (1:1 v/v osteogenic and adipogenic media). The cells were first stained (immunofluorescence) for STRO-1, a mesenchymal stem cell specific marker.[31] A significant decrease in the average STRO-1 expression was observed for the cells in all of the gels after 96 h of culture, indicating the onset of stem cell differentiation (Figure 5.3e). The expression of osteogenic and adipogenic differentiation markers was then examined. For cells cultured in the gel with the lowest critical stress (σ_C ~9.4 Pa, constructed from the shortest polymer **P1**) predominantly adipogenic commitment was observed (Oil-red O staining, Figure 5.3f; and Figure A5.1.9). With increasing σ_C (i.e. increasing the polymer length), osteogenesis was progressively favored over adipogenesis. This is demonstrated by immunofluorescent staining of Osterix, an osteogenic specific marker (Figure 5.3g) and is confirmed when considering the mean percentages of osteogenic and adipogenic commitments (Figure A5.1.10) in the various hydrogels (**P1-P6**). hMSCs cultured in the gel with the highest σ_C (**P6**) preferentially exhibited osteogenic commitment. This predominant osteogenesis observed for the cells grown in hydrogels made from the longer polymers (**P4-P6**) was further confirmed by differentiation tests after 3 weeks of culture (Figure A5.1.11).

Finally, hMSC osteogenic commitment was verified using RT-PCR to determine the expression of the osteogenic biomarker Core-binding factor alpha 1 (Cbfa-1), also called *RUNX2*, and the expression of the adipogenic biomarker *PPARγ*. After 96 h of culture, an increase in *RUNX2* gene expression was observed with increasing σ_C (Figure 5.3h). This result is in agreement with the

immunofluorescence staining results. Simultaneously, a decrease in gene expression of the adipogenic marker *PPARγ* is observed (Figure 5.3i).
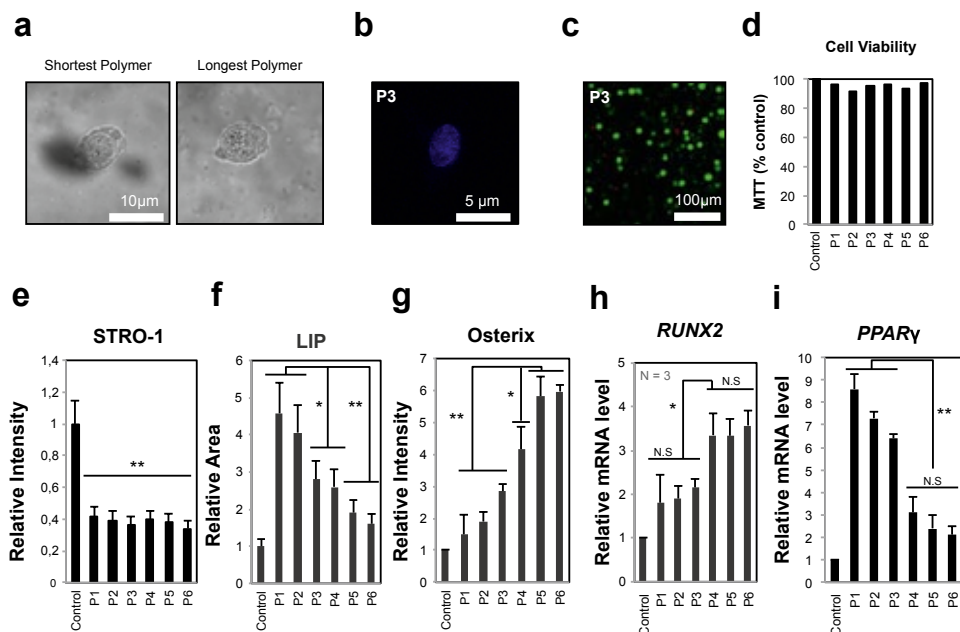

Figure 5.3. Effect of stress-stiffening on hMSC commitment. a) Representative micrographs showing cross-sections of hMSCs 36 h after encapsulation into 3D matrices made from the shortest (**P1**) and the longest polymer (**P6**) and constant GRGDS density, visualized by bright-field microscopy. b) Confocal image of fluorescence staining (DAPI) of the cell nucleus after 36 h of culture for the **P3** polymer. c) Live/dead viability test (calcein-AM) of hMSCs after 36 h of encapsulation. In the representative image, almost all cells in the matrix from polymer **P3** seem to be alive (green). Nuclei were stained with DAPI (Blue). d) Cell viability was assessed using the MTT assay in all matrices (from shortest to longest polymers). e) STRO-1 protein expression in the hMSCs is expressed as average fluorescence intensity, normalized by the number of cells. Compared to the control, STRO-1 expression decreased for all of the matrices, indicating that the hMSCs have lost their "stemness" and initiated differentiation. f) Total cellular area of immunofluorescence intensity of neutral lipid accumulation quantified for hMSCs cultured for 96 h in the various matrices. g) Total cellular Osterix protein immunofluorescence intensity was quantified for hMSCs cultured for 96 h in the various matrices. h) and i) Quantitative PCR analysis for *RUNX2* and *PPARγ,* significant differences were observed between the matrices displaying a high or low critical stress. For all the experiments, a non-functionalized soft polymer gel (cell culture in growth medium) served as the control (**$*P < 0.001$, *$*P < 0.01$).

To investigate the role of the GRGDS-ligand interaction with its receptors on the stem cell surface, cell commitment studies were performed where this interaction was blocked. Using the GRGDS-modified polymers **P1**, **P3**, **P4** and **P6,** cell culture

experiments were performed in the presence of antibodies recognizing specific integrin subunits (α1, 2, 3 and 5; β1 and 2). In the presence of these integrin-blocking antibodies, osteogenic commitment was suppressed. However, adipogenic commitment was maintained for all the polymers tested (Figure A5.1.12 and A5.1.13). This result is in agreement with the recent literature[19] and highlights the importance of the interaction between integrin receptors and the RGD ligands for mediating the stress-stiffening induced commitment switch. Interestingly, the presence of blebbistatin (a small molecule inhibitor of actomyosin contractility showing high affinity and selectivity toward myosin II) inhibited the hMSCs commitment. Stemness was mainted for all the polymer gels, as revealed by the high levels of STRO-1 in the encapsulated cells (Figure A5.1.14). This suggests that the inhibition of actomyosin contraction interferes with the mechanisms of hMSCs commitment both towards adipogenesis and osteogenesis. This is most likely due to the fact that the cells cannot apply any traction force to sense their microenvironmental (incl. its stress-stiffening properties). These results are consistent with previously published studies.[17] Finally, in order to demonstrate the direct interaction between the hMCSs and the polymer-bound GRGDS, the cell commitment studies were performed in the presence of soluble GRGDS ligands. Soluble ligands block the interaction between the cells and the matrix by competing for the integrin binding sites. Using the GRGDS-functionalized polymers **P1**, **P3**, **P4** and **P6,** no significant osteogenic or adipogenic commitment was detected. This clearly confirms that integrin disengagement from the matrix-bound RGD is interfering with the cell's ability to sense stress-stiffening (Figure A5.1.15 and A5.1.16). These data also suggest that the cells need a direct engagement with the bound RGD ligand, and not with the secreted ECM, for mediating the stress-stiffening induced commitment switch.

Although the macroscopic ligand density is kept constant in this study (one ligand every 14-18 nm of a polymer chain), the longer polymer chains (**P4**-**P6**) have an almost 2-fold higher number of ligands per chain (20-26), as compared to the corresponding shorter chains (**P1-P3**: 13-18). This could indeed impact the extent of cell-mediated local ligand clustering. To study the effect of ligand-density on the observed hMSC commitment switch, the commitment study was performed as a function of ligand density (RGD every 7 nm, 28 nm and 70 nm) for gels of the shortest (**P1**) and the longest polymer (**P6**). Varying the ligand density for both polymers, no indication was found that the ligand density interferes with the cell differentiation outcome (Figure A5.1.17). These results suggest that stress-stiffening is the primary governing variable in the system, without excluding the possibility that cell-mediated ligand clustering is occurring. The data demonstrates that hMSC fate

can be switched from adipogenesis to osteogenesis in a soft microenvironment (~0.2-0.4 kPa), simply by increasing the critical stress for the onset of stress-stiffening.

5.2.3 Role of DCAMKL1 in stem cell differentiation

Several reports have indicated that the cytoskeletal contractility as well as actin polymerization are responsible for osteogenic differentiation on 2D substrates. In this study, treatment with cytochalasin D (inhibitor of actin polymerization) resulted in an overall decreased commitment of the cultured stem cells towards both osteogenesis and adipogenesis (Figure A5.1.18a). Also this result suggests a role of actin polymerization in the stress-stiffening mediated hMSCs differentiation. At the same time, a decrease in hMSC commitment was observed after treatment with Taxol, a well-characterized microtubule-stabilizing agent known to inhibit tubulin de-polymerization (Figure A5.1.18b). Taxol treatment did not affect cell viability as indicated by a live/dead assay after 48 h and 96 h of culture (Figure A5.1.19). The effect of Taxol on the cell commitment outcome indicates that, in addition to actin, the microtubule dynamics could also be involved in the mechanotransduction pathways underlying hMSCs differentiation in the PIC matrix.

A recent report has indicated that the microtubule-associated protein DCAMKL1 represses RUNX2, an early osteogenesis marker, and thus regulates osteogenic differentiation *in vitro* and in an *in vivo* rat model.[32] DCAMKL1 is also known to enhance microtubule polymerization. Furthermore, it has been reported that microtubule de-polymerization can alter the myosin mechanochemical activity through myosin regulatory side chain phosphorylation, thus resulting in increased actomyosin contraction.[33] In this context, also the role of DCAMKL1 in the stress-stiffening mediated control of hMSC differentiation was investigated as a function of critical stress. Interestingly, Western blot analysis revealed a negligible DCAMKL1 expression for the polymer gel with the highest σ_C (**P6**) and a significant increase in the expression of this protein with decreasing σ_C (Figure 5.4a). Concomitantly, RUNX2 expression was not observed in the gels with lower σ_C (**P1-P3)** while the protein was clearly expressed in the hydrogels with higher σ_C (**P4-P6**). This result correlates with the observed osteogenic commitment in these gels. This is also in agreement with the observed overall increase in the *RUNX2* mRNA expression when comparing hydrogels assembled from the shorter (**P1-P3**) and longer (**P4-P6**) polymers (Figure 5.3h). This difference is smaller, but still significant. These observations correlate well with preferential osteogenesis in gels of higher critical stress and a lack of osteogenic commitment as the critical stress is lowered. A plot of the relative intensities (protein expression) of RUNX2 versus DCAMKL1 for all the conditions (**P1-P6**) shows a switch-like relationship between these two proteins with

the existence of a threshold value for the expression of DCAMKL1 (Figure 5.4a and Figure A5.1.20). The observation that RUNX2 antagonizes the adipogenic lineage commitment has functional relevance for mechanistic interpretations as it correlates with the observed stress-stiffening mediated commitment switch.

In order to further confirm the functional relationship between DCAMKL1 and RUNX2 in the stress-stiffening gel system, *DCAMKL1* gene silencing (through shRNA) and overexpression (via transient transfection) were performed for the hMSCs cultured in the **P1** and **P6** polymer gels. *DCAMKL1* silencing resulted in the increased expression of *RUNX2* for the **P1** polymer gel as well as for the **P6** polymer gel, but to a smaller extent (Figure A5.1.21). In contrast, DCAMKL1 overexpression did not significantly alter the expression of *RUNX2* in the **P1** polymer gel, while a significant decrease was observed for **P6** (Figure A5.1.22). These data confirm the functional relationship between the two proteins in this gel system. DCAMKL1 functions "upstream" of RUNX2 and directs its expression in a switch-like manner. Along with this, a threshold value exists that determines the expression of DCAMKL1, which inhibits the expression of RUNX2. These data are in agreement with a previous *in vivo* and *in vitro* study.[32]

a

b
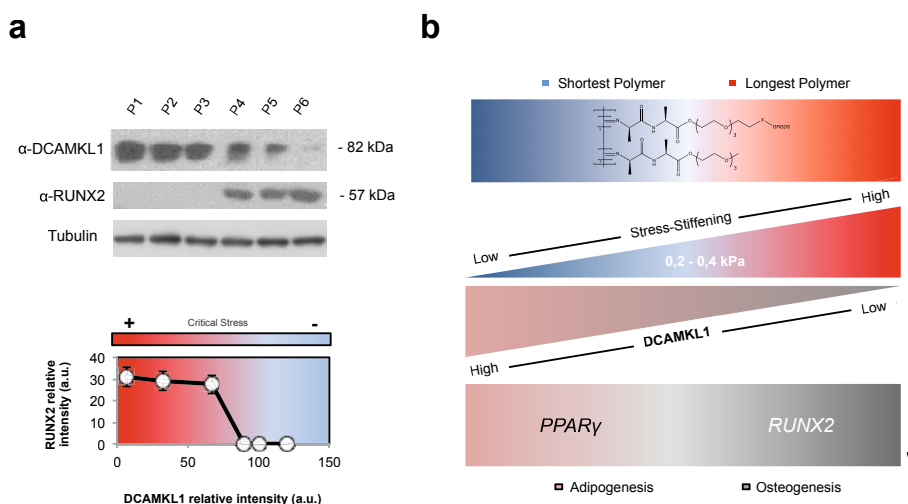
Figure 5.4. a) Western Blot analysis of DCAMKL1 and RUNX2 protein expression in hMSCs after 96 h of culture in all of the matrices (short and long polymers; **P1-P6**). The Western blot was performed in triplicate. A plot of the relative protein expression intensities of RUNX2 versus DCAMKL1 for all the conditions (**P1** to **P6**) shows a switch-like relationship between these two proteins. b) Schematic model illustrating the proposed mechanisms that underlies the stress-stiffening mediated hMSC commitment and differentiation towards adipogenesis and osteogenesis via modulation of the protein expression of DCAMKL1.

Altogether these results are the first report of the microtubule-associated protein DCAMKL1 being involved in a new stress-stiffening mediated mechanotransduction pathway involving microtubule dynamics for the control of hMSC differentiation (Figure 5.4b). These data indicate that stem cell fate is regulated by ECM stress-stiffening via a different molecular mechanism than the one described for classical 2D substrate rigidity sensing.

5.3 Discussion and conclusion

This chapter introduces polyisocyanopeptide-based hydrogels as a new class of 3D cell culture system for studying the physical cues of the microenvironment involved in stem cell fate control. Despite being fully synthetic, the gels discussed in this chapter closely resemble natural biopolymer gels. They exhibit stress-stiffening behavior, a property that is widely observed in biological tissues and is believed to have important ramifications for the design of artificial ECM mimetic scaffolds. In contrast to other synthetic polymer matrices such as polyacrylamides or polyethylene glycol gels, the bulk stiffness of this new class of gels does not need to be modulated in order to access different differentiation lineages of the encapsulated stem cells. Uniquely, despite being embedded in a soft microenvironment, the hMSC commitment can be switched from adipogenesis to osteogenesis simply by altering the polymer chain length, and thus the critical stress. This keeps the matrix stiffness and ligand density unaltered in the process. Such precise control of mechanical properties provides a platform for varying the stiffness and ligand density independently and allows for extracting their individual effects on stem cell fate. This culture system mimics the stiffness (0.2-0.4 kPa) of all the adult stem cell niches present in the human body (for example bone marrow, brain and adipose tissue) and hence provides a physiologically relevant soft 3D microenvironment for stem cells. This new system thus allows for assessing the effect of stress-stiffening on stem cell differentiation in a biologically relevant stress regime (Figure 5.1). It represents a soft 3D physiological microenvironment that can be tuned independently of matrix stiffness, ligand density and matrix porosity, thereby improving upon the traditional synthetic ECM mimetic scaffolds. Moreover, the thermoresponsive behavior of this hydrogel is advantageous for tissue engineering applications as the material can be injected as a fluid, which can then form a gel *in vivo* (37 ºC).

In recent years, after the seminal study of Engler and coworkers, bulk matrix stiffness has emerged as the most important mechanical cue to direct stem cell differentiation,[17] especially for 2D hydrogels. Recent work culturing stem cells in 3D hydrogels has, however, identified other crucial factors such as cellular traction-induced local deformation of the matrix (leading to integrin-ligand clustering),[19] cell-

mediated matrix degradation[20] and mechanical constraints. All these factors act in concert and are independent of the bulk matrix stiffness. This indicates that the actual mechanism of MSC lineage selection is likely to be considerably more complex than solely being the result of a response to tissue matrix elasticity. For instance, altering the degree of cell spreading in 2D was shown to impact MSC osteogenic differentiation.[9] This is not the case *in vivo* where the process of spreading in 3D is mechanically or physically constrained. When comparing with 2D cultures, most 3D systems show enhanced MSC osteogenesis with increased osteogenic gene expression, matrix formation and up-regulated autocrine BMP2 signaling.[34–37] The 3D culture system presented in this chapter mediates MSC osteogenesis in a very soft microenvironment similar to the one of the bone marrow niche, but different from the one reported in the study of Engler et al.[17] The results identify stress-stiffening as a new key regulator of stem cell differentiation, and suggest that the mechanical response (stiffening) of a matrix to cellular traction may be as important as bulk matrix stiffness in cellular fate determination. Based on the present data, a synergy between cell-mediated ligand clustering and stress-stiffening may be crucial for determining stem cell fate.

The exact sequence of events and the molecular mechanisms that determine the observed response to stress-stiffening remain to be unravelled. In this chapter a potential role of the microtubule-associated protein DCAMKL1 is shown. It is known from previous studies that DCAMKL1 regulates osteogenesis by antagonizing RUNX2, the master transcription factor for the osteoblast lineage.[32] Using the PIC hydrogel system, a correlation is established between the critical stress of the hydrogels and the expression of RUNX2 and DCAMKL1, on both the mRNA and the protein level. RUNX expression was only detectable when the hMSCs were grown in gels with high critical stress, while the expression of DCAMKL1 decreased with increasing critical stress. A functional relationship between DCAMKL1 and RUNX2 was further confirmed via *DCAMKL1* gene silencing and overexpression. Overall, the critical stress of the 3D hydrogel system affects the expression of DCAMKL1 and RUNX2, which in turn is responsible for the observed switch in hMSC differentiation from adipogenesis to osteogenesis.

In summary, the results and the previous reports have established a working model for understanding stress-stiffening mediated control of stem cell differentiation in polyisocyanopeptide 3D matrices. Initially, hMSCs sense the surrounding environment through the classical mechanisms described for 2D substrate rigidity perception via focal adhesion contacts and the actin cytoskeleton. Beyond the critical stress, this induces stress-stiffening of the surrounding polymer matrix. This can exert an overall tension on the cell in this 3D environment, which in turn is perceived

via the microtubule cytoskeleton that supports and controls cell shape. As previously shown, this can lead to microtubule reorganization and deformation. The extent of these deformations depends on the degree of stress-stiffening. Deformations can induce different conformational changes of signaling molecules co-localized at these deformation sites or of microtubule-associated proteins in order to activate or inactivate them. The activated proteins then mediate signal transduction via different signaling pathways in order to control the expression of various genes like for example different transcription factors for stem cell differentiation control. Further experiments are required with the new 3D culture system in order to precisely elucidate these mechanisms and the role of the stress-stiffening parameter in cell fate determination.

5.4 Experimental section

General procedure for the synthesis of azide-functionalized polymers[38]

A solution of the catalyst Ni(ClO$_4$)$_2$ .6H$_2$O (1 mM) in toluene/ethanol (9:1) was added to a solution of non-functionalized monomer **1** and azide-appended monomer **2** in freshly distilled toluene (50 mg/mL total concentration; molar ratio **1/2 =** 100). The reaction mixture was stirred at room temperature (20 ºC) for 72 h. The resultant polymer was precipitated 3 times from dichloromethane in di-isopropyl ether and dried overnight in air. The polymer was characterized by rheology, viscometry and AFM analysis.

Synthesis of P1': The catalyst to monomer (**1** + **2**) molar ratio used : 1/1000
Synthesis of P2': The catalyst to monomer (**1** + **2**) molar ratio used : 1/2500
Synthesis of P3': The catalyst to monomer (**1** + **2**) molar ratio used : 1/3000
Synthesis of P4': The catalyst to monomer (**1** + **2**) molar ratio used : 1/4000
Synthesis of P5': The catalyst to monomer (**1** + **2**) molar ratio used : 1/6000
Synthesis of P6': The catalyst to monomer (**1** + **2**) molar ratio used : 1/8000

Conjugation of azide-functionalized polymers with GRGDS peptide

The GRGDS peptide was dissolved in borate buffer (pH 8.4) at a concentration of 2 mg/mL. A solution of 2,5-dioxopyrrolidin-1-yl 1-(bicyclo[6.1.0]non-4-yn-9-yl)-3,14-dioxo-2,7,10-trioxa-4,13-diazaoctadecan-18-oate (BCN-NHS) in DMSO was added to the peptide solution in borate buffer in 1:1 molar ratio and incubated for 3 h at room temperature (20 ºC). The formation of the BCN-GRGDS conjugate was confirmed by mass spectrometry. MS calc.: 910.4, obtained: 911.4

The azide-functionalized polymer (**P1'-P6'**) was dissolved in acetonitrile at a concentration of 3 mg/mL. The appropriate volume of BCN-GRGDS dissolved in borate buffer was added to this solution (based on the molar equivalent of azide-functions of the polymer). This mixture was incubated for 72 h at room temperature (20 ºC). The resulting polymer-peptide conjugates (**P1-P6**) were precipitated by adding the reaction mixture drop wise to di-isopropyl ether.

Determination of the amount of azides on the azide-functionalized polymer

A dichloromethane solution of a BCN-functionalized lissamine dye was added to a dichloromethane solution of the polymer (1 mg/mL) in a 1:1.2 molar ratio w.r.t. the calculated amount of azides in an azide-functionalized polymer. The reaction mixture was rotated at 15 rpm in the dark for 12 h at room temperature (20 ºC). The polymer-dye conjugate was precipitated 4 times from dichloromethane in di-

isopropylether. The precipitate was dried in air overnight and re-dissolved in dichloromethane. To determine the amount of dye coupled, the absorption spectra of all samples were recorded. An extinction coefficient of 138,428 mol^{-1} cm^{-1} was used at a wavelength of 559 nm to determine the amount of dye attached to the polymer and to calculate the amount of azide present on the polymer (Table 5.1).

Rheology analysis

The polymers were dissolved at a concentration of 2 mg/mL in alpha-MEM (without serum) by gentle rotation (7-8 rpm) at 4 ^{o}C on a 90°-rotor for 36 h. For determining the bulk stiffness of the gel, a temperature sweep rheology experiment was performed (plate-plate geometry; 250 µm geometry gap), by heating the solution from 5 ^{o}C to 37 ^{o}C at a heating rate of 2 ^{o}C/min at a constant strain of 2% and constant frequency of 1 Hz. This experiment was immediately followed by a time sweep experiment (5 min) at 37 ^{o}C at a constant frequency of 1 Hz. The G' value observed at the end of the experiment was taken as the equilibrium bulk stiffness of the gel at this temperature. For non-linear rheology, the previously described pre-stress protocol[28] was employed immediately after the aforementioned time sweep experiment.

Atomic force microscopy

To visualize individual polymer chains and to determine the average length of the polymers, solutions (~1 µg/mL in CHCl$_3$) were spin-coated (300 rpm for 20 seconds) on freshly cleaved mica substrates and imaged by AFM using tapping mode. Polymer lengths were determined using ImageJ software. The length of at least 150 polymer chains was determined to obtain the distribution and the mean of the polymer chain length for any particular sample.

Cell culture

Human Mesenchymal Stem Cells (hMSCs) were obtained from Lonza, Inc. (Switzerland). Cells were then cultured in alpha-MEM medium (Invitrogen) supplemented with 10% fetal bovine serum (FBS), 1% penicillin/streptomycin and incubated in a humidified atmosphere containing 5% (v/v) CO$_2$ at 37 $^\circ$C. For the encapsulation of cells in the gels, the cell pellets were first obtained by centrifugation. Then, 500 µL of the cold polymer solution (~10 ^{o}C) was added directly to the pellet, followed by a gentle pipetting up and down 3-4 times to ensure homogeneous mixing. This mixture was directly put onto a cover slip in a 6-well plate (also kept cold). Thereafter, the solution was sandwiched between two cover slips and the well plate was transferred to a 37 ^{o}C incubator. The volume of the suspension was chosen (500 µL) in order to obtain hydrogel thickness in the range of 3 mm. After gel formation, the two cover slips were removed and alpha-MEM medium (without serum) was added. All cell culture experiments were carried out without any serum in the medium for the first 6 h of culture.[12] Then, alpha-MEM medium with 10% serum was added. All cells were used at low passage numbers (≤4). They were subconfluently cultured and were seeded at 10^6 cells/mL for the purpose of the experiments and in order to avoid cell-cell contacts.

The lineage commitment and differentiation of the gel-encapsulated hMSCs after 96 h and 3 weeks of culture, respectively, were investigated with bipotential differentiation medium (1:1 v/v osteogenic and adipogenic media, Lonza). For all the experiments, a non-functionalized soft polymer gel (cell culture in growth medium) served as control. The live/dead viability assay at 3 weeks in these control gels indicated excellent cell viability.

The pharmacological agents used were 50 µM Blebbistatin (EMD Biosciences-Calbiochem), 1 µM cytochalasin D (Sigma) and 50 nM Taxol (Abcam). The hMSCs were exposed to each

pharmacological agent for 1 h, 24 h and 72 h, respectively, after seeding them in a modified polymer gel. For the antibody inhibition studies, cells were pre-incubated with 5 ng/mL anti-α1, 2, 3 and 5-β1, 2 (all from Santa Cruz Biotechnology). For competition experiments with soluble GRGDS peptides, the cells were incubated in 1 mL of cell culture media containing 200 µg of GRGDS peptides during 20 min on plastic and then transferred to the polymer gels. To evaluate proliferation, total double-stranded DNA content was determined using the PicoGreen assay as previously reported.[39]

Confocal microscopy

In order to assess the homogeneous distribution of the cells in the hydrogels, very thin slices of the gel were cut transversely at various depths, including the two interfaces. The fluorescently labeled cells encapsulated in the gel slices were imaged by confocal microscopy with a Leica SP5 confocal microscope, 10x objective, 0.3 NA. 400 µm thick z-stacks were then acquired every 2.39 µm and the 3D images were reconstructed using the Imaris 7.0 software.

MTT assay

Cell viability was determined using the 3-(4,5-dimethylthiazol-2-yl)-2,5-diphenyltetrazolium bromide (MTT) assay as described in the literature.[40] The data are presented as a percentage of control viability.

Live/dead staining

Cell viability was determined with the live/dead viability/cytotoxicity kit (Molecular Probes), according to the manufacturer's protocol.

Real-time PCR analysis of gene expression

RT-PCR was performed as previously described.[41,42] Briefly, total RNA was extracted using the RNeasy total RNA kit from Qiagen in accordance with the manufacturer's instructions. Purified total RNA was used to obtain cDNA in a reverse transcription reaction (Gibco BRL) using random primers (Invitrogen). Real-time PCR was performed with SYBR green reagents (Bio-Rad). The data were analyzed using the iCycler IQTM software. The cDNA samples (1 µL in a total volume of 20 µL) were analyzed for the gene of interest and for the house-keeping gene GAPDH. The comparison test of the cycle-threshold point was used to quantify the gene expression level in each sample. The primers used for the amplification are listed in Table 5.2.

Table 5.2. Nucleotide sequences of primers used for quantitative RT-PCR detection.

Gene	Primer Sequences
Runx2	5'-GACGTGCCCAGGCGTATTTC-3'(Forward)
	5'-AAGTCTGGGGTCCGTCAAGG-3'(Reverse)
PPARγ	5'-GGCTTCATGACAAGGGAGTTTC-3''(Forward)
	5'-AACTCAAACTTGGGCTCCATAAAG-3' (Reverse)
GAPDH	5'-GCAGTACAGCCCCAAAATGG-3'(Forward)
	5'-ACAAAGTCCGGCCTGTATCCAA-3'(Reverse)

Western blotting

After 96 h, the polymer gels were exposed to a cold environment (around 10 ^{o}C). The cell pellet was obtained by centrifugation. The cells were permeabilized (10% SDS, 25 mM NaCl, 10 nM pepstatin and 10 nM leupeptin in distilled water and loading buffer), boiled for 10 min and analyzed with reducing SDS-PAGE (Invitrogen). The proteins were transferred onto nitrocellulose, blocked, and labeled with HRP-conjugated antibodies (Invitrogen). The microtubule associated protein DCAMKL1 was detected using the monoclonal anti-DCAMKL1 antibody (Santa Cruz Biotechnology). The transcriptional factor RUNX2 was detected with a monoclonal anti-Runx2 antibody (Abcam). All Western blots were run in triplicate, along with an additional blot for tubulin and Coomassie Blue staining to ensure consistent protein loading between samples. In order to construct the plot of the relative intensities of RUNX2 versus DCAMKL1 and to illustrate the switch-like relationship between the two proteins, the "zero" of the RUNX2 relative intensity was set at the corresponding level of expression of RUNX2 in hMSCs cultured on plastic, which was set to 1.

Immunostaining

After 96 h or 3 weeks of culture, the gels were exposed to a cold environment (~ 10 ºC). The cell pellet was collected from the fluid by centrifugation, transferred into the well plate and allowed to adhere to the well plate surface by culturing in alpha-MEM with serum for 16 h. The cells were then fixed for 20 min in 4% paraformaldehyde/PBS at ~37 °C. After fixation, the cells were permeabilized in a PBS solution containing 1% Triton X-100 for 15 min. The cells were then incubated with the corresponding primary antibodies (mouse anti-vinculin for adhesion; mouse anti-STRO-1 for differentiation) for 1 h at 37 °C. After washing, cells were stained with Alexa Fluor[®] 647 rabbit anti-mouse IgG secondary antibody for 30 min at ~ 37 °C. Cell cytoskeletal filamentous actin (F-actin) was visualized by treating the cells with 5 U/mL Alexa Fluor[®] 488 Phalloidin (Sigma, France) for 1 h at 37 °C. Vinculin was visualized by treating the cells with 1% (v/v) monoclonal anti-vinculin (clone hVIN-1 antibody produced in mouse) for 1 h at 37 °C. The cells were then stained with Alexa fluor[®] 568 (F(ab')2 fragment of rabbit anti-mouse IgG(H + L)) during 30 min at room temperature. After 96 h, Osterix was visualized by treating the cells with 1% (v/v) rabbit monoclonal anti-Osterix (antibody produced in rabbit) for 1 h at 37 °C. The cells were then stained with Alexa fluor[®] 568 (F(ab')2 fragment of mouse anti-rabbit IgG(H + L)) during 30 min at room temperature. Tubulin (stained by Anti-Tubulin β3 (Sigma, France)) was visualized by treating the cells with 1% (v/v) monoclonal anti-Tubulin β3 (Abcam, Cambridge), for 1 h at 37 °C and then with Alexa Fluor[®] 588 (F(ab')2 fragment of goat anti-rabbit IgG(H+L)) for 30 min at room temperature. There was no detection of the muscle transcription factor MyoD1 (stained with anti-MyoD1 (Santa Cruz Biotechnology, USA)). To stain lipid fat droplets, the cells were fixed in 4% paraformaldehyde, rinsed in PBS and 60% isopropanol, stained with 3 mg ml^{-1} Oil Red O (Sigma, France) in 60% isopropanol and rinsed in PBS at ~ 37 °C. For the purpose of assessing cell differentiation in 3D via Oil Red O staining, gel slices of the middle of the gel (height range at around 1.2-1.6 mm depth) are usually stained and imaged.

For quantification[14,15,43,44] of STRO-1, Osterix, Tubulin β3, MyoD1 and lipid fat droplets, positive contacts number and areas, the freeware image analysis ImageJ® software was used. First the raw image was converted to an 8-bit file, and the "unsharp mask" feature (settings 1:0.2) was used to remove the image background (rolling ball radius 10). After smoothing, the resulting image, which appears similar to the original photomicrograph but with minimal background, was then converted to a binary image by setting a threshold. The threshold values were determined by selecting a setting, which gave the most accurate binary image for a subset of randomly selected photomicrographs with varying glass substrates. The total contact area and mean contact area per

cell were calculated by "analyse particules" in Image J. A minimum of 20-30 cells were analyzed per condition.

Statistical analysis

In terms of fluorescence intensity, sub-cell contact area and real-time PCR assay, the data were expressed as the mean ± standard error, and were analyzed using the paired Student's t-test method. Significant differences were designated for *P* values of at least <0.01.

Overexpression of DCAMKL1

The overexpression of DCAMKL1 was performed as previously described by Lin et al[45]. Briefly, Human *DCAMKL1* was cloned by RT-PCR using primers directed toward the human sequence and subsequently sequenced. Full-length human *DCAMKL1* was subsequently cloned into the *KpnI* site of pcDNA3.1C(-) (Invitrogen, Carlsbad, CA) and overexpressed by transient transfection with Super-fectamine (Qiagen, Chatsworth, CA) according to the manufacturer's recommendations. The efficiency of the DCAMKL1 overexpression was assessed by Western blot for hMSCs cultured on plastic. A 180-200% increase in protein level was observed after 72 h.

***DCAMKL1* shRNA silencing**

DCAMKL1 silencing has been performed by transfecting hMSCs with a pool of 3 target-specific lentiviral vector plasmids each encoding 19-25 nt (plus hairpin) shRNAs designed to knock down gene expression (Santa Cruz Biotechnology). A mock plasmid was transfected as a control. Transient transfection was performed using Lipofectamine 2000 (Invitrogen) according to the manufacturer's protocol. The efficiency of the *DCAMKL1* silencing was assessed by Western blot for hMSCs cultured on plastic. The *DCAMKL1* silencing decreased the *DCAMKL1* mRNA level by 50-60% (not shown) and the DCAMKL1 protein level by 60-70% after 24 h.
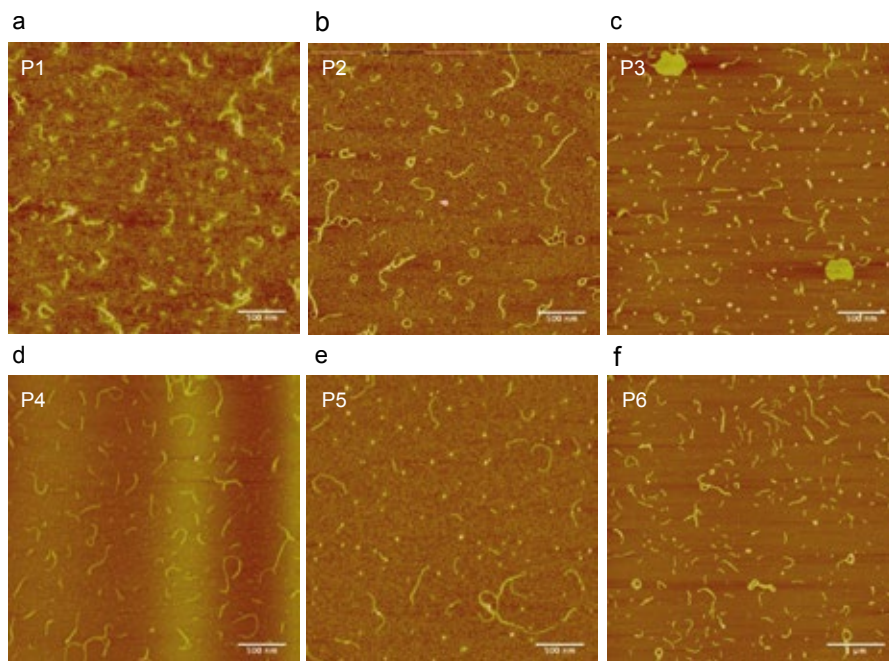
5.5 Appendix 5.1: Supplementary figures

Figure A5.1.1. a)-f) Representative AFM images of dilute (1 µg/mL) chloroform solution of polymers **P1-P6**, respectively, drop-casted on freshly cleaved mica. Scale bar: 500 nm for a)-e) and 1 µm for f).
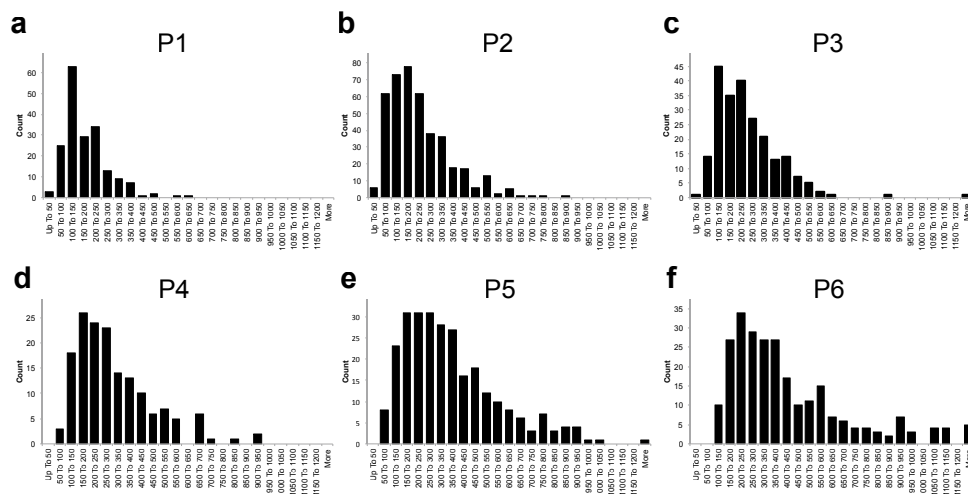

Figure A5.1.2. a)-f) Histograms showing the length distribution of single polymer chains in individual polymers (**P1-P6**), as obtained by observing at least 150 single polymer chains in AFM for dilute (1 µg/ mL) chloroform solution of the polymers, drop-casted on freshly cleaved mica. These data were used to obtain the mean polymer length for the polymers.
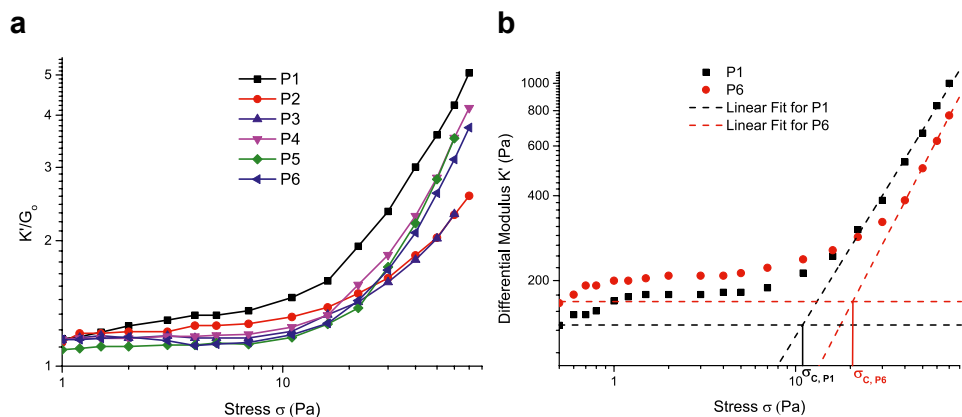
a

b

Figure A5.1.3. a) Non-linear rheology data of polymer gels **P1-P6** in alpha-MEM at 2 mg/ mL. The differential modulus K', scaled with the storage modulus G_o, is plotted as a function of applied stress σ. The experiments were repeated in triplicate and the mean plots are shown. b) Overlay of the plots of differential modulus K' as a function of applied stress σ, for the gels of shortest (**P1**) and the longest (**P6**) polymer. $σ_C$ denotes the critical stress for the onset of stress-stiffening.
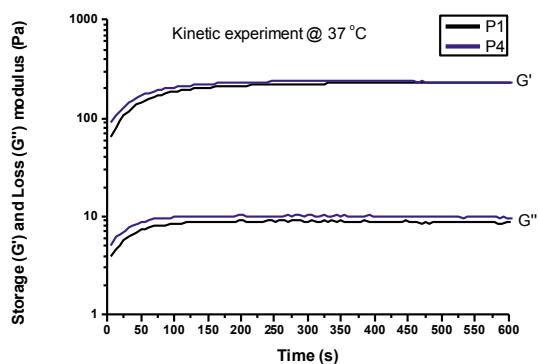

Figure A5.1.4. Representative time sweep rheology experiments after incubating the cold polymer solution at 37°C at an applied strain of 1% at a frequency of 1 Hz.
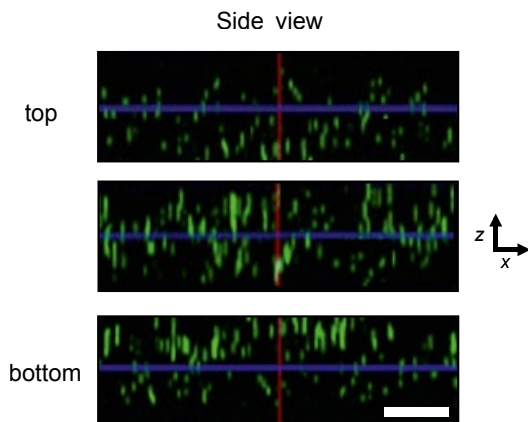
Side view

Figure A5.1.5. Confocal microscopy. 400 µm Z-stack side view (X,Z projections) images showing the top, middle and bottom distribution of gel-encapsulated hMSCs (after 96 h of culture) stained with calcein-AM. Scale bar: 200µm.
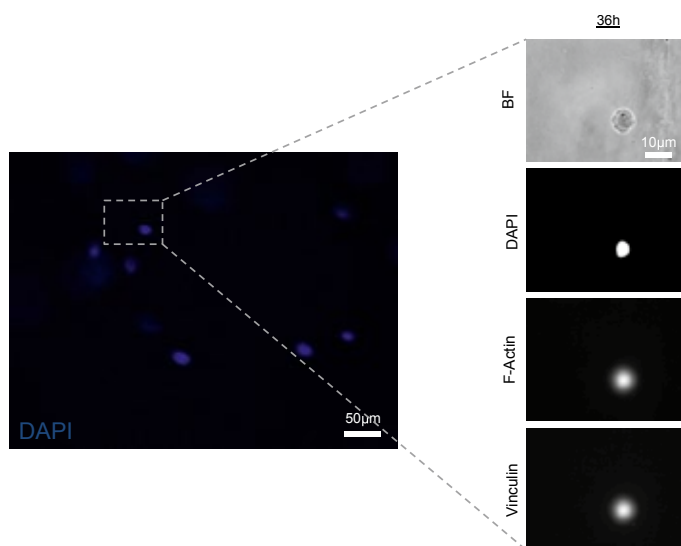

Figure A5.1.6. Representative micrographs showing cross-sections of hMSCs (DAPI staining) 36 h after encapsulation into the 3D soft hydrogel. On the right, hMSCs are shown in bright-field, DAPI, F-actin and vinculin stainings. Left scale bar: 50 µm and right scale bar: 10 µm.
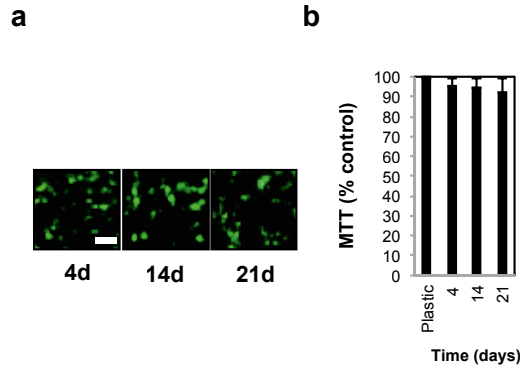
Figure A5.1.7. Live-dead viability test at different time points, for hMSCs encapsulated in control polymer gels (non-functionalized) in growth medium by a) calcein-AM (live cells fluoresce green), and by b) MTT assay. Scale bar: 20 µm.
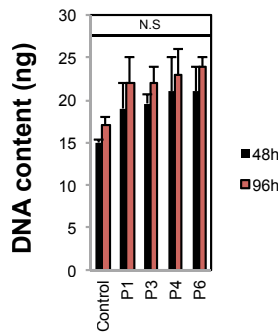
Figure A5.1.8. Total DNA content for hydrogels assembled from short and long polymers (**P1**, **P3**, **P4** and **P6**) after 48 h and 96 h of cell culture as determined by the PicoGreen assay. A non-functionalized hydrogel served as a control. Error bars, s.e.m. (n ≥ 3). NS. not significant (P > 0.05), Student's t-test.

Figure A5.1.9. Representative bright-field images (Oil red O staining) of hMSCs encapsulated in gels assembled from the polymers **P1**-**P6** after 96 h of culture in bipotential (osteogenic/adipogenic) medium. Scale bar: 10 µm.

a

b
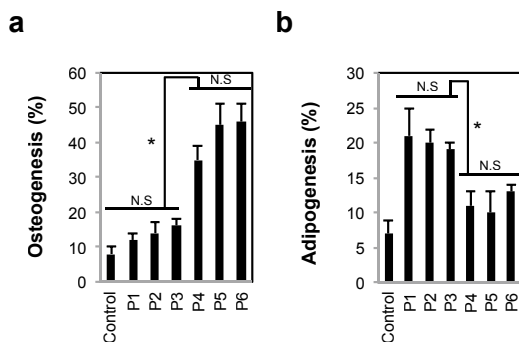
Figure A5.1.10. Mean percentages of hMSC osteogenesis a) and adipogenesis b) in different hydrogel materials from polymers **P1-P6** after 96 h of culture in bipotential medium. A non-functionalized hydrogel (cell culture in growth medium) served as a control. Error bars, s.e.m. (n ≥ 3). NS. not significant ($P > 0.05$), *$P < 0.05$; Student's t-test.
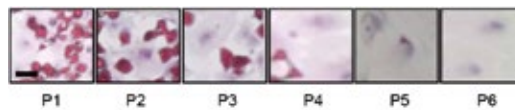
a

b

OPN

c
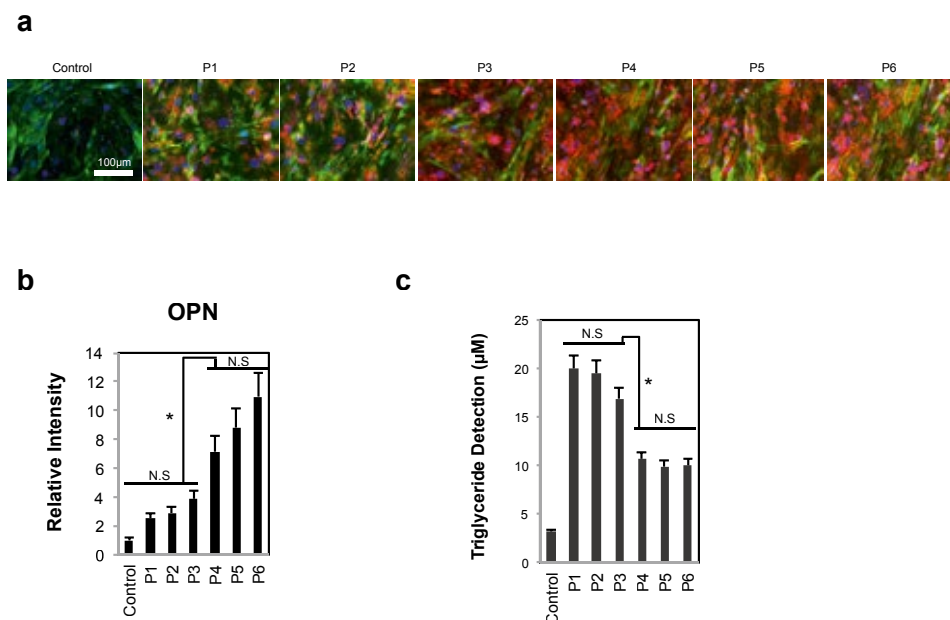
Figure A5.1.11. a) Immunofluorescent staining for OPN (red), actin (green), and nucleus (blue) in hMSCs encapsulated in different hydrogel materials from polymers **P1-P6** after 3 weeks of culture in bipotential medium. Scale bar: 100 µm. b) Total cellular immunofluorescence intensity of osteopontin quantified for hMSCs cultured for 3 weeks in different matrices. c) Triglyceride detection on hMSCs after 3 weeks on cell culture. A non-functionalized hydrogel (cell culture in growth medium) served as a control for all the experiments. Error bars, s.e.m. (n ≥ 3). NS. not significant ($P > 0.05$), *$P < 0.05$; Student's t-test.

a **b**

RUNX2 **LIP**
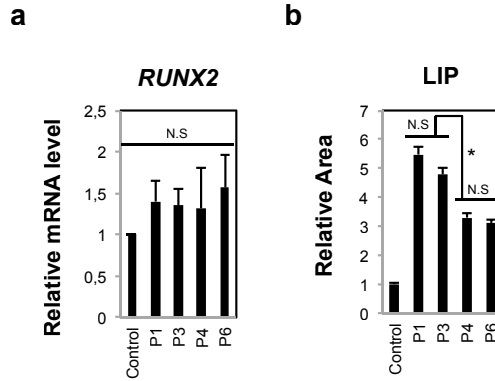
Figure A5.1.12. hMSCs commitment studies after 96 h of culture in different polymer gels in the presence of anti-integrin antibodies α1, 2, 3, 5 and β1, 2. a) Quantitative PCR analysis for RUNX2. No significant differences were observed between the matrix with the highest critical stress (**P6**) and the matrices displaying lower critical stress. b) Total cellular immunofluorescence area of neutral lipid accumulation in hMSCs. For all the experiments, a non-functionalized hydrogel (cell culture in growth medium) served as the control (*$P < 0.01$).

a **b**

Figure A5.1.13. Mean percentage of hMSC osteogenesis a) and adipogenesis b) in different polymer gels in the presence of anti-integrin antobodies α1, 2, 3, 5 and β1, 2. A non-functionalized hydrogel (cell culture in growth medium) served as the control. Error bars, s.e.m. (n ≥ 3). NS. not significant ($P > 0.05$), *$P < 0.01$; Student's t-test.

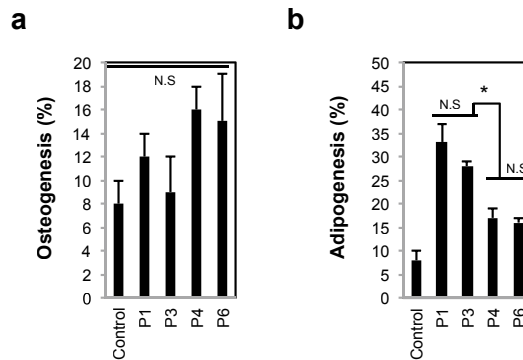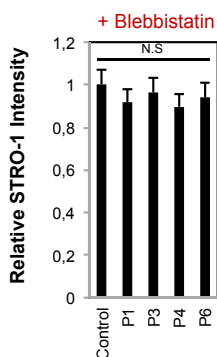**Figure A5.1.14.** The amount of STRO-1 present in the hMSCs. The values represent the average fluorescence intensity, normalized by the number of cells. Compared to the control (non-functionalized hydrogel), STRO-1 activity is present on matrices + blebbistatin, indicating that the hMSCs have kept "stemness" after 96 h of culture in bipotential medium.
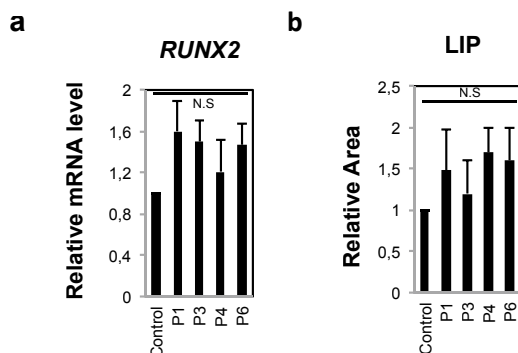
Figure A5.1.15. hMSCs commitment studies after 96 h of culture in different polymer gels in the presence of soluble GRGDS ligands. a) Quantitative PCR analysis for RUNX2. No significant increase in RUNX2 gene expression was observed for all the matrices and no significant differences could be detected between matrices displaying a higher (**P4** and **P6**) and lower (**P1** and **P3**) critical stress in the presence of soluble GRGDS. b) Total cellular immunofluorescence area of neutral lipid accumulation quantified for hMSC cultured for 96 h in different matrices. No significant increase in lipid accumulation was observed for all the matrices and no significant differences could be detected between the different polymers. For all the experiments, a non-functionalized soft polymer gel (cell culture in growth medium) served as a control. NS. not significant ($P > 0.05$). Student's t-test.
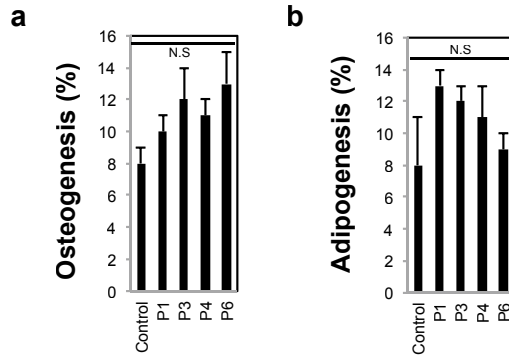
Figure A5.1.16. Mean percentage of hMSC osteogenesis a) and adipogenesis b) for different polymer gels (**P1**, **P3**, **P4** and **P6**) in the presence of soluble GRGDS ligands. A non-functionalized hydrogel served as a control. Error bars, s.e.m. (n ≥ 3). NS. not significant (P > 0.05), Student's t-test.
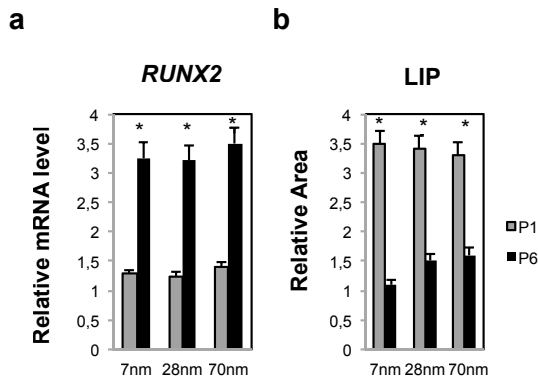
Figure A5.1.17. Commitment of hMSCs at different ligand densities (7 nm, 28 nm and 70 nm) in polymer gels displaying the lowest and highest critical stress (**P1** and **P6**, respectively). a) Quantitative PCR analysis for *RUNX2*. b) Total cellular immunofluorescence area of neutral lipid accumulation quantified for hMSC cultured for 96 h in bipotential medium. For all the experiments, a non-functionalized soft polymer gel (cell culture in growth medium) served as the control (*$P < 0.005$).

a **b**
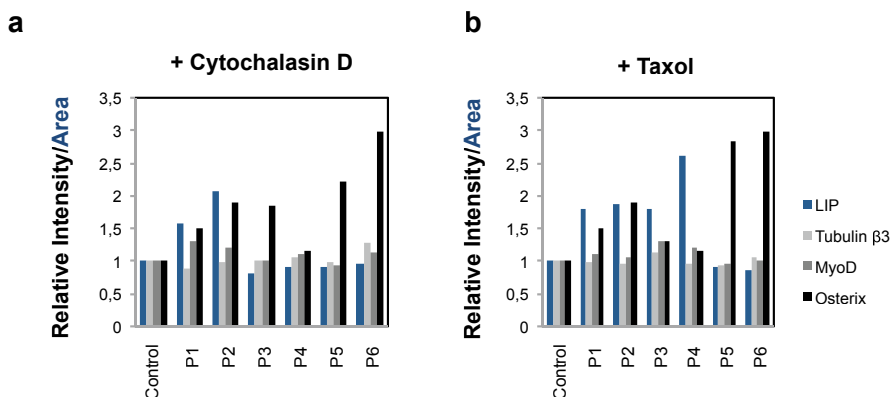
Figure A5.1.18. Immunofluorescent staining for MyoD, Tubulin β3 and Osterix in hMSCs encapsulated in different hydrogel materials from polymers **P1**-**P6** in the presence of a) Cytochalasin D and b) Taxol (inhibitor of actin and inductor of microtubule cytoskeleton polymerization) after 96 h of culture in bipotential medium. For the control naïve hMSCs were encapsulated in a non-functionalized soft hydrogel and cultured in growth medium.
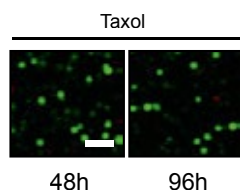
Figure A5.1.19. Calcein-AM live-dead viability test (live cells fluoresce green) at different time points (48 h and 96 h) for hMSCs treated with Taxol and encapsulated in polymer gel **P3** in growth medium. Scale bar: 20 μm.

a **b**
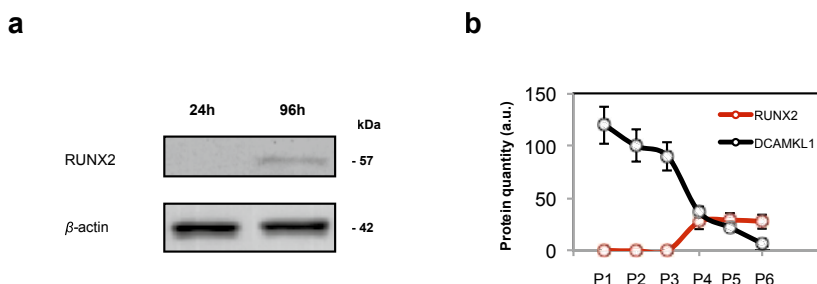
Figure A5.1.20. a) Western blot showing RUNX2 protein expression for hMSCs cultured on plastic for 24 h and 96 h. b) Relative protein expression for RUNX2 and DCAMKL1 of hMSCs grown in polymer gels **P1-P6.** The values have been obtained from the Western blot presented in Figure 5.4a. The graph clearly showing a switch-like relationship between the two proteins.

a

b

c
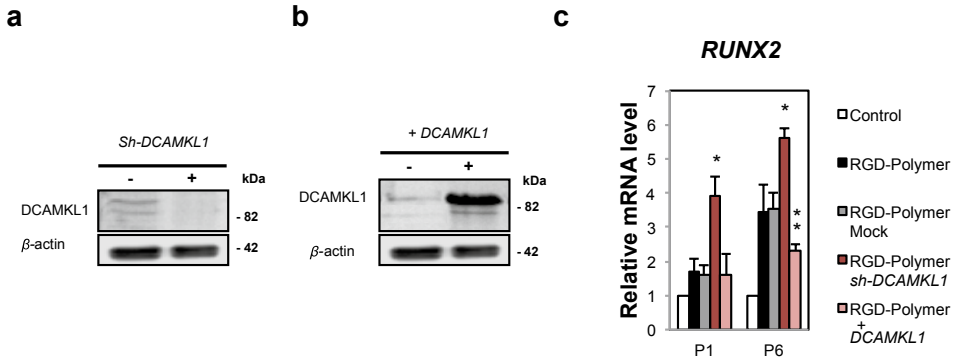
Figure A5.1.21. a) shRNA mediated *DCAMKL1* silencing was induced, as shown by Western blot for hMSCs cultured on plastic for 24h. b) Overexpression of *DCAMKL1* was enabled by transient transfection with a plasmid subcloned with the *DCAMKL1* gene, as shown by Western blot for hMSCs cultured on plastic for 72h. c) Non transfected cells or cells at 48 h post-transfection (mock plasmid, shRNA or *DCAMKL1*) were incorporated into GRGDS-functionalized hydrogels (**P1** or **P6**) for 96 h. Relative *RUNX2* mRNA levels were then measured using RT-PCR. Non-transfected cells incorporated into non-functionalized hydrogels served as a control. *P < 0.001; ** represents the comparison between GRGDS-functionalized polymers and +*DCAMKL1* for the **P6** hydrogel and P < 0.05 ; Student's t-test.

5.6 References

(1)   Discher, D. E.; Mooney, D. J.; Zandstra, P. W. *Science* **2009**, *324*, 1673–1677.
(2)   Discher, D. E.; Janmey, P.; Wang, Y.-L. *Science* **2005**, *310*, 1139–1143.
(3)   Baker, B. M.; Chen, C. S. *J. Cell Sci.* **2012**, 3015–3024.
(4)   Eyckmans, J.; Boudou, T.; Yu, X.; Chen, C. S. *Dev. Cell* **2011**, *21* (1), 35–47.
(5)   Das, R. K.; Zouani, O. F. *Biomaterials* **2014**, *35* (20), 5278–5293.
(6)   Vogel, V.; Sheetz, M. *Nat. Rev. Mol. Cell Biol.* **2006**, *7*, 265–275.
(7)   Chaudhuri, O.; Koshy, S. T.; Branco da Cunha, C.; Shin, J.-W.; Verbeke, C. S.; Allison, K. H.; Mooney, D. J. *Nat. Mater.* **2014**, *13* (June), 970–978.
(8)   Wen, J. H.; Vincent, L. G.; Fuhrmann, A.; Choi, Y. S.; Hribar, K. C.; Taylor-Weiner, H.; Chen, S.; Engler, A. J. *Nat. Mater.* **2014**, *13* (October), 979–987.
(9)   McBeath, R.; Pirone, D. M.; Nelson, C. M.; Bhadriraju, K.; Chen, C. S. *Dev. Cell* **2004**, *6*, 483–495.
(10)   McNamara, L. E.; Burchmore, R.; Riehle, M. O.; Herzyk, P.; Biggs, M. J. P.; Wilkinson, C. D. W.; Curtis, A. S. G.; Dalby, M. J. *Biomaterials* **2012**, *33*, 2835–2847.
(11)   Nikukar, H.; Reid, S.; Tsimbouri, P. M.; Riehle, M. O.; Curtis, A. S. G.; Dalby, M. J. *ACS Nano* **2013**, *7*, 2758–2767.
(12)   Zouani, O. F.; Chanseau, C.; Brouillaud, B.; Bareille, R.; Deliane, F.; Foulc, M.-P.; Mehdi, A.; Durrieu, M.-C. *J. Cell Sci.* **2012**, 1217–1224.
(13)   Zouani, O. F.; Kalisky, J.; Ibarboure, E.; Durrieu, M. C. *Biomaterials* **2013**, *34*, 2157–2166.
(14)   Das, R. K.; Zouani, O. F.; Labrugère, C.; Oda, R.; Durrieu, M.-C. *ACS Nano* **2013**, *7* (4), 3351–3361.
(15)   Cheng, Z. A.; Zouani, O. F.; Glinel, K.; Jonas, A. M.; Durrieu, M. C. *Nano Lett.* **2013**, *13*, 3923–3929.
(16)   Fu, J.; Wang, Y.-K.; Yang, M. T.; Desai, R. A.; Yu, X.; Liu, Z.; Chen, C. S. *Nat. Methods* **2010**, *7*, 733–736.
(17)   Engler, A. J.; Sen, S.; Sweeney, H. L.; Discher, D. E. *Cell* **2006**, *126* (4), 677–689.
(18)   Ingber, D. E. *Circ. Res.* **2002**, 877–887.
(19)   Huebsch, N.; Arany, P. R.; Mao, A. S.; Shvartsman, D.; Ali, O. A.; Bencherif, S. A.; Rivera-Feliciano, J.; Mooney, D. J. *Nat. Mater.* **2010**, *9* (6), 518–526.
(20)   Khetan, S.; Guvendiren, M.; Legant, W. R.; Cohen, D. M.; Chen, C. S.; Burdick, J. a. *Nat. Mater.* **2013**, *12*, 458–465.
(21)   Houseman, B. T.; Mrksich, M. *Biomaterials* **2001**, *22*, 943–955.
(22)   Keselowsky, B. G.; Collard, D. M.; García, A. J. *Proc. Natl. Acad. Sci. U. S. A.* **2005**, *102*, 5953–5957.
(23)   van Buul, A. M.; Schwartz, E.; Brocorens, P.; Koepf, M.; Beljonne, D.; Maan, J. C.; Christianen, P. C. M.; Kouwer, P. H. J.; Nolte, R. J. M.; Engelkamp, H.; Blank, K.; Rowan, A. E. *Chem. Sci.* **2013**, *4* (6), 2357–2363.
(24)   Kouwer, P. H. J.; Koepf, M.; Le Sage, V. A. A.; Jaspers, M.; van Buul, A. M.; Eksteen-Akeroyd, Z. H.; Woltinge, T.; Schwartz, E.; Kitto, H. J.; Hoogenboom, R.; Picken, S. J.; Nolte, R. J. M.; Mendes, E.; Rowan, A. E. *Nature* **2013**, *493* (7434), 651–655.
(25)   Winer, J. P.; Oake, S.; Janmey, P. a. *PLoS One* **2009**, *4* (7), e6382.
(26)   Trappmann, B.; Gautrot, J. E.; Connelly, J. T.; Strange, D. G. T.; Li, Y.; Oyen, M. L.; Cohen Stuart, M. a; Boehm, H.; Li, B.; Vogel, V.; Spatz, J. P.; Watt, F. M.; Huck, W. T. S. *Nat. Mater.* **2012**, *11* (7), 642–649.
(27)   Wilson, M. J.; Liliensiek, S. J.; Murphy, C. J.; Murphy, W. L.; Nealey, P. F. *Soft Matter* **2012**, *8* (2), 390–398.
(28)   Broedersz, C. P.; Kasza, K. E.; Jawerth, L. M.; Münster, S.; Weitz, D. a.; MacKintosh, F. C. *Soft Matter* **2010**, *6* (17), 4120.
(29)   Jaspers, M.; Dennison, M.; Mabesoone, M. F. J.; MacKintosh, F. C.; Rowan, A. E.; Kouwer, P. H. J. *Nat. Commun.* **2014**, *5*.
(30)   Benoit, D. S. W.; Schwartz, M. P.; Durney, A. R.; Anseth, K. S. *Nat. Mater.* **2008**, *7* (10), 816–823.
(31)   McMurray, R. J.; Gadegaard, N.; Tsimbouri, P. M.; Burgess, K. V; McNamara, L. E.; Tare, R.; Murawski, K.; Kingham, E.; Oreffo, R. O. C.; Dalby, M. J. *Nat. Mater.* **2011**, *10* (8), 637–644.
(32)   Zou, W.; Greenblatt, M. B.; Brady, N.; Lotinun, S.; Zhai, B.; de Rivera, H.; Singh, A.; Sun, J.; Gygi, S. P.; Baron, R.; Glimcher, L. H.; Jones, D. C. *J. Exp. Med.* **2013**, *210*, 1793–1806.
(33)   Kolodney, M. S.; Elson, E. L. *Proc. Natl. Acad. Sci. U. S. A.* **1995**, *92* (22), 10252–10256.

(34) Kabiri, M.; Kul, B.; Lott, W. B.; Futrega, K.; Ghanavi, P.; Upton, Z.; Doran, M. R. *Biochem. Biophys. Res. Commun.* **2012**, *419* (2), 142–147.

(35) Lund, A. W.; Bush, J. a; Plopper, G. E.; Stegemann, J. P. *J. Biomed. Mater. Res. B. Appl. Biomater.* **2008**, *87* (1), 213–221.

(36) Westhrin, M.; Xie, M.; Olderøy, M. Ø.; Sikorski, P.; Strand, B. L.; Standal, T. *PLoS One* **2015**, *10* (3), e0120374.

(37) Yamaguchi, Y.; Ohno, J.; Sato, A.; Kido, H.; Fukushima, T. *BMC Biotechnol.* **2014**, *14*, 105.

(38) Mandal, S.; Eksteen-Akeroyd, Z. H.; Jacobs, M. J.; Hammink, R.; Koepf, M.; Lambeck, A. J. a.; van Hest, J. C. M.; Wilson, C. J.; Blank, K.; Figdor, C. G.; Rowan, A. E. *Chem. Sci.* **2013**, *4* (11), 4168–4174.

(39) Singer, V. L.; Jones, L. J.; Yue, S. T.; Haugland, R. P. *Anal. Biochem.* **1997**, *249* (2), 228–238.

(40) Lai, L.-J.; Ho, T.-C. *Anticancer Res.* **2011**, *31* (4), 1173–1180.

(41) Zouani, O. F.; Chollet, C.; Guillotin, B.; Durrieu, M.-C. *Biomaterials* **2010**, *31* (32), 8245–8253.

(42) Zouani, O. F.; Rami, L.; Lei, Y.; Durrieu, M.-C. *Biol. Open* **2013**, *2* (9), 872–881.

(43) Lei, Y.; Zouani, O. F.; Rémy, M.; Ayela, C.; Durrieu, M.-C. *PLoS One* **2012**, *7* (7), e41163.

(44) Lei, Y.; Zouani, O. F.; Rami, L.; Chanseau, C.; Durrieu, M.-C. *Small* **2013**, *9* (7), 1086–1095.

(45) Lin, P. T.; Gleeson, J. G.; Corbo, J. C.; Flanagan, L.; Walsh, C. A. *J. Neurosci.* **2000**, *20* (24), 9152–9161.

6

DNA-responsive polyisocyanopeptide hydrogels with stress-stiffening capacity
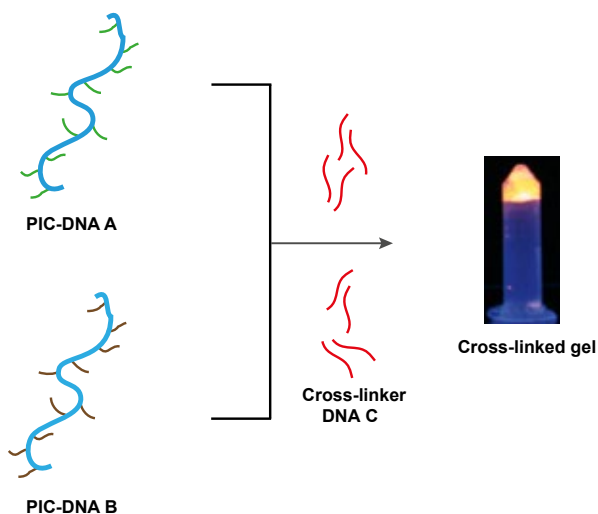
Parts of this chapter have been published:

Chapter 6: DNA-responsive polyisocyanopeptide hydrogels with stress-stiffening capacity

6.1 Introduction

Biomimetic stimuli-responsive hydrogels have gained a lot of attention in the materials science community, both from a fundamental and an application point-of-view.[1–5] In particular, the high specificity and predictability of DNA self-assembly has allowed for the design and synthesis of many functional DNA-hybrid hydrogels that are responsive to various external stimuli (such as pH,[6] temperature,[7] DNA[8]) with applications in sensing,[9] purification,[10] controlled release[7,11] and as bio-scaffolds.[12,13] Just as most other synthetic hydrogels, DNA-hybrid hydrogels lack one crucial property present in natural materials: the ability to stress-stiffen, i.e. to become stiffer when stressed beyond a certain critical stress (σ_C). Furthermore, these hydrogel assemblies are limited by slow reaction kinetics and the large DNA quantities needed for a measurable response. In this chapter a novel DNA cross-linked hydrogel is presented. This hydogel stress-stiffens in the biologically relevant stress range and is sensitive to micromolar concentrations of DNA.

This hydrogel is based on a previously developed synthetic, thermo-responsive hydrogel that consists of helical oligo(ethylene glycol)-functionalized polyisocyanopeptides (PIC).[14,15] These PIC hydrogels form a biomimetic network that stress-stiffens in a stress regime similar to natural scaffolds assembled from extracellular (collagen, fibrin) or intracellular (F-actin, microtubules) biopolymers.[16,17] Moreover, the onset of stress-stiffening was identified as an important parameter for controlling stem cell fate in these 3D biomimetic hydrogel scaffolds.[18] In this chapter, the favorable properties of DNA as a stimuli-responsive supramolecular assembly unit are combined with the stress-stiffening PIC hydrogel to achieve full user-defined control of its mechanical properties.[19] Single stranded (ss) DNA was grafted to PICs and these anchor points were used to cross-link the PIC polymers with a bridging complementary DNA strand. A thorough rheological analysis was used to precisely determine the influence of various parameters (cross-linker DNA, polymer concentration, polymer length and temperature) on the mechanical properties of the hydrogel. The stress-stiffening properties of the PIC hydrogel are shown to be retained in the DNA cross-linked hydrogel, and the stiffness and critical stress of the hydrogel network can be conveniently tuned by the DNA cross-linker concentration. Furthermore, the DNA-mediated gelation process can be reversed by adding toeholds on the bridging DNA, thereby allowing full bi-directional control of the mechanical material properties. This combination of thermo-responsive PIC polymers

with controllable and responsive DNA elements offers a versatile platform with various potential applications in biomedical and materials sciences.

6.2 Results

6.2.1 Synthesis and characterization of DNA-responsive polyisocyanopeptide hydrogels

The synthesis and working principle of the DNA-responsive hydrogel are depicted in Figure 6.1. It is based on tetra(ethylene glycol)-functionalized PIC polymers. Azide-functionalized PICs were synthesized via a nickel(II)-catalyzed co-polymerization of the tetra(ethylene glycol)-functionalized isocyano-(D)-alanyl-(L)-alanine monomer and the corresponding azide-appended monomer, similar as described in chapter 2 of this thesis.[20] Using a 30:1 molar ratio of the corresponding monomers, the statistical average distance between the functional azide groups on the polymer chains was 3.5 nm. These azide moieties were subsequently used to couple ssDNA oligonucleotides functionalized with a strained alkyne.[21] For DNA coupling, 5'-NH_2-DNA A and 3'-NH_2-DNA B (Table 6.1) were first reacted with the NHS ester-functionalized azadibenzocyclooctyne DBCO-PEG_4-NHS. The DBCO-groups were subsequently coupled to the azide-functionalized PIC using a strain promoted azide-alkyne cycloaddition reaction[22], resulting in two different DNA functionalized polymers PIC-DNA A and PIC-DNA B, respectively. The 3'-11 nucleotides of DNA A and 5'-11 nucleotides of DNA B were designed to complement DNA C (22 nucleotides) to form cross-links between the PIC-DNA A and PIC-DNA B polymers. A high reaction efficiency (~90 % ssDNA coupling) was obtained as determined using a fluorogenic coumarin dye assay that quantifies the concentration of DBCO (Figure A6.1.1).
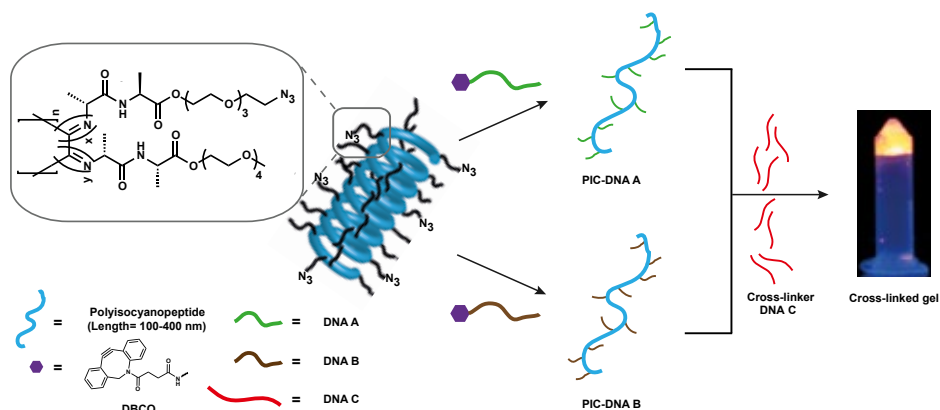
Figure 6.1. Synthesis of the DNA-responsive PIC hydrogel. The N_3-containing PIC polymer is functionalized with DNA carrying a DBCO reactive group. The resulting PIC-DNA A and PIC-DNA B conjugates are mixed with cross-linker DNA C to induce hydrogel formation at room temperature. Staining the dsDNA elements with ethidium bromide in an inverted Eppendorf tube proves the formation of a stable hydrogel network.

Table 6.1. DNA sequences used in this study.

Single-stranded DNA	DNA Sequence (5'-->3')	No. of Nucleotides
DNA A	NH_2-TTT TTT TCA ACA TCA GT	17
DNA B	CTG ATA AGC TAT TTT TT-NH_2	17
DNA C	TAG CTT ATC AGA CTG ATG TTG A	22
Non-complementary DNA (NC)	TCA ACA TCA GTC TGA TAA GCT A	22
DNA C'	C CAC ATA CAT TAG CTT ATC AGA CTG ATG TTG A	32
DNA D	TCA ACA TCA GTC TGA TAA GCT AAT GTA TGT GG	32
DNA M	TAG CTT ATC AGA CTG ATG TT**A** A	22

The PIC polymer exhibits a temperature-dependent sol-to-gel transition as a result of polymer bundling induced by the hydrophobic aggregation of the tetra(ethylene glycol) tails.[17,18] To obtain a first proof that DNA cross-links can promote gel formation below the PIC transition temperature, the rheological properties of samples prepared from polymers of different length were investigated over a range of different temperatures. Four DNA-functionalized PIC polymers were

synthesized with different average lengths of 125 nm (**P1**), 225 nm (**P2**), 297 nm (**P3**) and 350 nm (**P4**) by varying the nickel catalyst to monomer ratio (a lower ratio corresponds to a higher average polymer length). Polymer lengths were estimated using atomic force microscopy (Figure A6.1.2 and Figure A6.1.3). PIC-DNA A and PIC-DNA B polymers of identical length were mixed with complementary DNA C at 4 °C to facilitate easy handling. The total polymer concentration was kept constant at 1.8 mg mL^{-1} for all experiments.

Hydrogel formation was analyzed using rheological measurements over a range of different temperatures in the absence or presence of complementary DNA C in near stoichiometric amounts. For the longest DNA-functionalized polymer **P4**, a sharp sol-to-gel transition was observed at ~39 °C in the absence of DNA C (Figure A6.1.4a). In contrast, no sol-to-gel transition was detected for the shortest polymer **P1** measured under identical conditions. A very weak gel was only formed when the sample was heated above 50 °C (Figure A6.1.4b). When DNA C was added, however, stable hydrogels already formed at room temperature, independent of polymer length (Figure 6.2a). The presence of a network was confirmed by cryo-scanning electron microscopy of the DNA cross-linked **P4** hydrogel, which showed a fibrous and porous structure (Supporting Information, Figure A6.1.5). The addition of a non-complementary DNA strand (Figure 6.2b) did not result in hydrogel formation at room temperature. These results clearly show that the DNA interaction is able to induce gel formation below the PIC gelation temperature, independent of the previously established gelation mechanism dominated by hydrophobic interactions between PIC polymers.

6.2.2 Detailed rheological analysis of DNA-responsive polyisocyanopeptide hydrogels

The mechanical properties of the DNA cross-linked gels were subsequently characterized in more detail at 30 °C, where the PIC-DNA polymers do not gelate without the addition of cross-linker DNA. First, the kinetics of gel formation were determined by following the time evolution of the storage modulus (G') after the addition of cross-linker DNA C to a pre-mixed solution of PIC-DNA A and PIC-DNA B. All four polymers formed DNA cross-linked gels within seconds, as demonstrated by
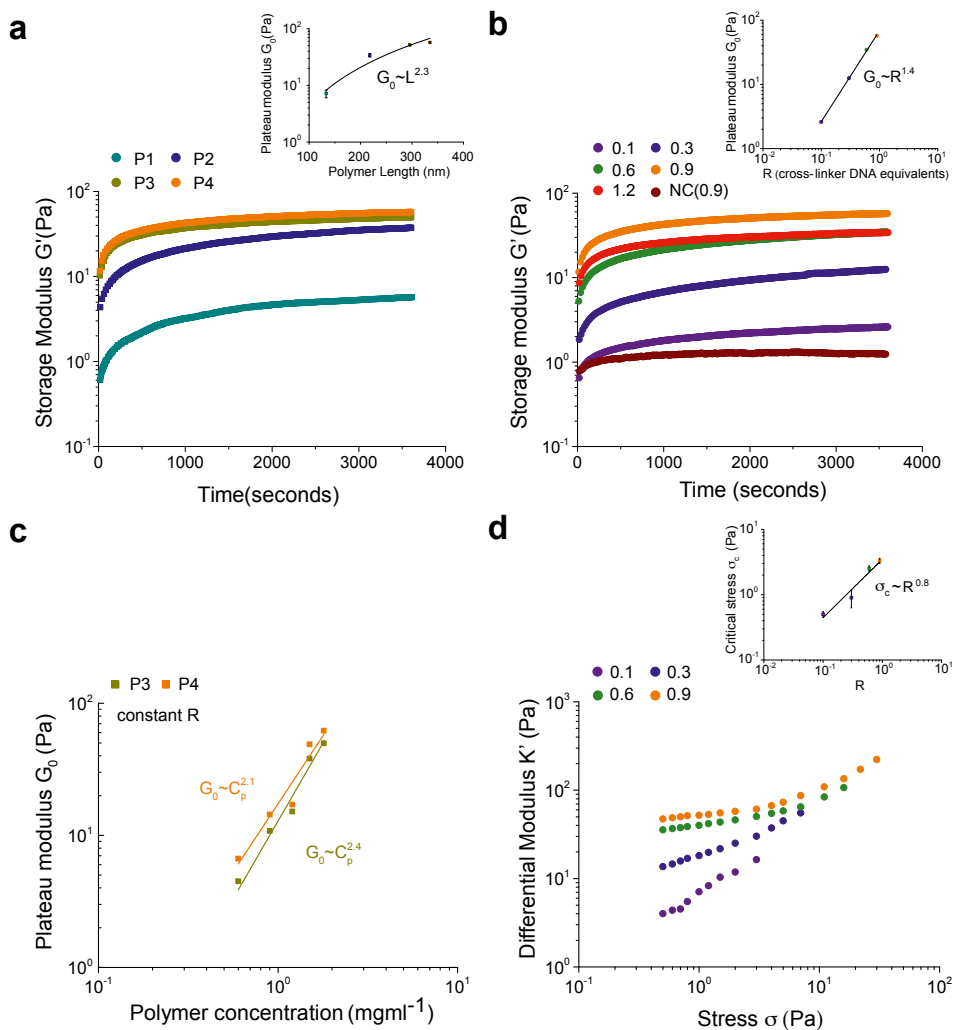
Figure 6.2. Kinetic rheology measurements of DNA cross-linked hydrogels at fixed frequency (1 Hz) and strain (2%) at 30 °C in PBS, 10 mM $MgCl_2$, pH 7.4. a) Time evolution of the storage modulus (G') after addition of cross-linker DNA C to DNA A and DNA B functionalized PIC polymers **P1**-**P4** at 1.8 mg mL^{-1} with cross-linker ratio (R) of 0.9. The inset shows the plateau modulus (G_0) as a function of polymer length. b) Time evolution of G' after addition of cross-linker DNA C at R = 0.1, 0.3, 0.6, 0.9 and 1.2 as well as non-complementary DNA NC. The inset shows the dependence of G_0 on R. c) G_0 as a function of concentration of the DNA functionalized polymers **P3** and **P4** (c_p = 0.6, 0.9, 1.2, 1.5, and 1.8 mg mL^{-1}) at R = 0.9. The solid lines are power law fits and show that **P3** scales with $c_p^{2.4}$ and **P4** scales with $c_p^{2.1}$. d) Differential modulus (K') against stress (σ) for the DNA cross-linked **P4** hydrogel at different R (0.1, 0.3, 0.6, and 0.9) showing stress-stiffening behavior of the PIC-DNA hydrogel. The inset shows that the critical stress ($σ_C$) scales directly with R.

a rapid increase of G'. The storage modulus levels off to plateau modulus G_0 over a period of 1 hour (Figure 6.2a). G_0 scales with polymer length L as $G_0 \propto L^{2.3}$ (Figure 6.2a inset). This is in perfect agreement with theoretical predictions for hydrogels derived from semi-flexible biopolymers[23] and compares to values reported for non-functionalized PIC hydrogels.[17,18] These results suggest that the DNA cross-linked hydrogel possesses similar mechanical properties at 30 °C as the original hydrophobically bundled PIC hydrogel that only forms at temperatures above 50 °C.

The mechanical properties of semi-flexible polymer networks do not only depend on polymer length, but also on the density of cross-links. Using the **P4** hydrogel, the influence of the DNA C concentration on gel stiffness was investigated. An optimal response, as expressed in the highest G_0 value, was obtained at 0.9 equivalents of cross-linker DNA C with respect to the DNA concentration (50 µM) on the PIC-DNA A and PIC-DNA B polymers (Figure 6.2b). As expected, an excess (1.2 eq.) of DNA C led to a lower gel stiffness due to saturation of the A and B binding sites. Importantly, stable DNA cross-linked hydrogels were already formed at DNA cross-linker concentrations as low as 5 µM. This is much lower than observed for other synthetic DNA cross-linked hydrogels, which generally require DNA concentrations above 1 mM to maintain a well-defined gel state.[9,24–26] G_0 scales with the cross-linker DNA concentration (defined as the ratio R: DNA C/DNA A or DNA B) as $G_0 \propto R^n$ with n = 1.4 for **P4** (Figure 6.2b). Additionally, G_0 scales with the polymer concentration (c_p) as $G_0 \propto c_p{}^n$ with n = 2.3 for **P3** and 2.1 for **P4** at constant R (0.9) (Figure 6.2c). These observations are fully consistent with theoretical predictions[27,28] ($G_0 \propto c_p{}^{11/5}$) and experimental observations of bundle formation in cross-linked semi-flexible biopolymer networks. For example, in fascin-directed self-assembly of the cytoskeletal protein actin G_0 scales with the actin polymer and fascin cross-linker concentrations with n equals ~1.5 and ~2.4, respectively.[29,30] For the assembly of intermediate filaments $G_0 \propto c_p{}^{2-2.5}$ was observed.[31]

The DNA cross-linked PIC hydrogels exhibit the same mechanical response as the original PIC hydrogel and typical protein-based networks in the linear rheological regime. As mentioned before, the key fundamental property of semi-flexible biopolymer networks is their stress-stiffening behavior. The next goal was therefore to establish if this similarity also extended to the nonlinear regime. Accordingly, the mechanical behavior of the DNA cross-linked **P4** gel (at 0.9 eq. DNA C) was studied in the non-linear regime, using a previously described pre-stress protocol at 30 °C.[17] The gel was subjected to a constant increasing pre-stress (σ) with a small oscillatory stress (δσ) superposed upon it. The resultant oscillatory strain (δγ) was recorded to extract the differential modulus K' (= δσ/δγ) at a specific frequency (1 Hz) for each value of σ. To validate the suitability of this measurement, it

was first experimentally verified using low-frequency rheological measurements that the cross-linked **P4** gel did not relax on a time scale 10 times the measurement time, even in very soft regimes (Figure A6.1.6). Plotting K′ as a function of applied stress for different concentrations of cross-linker DNA, clearly showed a linear regime at low σ and a non-linear regime at higher σ for all tested concentrations (Figure 6.2d). G_0 showed a $G_0 \propto \sigma_C^{1.5}$ dependence (Figure A6.1.7), which is again in perfect agreement with theory as well as experimental observations for intermediate filament gels.[31] The critical stress σ_C scaled linearly with the cross-linker concentration (Figure 6.2d) even at very low stress values of 0.5 - 4 Pa.

These results establish that this new class of DNA cross-linked PIC hydrogels perfectly mimics the mechanical properties of semi-flexible biopolymer networks. This newly developed hybrid material shows a biomimetic mechanical response in the biologically relevant stress range, spanning across both the linear and non-linear regime. The scaling response of G_0 and σ_C towards DNA cross-linker concentration makes this an effective parameter to tune the mechanical properties of this new biomimetic hydrogel.

6.2.3 Dual responsiveness of DNA cross-linked polyisocyanopeptide hydrogels

To better define the contribution of cross-link stability to gel formation and to explore the interplay between DNA-cross-linked hydrogels and hydrophobically-cross-linked PIC hydrogels, the rheology temperature profiles of the **P4** DNA-cross-linked hydrogel were examined in more detail. At high DNA C ratios (> 0.3 eq. DNA C), first a slight increase followed by a decrease in G' is observed upon raising the temperature (Figure 6.3a). The increase originates from the onset of PIC gelation as the same trend is observed in the absence of DNA C or at very low DNA C ratios (0.1 eq.). Simultaneously, the storage to loss modulus ratio G'/G" starts to decrease, however. It is lowest at the melting temperature of the 22 base pair (bp) nicked DNA duplex (45 °C, Figure A6.1.8), indicating a transformation from gel to viscous material upon DNA dissociation. When the temperature is further increased, the G'/G" ratio starts to increase again and eventually follows the trend observed for the non-cross-linked PIC polymer. Apparently, the hydrophobic bundling of the tetra(ethylene glycol) tails of the PIC polymers starts to dominate at temperatures above the DNA melting temperature, causing the material to adopt the mechanical properties of a normal PIC hydrogel (Figure 6.3a, Figure A6.1.9).
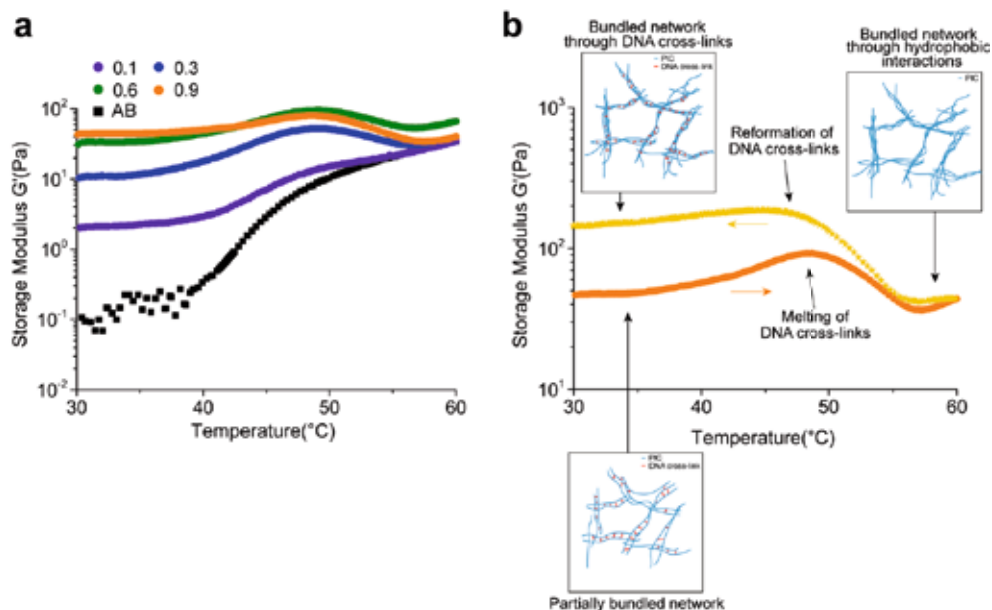
Figure 6.3. Temperature dependent gelation of PIC-DNA hydrogels. a) G' as a function of temperature for the **P4** hydrogel at different cross-linker C ratios (R = 0.1, 0.3, 0.6 and 0.9), including a control sample without cross-linker DNA (PBS, 10 mM MgCl$_2$, pH 7.4). b) G' as a function of temperature for the DNA-**P4** at R = 0.9 upon raising (orange) and lowering (yellow) the temperature. The insets show schematics of different gelation states.

The observed temperature profiles are consistent with an additive effect of DNA and hydrophobically-induced gelation of PIC hydrogels. Upon heating, the material undergoes a transition from a DNA-cross-linked hydrogel to a PIC-bundled hydrogel. It should therefore be possible to control the temperature-dependent mechanical properties of the hydrogel using DNA cross-links of different thermodynamic stability. Indeed, the downward transition attributed to DNA melting was shifted to lower temperatures when using a DNA cross-link containing a single mismatch (DNA M, Table 6.1). The observed 8 °C shift is in perfect agreement with the 8 °C lower melting temperature of the mismatched DNA duplex (Figure A6.1.10). We next introduced a DNA linker with the highest possible stability by introducing a covalent DNA cross-link. This covalent cross-link was obtained by enzymatic splint-ligation of the DNA ABC duplex. In this case a gradual increase in G' was observed (Figure A6.1.11), clearly showing the additive effect of DNA and hydrophobic cross-links. This interplay between DNA hydrogel and PIC hydrogel stability, which can be controlled by base pair composition and polymer length, opens the possibility for tuning and further separating the gel-to-sol and sol-to-gel transitions upon raising the temperature.

These observations are consistent with a model of gel formation as depicted in Figure 6.3b. Addition of DNA C to PIC-DNA A and PIC-DNA B at temperatures below the DNA melting and PIC gelation temperatures initially zips single polymer chains together to form a partially bundled network. A zipping mechanism instead of a random intermolecular interaction can be expected. The distance between adjacent DNA molecules on the polymers is only ~6 nm. In contrast, the average cross-distance between polymers as estimated from the total polymer length per volume unit (0.21×10^{15} m^{-2} at 1.8 mg mL^{-1} PIC) is ~52 nm. After linking, the DNA cross-linker length of ~13.5 nm (12 nt ssDNA + 22 bp double stranded DNA) brings the PIC polymers closer together, which can promote PIC bundling. Upon raising the temperature, the DNA cross-links are disrupted at the DNA melting temperature, thereby allowing the partially bundled network to evolve into a bundled network dominated by hydrophobic interactions. This is confirmed by the temperature dependence of σ_C and the independence of σ_C from the DNA cross-linker ratio at 60 $^{\circ}$C (Figure A6.1.9). This simple model predicts hysteresis for the first heating-cooling cycle. If a DNA-functionalized PIC bundled network is cooled down, cross-linker C can anneal to already bundled PIC polymers thereby stabilizing the existing structure. Indeed, cooling the network back to 30 $^{\circ}$C shows a different profile resulting in a higher G' when compared to the original DNA cross-linked gel. This clearly suggests a higher order of the re-assembled DNA hydrogel. This effect of pre-bundling remains identical with subsequent heating-cooling cycles (Figure 3b, Figure A6.1.12).

6.2.4 Dynamic control of the mechanical properties of DNA cross-linked polyisocyanopeptide hydrogels

Modulating the mechanical properties of hydrogels in a user-defined dynamic way is of critical importance in a variety of materials science applications.[12,32] In order to demonstrate dynamic control over the DNA cross-linked **P4** gel, a soft gel (G_0 ~10 Pa) was prepared by adding 0.3 equivalents of the cross-linker DNA C (Figure 6.4a). Within 1 hour after adding a higher amount (0.3 or 0.6 eq.) of DNA C the preformed gel was converted into a stiffer gel with G_0 ~25 Pa and ~31 Pa, respectively, while σ_C remained similar (Figure 6.4a,b and A6.1.13a,b). Conversely, softer gels could be generated from stiffer hydrogels using toehold-mediated strand displacement (Figure A6.1.14). Using this approach, an incoming DNA strand first binds to a short stretch of single-stranded nucleotides (the toehold) next to a double-stranded duplex. Toehold binding is followed by displacement of one or more pre-hybridized strands in the original duplex through branch migration.[33] DNA cross-linker C was extended with a 10 nucleotide toehold sequence to yield DNA C' (Table 6.1). This sequence was

used to prepare a hydrogel at 0.9 equivalents of DNA C'. The DNA C' hydrogel showed the same mechanical properties as the original DNA cross-linked gel (Figure A6.1.15). Strand displacement was initiated by adding the complement of C', DNA D (Table 6.1) at 0.3 or 0.6 equivalents to this pre-formed gel. The network dissolved rapidly into a softer gel with a marked decrease in G_0 as well as σ_C (Figure 6.4c,d and Figure A6.1.13c,d). Together, these results clearly demonstrate that the DNA cross-linked PIC hydrogel can be turned into a stiffer or softer network in a user-defined fashion, allowing for unprecedented control over the gel mechanical properties. Interestingly, the combination of cross-linker concentration, toehold strategy and temperature dependence opens up the possibility for designing oscillating gel networks with dual input.
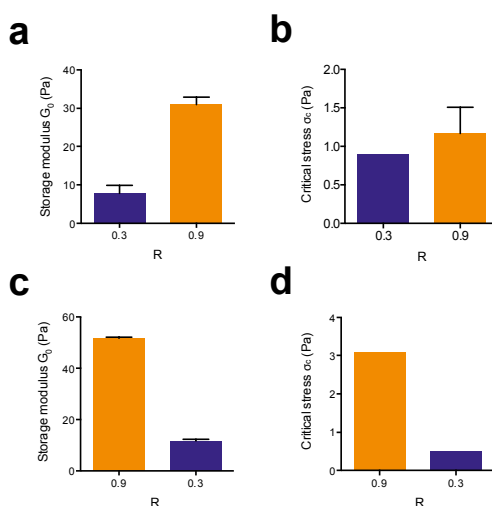
Figure 6.4. Tunable control of PIC-DNA hydrogels. a) Changes in G_0 and σ_C after adding 0.6 equivalents of DNA C to a pre-formed DNA-**P4** gel cross-linked with 0.3 equivalents of DNA C (PBS, 10 mM $MgCl_2$, pH 7.4, 30 °C). b) Changes in G_0 and σ_C after adding 0.6 equivalents of DNA D to a pre-formed gel cross-linked with 0.9 equivalents of toehold cross-linker DNA C' (PBS, 10 mM $MgCl_2$, pH 7.4, 30 °C).

6.3 Conclusion

In summary, a novel DNA-responsive hydrogel system composed of DNA cross-linked PIC polymers was designed. This hydrogel forms at micromolar concentrations of the DNA cross-linker and exhibits striking similarity with bundled networks formed from semi-flexible biological filaments. A thorough rheological analysis did not only show that this hydrogel does stress-stiffen, but also that its mechanical response can be tuned by changing a number of variables such as polymer length and concentration. Most importantly, the easily accessible cross-linker

ratio allows for controlling the gel stiffness as expressed in G_0 and σ_C. Furthermore, the bidirectional dynamic behaviour of the material is demonstrated by facile and rapid tuning of the gel stiffness by exogenous DNA delivery. Although relatively simple ssDNA sequences were selected as model systems to form the DNA cross-links, more complicated sequences with additional functionalities can also be applied to this hydrogel system, such as the pH-responsive i-motifs,[34] endonuclease restriction sites or aptamers specific for an analyte or protein.[35] The material developed in this chapter potentially allows for the design and synthesis of stimuli-responsive biomimetic scaffolds. Their controlled mechanical properties in physiologically relevant environments will allow for a large number of potential applications in 3D cell culture, tissue engineering, drug delivery and diagnostics.

6.4 Experimental section

Synthesis of azide-functionalized polyisocyanopeptides (P1-P4)

The azide-functionalized, water-soluble polyisocyanopeptide polymers (PIC) and the corresponding isocyanopeptide monomers were synthesized as described in chapter 2 of this thesis.[20] For all polymers, the ratio between the non-functional methoxy (OMe) and the functional azide (N_3) monomers was 30:1. After mixing the two monomers in freshly distilled toluene, the $Ni(ClO_4)_2 \cdot 6H_2O$ catalyst (dissolved in 9/1 toluene/ethanol) was added. The mixture was stirred for 2-3 days before it was precipitated 3x in di-isopropyl ether. A different molar ratio of catalyst over monomer was used to control the length of the polymers. Catalyst/monomer ratios of 1/1000 (**P1**), 1/2000 (**P2**), 1/5000 (**P3**) and 1/10000 (**P4**) were used to obtain polymers spanning a range from 125-350 nm.

Polymer characterization

The polymer length was determined using atomic force microscopy (AFM). The polymers (1 µg mL^{-1}) were drop-casted from water on freshly cleaved mica and incubated for 10 minutes. The remaining liquid was removed and the sample was dried in a stream of N_2. AFM images were recorded in tapping mode in air using Nanoscope IV or Dimension 3100 instruments (Bruker) and NSG-10 cantilevers (NT-MDT). The polymer length was determined manually using the program ImageJ[36] (Figure A6.1.3 and A6.1.4).

Functionalization of DNA with DBCO-PEG4-NHS

DNA oligonucleotides (Table 6.1) were obtained from Integrated DNA Technologies either in HPLC-purified or 'desalted-only' grades. 'Desalted-only' DNA was purified further in-house using preparative denaturing polyacrylamide gel electrophoresis (PAGE; 20%).[37] The DNA was eluted from the gel, concentrated using an ion exchange column (Resource Q, 1 ml column, ÄKTA FPLC; GE Healthcare) and desalted by ethanol precipitation. To functionalize the DNA with the strained alkyne azadibenzylcyclooctyne (DBCO), the NH_2-modified DNA was reacted with the heterobifunctional reagent DBCO-PEG4-NHS (Jena Bioscience). For a typical experiment, a solution of 500 µM NH_2-modified DNA and 1.25 mM DBCO-PEG4-NHS was prepared in 50 mM borate buffer pH 8.5 and incubated at 25 °C for 2 hours. The product was subsequently purified using Illustra Microspin G-25 columns (GE Healthcare). The final yield of DNA was determined from an absorption measurement at 260 nm on a Nanodrop fibre-optic spectrophotometer (ND-1000, Thermo Scientific). To confirm the

presence of DBCO on the DNA molecule, a small amount of the product was reacted with a fluorescent ATTO647-azide dye. After incubating the DNA with a 10-fold excess of dye, the DNA was purified by ethanol precipitation and analyzed using denaturing 20% PAGE (Figure A6.1.1a).

Synthesis of the DNA-functionalized PIC polymer

Stock solutions of the PIC polymers **P1**-**P4** were prepared by dissolving 5 mg mL^{-1} of PIC polymer (corresponding to 13.9 mM monomer concentration) containing statistically 1/30 azide-functionalized monomer (0.46 mM) in ultrapure water. DBCO-functionalized DNA A or DNA B were mixed with the azide-functionalized PIC polymer in a 1:50 ratio (125 µM DNA : 6.25 mM PIC monomer) in phosphate buffered saline (PBS, pH 7.4) and incubated at 25 °C for 12 hours. The yield of this conjugation reaction was determined based on the amount of non-conjugated DNA molecules, containing unreacted DBCO. The concentration of DBCO in the reaction mixture was quantified using a fluorogenic 3-azido-7-hydroxycoumarin dye, which shows an increase in fluorescence upon 'clicking' to DBCO. The fluorescence intensity of coumarin was measured using a Tecan Infinite 200 microplate reader and related to a calibration curve of clicked product (Figure A6.1.1b). As the yield of the reaction was ~90 % (Figure A6.1.1c), the polymer conjugate was used without further purification.

Hydrogel formation

PIC-DNA A and PIC-DNA B conjugates were mixed at 4 °C in PBS, 10 mM MgCl$_2$, pH 7.4. To induce gel formation, complementary DNA C or C' was added at defined ratios.

Enzymatic ligation of DNA-functionalized PICs

5'-Phosphorylated DNA B was conjugated to the PIC polymer using the procedure described above. DNA C was used as a splint to ligate DNA A and 5'-PO$_4$-DNA B coupled to the PIC polymers. The reaction was performed at 30 °C (PBS, 10 mM MgCl$_2$) using T4 DNA ligase (Thermo Fisher Scientific). Before performing an enzymatic ligation with polymer conjugated DNA, the reaction was first evaluated under identical conditions using non-conjugated DNA and confirmed with denaturing 20% PAGE (Figure A6.1.11).

Rheology

The total polymer concentration was kept constant at 1.8 mg mL^{-1} corresponding to 50 µM of the respective DNA linkers for all experiments. Time-sweep oscillatory rheology measurements were carried out with a stress-controlled rheometer (Discovery HR-1, TA Instruments). A parallel plate geometry (40 mm diameter; aluminum) was used with a gap of 200 µm. All measurements were performed in a temperature-controlled environment and an oil sealing was used to minimize sample evaporation. Linear rheology experiments were performed at a fixed frequency (1 Hz) and strain (2%). For the variable temperature rheology experiments, the temperature was ramped at 1 °C min^{-1}.

The non-linear regime (critical stress, σ_c) was investigated using a previously described pre-stress protocol.[17] The gel sample (kept at 30 °C) was subjected to a constant pre-stress with a small oscillatory stress ($\delta\sigma$) superposed upon it. The resultant oscillatory strain ($\delta\gamma$) was recorded in a frequency sweep experiment (0.1-10.0 Hz). The measurement was repeated for increasing values of applied pre-stress (σ) to extract the differential modulus K' ($\delta\sigma/\delta\gamma$) at a specific frequency (1 Hz) at each value of σ. σ_c is defined as the stress at which the ratio between the stress σ and the strain γ is not constant, but increases with increasing stress (or strain). The onset of the non-linear region was defined as the stress regime where σ increased by at least 10 % over its original value.

For the experiments where the mechanical properties of the hydrogel were varied by the step-wise addition of new DNA, gels with a pre-defined cross-linker DNA C or DNA C' (including the 10

nucleotide toehold) concentration were pre-formed on the rheometer. Subsequently, additional aliquots of cross-linker DNA C or complementary DNA D were added. The time evolution of G' was then followed on the rheometer as described above.

Cryo-SEM of DNA cross-linked hydrogels

Cryo-scanning electron microscopy (cryo-SEM) was performed on a JEOL 6330 cryo-scanning electron microscope. All samples were loaded onto suitable stub holders with a 20 µL micropipette fitted with sterile tips. Samples were cryo-fixed by plunging them into sub-cooled nitrogen (nitrogen slush) close to the freezing point of nitrogen at -210 °C. The samples were then transferred *in vacuo* to the cold stage of the SEM cryo-preparation chamber. Images were acquired using an electron beam of 7–22 kV.

Melting temperature determination of the different DNA sequences

The melting temperature (T_m) of the DNA duplexes used was determined from UV absorption measurements at 260 nm. Temperature-ramping experiments were carried out from 10 °C to 90 °C at a rate of 1 °C min^{-1} using a Cary 300 Bio UV-VIS spectrometer (Varian) equipped with a temperature controller. The T_m was calculated from the first derivative of the melting curve according to van der Werf *et al*. [38]

6.5 Appendix 6.1: Supplementary figures

a   **b**

c

Samples	Fluorescence Intensity	DBCO concentration (µM)
PIC	20641	17.8
PIC-DNA-A (P4), Zero time	22588	19.3
PIC-DNA-A (P4), After 12 hours	2065	2
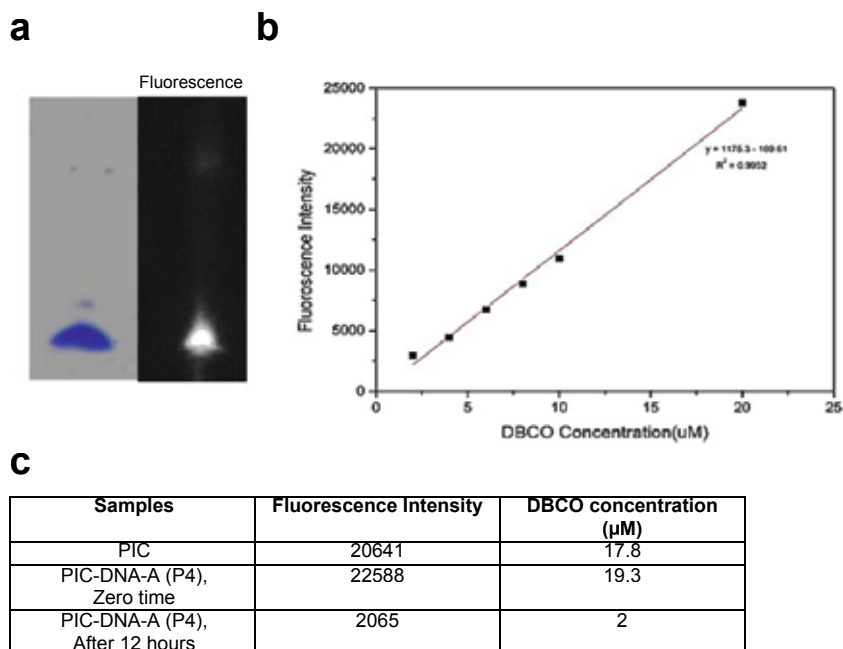
Figure A6.1.1. Experiments to confirm conjugation of DBCO to DNA. a) PAGE analysis (20 %) of the DBCO-functionalized DNA after reaction with the fluorescent dye ATTO647-azide. The left lane shows the DBCO-DNA A conjugate stained with Stains-All. The right lane shows the fluorescent signal of DBCO-DNA A labeled with ATTO647. b, c) 3-azido-7-hydroxy-coumarin dye assay used to quantify the concentration of free DBCO-functionalized DNA before and after reaction with the azide-functionalized PIC polymer. A calibration curve was first established to correlate the fluorescence intensity to the amount of clicked product (b). Comparing the amount of free DBCO before and after incubation with the polymer (12 hours) reveals a high reaction efficiency of ~90 % (c).

a

b

c

d

Figure A6.1.2. AFM analysis. AFM images showing the PIC polymers **P1**-**P4**, dropcasted on freshly cleaved mica.

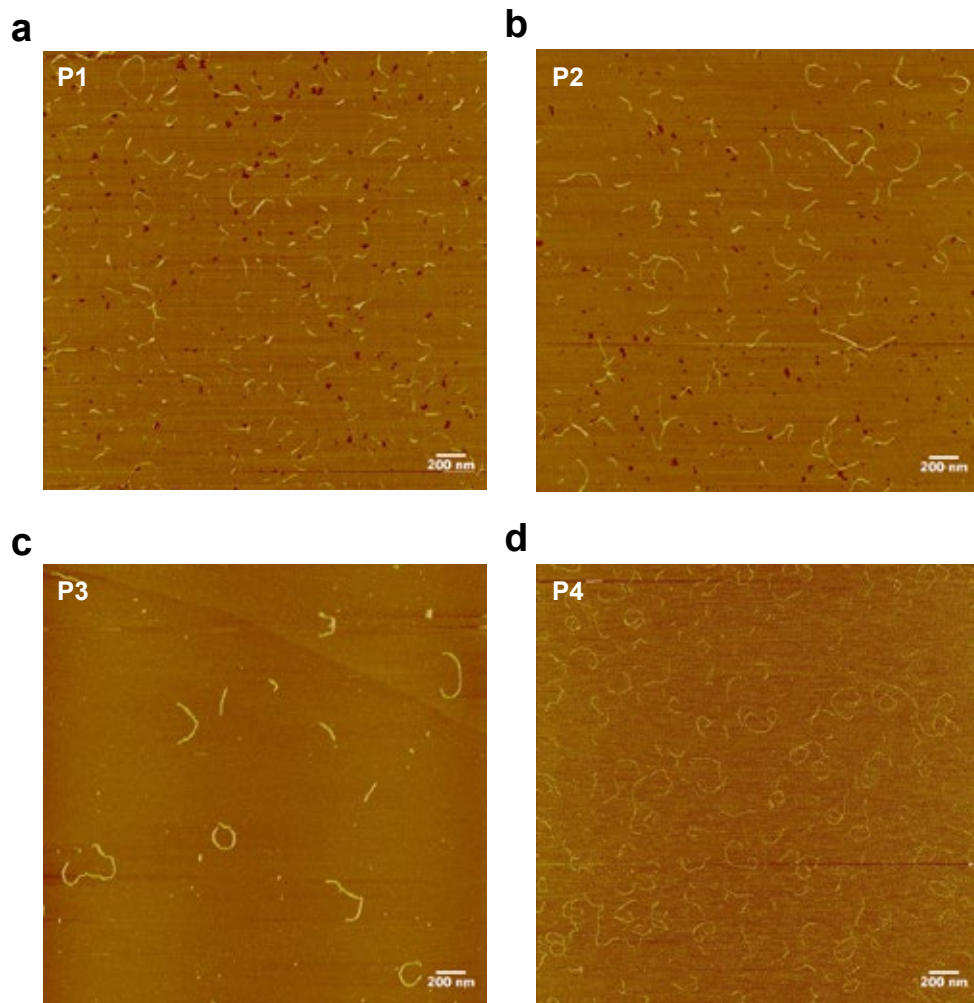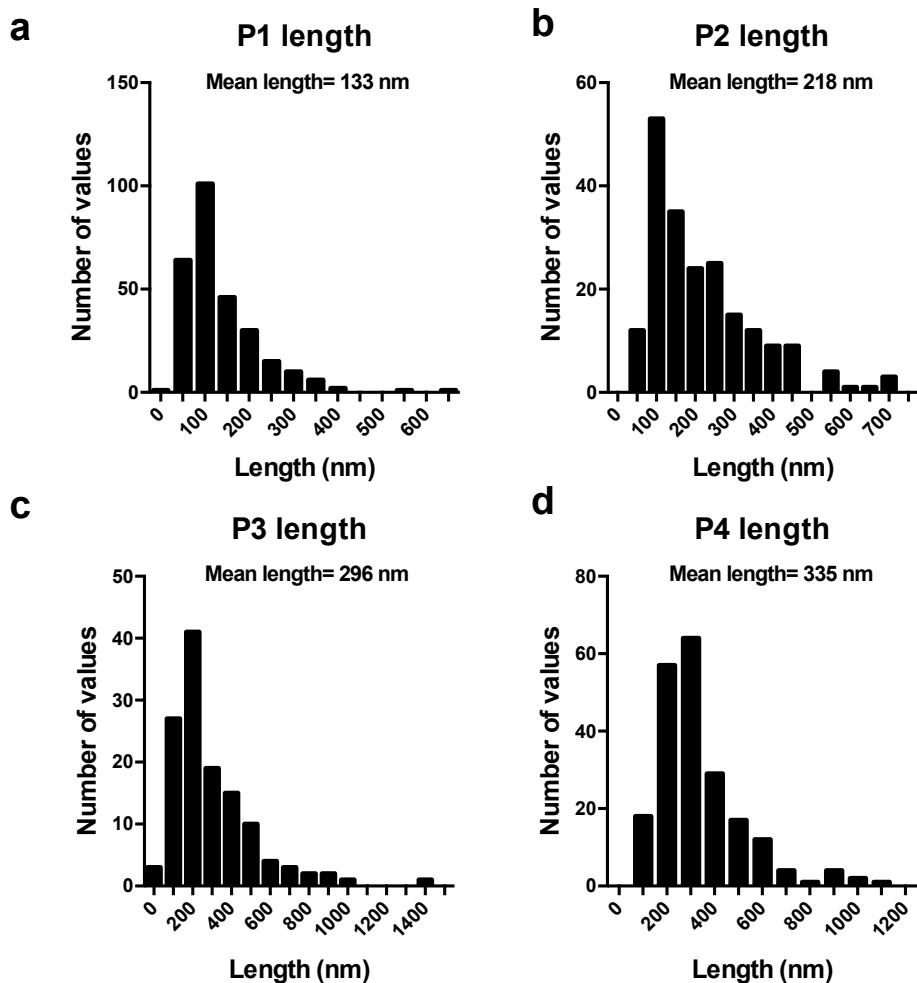**Figure A6.1.3.** Polymer lengths obtained from the AFM images. a) The mean length of **P1** was 133 nm (n = 277), b) the mean length of **P2** was 218 nm (n = 203), c) the mean length of **P3** was 296 nm (n = 296) and d) the mean length of **P4** (n = 209) was 335 nm.

a

b
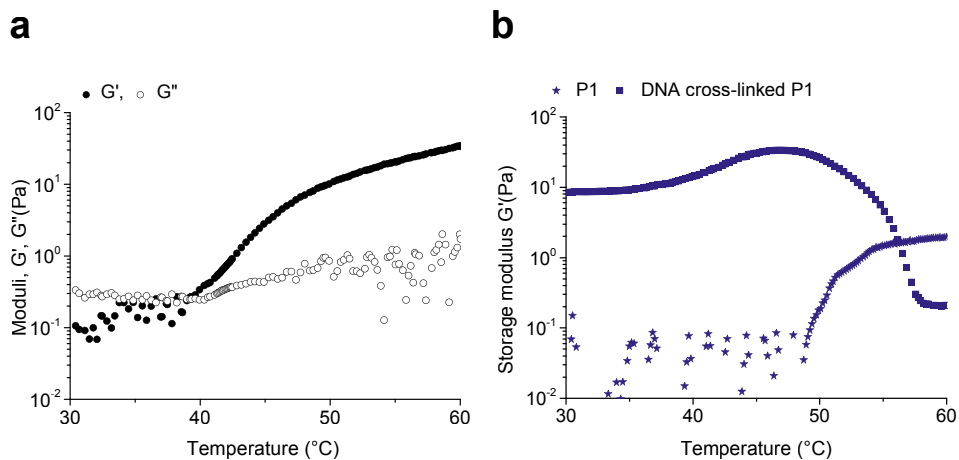
Figure A6.1.4. Temperature-induced gel formation. a) G' as a function of temperature of a mixture for **P4**-DNA A and **P4**-DNA B in the absence of cross-linker DNA C (PBS, 10 mM MgCl$_2$, pH 7.4, 1.8 mg mL^{-1} polymer). The sample shows a sol-to-gel transition above 40 °C indicating that gelation is a result of the hydrophobic interaction between the tetra ethylene glycol side chains. b) Comparison of the gelation behavior of the non-functionalized **P1** polymer and the DNA cross-linked **P1** polymer (0.9 eq. DNA C; PBS, 10 mM MgCl$_2$, pH 7.4; 1.8 mg mL^{-1} polymer). The two samples show very different profiles. At 30 °C, a stable hydrogel is only formed in the case of the DNA cross-linked **P1** polymer.

a

b
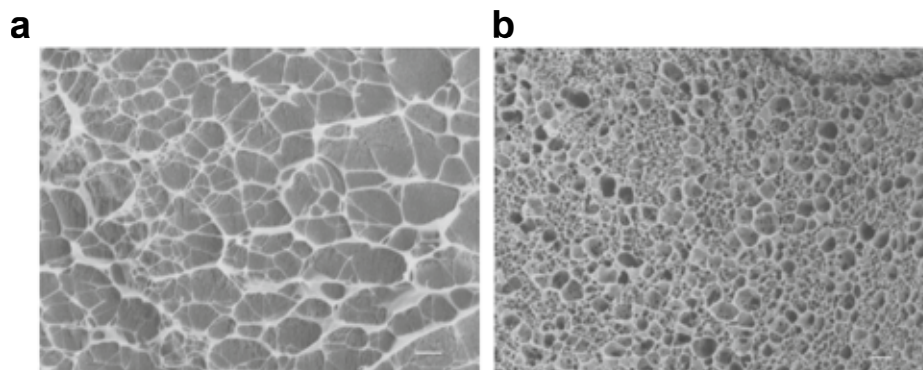
Figure A6.1.5. Cryo-scanning electron micrographs of freeze-dried DNA cross-linked P4 hydrogels at different cross-linker concentrations. a) 0.1 eq. DNA C and b) 0.9 eq. DNA C. The scale bar is 1 μm.
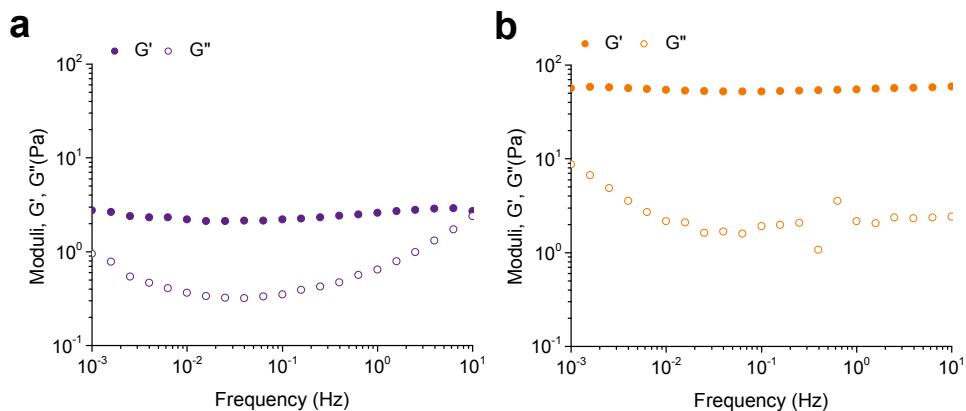
Figure A6.1.6. Frequency dependent rheology of DNA cross-linked hydrogels. Using either 0.1 eq. a) or 0.9 eq. b) of DNA C. The hydrogels, made from polymer **P4**, were stable and did not relax as demonstrated by measuring G' and G" over a range of frequencies (10^{-3} to 10 Hz). All measurements were performed at 30 °C (PBS, 10 mM MgCl$_2$, pH 7.4; 1.8 mg mL^{-1} polymer).
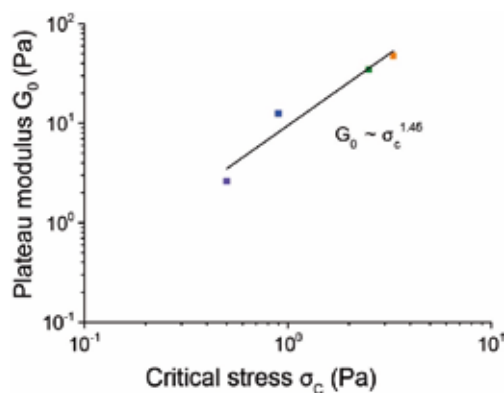
Figure A6.1.7. Relationship between G$_0$ and σ$_C$ obtained from a series of measurements determined at different concentrations of cross-linker DNA C. The polymer concentration (**P4**) was constant at 1.8 mg mL^{-1}. The exponent of 1.45 was obtained from a power law fit.
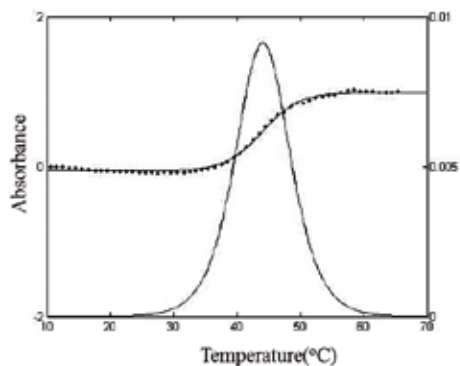
Figure A6.1.8. Melting curve of the non-conjugated DNA ABC complex in PBS, 10 mM MgCl$_2$, pH 7.4. Curve fitting and first derivative analysis yields a T_m of 44.7 ± 1 °C.
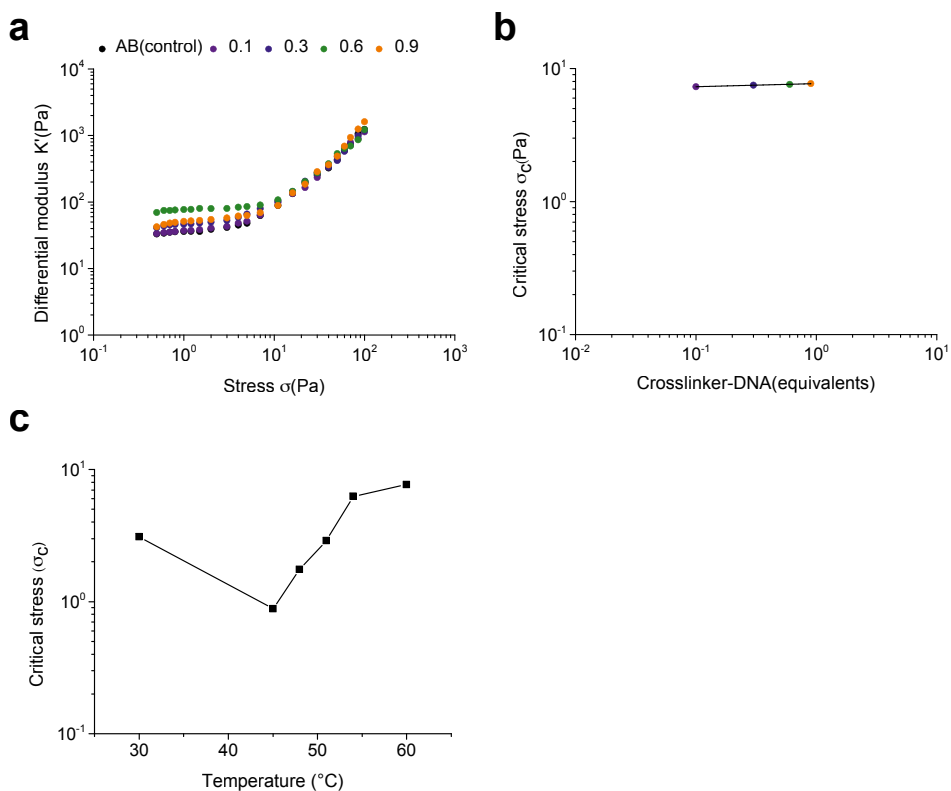
Figure A6.1.9. Non-linear rheology of the DNA cross-linked P4 hydrogel. Differential modulus K' a) and critical stress σ_C b) showing similar non-linear behavior for all samples at 60 °C. At 60 °C σ_C is independent of the DNA cross-link ratio. c) Critical stress measured at a range of temperatures from 30 °C to 60 °C, showing the transition from a DNA cross-linked hydrogel to a PIC-bundled hydrogel.

a

b
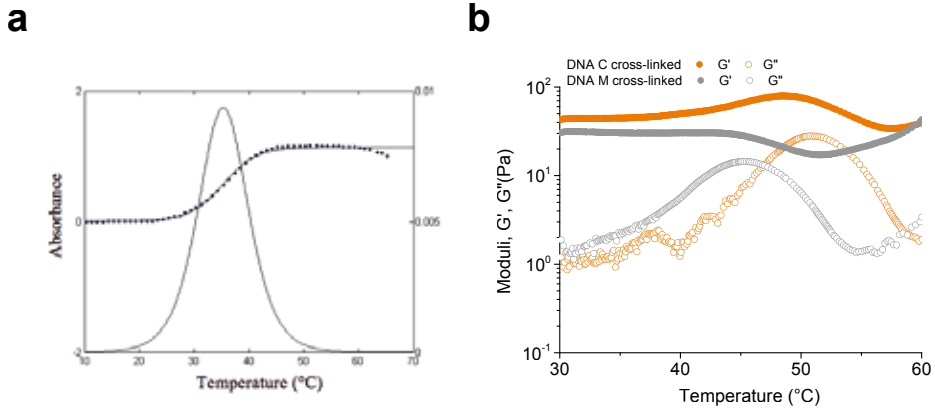
Figure A6.1.10. Temperature-dependent hydrogel formation using a DNA cross-linker with a single mismatch. a) Melting curve of the non-conjugated DNA ABM complex (PBS, 10 mM MgCl$_2$, pH 7.4). The T_m was determined to be 36.2 °C. b) G' and G'' as a function of temperature for the DNA M cross-linked **P4** hydrogel. The G' and G'' temperature profiles are shifted with respect to the DNA C cross-linked hydrogel due to the less stable DNA ABM cross-links (PBS, 10 mM MgCl$_2$, pH 7.4; 1.8 mg mL^{-1} polymer).

a

b
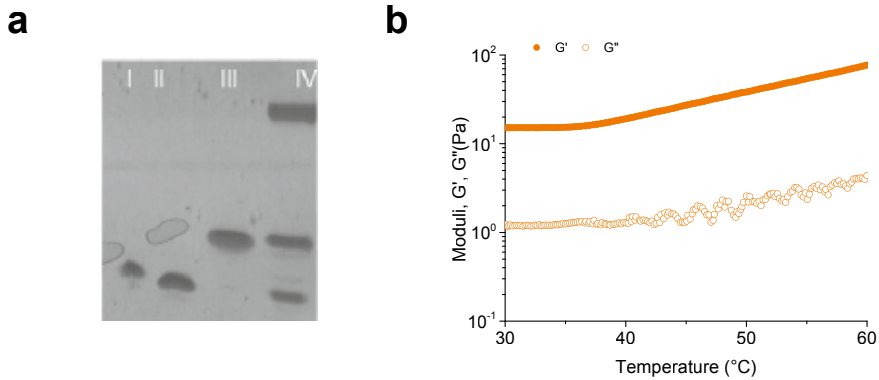
Figure A6.1.11. Hydrogel formation following ligation of DNA A and B**.** a) Analysis of the non-conjugated ABC splint ligation product on 20 % denaturing PAGE. Lane I: DNA A; Lane II: DNA B; Lane III: DNA C; Lane IV: Ligated DNA A and B. b) G' and G'' as a function of temperature for the covalently cross-linked (i.e. ligated) **P4** hydrogel (PBS, 10 mM MgCl$_2$, pH 7.4, 30 °C; 1.8 mg mL^{-1} polymer).

151
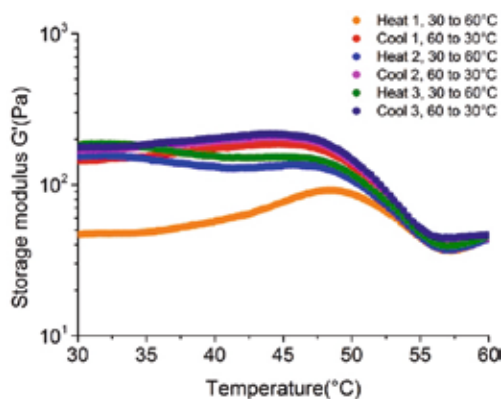
Figure A6.1.12. Heating and cooling cycles. Series of temperature scans for one DNA cross-linked hydrogel sample (**P4**-DNA A and **P4**-DNA B cross-linked with 0.9 eq. of DNA C; 1.8 mg mL^{-1} polymer). The sample was subjected to 3 consecutive cycles of heating (30 °C to 60 °C) and cooling (60 °C to 30 °C).
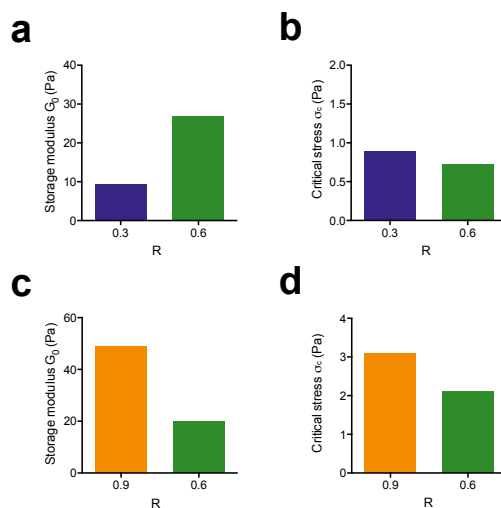
Figure A6.1.13. Tunable control of DNA-PIC hydrogels. a,b) Changes in G_0 a) and σ_C b) when increasing the concentration of DNA C from 0.3 eq. to 0.6 eq. (1.8 mg mL^{-1} polymer). c,d) Changes in G_0 c) and σ_C d) following toehold-initiated strand displacement (addition of 0.3 eq. of complementary DNA D to a **P4** gel cross-linked with 0.9 eq. of DNA C'; 1.8 mg mL^{-1} polymer).
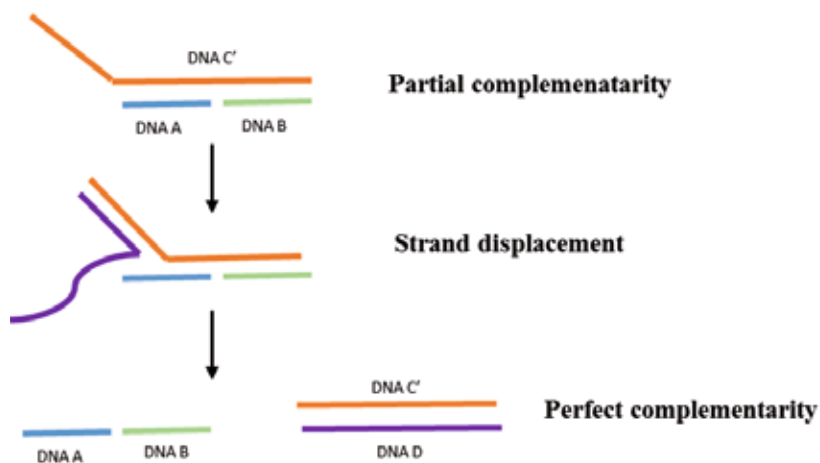
Figure A6.1.14. Toehold strategy. A DNA hydrogel is formed with cross-linker DNA C' containing a 10 nucleotide toehold at the 5'-end. Complementary DNA D binds the toehold sequence, initiating displacement of the DNA A and DNA B sequences by branch migration.
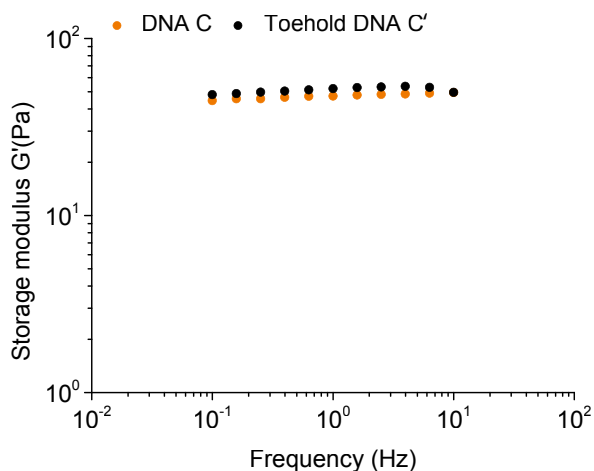
Figure A6.1.15. Control experiment to compare the properties of DNA C and toehold DNA C' cross-linked P4 hydrogels. The measured G' values demonstrate a similar stiffness of both hydrogels over the frequency range tested (PBS, 10 mM MgCl$_2$, pH 7.4, 30 °C; 0.9 eq. DNA C or DNA C'; 1.8 mg mL^{-1} polymer).

6.6 References

(1)   Wang, H.; Heilshorn, S. C. *Adv. Mater*. **2015**, *27* (25), 3710.
(2)   Stuart, M. A. C.; Huck, W. T. S.; Genzer, J.; Muller, M.; Ober, C.; Stamm, M.; Sukhorukov, G. B.; Szleifer, I.; Tsukruk, V. V; Urban, M.; Winnik, F.; Zauscher, S.; Luzinov, I.; Minko, S. *Nat. Mater.* **2010**, *9* (2), 101–113.
(3)   N. A. Peppas A. Khademhosseini, R. Langer, J. Z. H. *Adv. Mater.* **2006**, *18* (11), 1345–1360.
(4)   Guvendiren, M.; Burdick, J. A. *Nat. Commun.* **2012**, *3*, 792.
(5)   Kloxin, A. M.; Benton, J. A.; Anseth, K. S. *Biomaterials* **2010**, *31* (1), 1–8.
(6)   Cheng, E.; Xing, Y.; Chen, P.; Yang, Y.; Sun, Y.; Zhou, D.; Xu, L.; Fan, Q.; Liu, D. *Angew. Chem., Int. Ed. Engl.* **2009**, *48* (41), 7660–7663.
(7)   Chen, C.; Geng, J.; Pu, F.; Yang, X.; Ren, J.; Qu, X. *Angew. Chem., Int. Ed. Engl.* **2011**, *50* (4), 882–886.
(8)   Murakami, Y.; Maeda, M. *Biomacromolecules* **2005**, *6* (6), 2927–2929.
(9)   Yang, H.; Liu, H.; Kang, H.; Tan, W. *J. Am. Chem. Soc.* **2008**, *130* (20), 6320–6321.
(10)   He, X.; Wei, B.; Mi, Y. *Chem. Commun.* **2010**, *46* (34), 6308–6310.
(11)   Liedl, T.; Dietz, H.; Yurke, B.; Simmel, F. *Small* **2007**, *3* (10), 1688–1693.
(12)   Jiang, F. X.; Yurke, B.; Schloss, R. S.; Firestein, B. L.; Langrana, N. A. *Biomaterials* **2010**, *31* (6), 1199–1212.
(13)   Um, S. H.; Lee, J. B.; Park, N.; Kwon, S. Y.; Umbach, C. C.; Luo, D. *Nat. Mater.* **2006**, *5* (10), 797–801.
(14)   Arend M. van Buul   Patrick Brocorens , Matthieu Koepf , David Beljonne , Jan C. Maan , Peter C. M. Christianen , Paul H. J. Kouwer , Roeland J. M. Nolte , Hans Engelkamp , Kerstin Blank and Alan E. Rowan, E. S. *Chem. Sci.* **2013**, *4*, 2357–2363.
(15)   Koepf, M.; Kitto, H. J.; Schwartz, E.; Kouwer, P. H. J.; Nolte, R. J. M.; Rowan, A. E. *Eur. Polym. J.* **2013**, *49* (6), 1510–1522.
(16)   Kouwer, P. H. J.; Koepf, M.; Le Sage, V. A. A.; Jaspers, M.; van Buul, A. M.; Eksteen-Akeroyd, Z. H.; Woltinge, T.; Schwartz, E.; Kitto, H. J.; Hoogenboom, R.; Picken, S. J.; Nolte, R. J. M.; Mendes, E.; Rowan, A. E. *Nature* **2013**, *493* (7434), 651–655.
(17)   Jaspers, M.; Dennison, M.; Mabesoone, M. F. J.; MacKintosh, F. C.; Rowan, A. E.; Kouwer, P. H. J. *Nat. Commun.* **2014**, *5*.
(18)   Das, R. K.; Gocheva, V.; Hammink, R.; Zouani, O. F.; Rowan, A. E. *Nat. Mater.* **2015**.
(19)   Seeman, N. C. *Nature* **2003**, *421* (6921), 427–431.
(20)   Mandal, S.; Eksteen-Akeroyd, Z. H.; Jacobs, M. J.; Hammink, R.; Koepf, M.; Lambeck, A. J. a.; van Hest, J. C. M.; Wilson, C. J.; Blank, K.; Figdor, C. G.; Rowan, A. E. *Chem. Sci.* **2013**, *4* (11), 4168–4174.
(21)   Cornelissen, J. J.; Donners, J. J.; de Gelder, R.; Graswinckel, W. S.; Metselaar, G. A.; Rowan, A. E.; Sommerdijk, N. A.; Nolte, R. J. *Science* **2001**, *293* (5530), 676–680.
(22)   Debets, M. F.; van Berkel, S. S.; Schoffelen, S.; Rutjes, F. P. J. T.; van Hest, J. C. M.; van Delft, F. L. *Chem. Commun.* **2010**, *46* (1), 97–99.
(23)   Broedersz, C. P.; Sheinman, M.; Mackintosh, F. C. *Phys Rev Lett* **2012**, *108* (7), 78102.
(24)   Kang, H.; Liu, H.; Zhang, X.; Yan, J.; Zhu, Z.; Peng, L.; Yang, H.; Kim, Y.; Tan, W. *Langmuir* **2011**, *27* (1), 399–408.
(25)   Maeda, Y. M. and M. *Macromolecules* **2005**, *38*, 1535–1537.
(26)   Zhu, Z.; Wu, C.; Liu, H.; Zou, Y.; Zhang, X.; Kang, H.; Yang, C. J.; Tan, W. *Angew. Chem., Int. Ed. Engl.* **2010**, *49* (6), 1052–1056.
(27)   Gardel, M. L.; Shin, J. H.; MacKintosh, F. C.; Mahadevan, L.; Matsudaira, P.; Weitz, D. A. *Science* **2004**, *304* (5675), 1301–1305.
(28)   MacKintosh, F. C.; Kas, J.; Janmey, P. A. *Phys. Rev. Lett.***1995**, *75* (24), 4425–4428.
(29)   Lieleg, O.; Claessens, M. M.; Heussinger, C.; Frey, E.; Bausch, A. R. *Phys. Rev. Lett.* **2007**, *99* (8), 88102.
(30)   Luan, Y.; Lieleg, O.; Wagner, B.; Bausch, A. R. *Biophys. J.* **2008**, *94* (2), 688–693.
(31)   Lin, Y. C.; Yao, N. Y.; Broedersz, C. P.; Herrmann, H.; Mackintosh, F. C.; Weitz, D. A. *Phys. Rev. Lett.* **2010**, *104* (5), 58101.
(32)   Stowers, R. S.; Allen, S. C.; Suggs, L. J. *Proc. Natl. Acad. Sci. U.S.A* **2015**, *112* (7), 1953–1958.
(33)   Zhang, D. Y.; Seelig, G. *Nat. Chem.* **2011**, *3* (2), 103–113.
(34)   Guéron, M.; Leroy, J.-L. *Curr. Opin. Struct. Biol.* **2000**, *10* (3), 326–331.
(35)   Wang, F.; Liu, X.; Willner, I. *Angew. Chem. Int. Ed. Engl.* **2015**, *54* (4), 1098–1129.
(36)   Schneider, C. A.; Rasband, W. S.; Eliceiri, K. W. *Nat. Methods* **2012**, *9* (7), 671–675.

(37)   Ellington, A.; Pollard Jr., J. D. *Curr. Protoc. Mol. Biol.* **2001**, *Chapter 2*, Unit2 12.
(38)   van der Werf, R.; Wijmenga, S. S.; Heus, H. A.; Olsthoorn, R. C. *RNA* **2013**, *19* (12), 1833–1839.

7

Affinity-based purification of polyisocyanopeptide bioconjugates
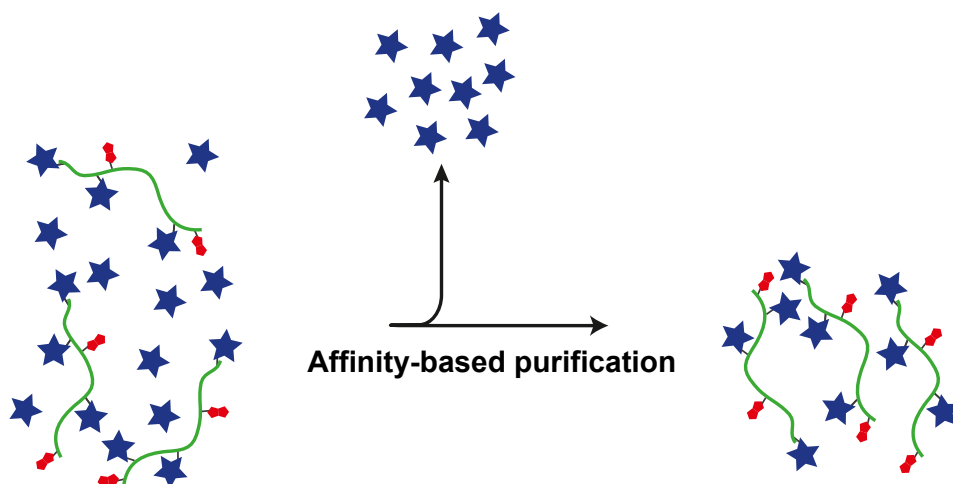
Affinity-based purification

Chapter 7: Affinity-based purification of polyisocyanopeptide bioconjugates

7.1   Introduction

Over the last years, water-soluble polyisocyanopeptides (PICs) have proven their application potential as novel and versatile biomaterials[1]. These polymers are long, helical and semi-flexible, thereby matching the properties of many filaments found in nature.[2,3,4] PIC polymers are build up from isocyanide monomers that carry two alanine substituents to stabilize the helix. In addition, they are functionalized with either tri- or tetra ethylene glycol side chains to provide water solubility. When functionalized with a tri ethylene glycol chain, the corresponding PICs form a hydrogel material at room temperature which has been used in many biological applications like tissue engineering, cell growth or sensing.[5,6] On the other hand, tetra ethylene glycol bearing polymers undergo a sol-to-gel transition at 40-45 °C. These PICs are therefore in a liquid state at physiologically relevant temperatures. They are excellent scaffolds for the synthesis of polymer-drug conjugates as tested for the immunotherapeutic applications described in chapters 2-4 of this thesis.[7,8]

All these applications have in common that the PICs have to be functionalized with biomolecules to make them biofunctional. To provide cell adhesion to the hydrogel, for example, a short integrin-binding GRGDS peptide was grafted onto PIC polymers (chapter 5). In the sensing application (chapter 6), short DNA oligonucleotides were coupled to the PIC that were subsequently cross-linked upon binding of the analyte. For the immunotherapeutic application, the polymers were functionalized with streptavidin to allow for the binding of biotinylated T cell stimulating antibodies (chapters 2,3 and 4).

PICs are long (100-1000 nm), semi-flexible polymers that adopt a stable helical conformation. As a consequence, they do not form a typical random coil in solution, making the purification of PIC-bioconjugates troublesome. Standard size exclusion and field flow fractionation methods were tested to separate unreacted biomolecules from the PIC-bioconjugates, but without any success. Ultrafiltration was identified as the only possible method for the purification of freshly synthesized PIC-bioconjugates, but more than 99% of the material was lost during the process (chapters 2,3 and 4).[7,8] As an alternative, the reaction between the PIC and the biomolecule was carefully optimized so that an almost quantitative coupling of the biomolecule was achieved and no purification was needed (chapters 5 and 6). For small molecules, such as short peptides and DNA oligonucleotides, this method was successful. For larger proteins and antibodies the reaction with the PIC is difficult to optimize, however, as steric

effects start to limit the reaction efficiency. Clearly, an alternative and efficient purification method is needed to obtain pure PIC-bioconjugates in good yield.

Affinity tags such as hexahistidine, Strep-tag or biotin are frequently used for the purification of recombinantly expressed proteins from crude cell extracts.[9–11] Inspired by this method, a PIC polymer bearing the affinity tag biotin was designed. Using this biotin-functionalized PIC, affinity purification on a mono-avidin resin can potentially be used to remove unreacted biomolecules (Figure 7.1). Mono-avidin is a monomeric derivative of avidin that possesses a highly reduced affinity for biotin. It is frequently used for the purification of biotinylated proteins. Biotinylated molecules bind to mono-avidin agarose beads in a reversible manner and can be eluted competitively when adding high concentrations of free biotin.
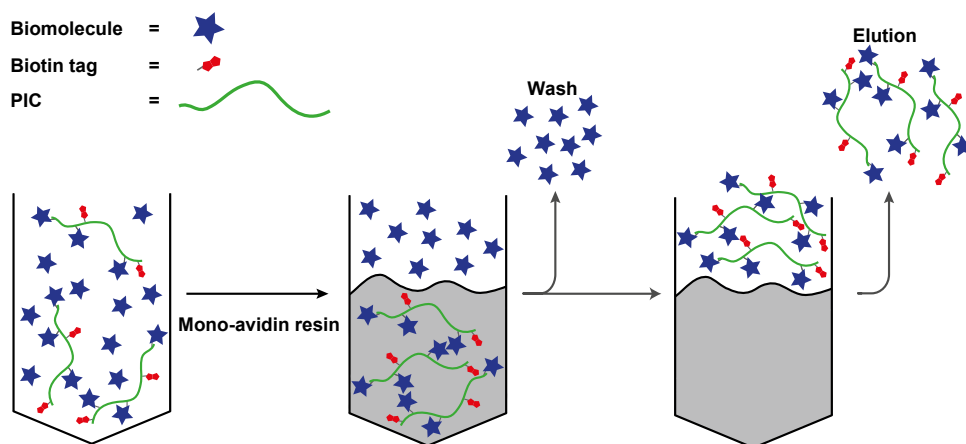
Figure 7.1. Principle of the affinity-based purification method. During synthesis of the PIC-bioconjugates, the PICs are biotinylated first and then reacted with the biomolecule of interest. The resulting reaction mixture, containing biotinylated PIC-bioconjugates and non-reacted biomolecules, is incubated with mono-avidin agarose beads, followed by washing to remove the non-reacted biomolecules. The PIC-bioconjugate remains bound to the beads and is released using a high concentration of biotin to compete with the biotin-tagged PIC-bioconjugates.

This chapter describes the synthesis and characterisation of biotin-containing PIC polymers. It is further tested if a mono-avidin resin can reversibly bind these polymers and if this affinity purification strategy can be used for the purification of PIC-bioconjugates. Two model proteins, an antibody and an enzyme, were selected for coupling to the PIC polymer. The antibody of choice is the same anti-CD3 antibody (αCD3) that has already been used for stimulating T cells (chapters 2, 3 and 4). To further develop these therapeutic PICs, an easy, efficient and reproducible purification method is needed. As an alternative to the antibody, the synthesis and purification of

an enzyme-PIC conjugate was investigated. As a model enzyme, alkaline phosphatase (PhoA) was used to show the versatility of the purification method developed in this chapter.

7.2   Results and discussion

7.2.1 Synthesis and characterization of biotin-functionalized polyisocyanopeptides

To investigate if the biotin affinity tag can be used for the purification of PIC-bioconjugates, first biotin-containing polymers were synthesized (Figure 7.2). For this purpose, PICs with azide groups were synthesized using the same method as described in chapter 2 of this thesis. The ratio of non-functional methoxy to functional azide monomers was chosen to be 30:1, yielding a statistical average distance between azides of 3 nm.[12] Subsequently, the azide-functionalized PIC was reacted with different amounts of biotin-azadibenzocyclooctyne (biotin-EG$_4$-DBCO)carrying a short poly ethylene glycol (PEG) spacer. Assuming a quantitative yield of the reaction, PICs with an average biotin spacing of 5, 7.5, 10 and 40 nm were prepared.[13] Using this strategy, the remaining azide groups can be used for the subsequent coupling of DBCO-functionalized biomolecules as described in the previous chapters.
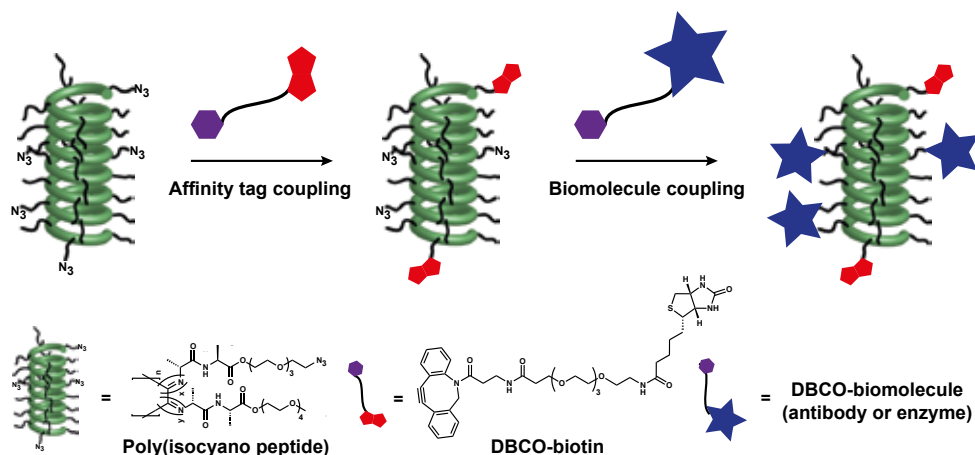
Figure 7.2. Conjugation strategy for the synthesis of biotin-functionalized polyisocyanopeptides that can be used for the subsequent coupling of DBCO-containing biomolecules. In this chapter, the biomolecule is either an antibody (αCD3) or an enzyme (PhoA).

To optimize the biotin density necessary to bind and elute the PICs from mono-avidin containing beads in a batch purification process, an incubation and elution protocol was developed. The polymers were diluted to 0.1-0.2 mg/ml in phosphate buffered saline (PBS) and mixed with mono-avidin beads in a 1:1 (v/v) ratio. The

binding of the PICs to the beads was determined by measuring the concentration of unbound PIC in the supernatant using circular dichroism (CD) spectroscopy. Due to the helical conformation of the PICs, this technique provides an indication of the polymer concentration, assuming that the polymer conformation is not altered during the experiment.[1,14,15] The CD spectrum of the biotinylated PIC is characterized by a negative peak at λ = 360 nm and a larger positive peak with a maximum at λ = 272 nm. Calibration curves of the azide-functionalized PIC were determined at both wavelengths, showing that the corresponding peak heights scale linearly with polymer concentration (Figure 7.3a, Figure A7.1.1). The analysis of the supernatants after 2.5 and 4 hours of incubation shows no significant differences in binding of the biotin-PIC polymers, indicating that maximal binding was already achieved after 2.5 hours.
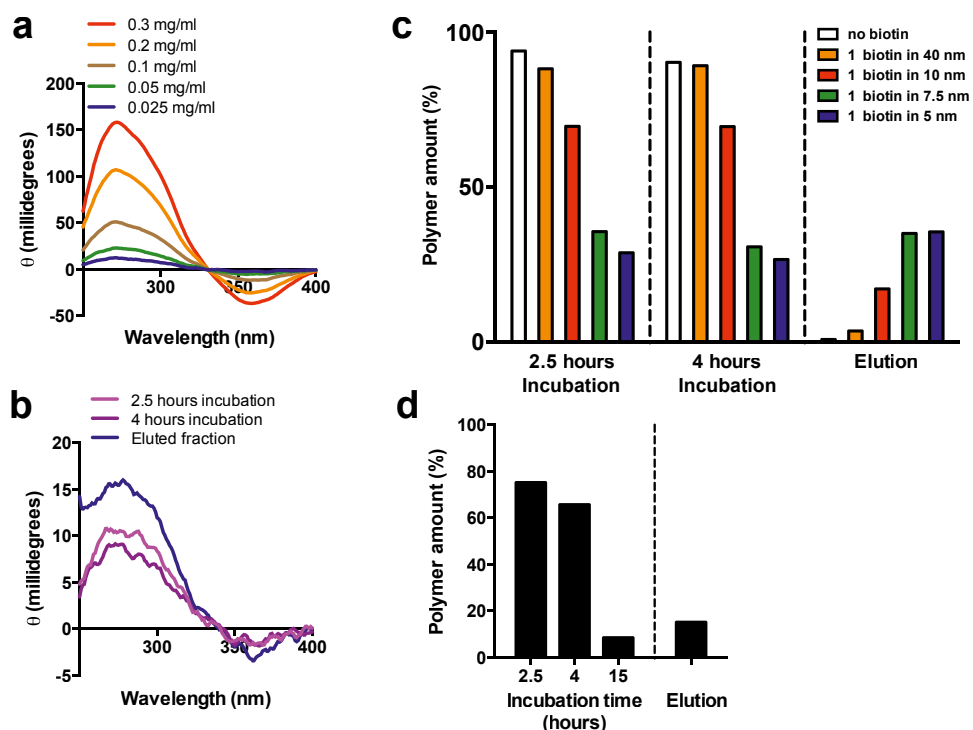
Figure 7.3. Binding and elution of biotin-PICs to and from mono-avidin beads. a) CD spectra of the azide-functionalized PIC measured at different concentrations. b) CD spectra taken at different steps of the purification. The supernatant was measured at different time points (2.5 and 4 hours). In addition, the eluted fraction is shown (data shown for 1 biotin in 7.5 nm. c) Binding and elution profiles for biotin-PICs containing a different biotin density (EG$_4$ linker). Shown is the relative amount of biotin-PIC in the supernatant after binding or elution. d) Binding and elution profile of biotin-PIC prepared with the long (3000 Da) PEG linker and a biotin density of 7.5 nm. Shown is again the relative amount of biotin-PIC in the supernatant after binding and elution.

More pronounced differences in binding efficiency were found when comparing the samples with increasing biotin density. Polymers containing 1 biotin every 40 nm showed binding of the biotin-PIC to the mono-avidin beads, however, the relative amount of bound material was small (~12%). Increasing the biotin density to 10 nm increased the amount of bound polymer to ~30% and maximum binding was found for the samples with a biotin density of 7.5 or 5 nm (both ~65-70%, Figure 7.3c). No biotin-PIC binding was observed for azide-PICs that did not carry any biotin. The biotin density was not increased further as this would yield polymers that do not have a sufficient amount of azides left for further bioconjugation.

After having confirmed binding of the biotin-PICs to mono-avidin beads, the elution protocol was optimized. The beads were first washed with PBS containing 0.1% Tween 20 (PBS-T, 2x) and PBS (4x) to remove any non-specifically bound polymers. During this extensive washing protocol, ~30% of the beads were lost, which reduces the total yield of eluted polymers. Following washing, PBS containing 2 mM biotin was added to the beads to elute the bound biotin-PICs competitively. The CD spectrum of the eluted fractions is not altered when compared to the original polymer samples before purification, which indicates that the helical structure is not affected during the whole process (Figure 7.3b). The amount of eluted biotin-PICs clearly correlates with the amount of biotin-PIC initially bound to the beads and, consequently, also with the density of biotin on the polymer. Only a small amount (4 % of the original amount) was obtained for the polymer with a biotin density of 40 nm. Higher amounts of 17, 34 and 35 % were obtained for the other polymers with biotin densities of 10, 7.5 and 5 nm, respectively (Figure 7.3c). Considering the loss of beads during the washing steps and the fraction of polymer that did not bind, elution with 2 mM biotin is sufficient to release more than 50 % of the bound biotin-PIC polymers from the beads.

In addition to the biotin density, also the linker length between biotin and the PIC polymer backbone was investigated. To test for possible steric hindrance, the length of the PEG spacer between the between the biotin moiety and the DBCO functional group was increased. Using a PEG linker with a molecular weight of 3000 Da, biotin-PIC polymers were prepared with an average biotin density of 7.5 nm. Binding of this polymer to the beads was considerably slower when compared to the previously used biotin-PICs containing only the EG$_4$ linker. After 15 hours of incubation more than 90% of the polymer was bound. Unfortunately, elution of this polymer recovered only 15 % of the original amount (Figure 7.3d). Overall, it appears that the longer linker does not reduce, but instead increase steric hindrance thereby affecting both the kinetics of the interaction as well as the yield of the purification protocol.

Taken together, these results show that the biotin-PIC with a biotin density of 7.5 nm coupled via the short linker performs best when considering both the requirements for an efficient purification as well as its future application. It shows good

binding and a reasonable amount is eluted from the mono-avidin beads. At the same time, a sufficient amount of azides is left for further conjugation. This biotin-PIC was therefore selected as a model system to test whether this purification method can be used for the purification of PIC-bioconjugates.

7.2.2 Purification of anti-CD3 functionalized PICs using the biotin affinity tag

To investigate if PIC-bioconjugates can be purified with the newly developed affinity-based method, biotin-PICs were functionalised with antibodies. To improve the efficiency of the synthetic dendritic cells described in chapters 2-4 of this thesis, the same anti-CD3 antibody (αCD3) was used. In chapters 2 and 4 it was shown that PICs bearing this antibody (αCD3-sDCs) are more efficient in stimulating T cells when compared to the antibody in solution or coupled to bead-like particles. Moreover, in chapter 3 it was shown that multivalency is an important parameter responsible for this higher efficiency.[7,8] Although these αCD3-PIC conjugates are a very promising starting point for immunotherapeutic applications, their usefulness is limited because of the difficult purification. To obtain an acceptable purity, the samples had to be purified extensively using ultrafiltration that resulted in a huge loss of both polymer and antibody (<1 % yield). These low yields also complicated the analysis of the antibody-PIC bioconjugates.

The affinity-based purification method proposed here has the potential to overcome these problems, providing bioconjugates with increased yield and purity. This would not only allow for a more straightforward analysis with UV or CD spectroscopy, but also facilitate the development of large-scale synthesis and purification protocols. In the previous method, αCD3 was biotinylated and bound to a streptavidin-functionalized PIC polymer. As biotin is now used as the affinity tag for purification, the original design had to be adjusted to allow for a direct conjugation of αCD3 to the azide-functionalized PIC. To achieve this, αCD3 was functionalized with DBCO (DBCO-αCD3) and coupled to biotin-PIC with a 7.5 nm biotin density. To synthesize DBCO-αCD3, a *N*-Hydroxysuccinimide (NHS) ester of DBCO was reacted with the lysine residues of the antibody (Figure 7.4a). The degree of labelling, as determined by UV/VIS spectroscopy, was between 2 and 2.5 DBCO molecules per antibody.[16]

To investigate the influence of the antibody density on the performance of the biotin-tag based purification method, 4 different αCD3-PIC bioconjugates were synthesized. DBCO-αCD3 was reacted with biotin-PIC in PBS using 0.1, 0.3, 0.5 and 1 equivalents of antibody compared to the azide groups. The resulting reaction mixtures were purified using the protocol described above. The ability to bind to the mono-avidin beads was estimated by analysing the supernatant with CD at a wavelength of 360 nm (Figure 7.4b, Figure A7.1.1). The binding efficiency of the αCD3-

PIC to the mono-avidin beads was typically in the range of 35-55 %, which was lower than for the biotin-PIC without αCD3 (65-70 %). This may be due to the large antibodies blocking some of the biotin tags from binding. After extensive washing (2x PBS-T, 4x PBS), typically 10-25 % of the original amount of αCD3-PIC could be eluted (Figure 7.4b). Compared to biotin-PIC without αCD3 these yields are slightly lower, but still significantly better then the yields obtained with the ultrafiltration protocol used before (<1 % yield).
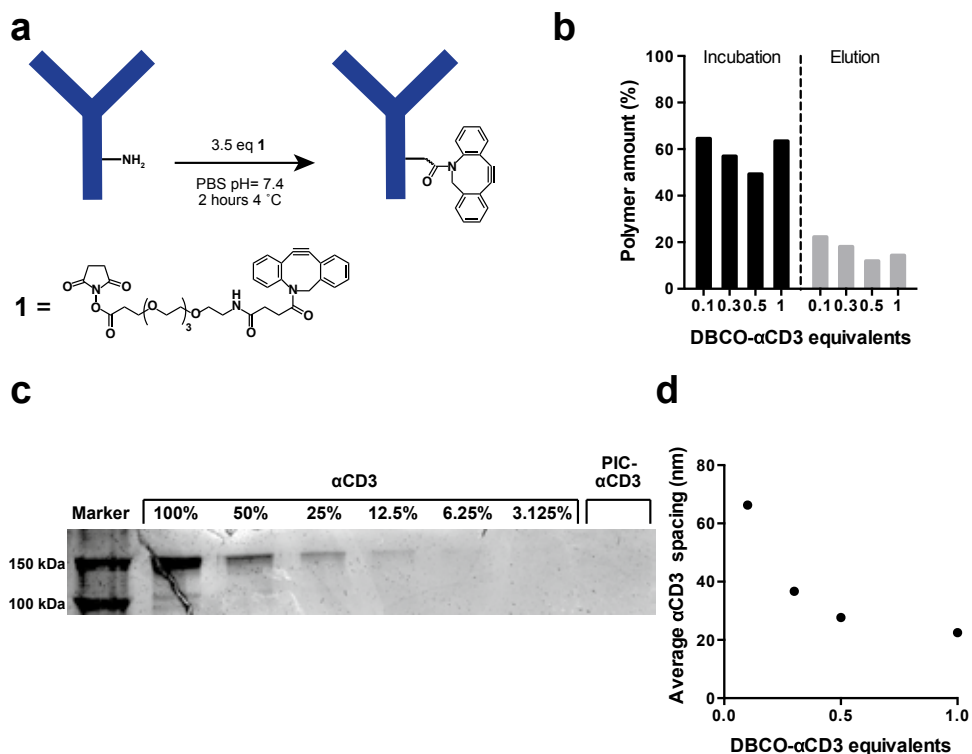
Figure 7.4. Purification of αCD3-PIC bioconjugates using a biotin affinity tag. a) Reaction scheme for the synthesis of DBCO-αCD3. b) Binding and elution profile of αCD3-PIC to and from mono-avidin agarose beads. Shown is the relative amount of αCD3-PIC in the supernatant, determined using CD measurements. c) Non-reducing SDS-PAGE of the PIC-αCD3 sample (1 eq. of antibody with respect to azide groups) in comparison to different concentrations αCD3. Shown are relative concentrations with respect to the amount of αCD3 used in the reaction mixture. d) Calculated average distances between αCD3 on the biotin-PIC backbone obtained for different equivalents of DBCO-αCD3 during the reaction.

In addition to the yield, also the purity of the αCD3-PIC bioconjugates is important. A combination of methods was used to determine the remaining amount of non-conjugated αCD3 in the samples. Gel electrophoresis (SDS-PAGE) was performed under non-reducing conditions to keep the disulfide bonds of the antibody intact (Figure 7.4c). As the polymer bioconjugate is too large to enter the SDS-PAGE

gel (Figure A7.1.2), it can be directly concluded that any protein of the size of ~150 kDa represents non-conjugated antibody. Comparing the PIC-αCD3 sample (1 eq. of antibody with respect to azide groups) with different concentrations of free αCD3 shows that more than 92 % of the antibody was conjugated to the polymer.

This high purity of the αCD3-PIC conjugates allows for a simple determination of the number and the spacing of αCD3 on the polymer backbone. Knowing the molar concentrations of both the antibody and the biotin-PIC, the number of αCD3 per polymer can simply be determined by dividing the two values (Figure 7.4d). The biotin-PIC concentration was again determined by CD measurements and the αCD3 concentration was obtained from a BCA assay. For 0.1, 0.3, 0.5 and 1 equivalents of αCD3 during the reaction, average antibody distances of around 70, 40, 30 and 20 nm were found, respectively. These results clearly show that the purification of PIC bioconjugates with an affinity tag is a powerful method to obtain pure bioconjugates in high yield that can now be easily analysed with standard spectroscopic methods.

7.2.3 Purification of alkaline phosphatase PIC conjugates

To further demonstrate the versatility of the new purification method, also an enzyme was conjugated to the biotin-PIC scaffold. As a model enzyme, alkaline phosphatase (PhoA) from *E. coli* was used. PhoA is a dimeric metalloenzyme involved in the dephosphorylation of molecules.[17] The active form of this enzyme is an allosteric dimer that possesses negative cooperativity and allosteric communication across the dimer interface. The factors affecting this negative cooperativity are currently investigated using single-molecule fluorescence experiments.[18,19] These experiments require the immobilisation of PhoA onto a surface. Many different methods have been tested for enzyme immobilization for this type of experiment, ranging from non-specific adsorption to gel encapsulation and covalent coupling utilizing heterobifunctional poly ethylene glycol linkers.[20–22] Enzyme-PIC conjugates can potentially be used for the formation of enzyme-PIC hydrogels. In this way, the enzymes are immobilized in a nature-like hydrogel with a large pore size[2] that allows for free substrate and product diffusion.
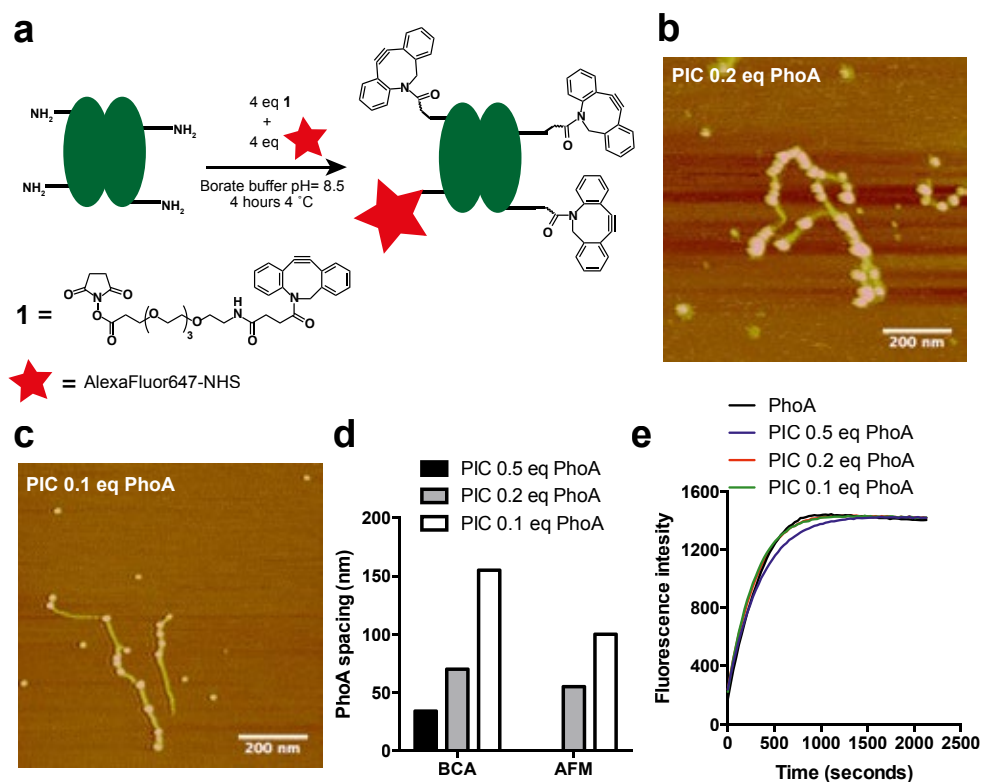
Figure 7.5. Synthesis and purification of PhoA-PIC bioconjugates. a) Reaction scheme used for coupling the NHS-esters of DBCO and AlexaFluor647 to PhoA in a one-pot reaction. b-c) AFM images of PIC with 0.2 eq. PhoA or PIC with 0.1 eq. PhoA drop-casted on mica. The bright 'dots' correspond to the enzyme while the connecting 'line' represents the polymer. d) Calculated PhoA distances on the PIC backbone, determined either from the measured bulk concentrations (BCA) or the AFM measurement. e) Enzyme activity measurements of the PhoA-PIC conjugates in comparison to non-conjugated PhoA. The curves display the mean of three independent measurements.

To investigate this possibility, DBCO- and fluorophore-functionalized PhoA was prepared by reacting the NHS esters of DBCO and AlexaFluor647 with the lysine residues of the enzyme (Figure 7.5a). To determine the degree of labelling, the protein concentration was estimated with a BCA assay and the DBCO and AlexaFluor647 concentrations were determined with UV/VIS spectroscopy. On average, 1.1 fluorophore molecules and 2.4 DBCO functional groups were coupled to the PhoA dimer. DBCO- and AlexaFluor647-labelled PhoA was then reacted with the biotin-PIC polymer (7.5 nm biotin spacing). Three different ratios of PhoA:azide were used for coupling the enzyme to the polymer (0.1, 0.2 and 0.5 eq. of PhoA with respect to azide groups). Assuming a quantitative reaction, this leads to average PhoA distances of 50, 25 and 10 nm.

The PhoA-PIC bioconjugates were again purified over mono-avidin beads using the method described earlier and the purified PhoA-PICs were analysed with atomic force spectroscopy (AFM). The AFM images were used to count the number of enzymes attached to every individual polymer chain (Figure 7.5b and c, Figure A7.1.3) and the average distances between PhoA molecules were determined to be 55 nm (PIC 0.2 eq PhoA) and 100 nm (PIC 0.1 eq PhoA). These values are similar to the distances determined from the overall biotin-PIC (CD) and PhoA (BCA assay) concentrations (70 nm for the PIC sample with 0.2 eq. PhoA and 155 nm for the PIC sample with 0.1 eq PhoA sample; Figure 7.5d), which proves that these PhoA conjugates are highly pure. Unfortunately, the PIC 0.5 eq PhoA sample could not be visualised with AFM, but the spacing determined from the bulk concentrations was 34 nm. On average the determined distances are a factor 3 larger than the distances expected for a quantitative reaction, indicating a coupling efficiency of 30 %.

Next, it was examined if the PIC-conjugated PhoA was still able to perform its function (Figure 7.5e). The activity of the enzyme was tested using the fluorogenic substrate 9H-(1,3-dichloro-9,9-dimethylacridin-2-one-7-yl) phosphate (DDAO-phosphate). Dephosphorylation by PhoA alters the photophysical properties of the DDAO chromophore so that substrate and product are easily distinguished in a fluorescence measurement (Figure A7.1.4).[23] Enzymatic activity results in an increase in product fluorescence (λ_{ex} = 645 nm) allowing for a straightforward kinetic measurement. The increase in product fluorescence was determined for the three PhoA-PIC conjugates and for a control sample containing non-conjugated enzyme of the same concentration. All samples show very similar enzyme activities (Figure 7.5e), indicating that the coupling and purification process does not affect the enzyme. Taken together, these results show that the new purification protocol is a highly powerful method for the purification of enzyme-PIC without altering their function. The next step will clearly be to prepare PIC hydrogels that contain a small concentration of PhoA-PIC conjugates and to perform single-molecule experiments with PhoA conjugated to this biomimetic scaffold.

7.3 Conclusion

In this chapter, an affinity-based purification method was developed that increases both the total yield as well as the purity of the PIC bioconjugates. PIC polymers were equipped with biotin tags that allow for the reversible binding of the resulting biotin-PIC polymers to mono-avidin beads. For optimal binding, a minimum statistical distance between individual biotin moieties of at least 7.5 nm was required. To demonstrate the application potential of this new purification method, two different PIC-bioconjugates were successfully synthesized and purified. Although the final yield of the purification is only 10-25 %, it is still significantly better than the previous

ultrafiltration method where the yield was below 1 %. More importantly, the new method was able to remove almost all non-reacted biomolecules (>95 %) leading to highly pure PIC-bioconjugates. As a consequence of this high purity, the analysis of these constructs was straightforward and the spacing of the conjugated biomolecules could be calculated by simply dividing the concentration of polymer by the concentration of the respective biomolecule. The densities calculated from bulk concentrations were in good agreement with the results from AFM imaging, where every individual biomolecule coupled to the polymer was visualized and counted. Furthermore, the developed purification method preserved the activity of the coupled biomolecule as was demonstrated with activity measurements for alkaline phosphatase. Altogether, a new versatile and standardized protocol for the synthesis and purification of PIC-bioconjugates was developed that will be highly useful for future applications of these molecules.

7.4 Experimental Section

Materials

Unless stated otherwise, all chemicals were obtained from Sigma Aldrich and used without further purification. DBCO-EG$_4$-biotin and DBCO-EG$_4$-NHS were purchased from Click Chemistry Tools. DBCO-PEG$_{3000Da}$-biotin was obtained from Nanocs Inc. and DIBO-AlexaFluor647, AlexaFluor647-NHS and DDAO-phosphate were obtained from Thermo Scientific, as well as the mono-avidin beads (agarose-based). Monoclonal mouse anti-human αCD3 antibodies were obtained from bioXcell (clone OKT3). Ultrafiltration units with a cut-off of 30 kDa (Amicon Ultra-15 Centrifugal Filter Units) were purchased from Merck Millipore and the Micro BCA assay was obtained from Thermo Scientific. 1 ml columns with a 20 μm frit were obtained from Screening Devices. Recombinant alkaline phosphatase (PhoA-His) was obtained from an *E. coli* expression system,[24] followed by purification on a Zn^{2+}-NTA column. The enzyme was provided by Reinhild Dünnebacke (Max Planck Institute of Colloids and Interfaces, Potsdam, Germany). UV/VIS spectra were recorded using a Nanodrop ND1000 (Thermo Scientific) and CD spectra were recorded using a J-810 (JASCO) instrument. Tapping mode AFM imaging was performed in air using a Nanoscope IV instrument (Bruker) and NSG-10 tapping mode tips (NT-MDT). The PhoA activity was measured using a microplate reader (Tecan Infinite M200 PRO).

Polymer synthesis

The PIC polymer used in this study was synthesized according to the procedure described in chapter 2 of this thesis.[7] In short, a 30:1 ratio of methoxy-terminated (1.124 g, 3.12 mmol) and azide-terminated (0.0038 g, 0.104 mmol) isocyanopeptide monomers were mixed in toluene (50 mg/ml) in a round bottom flask and stirred for 2 days until IR measurements showed the complete disappearance of the isocyanide peak. The solution was diluted with dichloromethane and precipitated in diisopropyl ether three times, resulting in an off-white solid (0.937 g, 82%). The resulting polymer contains a statistical density of 1 azide per 3 nm. The polymer was analysed using viscometry as described in chapter 2 of this thesis[7] (M_v= 490 kg/mol).

Biotin-functionalization of PICs

The PIC polymer was dissolved in PBS in a concentration of 1 mg/ml. Biotin-EG$_4$-DBCO dissolved in DMSO was added to this solution in the required amount (less than 5% of the total volume, see below).

The mixture was stirred overnight and subsequently used for testing the mono-avidin purification protocol or for the conjugation of biomolecules. Four different biotin-PIC polymers were prepared with a different density of biotin. To achieve this, the molar ratio of biotin-EG_4-DBCO: monomer was varied from 1:75, 1:100 and 1:400. Assuming a quantitative reaction, this yields an average biotin distance of 7.5, 10 and 40 nm, respectively. During the synthesis of the fourth polymer with a 1:50 molar ratio (5 nm biotin spacing) DIBO-AlexaFluor647 was added in a 1:500 ratio of dye: monomer to obtain a fluorescently labelled biotin-PIC polymer for control experiments. After stirring overnight, the mixture was precipitated in diisopropyl ether and dried in air. The dried material was dissolved in a concentration of 1 mg/ml in PBS.

Synthesis of αCD3-DBCO

DBCO-EG_4-NHS was dissolved in DMSO to prepare a stock solution of 50-100 mM. The αCD3 antibodies were dissolved in PBS (pH 7.4). DBCO-EG_4-NHS (3.5 equivalents) was added to the antibody solution. The final concentration of αCD3 in the reaction mixture was 4 mg/ml. The mixture was stirred for 2 hours at 4 °C and subsequently purified using ultrafiltration (30 kDa cut-off) to remove non-reacted DBCO-EG_4-NHS. The degree of labelling was determined from absorption measurements at 309 nm (DBCO) and 280 nm (αCD3). The signal at 280 nm was corrected for the absorption of DBCO using the following equation: Corrected absorption (280 nm) = absorption at 280 nm – (1.089 * absorption at 309 nm).[16] The DBCO concentration was calculated from the absorption at 309 nm (ε = 12,000 $M^{-1} \cdot cm^{-1}$). To obtain the αCD3 concentration, the corrected absorption at 280 nm (ε = 210,000 $M^{-1} \cdot cm^{-1}$) was used. Typically, this reaction yields a degree of labelling of 2-2.5 DBCO molecules per antibody.

Synthesis of AlexaFluor647-DBCO-PhoA

PhoA was labelled with AlexaFluor647-NHS and DBCO-EG_4-NHS simultaneously. The enzyme was dissolved in a concentration of 15.4 µM in borate buffer (pH 8.5). Using DMSO stock solutions, 4 equivalents of AlexaFluor647-NHS and 4 equivalents of DBCO-EG_4-NHS were added, yielding a final concentration of 62 µM AlexaFluor647-NHS and DBCO-EG_4-NHS. The DMSO content was ~10% of the total volume. The reaction was incubated for 3-4 hours at 4 °C, followed by ultrafiltration with a 10 kDa cut-off. During ultrafiltration, the buffer was changed to 50 mM HEPES pH 8.0. To determine the degree of labelling of the resulting AlexaFluor647-DBCO-PhoA, the protein concentration was first determined with a BCA assay. The DBCO and AlexaFluor647 concentrations were determined from UV/VIS measurements using an extinction coefficient of 12,000 $M^{-1} cm^{-1}$ for DBCO (309 nm) and of 270,000 $M^{-1} cm^{-1}$ for AlexaFluor647 (650 nm). This analysis yielded a degree of labelling of 2.5 DBCO and 1.1 AlexaFluor647 molecules per PhoA dimer.

Synthesis of PIC-bioconjugates

All PIC-bioconjugates were prepared using a similar protocol. A solution of biotin-PIC (1 mg/ml stock solution in PBS) was added to the DBCO-functionalized biomolecules to obtain the desired ratios. The reaction mixture was stirred overnight at 4 °C and directly used for purification over mono-avidin beads. PBS was used for the coupling and purification of αCD3-DBCO. HEPES was used for AlexaFluor647-DBCO-PhoA.

Circular Dichroism (CD) measurements

To prepare the CD standard curves, the azide-functionalized PIC was dissolved in a concentration of 1 mg/ml in PBS (Figure A7.1.1). This stock solution was used to prepare the following concentrations of

the polymer: 0.025, 0.05, 0.1, 0.2 and 0.3 mg/ml. The CD spectrum of these samples was measured and corrected using a PBS blank. Standard curves were constructed for the CD signals measured at 272 nm or 360 nm, yielding calibration factors of ε_{272nm}= 525.6 mdeg mg^{-1} ml^{-1} and ε_{360nm}= -121.1 mdeg mg^{-1} ml^{-1}.

Purification with mono-avidin agarose

All buffers were freshly prepared and filtered before use. In general, 500-800 μl of a 50 % slurry containing regenerated and blocked mono-avidin beads was spun down in a Eppendorf tube and the supernatant was removed. The PIC-biomolecule mixture was added (250-400 μl) and the beads were incubated for 2.5-4 hours. Following incubation, the beads were again spun down, the supernatant was removed and the remaining beads were washed with PBS containing 0.1% (v/v) Tween 20 (PBS-T, 2x) and with PBS (4x). The beads were then incubated with PBS containing 2 mM biotin for 1-2 hours to release the purified PIC-bioconjugate. The samples were filtered to remove a small portion of remaining beads in the elution fraction. Filtering the samples with standard filters of 0.2-0.45 µm pore size did result in a huge loss of polymer so that a 20 µm pore size was used instead. Using this larger pore size, the loss of polymer during filtration was reduced to 10%. During all steps of the purification, PBS was used for the αCD3-PIC bioconjugate, while HEPES was used for the PhoA-PIC samples.

BCA assay

To determine the protein concentration, a micro BCA Protein Assay Kit was used. The assay was performed using the protocol supplied by the manufacturer. When determining the αCD3 or PhoA concentration, non-reacted αCD3 was used as the standard, spanning a concentration range from 7.8 μg/ml to 1 mg/ml. αCD3-PIC samples were freeze-dried before the BCA assay and re-dissolved in PBS, to increase the sample concentration by a factor of 5-6.

AFM measurements

The mono-avidin purified and filtered PhoA samples were drop casted (20 μl) onto freshly cleaved mica. After incubation on the surface for 20 seconds, the samples were removed and the surface was dried in a nitrogen stream. The samples were imaged using tapping mode in air and analysed with ImageJ software.[25] The average spacing of PhoA molecules was calculated from the number of enzymes counted on a polymer of given length (Figure A7.1.3).

PhoA activity measurements

The fluorogenic substrate DDAO-phosphate (9H-(1,3-Dichloro-9,9-Dimethylacridin-2-One-7-yl) phosphate, diammonium salt) was used for measuring the activity of the PhoA-PIC bioconjugates. The substrate was dissolved in dry DMSO at a concentration of 40 μM. The PhoA-PIC bioconjugates were diluted in activity buffer (50 mM HEPES pH 8.0, 100 mM KCl, 20 mM MgCl$_2$, 100 µM ZnCl$_2$) to obtain a PhoA concentration of 500 pM. DDAO-phosphate was added to a final concentration of 2 μM to start the measurement. The release of the fluorophore DDAO was followed in a microplate reader (λ_{ex} = 620 nm; λ_{em} = 660 nm). The measurement was performed at 37 °C for 40 min (30 s intervals). All measurements were performed in triplicate. The data was corrected for auto-hydrolysis of the substrate.

7.5 Appendix 7.1: Supplementary figures

a
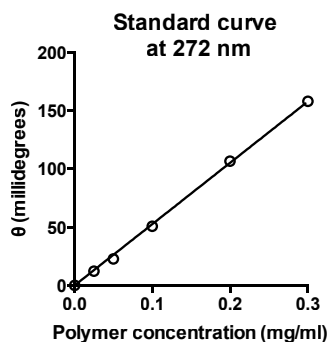
b
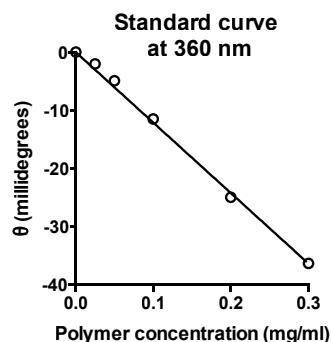
Figure A7.1.1. Calibration curves for determining the polymer concentration from CD spectroscopy. a) Standard curve determined at 272 nm at 1 cm path length (slope: 525.6 mdeg mg^{-1} ml^{-1}) b) Standard curve determined at 360 nm at 1 cm path length (slope: -121.1 mdeg mg^{-1} ml^{-1}).
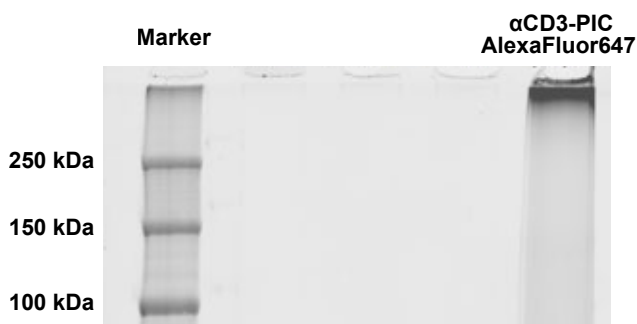
Figure A7.1.2. SDS-PAGE (non-reducing conditions) of an AlexaFluor647-labelled and mono-avidin purified αCD3-PIC bioconjugate (biotin-PIC, 1 in 50 nm biotin). The gel has been scanned at a wavelength of 700 nm to visualize the AlexaFluor647 fluorophores. The gel clearly shows that the αCD3-PIC bioconjugate does not enter the gel.

a

0.2 eq PhoA

b
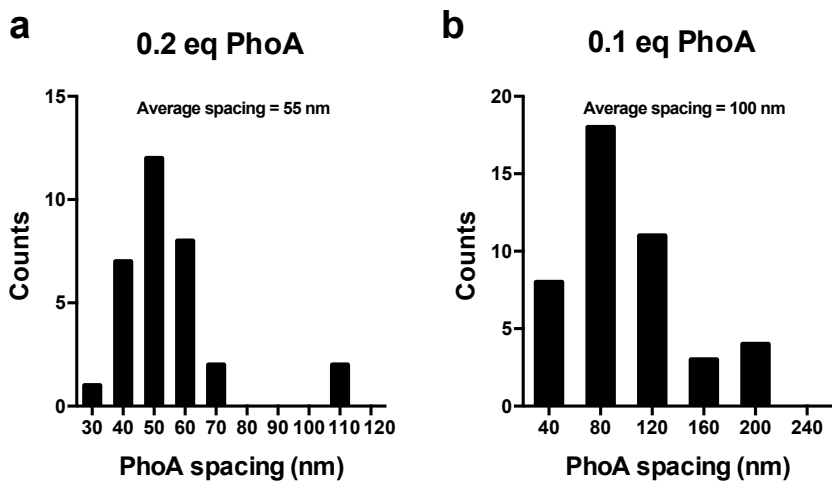
0.1 eq PhoA

Figure A7.1.3. Average distance between PhoA molecules on the PhoA-PIC conjugates determined from AFM imaging. a) PIC sample with 0.2 eq. PhoA and b) PIC sample with 0.1 eq. PhoA.

λ_{ex} = 460 nm
λ_{em} = 610 nm

PhoA
50 mM HEPES
100 mM KCl
1mM MgCl$_2$
0.1 mM ZnCl$_2$

λ_{ex} = 645 nm
λ_{em} = 660 nm

Figure A7.1.4. Enzymatic reaction converting DDAO phosphate into DDAO

7.6 References

(1)   Koepf, M.; Kitto, H. J.; Schwartz, E.; Kouwer, P. H. J.; Nolte, R. J. M.; Rowan, A. E. *Eur. Polym. J.* **2013**, *49* (6), 1510–1522.

(2)   Kouwer, P. H. J.; Koepf, M.; Le Sage, V. A. A.; Jaspers, M.; van Buul, A. M.; Eksteen-Akeroyd, Z. H.; Woltinge, T.; Schwartz, E.; Kitto, H. J.; Hoogenboom, R.; Picken, S. J.; Nolte, R. J. M.; Mendes, E.; Rowan, A. E. *Nature* **2013**, *493* (7434), 651–655.

(3)   Jaspers, M.; Dennison, M.; Mabesoone, M. F. J.; MacKintosh, F. C.; Rowan, A. E.; Kouwer, P. H. J. *Nat. Commun.* **2014**, *5*.

(4)   Jaspers, M.; Rowan, A. E.; Kouwer, P. H. J. *Adv. Funct. Mater.* **2015**, *25* (41), 6503–6510.

(5)   Deshpande, S. R., Hammink, R., Das, R. K., Nelissen, F. H.T., Blank, K. G., Rowan A. E., Heus, H. A. *Manuscript accepted for publication in Adv. Funct. Mater.*

(6)   Das, R. K.; Gocheva, V.; Hammink, R.; Zouani, O. F.; Rowan, A. E. *Nat. Mater.* **2016**, *15* (3), 318–325.

(7)   Mandal, S.; Eksteen-Akeroyd, Z. H.; Jacobs, M. J.; Hammink, R.; Koepf, M.; Lambeck, A. J. a.; van Hest, J. C. M.; Wilson, C. J.; Blank, K.; Figdor, C. G.; Rowan, A. E. *Chem. Sci.* **2013**, *4* (11), 4168–4174.

(8)   Mandal, S.; Hammink, R.; Tel, J.; Eksteen-Akeroyd, Z. H.; Rowan, A. E.; Blank, K.; Figdor, C. G. *ACS Chem. Biol.* **2015**, *10* (2), 485–492.

(9)   Henrikson, K. P.; Allen, S. H. G.; Maloy, W. L. *Anal. Biochem.* **1979**, *94* (2), 366–370.

(10)   Hochuli, E.; Bannwarth, W.; Dobeli, H.; Gentz, R.; Stuber, D. *Nat. Biotech.* **1988**, *6* (11), 1321–1325.
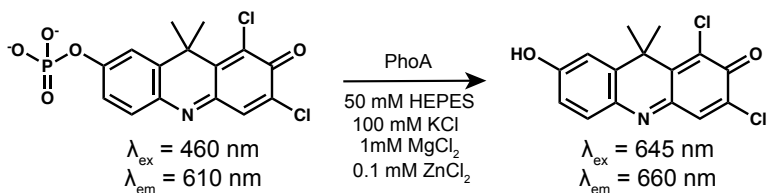
(11)   Schmidt, T. G. M.; Skerra, A. *Nat. Protoc.* **2007**, *2* (6), 1528–1535.

(12)   Cornelissen, J. J.; Donners, J. J.; de Gelder, R.; Graswinckel, W. S.; Metselaar, G. A.; Rowan, A. E.; Sommerdijk, N. A.; Nolte, R. J. *Science* **2001**, *293* (5530), 676–680.

(13)   Debets, M. F.; van Berkel, S. S.; Schoffelen, S.; Rutjes, F. P. J. T.; van Hest, J. C. M.; van Delft, F. L. *Chem. Commun.* **2010**, *46* (1), 97–99.

(14)   Kitto, H. J.; Schwartz, E.; Nijemeisland, M.; Koepf, M.; Cornelissen, J. J. L. M.; Rowan, A. E.; Nolte, R. J. M. *J. Mater. Chem.* **2008**, *18* (46), 5615–5624.

(15)   Schwartz, E.; Koepf, M.; Kitto, H. J.; Nolte, R. J. M.; Rowan, A. E. *Polym. Chem.* **2011**, *2* (1), 33–47.

(16)   Kotagiri, N.; Li, Z.; Xu, X.; Mondal, S.; Nehorai, A.; Achilefu, S. *Bioconjug. Chem.* **2014**, *25* (7), 1272–1281.

(17)   Coleman, J. E. *Annu. Rev. Biophys. Biomol. Struct.* **1992**, *21*, 441–483.

(18)   Blank, K.; De Cremer, G.; Hofkens, J. *Biotechnol. J.* **2009**, *4* (4), 465–479.

(19)   Claessen, V. I.; Engelkamp, H.; Christianen Peter C.M.; Maan, J. C.; Nolte, R. J. M.; Blank, K.; Rowan, A. E. *Annu. Rev. Anal. Chem.* **2010**, *3* (1), 319–340.

(20)   Gumpp, H.; Puchner, E. M.; Zimmermann, J. L.; Gerland, U.; Gaub, H. E.; Blank, K. *Nano Lett.* **2009**, *9* (9), 3290–3295.

(21)   Terentyeva, T. G.; Hofkens, J.; Komatsuzaki, T.; Blank, K.; Li, C.-B. *J. Phys. Chem. B* **2013**, *117* (5), 1252–1260.

(22)   Velonia, K.; Flomenbom, O.; Loos, D.; Masuo, S.; Cotlet, M.; Engelborghs, Y.; Hofkens, J.; Rowan, A. E.; Klafter, J.; Nolte, R. J. M.; de Schryver, F. C. *Angew. Chem., Int. Ed.* **2005**, *44* (4), 560–564.

(23)   Leira, F.; Vieites, J. M.; Vieytes, M. R.; Botana, L. M. *Toxicon* **2000**, *38* (12), 1833–1844.

(24)   Blank, K.; Morfill, J.; Gumpp, H.; Gaub, H. E. *J. Biotechnol.* **2006**, *125* (4), 474–483.

(25)   Schneider, C. A.; Rasband, W. S.; Eliceiri, K. W. *Nat. Methods* **2012**, *9* (7), 671–675.

8

Epilogue

Chapter 8: Epilogue

This thesis introduces a general strategy for the synthesis of a new class of functional bioconjugates. These bioconjugates are based on a polymeric scaffold that is made from water-soluble polyisocyanopeptides. The scaffold carries a defined and controllable number of azide-functional groups that can be used for the conjugation of a large variety of different biomolecules functionalized with strained alkynes. Using functional polymers based on either **PIAA-OEG$_3$-OMe** or **PIAA-OEG$_4$-OMe**, different applications of these bioconjugates were explored. Freely soluble **PIAA-OEG$_4$-OMe**-based polymers were used as scaffolds for the multivalent display of effector molecules in immunotherapy applications. Using **PIAA-OEG$_3$-OMe-**based polymers, different bio-functional hydrogels were synthesized and tested in cell culture and sensing applications. Clearly, polyisocyanopeptides bioconjugates represent highly powerful molecular entities that may find application in many different areas, ranging from nanomedicine to diagnostics and biomaterial synthesis. This chapter discusses several aspects considering the envisioned applications of these functional polymer bioconjugates. The chapter starts with a critical assessment of the risks and societal impacts of nanomedicine, with a special focus on the polymer bioconjugates developed in this thesis. Subsequently, the chapter discusses the current status of the newly developed bioconjugates as well as future developments to improve these molecular entities and to extend their possible range of applications.

8.1 Risk Analysis and Technology Assessment

The research described in this thesis was carried out as part of the drug delivery program in the NanoNextNL consortium. In this consortium, researchers, companies and medical centres from all over the Netherlands are united to perform research aimed at the further development of nanotechnology. Nanotechnology is a broad term used for all technologies that deal with entities of nanometer size (10^{-9} m). Nanotechnology is a very promising field of research with a strong application potential in many different areas. With this increasing popularity, also the public concerns about the risks of nanotechnology have been growing. For this reason, NanoNextNL stimulates researchers to think about the potential risks and impact of their research on society. In this way, more awareness can be generated in the general public.

A first potential risk that comes to mind when developing a new nanomaterial is its toxicity. Although the polyisocyanopeptide bioconjugates described in this thesis are still far from a final application, their toxicity was tested before any other research was carried out. The first part of this thesis (chapters 2-4) describes potential applications of polyisocyanopeptides as a molecular scaffold in the area of immunotherapy. The toxicity of this potential new nanomedicine was tested and the

results are described in chapter 2 of this thesis. No toxic effect was seen on the cells under study. Specifically, no loss in cell viability was observed when treating cells with different concentrations of polymer over a period of weeks. Of course, long-term effects should be investigated further when moving towards *in vivo* applications. But these first toxicity tests indicate that no severe side effects are to be expected. The second part of this thesis (chapters 5 and 6) describes the use of water-soluble polyisocyanopeptides for the synthesis of biofunctional hydrogels. The toxic effect of these hydrogels on stem cells was also investigated, and the results are described in chapter 5. Live-dead assays showed a high viability (>95%) of cells encapsulated in these gels.

Apart from the toxicity of the material in question, it is further important to critically evaluate the synthetic processes carried out to fabricate such materials. To make a new material suitable for biological applications, the processes should be carried out in a sterile environment. Further, they should be easy to perform with a minimal number of steps, keeping material consumption low. This is not only an important cost factor, but also minimizes the impact of a chemical process on the environment. For this reason, a novel protocol for the purification of polyisocyanopeptides bioconjugates was developed in chapter 7 of this thesis. The new affinity-based method allows for the sterile purification of the final polymer bioconjugates with a significantly increased yield. This does not only lead to a clean and sterile product, but also minimizes the amount of expensive starting materials. The research described in this thesis is only a first step towards the use of water-soluble polyisocyanopeptides for the mentioned applications. Consequently, it is hard to predict their impact on society. More research is still needed before a final product can come to the market. Clearly, potential risks and their impact should be considered in every step.

8.2 Immunotherapy & Drug Delivery Applications using Polyisocyanopeptide Scaffolds

In chapters 2, 3 and 4 of this thesis the potential of polyisocyanopeptide scaffolds for the development of artificial antigen-presenting cells (aAPC) was investigated. Considering the natural interaction of natural APCs with T cells, it was hypothesized that the ideal aAPC contains multiple effector molecules on a dynamic scaffold to allow for the efficient formation of multivalent interactions between both cell types. Water-soluble polyisocyanopeptides are interesting polymers that are hundreds of nanometres long and possess a helical secondary structure. This helical structure is stabilized by hydrogen bonds that form between alanine-containing side chains. As a result, polyisocyanopeptides are significantly stiffer than many other polymers, which usually lack a helical secondary structure. Considering length and

stiffness, this polymer is a unique scaffold, with a very high aspect and surface-to-volume ratio. This ensures that all effector molecules coupled to this scaffold can interact with, their complementary binding partner (e.g. a cell surface) simultaneously and in a multivalent fashion. At the same time, the semi-flexible nature of the polymer scaffold allows for receptor rearrangements on the cell surface as they occur during T cell activation.

The results described in the first chapters of this thesis indeed support the hypothesis that long, semi-flexible molecules are highly powerful multivalent scaffolds. Functionalized with T cell-stimulating antibodies, the polyisocyanopeptide scaffold outperformed freely soluble antibodies and spherical particles carrying a similar number of antibodies in all cases (chapter 2). Polymer length as well as effector molecule density are important design parameters that can be easily controlled when synthesizing the bioconjugate (chapter 3). Surprisingly, the multivalent polyisocyanopeptides conjugate did not only lower the antibody concentration needed to obtain a T cell response, but also altered signalling pathways involved in T cells activation. This suggests that the polymeric aAPC described in this thesis may become a new tool for studying, manipulating and regulating the obtained immunoresponse. This potential was partly shown in chapter 4. Coupling a second, co-stimulatory antibody to the same polymer molecule increased the efficacy and specificity of T cell activation, providing evidence that the polymer conjugate can be used for shaping the obtained immunoresponse.

In this thesis the polyisocyanopeptide scaffold was solely used for the activation of T cells *in vitro*, towards the design of a vaccine that can be used in immunotherapy. This new scaffold is clearly also a highly powerful starting point for the development of other polymer bioconjugates. Many other biomedical applications require multivalent ligands for increasing their binding efficiency, for example drug delivery or *in vivo* imaging. The unique structure of the polymer developed in this work will be highly beneficial in these cases. The biofunctionalization of the polyisocyanopeptide polymers follows a simple post-modification approach, using well-established click chemistry methods. Coupling other biomolecules onto the polymer, as required for the previously mentioned applications, can consequently be realized in a fast and straightforward manner.

An essential next step towards using these polymers *in vivo* is a detailed investigation of their biodistribution in an organism. From the literature it is known that filamentous particles circulate much longer in the body compared to spherical particles.[1] If this were also the case for the polymer conjugates developed here, this would greatly strengthen their potential for immunotherapy and drug delivery applications. Considering their shape, also other interesting effects may be observed. The polymers have a very small diameter (< 2 nm). This may allow them to cross the

blood brain barrier, allowing for the delivery of multivalent drugs to the brain. This would clearly open up a completely new range of possibilities.

8.3 Polyisocyanopeptide Hydrogels as Multifunctional Materials for Cell Culture and Sensing

In the second part of this thesis (chapters 5 and 6) the focus was moved towards hydrogel-forming polyisocyanopeptide bioconjugates. A highly useful property of these hydrogels is their thermo-responsive behaviour. At physiological temperatures of 37 °C, stable gels are formed that support cells in a 3D environment. Cooling down liquefies the mixture so that the encapsulated cells can be retrieved easily for further analysis. Apart from this practical advantage, polyisocyanopeptide hydrogels possess a non-linear viscoelastic behavior; that is they stiffen upon increasing the applied stress. This property is common for biological hydrogels, e.g. made from cytoskeletal filaments or extracellular matrix polymer such as collagen. It is believed that stress-stiffening is an important functional characteristic of natural biological hydrogels and it has been difficult to mimic this property in synthetic hydrogels. Water-soluble polyisocyanopeptides are a rare and highly versatile example of a synthetic polymer that forms stress-stiffening hydrogels. Considering its synthetic nature, an unprecedented level of control is obtained, being able to adjust polymer length and ligand density, for example.

In chapter 5, hydrogels made from polymers of different length were used to investigate the effect of stress-stiffening on the differentiation of stem cells. Changing the polymer length directly controls the onset of stress-stiffening (critical stress). After conjugation of a cell-adhesive peptide, stem cells were cultured in these hydrogels. When using hydrogels with low critical stresses (short polymers), stem cells differentiated towards fat cells. On the other hand, osteogenic differentiation was observed in the hydrogels with higher critical stresses. For the first time, this study of the effect of stress-stiffening shows that this mechanical property is an important parameter that determines the differentiation of cells. It also establishes polyisocyanopeptide hydrogels as a very powerful cell culture platform for performing systematic studies aimed at understanding the complex interplay of different parameters involved in stem cell differentiation. Synthetic, physically cross-linked hydrogels allow for decoupling mechanical and (bio)chemical parameters that are often intrinsically linked when using biological hydrogels. Furthermore, their thermo-responsive behavior makes them an ideal 3D cell culture system that perfectly mimics the extracellular environment. In the future, it may find application in many areas ranging from fundamental research to tissue engineering.

To further control the mechanical properties of polyisocyanopeptide hydrogels, additional stimuli-responsive cross-links were introduced (chapter 6). The polymer

was functionalized with short DNA oligonucleotides that cross-link upon addition of a hybridizing complementary sequence. This strategy allowed for the formation of a dynamic hydrogel. It was shown that the hydrogel properties could be controlled by altering the concentration and the thermal stability of the hybridizing sequence. More importantly, the cross-links could be specifically removed using strand displacement. In this way, it was possible to alter the hydrogel stiffness and its critical stress *in situ*. Ultimately, this strategy is a starting point for the development of a novel hydrogel sensor that stiffens or softens upon binding a bridging analyte like, for example, microRNA molecules. Moreover, culturing cells in a DNA-responsive polyisocyanopeptide hydrogels may allow for the dynamic regulation of hydrogel stiffness and critical stress during cell growth or differentiation.

8.4 Conclusions

This thesis introduces helical polyisocyanopeptide polymers as a highly powerful scaffold for the functionalization with biomolecules and highlights a number of potential applications of the resulting bioconjugates. This thesis shows that many different kinds of biomolecules such as antibodies, enzymes, DNA oligonucleotides or peptides can all be easily coupled to the polymeric scaffold using one and the same coupling method. The scaffold is long, semi-flexible and non-toxic, making it a highly versatile molecular entity for immunotherapy and drug delivery applications. Hydrogels formed by polyisocyanopeptides possess unique non-linear mechanical properties that make these materials interesting candidates for a range of biomedical applications where these properties are essential, e.g. in cell culture and tissue engineering. Many more exciting and currently unexplored applications can be imagined with this new class of polymers and this thesis just provides a starting point for future research in this field.

8.5 References

(1)   Geng, Y.; Dalhaimer, P.; Cai, S.; Tsai, R.; Tewari, M.; Minko, T.; Discher, D. E. *Nat. Nanotechnol.* **2007**, *2* (4), 249–255.

Summary

Synthetic polymeric materials have become crucial components of modern day health care. They find their use in a wide range of applications such as drug delivery, implants, regenerative medicine, biosensors and many more. Water-soluble polyisocyanopeptides possess unique properties that make them ideal candidates for many of these applications. The work in this thesis describes the synthesis of polyisocyanopeptide bioconjugates and explores a number of different biological applications of these novel biofunctional molecules.

Chapter 1 provides a short overview of the history of water-soluble polyisocyanopeptides and introduces the biological and medical applications that were explored in this thesis. Water-soluble polyisocyanopeptides are long, semi-flexible and biocompatible polymers that form a hydrogel upon increasing the temperature. Depending on the length of the oligo ethylene glycol side chain used in the isocyanopeptide monomer, the gelation temperature of polyisocyanopeptide hydrogels can be tuned. Tri ethylene glycol substituted polymers (**PIAA-OEG₃-OMe**) possess a gelation temperatures of ~20 °C. In contrast, tetra ethylene glycol substituted polymers (**PIAA-OEG₄-OMe**) gelate at a temperature of ~42 °C. As a direct consequence, **PIAA-OEG₃-OMe** forms a hydrogel at the physiologically relevant temperature of 37 °C, whereas **PIAA-OEG₄-OMe** does not. Hydrogels consisting of **PIAA-OEG₃-OMe** may find application as wound dressing materials, as cell growth matrices or even in tissue engineering. Alternatively, freely soluble **PIAA-OEG₄-OMe** polymers are ideal fibre-like, multivalent scaffolds for drug delivery or other *in vivo* applications that utilize polymeric scaffolds.

A first application of **PIAA-OEG₄-OMe** is described in chapter 2. Utilizing the length and semi-flexibility of these polymers, the goal of this chapter was to synthesize a novel multivalent scaffold that facilitates a more efficient interaction of effector molecules with their respective binding partners. Aiming at the development of a new vaccine for immunotherapy as a first application, this scaffold was used for the activation of T cells. Functional azide handles were introduced into the polymer scaffold, which allowed for the further functionalization with T cell stimulating anti-CD3 antibodies. The resulting non-toxic bioconjugates were able to activate T cells more efficiently when compared to soluble antibodies or spherical particles carrying the same antibody. Furthermore, the antibody concentration required to obtain a T cell response was much lower when the antibody was conjugated to the polyisocyanopeptide.

In this first proof-of-principle study, the polymer length and antibody density were kept constant. In chapter 3, these parameters were systematically varied to gain more detailed insight into the importance of establishing a multivalent

interaction. Increasing either polymer length or antibody density induced stronger activation, clearly highlighting the importance of multiple interactions between the antibody-functionalized polymer and the T cell. When comparing the longest polymer carrying the highest number of antibodies with soluble antibodies, a multivalent enhancement factor of 67 was calculated. It was further shown that this highly multivalent bioconjugate did not only lower the effective concentration required, but also altered T cell signalling. When monitoring signalling T cells over time, it was observed that the multivalent scaffold significantly extended the duration of activation.

In a next step towards the development of a vaccine for immunotherapy, the polymers were functionalized with a second, co-stimulating anti-CD28 antibody (chapter 4). Focussing on the effect of these new bioconjugates on T cell differentiation, it was observed that polymers carrying both antibodies induced effector ($CD8^+$) and helper (T_h1 $CD4^+$) cell populations without inducing regulatory T cells. This specific response required co-stimulation with anti-CD28 antibodies. More importantly, an optimal response was only obtained when both antibodies were coupled to one and the same polymer backbone. This clearly shows that the spatial arrangement of both signals is an important parameter for effectively stimulating T cells and that such geometry effects need to be taken into consideration when designing a T cell stimulating vaccine.

In chapter 5 the attention was moved towards the biofunctionalization and application of **PIAA-OEG₃-OMe** hydrogels. These hydrogels show a non-linear, stress-stiffening response. This behaviour is common for biological materials, but it is very rare in synthetic hydrogels. Polyisocyanopeptide hydrogels are, therefore, an ideal model system for studying the effect of stress-stiffening on cellular mechanosensing and transduction processes. For these experiments, the synthetic polyisocyanopeptide hydrogel is unique in that it allows for the decoupling of mechanical and biochemical parameters, which is difficult to achieve with natural, biological hydrogels. One such parameter is the onset for stress-stiffening (critical stress). This parameter can be tuned by varying the **PIAA-OEG₃-OMe** length without altering the general hydrogel stiffness. In this chapter, the effect of the critical stress on stem cell differentiation was investigated. For this purpose, the azide handles in the polymer were functionalized with GRGDS integrin-binding peptides to provide cell adhesion sites. Stem cells cultured in hydrogels with low critical stress showed differentiation into fat cells, whereas stem cells cultured in hydrogels with high critical stress showed differentiation into bone cells. This important result highlights the potential of these hydrogels as a novel 3D cell culture matrix that can be used for investigating fundamental mechanobiological processes. At the same time it may provide a new platform for tissue engineering applications.

In chapter 6, the **PIAA-OEG$_4$-OMe** polymer was functionalized with two small DNA oligonucleotides that were subsequently hybridized with a third bridging DNA sequence. The mechanical properties of this DNA cross-linked hydrogel could be dynamically tuned by the concentration of the DNA cross-linker as well as the temperature. In this way a multifunctional stimuli-responsive hydrogel was obtained, which could serve as a new material for the development of new bio-sensing devices.

The synthesis of the polyisocyanopeptide bioconjugates requires extensive and difficult purification steps. Especially when the biomolecule has a high molecular weight (i.e. large size), a high amount of polymer is lost during these purification steps. To increase the yield and to reduce the number of steps, an affinity-based method was developed (chapter 7). The polyisocyanopeptides were functionalized with biotin affinity tags, which were subsequently used to purify the polymer conjugate on mono-avidin beads. The suitability of this method was shown with both an antibody- and an enzyme-functionalized polymer. Both conjugates were purified in yields ranging from 10-25 %, which is a significant improvement over the previously used method based on dialysis and ultrafiltration (<1 % yield). Most importantly, the conjugates were highly pure. This does not only facilitate a straightforward quantitative analysis, but is further expected to improve bioconjugate functionality in the intended application.

The last chapter of this thesis aims at integrating the knowledge obtained when synthesizing, purifying and testing the different bioconjugates. It further summarizes important aspects to be considered when implementing possible applications and highlights possible future directions. Overall, this thesis shows that water-soluble polyisocyanopeptides are a highly interesting and versatile class of biocompatible polymers with a broad range of possible applications.

Samenvatting

In de moderne gezondheidszorg zijn materialen van synthetische polymeren niet meer weg te denken. Ze worden gebruikt in een breed scala aan toepassingen zoals in de toediening van medicijnen, regeneratieve geneeskunde, biosensoren en vele andere. Water-oplosbare polyisocyanopeptiden bezitten unieke eigenschappen die deze klasse van polymeren zeer geschikt maakt voor vele van deze toepassingen. Het werk in dit proefschrift beschrijft de synthese van polyisocyanopeptide-bioconjugaten en verkent verschillende toepassingen van deze nieuwe biofunctionele moleculen.

Hoofdstuk 1 geeft een kort overzicht van de geschiedenis van water oplosbare polyisocyanopeptiden en introduceert de biologische en medische toepassingen die zijn onderzocht in dit proefschrift. Water oplosbare polyisocyanopeptiden zijn lange, semi-flexibele en biocompatibele polymeren die een hydrogel vormen als de temperatuur verhoogd wordt. De temperatuur waarbij de gel gevormd wordt kan worden veranderd door de lengte van de oligo-ethyleenglycol zijketen aan te passen. Zo vormt een polymeer met een tri-ethyleenglycol zijketen (**PIAA-OEG$_3$-OMe**) een gel bij ~ 20 ºC en een polymeer met een tetra-ethyleenglycol zijketen (**PIAA-OEG$_4$-OMe**) bij ~ 42 ºC. Als gevolg hiervan vormt **PIAA-OEG$_3$-OMe** een hydrogel bij de fysiologische temperatuur van 37 ºC en **PIAA-OEG$_4$-OMe** niet. Hydrogels van **PIAA-OEG$_3$-OMe** kunnen goed gebruikt worden als wondbedekkers, celgroei matrices of zelfs in weefselkweek. De vrije, oplosbare **PIAA-OEG$_4$-OMe** polymeren daarentegen zijn ideale vezelachtige, multivalente structuren om te gebruiken in de toediening van medicijnen of andere *in vivo* toepassingen.

Een eerste toepassing van **PIAA-OEG$_4$-OMe** is beschreven in hoofdstuk 2. Het doel van dit hoofdstuk was om een nieuw multivalent polymeer te ontwikkelen dat, door gebruik te maken van zijn lengte en semi-flexibiliteit, effector moleculen een efficiëntere interactie geeft met hun bindingspartners. Deze nieuwe structuur is gebruikt om T-cellen te activeren, omdat het ontwikkelen van een nieuw vaccin voor immuuntherapie de achterliggende toepassing was. In het polymeer werden functionele azide handvatten ingebouwd die op hun beurt weer gefunctionaliseerd werden met T-cel stimulerende anti-CD3 antilichamen. De resulterende, niet giftige bioconjugaten zijn in staat om T-cellen efficiënter te stimuleren dan de vrije antilichamen of bolvormige deeltjes waaraan hetzelfde antilichaam vastzit. Bovendien is de concentratie van het antilichaam die nodig is om een respons te krijgen vele malen lager wanneer het antilichaam geconjugeerd is aan de polyisocyanopeptide.

In hoofdstuk 2 werden de polymeer lengte en antilichaam dichtheid constant gehouden. In hoofdstuk 3 worden deze parameters gevarieerd om meer inzicht te

krijgen in het belang van de verkregen multivalente interactie. Het vergroten van de polymeer lengte of de antilichaam dichtheid leidt tot een sterkere activatie, wat overduidelijk aangeeft dat de multivalente interacties tussen het polymeer gefuntionaliseerd met antilichamen en de T-cellen erg belangrijk zijn. Het langste polymeer met de hoogste antilichaam dichtheid geeft een multivalente versterkings factor van 67 ten opzichte van het vrije antilichaam. Verder laat dit hoofdstuk zien dat dit multivalente bioconjugaat niet alleen de effectieve concentratie verlaagd die nodig is om een respons te krijgen, maar dat het ook de T-cel signalering verandert. De signalerende T-cellen werden voor langere tijd gemonitord en er werd waargenomen dat het multivalente polymeer de duur van de activatie significant verlengt.

Een volgende stap in de ontwikkeling van een vaccin voor immuuntherapie is de functionalisatie van de polymeren met een tweede, co-stimulerend anti-CD28 antilichaam (hoofdstuk 4).   Het effect van deze nieuwe bioconjugaten op T-cel differentiatie werd onderzocht, waarbij er werd aangetoond dat polymeren gefunctionaliseerd met beide antilichamen, de effector ($CD8^+$) en helper (T_h1 $CD4^+$), cel populaties vergroten zonder dat de regulatorische T-cel populatie verhoogd wordt. Deze specifieke respons heeft de co-stimulatie van anti-CD28 antilichamen nodig. Een optimale respons wordt alleen verkregen wanneer beide antilichamen aan hetzelfde polymeer gekoppeld zitten. Dit laat overduidelijk zien dat de ordening van beide signalen een belangrijke parameter is in de effectieve stimulatie van T-cellen en dat zulke geometrische effecten meegenomen moeten worden in het ontwerpen van T-cel stimulerende vaccins.

In hoofdstuk 5 wordt de aandacht verlegd naar de biofunctionalisatie en toepassingen van **PIAA-OEG$_3$-OMe** hydrogels. Deze hydrogels worden stijver wanneer ze vervormd worden. Deze niet-lineaire mechanische eigenschap is normaal in biologische materialen maar erg zeldzaam in synthetische hydrogels. Polyisocyanopeptide hydrogels zijn daarom een uitermate geschikt systeem om het effect van deze verstijving op cellulaire, mechanogevoelige transductie processen te bestuderen. Bovendien kan de synthetische polyisocyanopeptide hydrogel mechanische en biochemische parameters ontkoppelen, wat bijna onmogelijk is in biologische hydrogels. Een van deze parameters is de stress waarbij de verstijving van de hydrogel optreedt, de kritische stress. Door de lengte van de **PIAA-OEG$_3$-OMe** polymeren te variëren kan deze parameter verandert worden zonder dat andere parameters zoals de algehele hydrogel stijfheid veranderen. In dit hoofdstuk wordt de invloed van de kritische stress op stamcel differentiatie onderzocht.   Om dit te bewerkstelligen werden de azide handvatten gefunctionaliseerd met GRGDS-peptiden die binden aan integrines, zodat cellen zich aan de hydrogel kunnen hechten. Stamcellen die gekweekt werden in hydrogels met een lage kritische stress differentieerden tot vetcellen, terwijl stamcellen die gekweekt werden in hydrogels

met een hogere kritische stress zich ontwikkelden tot botcellen. Deze belangrijke vinding laat zien dat deze hydrogels een hoog potentieel hebben als 3D celkweek matrices om fundamentele mechanobiologische processen te bestuderen. Tegelijkertijd biedt het een nieuw platvorm voor weefselkweek toepassingen.

In hoofdstuk 6 werd het **PIAA-OEG₄-OMe** polymeer gefunctionaliseerd met twee kleine stukjes DNA, die op hun beurt gehybridiseerd kunnen worden met een derde overbruggende DNA-sequentie. De mechanische eigenschappen van de resulterende DNA gecrosslinkte hydrogel konden dynamisch beïnvloed worden door de concentratie van de DNA crosslinker of de temperatuur aan te passen. Op deze manier werd een multifunctionele, stimuli gevoelige hydrogel verkregen, die als nieuw materiaal voor biosensoren kan dienen.

Het synthetiseren van de polyisocyanopeptide bioconjugaten vergt een uitgebreide en moeilijke zuivering. Een groot gedeelte van het polymeer gaat verloren tijdens deze zuivering, vooral als het gekoppelde biomolecuul een groot molecuulgewicht (grote afmeting) heeft. Om de opbrengst te vergroten en het aantal stappen te verkleinen werd een op affiniteit gebaseerde zuiveringsmethode ontwikkeld (hoofdstuk 7). De polyisocyanopeptiden werden gefunctionaliseerd met biotine affiniteits labels, die vervolgens gebruikt worden om het polymeer-bioconjugaat te zuiveren met agarose gebonden mono-avidine. De toepasbaarheid van deze methode werd gedemonstreerd door zowel een antilichaam als een enzym-polymeer conjugaat te maken en te zuiveren. Beide conjugaten werden gezuiverd met een opbrengst tussen de 10-25%, wat een significante verbetering is in vergelijking met de oude, op dialyse of ultrafiltratie gebaseerde zuiveringsmethoden (<1 % opbrengst). Bovenal, zijn de op deze manier verkregen polymeer conjugaten erg zuiver. Dit zorgt er niet alleen voor dat de analyse van de conjugaten vergemakkelijkt wordt, maar zal hoogstwaarschijnlijk ook leiden tot een verbetering van de functionaliteit in de toepassing waarin ze gebruikt worden.

Het laatste hoofdstuk van dit proefschrift vat de kennis samen die verkregen is tijdens het synthetiseren, zuiveren en testen van de verschillende bioconjugaten. Het beschrijft ook belangrijke aspecten die in acht moeten worden genomen wanneer deze toepassingen geïmplementeerd worden in de samenleving. Verder worden toekomstige richtingen voor vervolgonderzoek belicht. Alles bij elkaar, laat dit proefschrift zien dat water oplosbare polyisocyanopeptiden een zeer interessante en veelzijdige klasse van biocompatibele polymeren zijn, met een brede toepasbaarheid.

Dankwoord/ Acknowledgements

Alle hoofstukken zijn af, de omslag is ontworpen en mijn hele proefschrift is netjes opgemaakt en geredigeerd, maar de belangrijkste pagina's moeten nog geschreven worden. Bladzijden waarin ik graag iedereen wil bedanken die heeft bijgedragen aan mijn promotie. Zonder jullie was dit boekje er nooit geweest.

Allereerst wil ik mijn promotor, Prof. dr. Alan Rowan bedanken. Bedankt dat ik in je groep mocht werken en dat je me altijd alle vrijheid hebt gegeven om mijn eigen plan te trekken. Ook wil ik graag mijn tweede promotor Prof. dr. Carl Figdor bedanken voor de goede samenwerking in het synthetische dendritische cel project. De communicatie tussen chemici en immunologen was soms best lastig, maar ik denk dat we door de jaren heen onze eigen "taal" hebben ontwikkeld en we elkaar steeds beter begrijpen. Ik ben daarom ook blij dat ik momenteel nog vervolgonderzoek kan doen in jouw groep, dank daarvoor.

Next, I would like to thank Dr. Kerstin Blank. Without your guidance I would be nowhere. Thanks for everything you did for me. I enjoyed all the scientific discussion we had over the last 5 years and you taught me so much about how to perform research. Your precise approach is a true inspiration for us PhD students. I wish you and your group at the Max Planck Institute in Potsdam all the best.

Tijdens mijn promotieonderzoek heb ik het geluk gehad om meerdere studenten te begeleiden. Als eerste bedank ik San-san, met wie ik de synthese van de azide gefunctionaliseerde polyisocyanopeptiden geoptimaliseerd heb. Ook dank ik Joris. Helaas heeft jouw werk niet een hoofdstuk opgeleverd in deze thesis, maar van jouw levensverhaal heb ik veel belangrijkere dingen geleerd. Ik bedank ook Jeroen, uiteindelijk waren de polymeren die jij hebt gemaakt tijdens je stage een succesvolle basis voor een mooie publicatie! Bovenal ben je tijdens je stage een vriend geworden en ik wens je alle goeds met je eigen promotieonderzoek in Milaan. Verder bedank ik Stijn, heel veel succes in Eindhoven! Anne, ook jij bedankt voor het werk dat je voor mij gedaan hebt. Mijn laatste student was Bob, jij heb zowel je bachelor als je master stage bij mij gedaan. Bedankt voor de leuke tijd en ik wens je veel succes met het afronden van je studie. Hopelijk komen we elkaar later nog eens tegen.

Maarten en Danny, bedankt dat jullie mijn paranimfen willen zijn. Jullie zijn fijne lunchmaatjes en zonder jouw gemopper Maarten en jouw lompe grappen Danny had ik het niet gered. Maarten, ik wens je veel sterkte met het afronden van je proefschrift, alhoewel dat met het aantal publicaties dat jij op je naam hebt staan geen enkel probleem mag zijn. Danny, ook jij veel succes in de komende jaren van je promotieonderzoek.

Ik bedank alle technici die mij de afgelopen jaren zo goed geholpen hebben. Theo, Ad, Paul. S, Paul. W, Helene, Peter van G. en Jan, dank! Een speciaal woord van dank voor Peter van D., jouw lach en vriendelijkheid gaven me dikwijls een goed gevoel en weer energie om door te gaan. Ook dank ik Paula voor alle administratieve zaken.

I thank all my colleagues inside and outside my own department, that I met over the last years: Themis, Petri, Sophie, Monique, Anna, Emilia, Gosia, Rajat, Swapneel, Subhra (I never met someone that worked harder then you), Zaskia, Dion, Paul, Daniel, Arjan, Hongbo, Bao, Pim, Onno, Daniel, Kathleen, Alexandra, Jialiang, Masoumeh, Joris, Joan, Jos, Roman, Jasmin, Vijay, Joep, Lianne, Nanda, Mark, David, Marlies Frank, Hans, Shaji, Albert, Bas, Iris, Martijn, Jurjen, Jorieke and all the ones that I forgot, thank you all!

Ik wil graag twee collega's in het bijzonder bedanken. Abbas, mijn Iraaks-Nederlandse vriend. Bedankt voor je gulle lach, en je bereidheid om iedereen te helpen. Jij bent een voorbeeld voor ons allemaal. Loek, ook jij bedankt. We werken nog steeds samen en dat bevalt me erg goed, hopelijk kunnen we samen nog een paar mooie projecten afronden. Ik moet altijd weer lachen om onze Whatsapp vergaderingen.

Natuurlijk zijn er ook naast het werk vele mensen die ik wil bedanken. Ik dank Maarten B. Richard, David, Jacco, Geert, JW, Maarten M., en de Bazalea boys voor de nodige afleiding buiten het werk. Natuurlijk dank ik ook mijn lieve schoonfamilie, bedankt voor de interesse en dat jullie altijd klaar staan voor ons.

Ik heb het geluk om uit een groot gezin te komen, ik dank al mijn broers, zussen, zwagers, schoonzus en neefjes en nichtjes voor de ondersteuning en de gezelligheid als we met zijn allen bij elkaar zijn. Jos, Aafke, Dorieke, Axel, Lauren, Mathis, Mels Trienke, Wessel, Julia, Daan, Alice, Edwin, Judie, Vera en Gerjan, bedankt! Een speciaal woord van dank voor mijn lieve ouders. Pa en Ma, ik ben jullie eeuwig dankbaar voor de vrijheid die ik altijd gekregen heb. Zonder jullie hulp in de afgelopen drukke tijd, van verhuizen, de geboorte van de tweeling en het afronden van dit boekje hadden we het niet gered.

De laatste woorden van dank gaan naar mijn lieve vrouw Annette en onze mooie tweeling Jonas en Lotte. Jullie zijn alles voor me, en ik zou niet weten wat ik zonder jullie zou moeten. Annette, wat is het heerlijk om een vrouw te hebben die helemaal niks van scheikunde afweet, maar toch altijd de moeite neemt om naar mijn verhaal te luisteren. Jij bent mijn beste vriend, je bent er altijd voor me, ik ben niks zonder jou! Samen kunnen wij de hele wereld aan!

Roel

Curriculum vitae

Roelof (Roel) Hammink was born on July 29th 1986 in Hengelo, the Netherlands. After attending secondary school at the Greijdanus College in Zwolle, he studied chemistry at the Saxion University of Applied Sciences. After one year, in 2004, he moved to the Radboud University in Nijmegen to continue his study in chemistry. He obtained his Master's degree in 2011, after which he started his PhD research in the Molecular Materials group, under the supervision of Prof. dr. Alan E. Rowan and Dr. Kerstin G. Blank. This research was funded by NanoNextNL and the most important result are described in this thesis. During his PhD research he had a close collaboration with the Tumor Immunology group of Prof. dr. Carl G. Figdor. Therefore, he decided to join this department in early 2016, where he is currently working as a postdoctoral researcher.

List of publications

Affinity-based purification of polyisocyanopeptide bioconjugates.
Hammink, R.*; Eggermont, L. E.*; Zisis, T.*; Figdor, C. G,; Rowan. A. E.; Blank, K. G. *Manuscript in preparation.*

Controlling T-cell activation with synthetic dendritic cells using the multivalency effect.
Hammink, R.*; Mandal, S.*; Eggermont, L.; Nooteboom, M.; Willems, P. H. G. M.; Tel, J.; Rowan, A. E.; Figdor, C. G.; Blank, K. G. *Manuscript ready for submission.*

Order at extreme dilution.
Alvarez Fernandez, A.*; Hammink, R.*; Kragt, S.*; Cattaneo, L.; van der Velden, J.; Savoini, M.; Rasing, T.; Rowan, A. E.; Collings, P. J.; Kouwer, P. H. J. *Adv. Funct. Mater.* **2016**, doi:10.1002/adfm.201602913

DNA-responsive polyisocyanopeptide hydrogels with stress-stiffening capacity.
Deshpande, R. S.*; Hammink. R.*; Das, R. K.; Nelissen, F. H. T.; Blank, K. G.; Rowan, A. E.; Heus, H. A. *Adv. Funct. Mater.* **2016**, doi:10.1002/adfm.201602461

Stress-stiffening-mediated stem-cell commitment switch in soft responsive hydrogels.
Das, R. K.; Gocheva, V.; Hammink, R.; Zouani, O. F.; Rowan, A. E. *Nat. Mater.* **2016**, *15* (3), 318–325.

Polymer-Based Synthetic Dendritic Cells for Tailoring Robust and Multifunctional T Cell Responses.
Mandal, S.; Hammink, R.*; Tel, J.*; Eksteen-Akeroyd, Z. H.; Rowan, A. E.; Blank, K.; Figdor, C. G. *ACS Chem. Biol.* **2015**, *10* (2), 485–492.

Therapeutic nanoworms: towards novel synthetic dendritic cells for immunotherapy.
Mandal, S.; Eksteen-Akeroyd, Z. H.; Jacobs, M. J.; Hammink, R.; Koepf, M.; Lambeck, A. J. a.; van Hest, J. C. M.; Wilson, C. J.; Blank, K.; Figdor, C. G.; Rowan, A. E. *Chem. Sci.* **2013**, *4* (11), 4168–4174.

* = equal contribution